EXTREME HYDRODYNAMIC LOADING ON NEAR-SHORE STRUCTURES

Taofiq Qassim Al-Faesly

Thesis submitted to the

Faculty of Graduate and Postdoctoral Studies
In partial fulfillment of the requirements for the degree of
Doctor of Philosophy in Civil Engineering

Department of Civil Engineering

Faculty of Engineering
University of Ottawa

THESIS SUPERVISORS

Ioan Nistor .....Professors - University of Ottawa

Dan Palermo .....Associate Professor - York University

Andrew Cornett .....Adjunct Professor - National Research Council of Canada

THESIS EXAMINERS COMMITTEE

Ana Maria da Silva .....Professor - Queen's University

Majid Mohammadian .....Associate Professor - University of Ottawa

Jeffery Erochko .....Assistant Professor - Carleton University

Julio Angel Infante Sedano .....Assistant Professor - University of Ottawa

Date of Oral Defence

Wednesday, December 16, 2015

ABSTRACT

The main objective of this study was to investigate and quantify the impact of extreme hydrodynamic forces, similar to those generated by tsunami-induced inundation, on structural elements. As part of a comprehensive experimental program and analytical study, pressures, base shear forces, and base overturning moments generated by hydraulic bores on structural models of various shapes were studied. In addition, the impact force induced by waterborne wooden debris of different shapes and masses on the structural models was also investigated. Two structural models, one with circular and the other with square cross-section, were installed individually downstream of a dam-break wave in a high-discharge flume. Three impounding water heights (550, 850 and 1150 mm) were used to produce dam-break waves, which have been shown to be analogous to tsunami-induced coastal inundation in the form of highly turbulent hydraulic bores. Time-history responses of the structural models were recorded, including: pressures, base shear forces, base overturning moments, lateral displacements, and accelerations. In addition, the flow depth-time histories were recorded at various locations along the length of the flume. Regular and high-speed video cameras were used to monitor the bore-structure interaction. The effect of initial flume bed condition ("wet" or "dry" bed) on the forces and pressures exerted on the structural models were also investigated. Moreover, the vertical distribution of pressure around the models was captured. Simple low-height walls with various geometries were installed upstream from the structural models to investigate their efficiency as tsunami

mitigation measures. The experimentally recorded data were compared with those estimated from currently available formulations.

The results and analysis of the simulated tsunami-induced bore presented in this study will be of significant use to better estimate forces exerted on structures by tsunami-induced turbulent bores. It is expected that this work will contribute to the new ASCE7 Chapter 6 - Tsunami Loads and Effects in which two of this author's academic supervisors, Drs. Ioan Nistor and Dan Palermo, are members.

ACKNOWLEDGEMENTS

I would like to express my appreciation to my supervisors Dr. Dan Palermo, Dr. Ioan Nistor, and Dr. Andrew Cornett for their advice, helpful critique, encouragement, and diligence. The revisions, suggestions, and comments of my supervisors have improved the content and quality of this thesis: for their efforts I am grateful.

I would like to extend my sincere acknowledgements for the help of everyone working in the Coastal, Ports, and Offshore Group at the Ocean, Coastal and River Engineering (OCRE) of the National Research Council (NRC) of Canada in Ottawa. Using their facilities to perform the experiments and their significant assistance in the preparation of the flume and sensors greatly facilitated the experimental set-up and subsequent extensive testing program. The close mentoring of Dr. Andrew Cornett, the Coastal, Ports and Offshore Group Leader, throughout the experimental program had quite an impact on the research outcomes. I would like to acknowledge the help of David Hnatiw, technician-in-charge with instrumentation, and of Nathalie Brunette. I would like to thank to John Perrins, senior technical officer of the machine shop at the University of Ottawa, for building the acrylic structural models used in this research.

Also, I would like to offer my thanks to the following students, who helped me in performing the physical experiments:

- Takahito Mikami: Graduate student at the Department of Civil and Environmental Engineering, Waseda University, Tokyo, Japan.
- Matthieu Stapor: Quality and safety coordinator in Port of La Rochelle, France.
- Gildas Lechevretel: Student at ENSIL in Limoges, France.
- Julien Neau: Engineer with E3D-Environnement in Paris, France.
- Anna Lena Reinbold: Research visiting student from the Department of Hydromechanics and Coastal Engineering at the Technical University of Braunschweig, Germany.

Thanks to my research colleagues at the University of Ottawa, specifically Dr. Muslim Majeed, the structures laboratory technical officer for his help.

Finally, I would like to thank my parents, my wife, and my children to whom I owe everything for their patience and continuing love and support.

TABLE OF CONTENTS

LIST OF FIGURES

Chapter FOUR: EXPERIMENTAL PROGRAM.....

LIST OF TABLES

LIST OF SYMBOLS

Symbol	Explanation of symbol	Unit
English symbols		
A_f	Area of the floor panel	[m]
a_H	Tsunami wave amplitude	[m]
B_h	Width of the structure perpendicular to flow direction	[m]
c	Hydrodynamic mass coefficient	[ND]
C_B	Blockage coefficient	[ND]
C_D	Drag coefficient	[ND]
C_F	Force coefficient	[ND]
C_I	Importance coefficient	[ND]
C_M	Added-mass coefficient	[ND]
C_o	Orientation coefficient	[ND]
C_p	Pressure coefficient	[ND]
C_s	Slope coefficient	[ND]
C_u	Uplift force coefficient (used by FEMA P646 and taken equal to 3.0)	[ND]
C_v	Velocity coefficient	[ND]
D	Debris diameter	[m]
d_S	Inundation depth	[m]
DWT	Dead-weight tonnage of the debris	[N]
e	Eccentricity of the debris impact from the center of the model	[m]
F_b	Buoyant force	[N]
F_d	Hydrodynamic force	[N]
F_{dm}	Debris damming force	[N]
F_H	Hydrodynamic force	[N]

F_I	Debris impact force	[N]
F_s	Total surge force per unit width of structural wall	[N]
f_M	Darcy friction factor for model	[ND]
f_p	Darcy friction factor for prototype	[ND]
f_R	Darcy friction ratio	[ND]
g	Gravitational acceleration	[m. s^{-2}]
H_s	Wave height at the shoreline or the toe of a beach	[m]
h	Bottom boundary elevation from a reference datum	[m]
h_b	Water bore height	[m]
h_f	Inundation depths at the front of a rectangular building	[m]
h_r	Inundation depths at the rear of a rectangular building	[m]
k	Effective combined stiffness of the debris and the impacted structural element	[N. m^{-1}]
k	Constant with value of 0.06	[ND]
$\hat{k}$	Effective contact stiffness of debris impact	[N. m^{-1}]
L	Debris length	[m]
L_M	Length at the model scale	[m]
L_P	Length at the prototype scale	[m]
L_R	Geometric similarity ratio	[ND]
M	Mass	[kg]
m_d	Debris mass	[kg]
n	Manning's coefficient	[ND]
p_m	Maximum tsunami-wave pressure	[Pa]
R	Tsunami inundation depth	[m]
R_h	The hydraulic radius	[ND]
R_{max}	Maximum tsunami inundation depth	[m]
t	Time	[s]
u	Depth-average horizontal velocity in x-direction	[m/s]
u_{max}	Maximum horizontal velocity of the bore flow	[m/s]
u_p	Normal component of velocity against a wall model	[m/s]
u_s	Tsunami bore velocity at the shoreline	[m/s]

u_v	Vertical velocity of the bore flow	[m/s]
V	Volume of water displaced by the structure	[m^3]
x	Horizontal axis along the flow direction	[m]
y	Horizontal axis transverse to the flow direction	[m]
z	Vertical axis	[m]

Greek symbols

α	Impact coefficient equal to 1.36	[ND]
Δt	Debris impact duration	[s]
Δx	Stopping distance of the debris in (m), distance that debris travels from point of contact with the structure until debris fully stopped	[m]
γ_w	Specific weight of water	[$N.m^3$]
λ	Similarity variable	[ND]
λ_w	Value of λ at the wall	[ND]
η	Water surface	[m]
η_{max}	Maximum inundation depth	[m]
ρ	Water density	[kg. m^{-3}]
ρ_s	Seawater density, including entrained sediment load	[kg. m^{-3}]
σ_f	Yield stress of wood	[Pa]
θ	Orientation angle of the debris	[degree]
θ_b	Bed slope	[degree]
φ	Debris impact angle (angle between the impact point on the model surface and the flume centerline)	[degree]

LIST OF ABBREVIATIONS

Abbreviation	Explanation of abbreviation
850_NW_SQ_0R	Test with 850 mm impoundment depth, no mitigation wall, square structural model, 0˚ rotation angle (pressure measured on the upstream face of the model)
850_NW_SQ_90R	Same as above, 90˚ rotation angle (pressure measured on the side face of the model)
10W45-1D	100 mm height, 45˚-inclined mitigation wall installed at 1D (305 mm) upstream from the structural model
15W90-3D	150 mm height, 90˚ (vertical) mitigation wall installed at 3D (915 mm) upstream from the structural model
10WAR-1D	100 mm curved mitigation wall installed at 1D (305 mm) upstream from the model
2kg1P	Wooden debris of two kilograms with dimensions of 76.2 x 76.2 x 916 mm
2kg2P	Wooden debris of two kilograms with dimensions of 76.2 x 152.4 x 490 mm
6DOF	Six-degree of freedom load cell
ASCE	American Society of Civil Engineers.
CCH	City and County of Honolulu
CCM	Coastal Construction Manual
CHC	Canadian Hydraulic Centre
EERI	Earthquake Engineering Research Institute
FEMA	Federal Emergency Management Agency
FFT	Fast Fourier Transform
IHS	Hydrostatic pressure distribution at the impulsive flow state
IRS	Hydrostatic pressure distribution at the run-up flow state
IQS	Hydrostatic pressure distribution at the quasi-steady flow state
LVDT	Linear Variable Distance Transformer

NRC	National Research Council of Canada
OCRE	Ocean, Coastal and River Engineering
PT	Pressure Transducers
RMS	Risk Management Solutions
SMBTR	Structural Method of Design Buildings for Tsunami Resistant
WG 1, 2 ...	Water level gauge No. 1, 2...

DEFINITIONS

The following are definitions of significant terms which appear in this thesis. The terminologies are consistent with ASCE-7 (2010), FEMA P646 (2012), and the Coastal Construction Manual (FEMA, 2005).

Bathymetry: Underwater configuration of a bottom surface of an ocean, estuary, or lake.

Bore: A long, broken wave propagating into a quiescent body of water, with an abrupt increase in water depth at its front face covered with turbulent, tumbling water.

Bore Height: The height of a broken tsunami surge above the water level in front of the bore or grade elevation if the bore arrives on nominally dry land.

Building Codes: Regulations adopted by local governments that establish standards for construction, modification, and repair of buildings and other structures.

Celerity: The velocity of the tsunami wave form, equal to wavelength divided by period.

Channelized Scour: Scour that results from broad flow that is diverted to a focused area such as return flow in a pre-existing stream channel or alongside a seawall.

Closure Ratio: (of Inundated Projected Area): Ratio of the area of enclosure, not including glazing and openings that are inundated, to the total projected vertical plane area of the inundated enclosure surface exposed to flow.

Collapse Prevention Structural Performance: The post-event damage state in which a structure has damaged components and continues to support gravity loads but retains little or no margin against collapse. Structural component acceptability criteria are given in ASCE 41.

Critical Facility: Buildings and structures that provide services that are determined by local governments to be essential for the continued functioning of a community, such as facilities for power, fuel, water, and communications, public health, major transportation infrastructure, and essential government operations.

Deadweight Tonnage: Deadweight Tonnage (DWT) is the vessel's Displacement Tonnage (DT) minus its Lightship Weight (LWT). A classification used for the carrying capacity of a

vessel that is the sum of the weights of cargo, fuel, fresh water, ballast water, provisions, passengers, and crew. It does not include the weight of the vessel itself.

Debris: Solid objects or masses carried by or floating on the surface of moving water.

Debris impact loads: Loads imposed on a structure by the impact of waterborne debris.

Design Basis Tsunami Parameters: The tsunami parameters used for design, consisting of the inundation depths and flow velocities at the stages of inflow and outflow most critical to the structure.

Displacement Tonnage: The total weight of a fully loaded vessel.

Froude Number: $Fr = u/\sqrt{(gh)}$: Used to quantify the normalized tsunami flow velocity.

Grade Plane: A horizontal reference plane representing the average of finished ground level adjoining the structure at all exterior walls. Where the finished ground level slopes away from the exterior walls, the grade plane is established by the lowest points within the area between the structure and the property line or, where the property line is more than 6 ft (1.83 m) from the structure, between the structure and points 6 ft (1.83 m) from the structure.

Hydraulic Radius: The measure of channel flow efficiency; it is the ratio of the cross-sectional area of the flow to its wetted perimeter.

Hydrodynamic Loads: Loads imposed on an object, such as a building, by water flowing against and around it. Among these loads are positive frontal pressure against the structure, drag effect along the sides, and negative pressure on the downstream side.

Hydrostatic Loads: Loads imposed on a surface, such as a wall or floor slab, by a standing mass of water. The water pressure increases linearly with the water depth; hence, the hydrostatic loads increase with the square of the water depth.

Impact Loads: Loads that result from debris or other object transported by the tsunami and striking a structure or portion thereof.

Inundation Depth: The depth of design tsunami water level with respect to the grade plane at the structure.

Momentum Flux: The quantity $\rho_s hu^2$ for a unit width based on the depth-averaged flow speed over the flow depth h, for equivalent fluid density ρ_s having the units of force per unit width.

Reynolds Number: The ratio of the inertial forces to viscous forces and usually used to determine dynamic similitude.

Sea Wall: Solid barricade built at the water's edge to protect the shore and to prevent inland flooding.

Shoaling: The increase in wave height caused by the decrease in water depth as a wave travels into shallower water.

Soliton Fission: Short period waves generated on the front edge of a tsunami waveform under conditions of shoaling on a long and gentle seabed slope, or having abrupt seabed discontinuities such as fringing reefs.

Storm Surge: Rise in the water surface above normal water level on an open coast due to the action of wind stress and atmospheric pressure on the water surface.

Surge: Rapidly rising water level resulting in horizontal flow inland.

Topography: Configuration of a terrain, including its relief and the position of its natural and man-made features.

Tsunami: A series of waves with variable long periods, mostly resulting from earthquake induced uplift or subsidence of the sea floor. Other causes include large landslides near the coast or underwater, and undersea volcanic eruptions.

Tsunami Bore: Broken wave generated on the steep front edge of a long period tsunami waveform when shoaling over mild seabed slopes or abrupt seabed discontinuities such as fringing reefs.

Tsunami Inundation Elevation: The elevation, measured from sea level, at the location of the maximum tsunami penetration.

Tsunami Prone Region: The region where a quantified probability in the recognized literature of tsunami inundation hazard due to tsunamigenic earthquakes in accordance with the Probabilistic Tsunami Hazard Analysis.

Tsunami Vertical Evacuation Refuge: A structure designated to serve as a point of refuge to which a community's population can evacuate above a tsunami when high ground is not available.

Waterborne Debris: Any object transported by tsunami waves (e.g., driftwood, small boats, shipping containers, automobiles, etc…).

CHAPTER 1

INTRODUCTION AND SCOPE

1.1 Introduction and Motivation

Near-shore infrastructure located in coastal flooding- or tsunami-prone areas is vulnerable to extreme hydrodynamic loading due to surging seawater that propagates inland. Such coastal surges may arise due to storms, hurricanes, or tsunamis. Recent tsunami events (2004 Indian Ocean Tsunami, 2010 Chile Tsunami, and 2011 Tohoku, Japan Tsunami) caused widespread damage resulting in unprecedented human and economic losses which overwhelmed the capacity of many countries, such that international aid was necessary in the recovery and reconstruction process (particularly for the 2004 and 2011tsunami events). Many international, interdisciplinary research teams conducted post-tsunami reconnaissance visits to the damaged regions to investigate and understand the effects of tsunamis on infrastructure and communities [Ghobarah et al. (2006); and Earthquake Engineering Research Institute, EERI (2011)]. The coastal engineering reports that followed these reconnaissance trips highlighted four main themes: (1) spatial extent of the coastal flooding was significant for large tsunami events; (2) damaged structures were exposed to extreme hydrodynamic and debris impact forces for which they were not designed; (3) failure modes of the structures were associated with different force components and demonstrated the complexity of the tsunami bore/surge-structure interaction; and (4) well-engineered

buildings survived the tsunami event with only non-structural damage. However, to date, there is no mandatory engineering code/standard that provides explicit guidance on estimating tsunami forces to enable engineers to design tsunami-resilient structures. Therefore, to address this lack of information, experimental testing of tsunami-like hydraulic bores impacting structural models is the first step to better understand the tsunami bore behaviour, bore-structure interaction and structural response. Such comprehensive experimental testing would provide data necessary to develop tsunami-resistant engineering guidelines, which will help reduce structural damage and subsequent loss of lives.

Observations from past tsunami events demonstrated that certain types of construction are susceptible to damage due to the high flow velocity of the water. However, there is evidence that properly engineered structural systems can survive tsunami inundation and serve as evacuation shelters. This has led researchers and engineers to propose and verify tsunami loading formulas to be used in the structural design process.

Over the past decade, flooding of residential and industrialized communities from various sources (tsunamis, storms, riverine floods, etc.) became one of the more significant hazards with tremendous impact on human lives and economic activity. Particularly, tsunami events demonstrated that communities located in coastal regions that lie close to seismically active subduction zones are at high risk. The most recent disaster report published by the US Disaster Center (Guha-Sapir 2011) indicated that the first six months (1st semester) of 2011 was witness to devastating impacts on human communities as a result of natural disasters. Table 1.1 provides a comparison of the number of disasters and the losses during this period, with corresponding averages from years 2001-2010. Figure 1.1 displays the percentage of natural disasters and the number of people affected by disaster type during the first six months of 2011. The percentage of deceased due to flood was 90.5% (86% of those were due to tsunami). The significant human loss highlights the need for designing and building flood-resilient structures. Moreover, the fourth most deadly and the most costly disaster in human history were due to the 2004 Indian Ocean Tsunami and the 2011 Tohoku Tsunami, respectively. The report cited that four of the ten largest disasters by number of people killed and five of the ten most costly disasters that occurred during the first six months of 2011 were caused by flood. These numbers reflect the threat posed by

floods in general and for tsunamis in particular: unlike floods which can often be forecasted in advance, the occurrence of tsunamis is unpredictable.

Table 1.1 Global statistics of disasters during 2001-2011 (Guha-Sapir, 2011)

Attribute	**2011 1st semester**	**2001-2010 1st semester (average)**
No. of disasters	108	164
No. of people killed	23,638	52,579
No. of people affected	43,784,902	73,685,153
Economic damages (million $US)	253,230	35,356

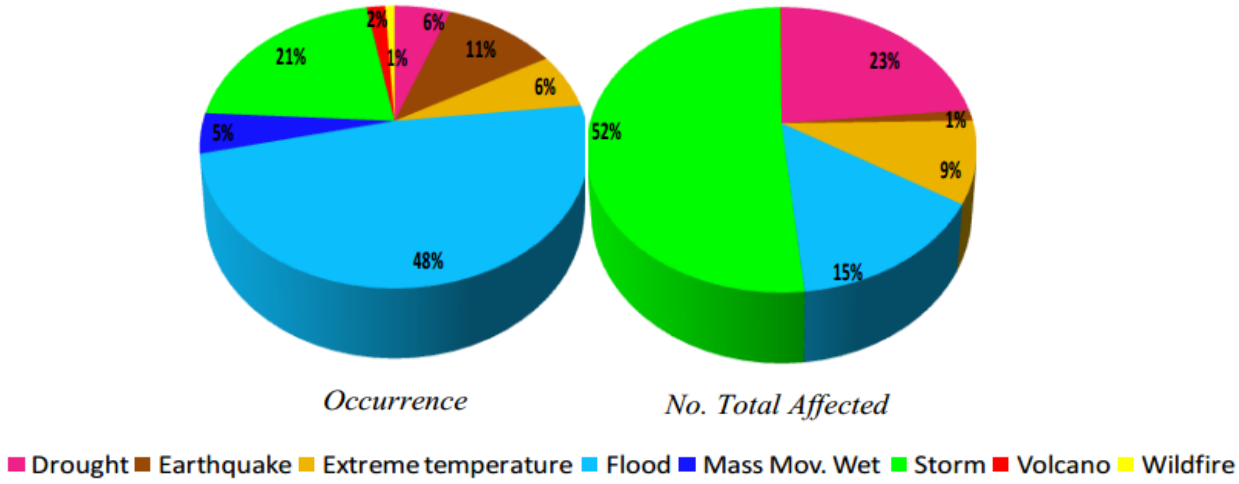

Figure 1.1 Percentage of natural disasters by type and percentage of people affected by disaster type during the 1st semester of 2011 (Guha-Sapir 2011)

The strategy to mitigate tsunami hazard in the past mostly focused on vertical and horizontal evacuation. However, while evacuation saves lives, it does not address deficiencies in resistance of structures to such loading; therefore, this study evolved to address the current lack of knowledge in structural design against tsunami loading and to investigate existing tsunami load formulas.

According to the U.S. Geological Survey, more than 227, 000 lives were lost due to the 2004 Indian Ocean Tsunami, Tsunamis and Earthquakes (2004). In spite of being a low-probability, high-consequence event, an analogous disaster could happen elsewhere,

specifically in the Pacific Ocean, the Caribbean Sea, or the Mediterranean Sea. There is usually a short lead time preceding the arrival of the first tsunami wave; this ranges from minutes for near-shore sources to hours in the case of distant sources. Given that mega-tsunamis are rare events, and since early warning is possible for the case of the Pacific Ocean region, evacuation has been, for decades, the primary mitigation strategy. Therefore, most research has concentrated on the advancement of efficiency of tsunami generation, propagation and coastal flooding, on the development of efficient warning systems, tsunami-flood maps, and on tsunami awareness and training. From the perspective of saving lives, this approach can only be effective if evacuation to higher ground is available and feasible. However, this approach does not address the potentially major damage to critical coastal infrastructure, such as buildings, bridges, oil and liquefied natural gas (LNG) storage facilities, power plants, and harbours: failure to such infrastructure creates significant economic and collateral damage. The proliferation of construction of critical infrastructure in coastal zones has, in turn, required a more advanced understanding of design procedures for building structures that are tsunami-resistant. In low-elevation coastal pits or flat zones, evacuating people to higher ground may not be possible. "*In these situations, the only feasible way to minimize human casualties is to evacuate people to the upper floors of tsunami-resistant buildings*", as stated by Yeh and Shuto (2009). In the case of near-source events, these buildings need to be designed and constructed to survive both strong earthquakes and ensuing tsunamis.

1.2 Research Objectives

The onshore run-up behaviour of tsunami waves is a challenging hydrodynamic problem. Flow motion near the run-up front is characterized by strong nonlinearity. Near-shore tsunami waves break resulting in a turbulent and intrinsically three-dimensional flow. The effects of bottom friction along the shoreline are very important particularly when the flow depth is relatively small near the wave front. Therefore, the flow dynamics of the run-up process are complex and many aspects are still not well understood. Nevertheless, an accurate method for estimating run-up motion is crucial for the prediction of the forces induced on structures exposed to the effects of tsunamis and storm surges.

Past studies in this field focused on small-scale tests and/or on a specific structural element (e.g. walls). In those tests, the structural models blocked the bore flow which is not representative of actual tsunami-structure interaction. Tsunami waves will impact a structure and then flow around it. Thus, the hydraulic bore-structure interaction is more complex than what is demonstrated through testing of walls with widths extending across the full width of the test facility. Moreover, surface tension effects are important in the bore run-up front dynamics for past small-scale experimental studies.

Based on the above, this study aimed to investigate the following overarching areas of tsunami-induced forces on near-shore structures and tsunami mitigation measures:

1. Improve the understanding of tsunami-induced hydraulic bores propagating onshore, and study the relation between the maximum inundation depth and the bore velocity.
2. Understand the tsunami-induced bore-structure interaction mechanisms and the effect of the velocities and pressures of simulated hydraulic bores on the hydrodynamic loading induced on structural models. The following aspects were investigated as part of this objective:
    a. The correlation between the bore-induced force- and the bore depth-time histories;
    b. The effect of initial field-bed condition (wet or dry) on the magnitude of the exerted forces; and
    c. The assessment of tsunami bore-induced force formulae available in recent engineering guidelines.
3. Investigate impact forces due to waterborne debris on a structural model, and investigate the effects of mass, size, angle of impact and geometry of debris on the magnitude of the force. Furthermore, assess currently available debris impact force formulae.
4. Propose simple structural elements (walls) to be used as tsunami mitigation measures. Additionally, investigate the effects of different configurations of those elements, including: height, shape (cross-section), and location relative to the

structure to optimize their function in reducing the bore-induced forces on the structural models.

To achieve the objectives, the following research has been completed and presented in this thesis:

- Selection and set up of instrumentation for the two structural models to record: pressures, base shear forces, base overturning moments, lateral displacements, and accelerations.
- Comprehensive experimental testing of two structural models subjected to hydraulic bores.
- Investigation of various test parameters (e.g. impoundment depth, initial flume bed condition, and effect of floating debris) on two structural models with different cross-sections (square and cylinder) subjected to hydraulic bores.
- Utilization of high-speed digital camera (up to 10 000 frames per second) and two regular digital video cameras to capture the hydrodynamics of the bore and the bore-structure interaction, and to capture debris impact on the structural models.
- Investigation of the effects of low-height structural elements placed in different configurations upstream of the structural models on pressures, base shear forces, base overturning moments, lateral displacements, and accelerations experienced by the two structural models.
- Comparison of the base lateral shear forces from state-of-the-art tsunami guidelines (FEMA P-646, 2008 and 2012) with the experimental forces recorded during this study.

1.3 Scope of Research

Videos from the 2004 Indian Ocean and 2011 Tohoku tsunamis illustrated that the tsunami waves broke offshore and advanced inland as hydraulic bores. Chanson (2005 and 2006) discussed the analogy of tsunami-induced bores with those generated by dam-break events. Tsunami bores propagate onshore with considerable depths and high velocities leading to massive damage to near-shore infrastructure. Post-tsunami reconnaissance trips [Chock et al.

2012, EERI 2011, Guha-Sapir 2011, Palermo et al. 2011, Lukkunaprasit and Ruangrassamee 2008, Nistor et al. 2006, RMS 2006, and Nistor et al. 2005] reported structural failures due to bore-structure interaction and due to the impact of waterborne debris. In this research study, a dam-break technique is employed to generate simulated tsunami hydraulic bores to investigate their characteristics and the bore-structure interaction. As the tsunami bore advances towards the shore, its velocity decreases due to bottom friction, local bathymetry and interaction with potential obstacles. To study the relation between bore depth and bore velocity with bore-induced forces, three different impounding water levels were used in this study. In addition, the structural cross-sectional shape was one of the main parameters of this study and included hollow square and hollow circular sections. Limitations of this study are outlined below:

- Only two structural models, set in three different configurations (square, diamond and circular) were investigated: impact of walls was not considered due to the flume geometry limitations.
- Flow conditions in the form of rapid surge, which occur when the bathymetry of the beach is very steep, was not considered in this study.
- The dry bed condition was difficult to achieve due to imperfections of the experimental facility such as the imperfect sealing mechanism of the swinging gate employed in the flume.
- Due to the limited volume of the impounding reservoir, the duration of the sustained flow was limited when compared to actual tsunami-induced bores. However, the duration of sustained flow attained in this experimental program was sufficient to adequately quantify the quasi-steady hydrodynamic flow.

1.4 Novelty of the Research

Although the literature contains several studies [Arikawa 2009, Nistor 2008, Palermo et al. 2007, and Arnason 2005] of near-shore infrastructure subjected to tsunami loading, many of these studies involved structures that were either vertical or inclined walls [Arikawa 2009, Ohmori et al. 2000, and Ramsden and Raichlen 1990]. Others studies investigated the effect of solitary waves, generated by paddles connected to a hydraulic piston of a wave-making machine, on walls or columns. However, tsunami waves often break offshore and propagate

inland as a turbulent hydraulic bore. Furthermore, as the flow impacts external structural elements, part of the flow passes through openings and part is redirected around the structure or structural elements. The forces experienced by the structure must account for the contributions as the flow moves along the sides and back of the structure. Limited studies [Lukkunaprasit et al. 2009, Arnason 2005, Asakura et al. 2002, and Ikeno et al 2001] investigated the effect of the tsunami-induced turbulent bores on structures. Therefore, the novelty of this study is summarized as follows:

- This is one of the first detailed and comprehensive experimental investigations of the effects of tsunami-induced hydraulic bores on structural models by impacting them with hydraulic bores of varying inundation depths.
- While all previous studies focused only on a single wall or column, in this study, two structural models of different cross-sectional shape (circular and square) and three different orientations (circular, square and diamond) were investigated.
- A unique characteristic which distinguishes this study from others is the investigation of the effect of the initial flume bed condition (dry or wet) on the base shear forces, base overturning moments, and pressures experienced by the structural models. This is the first such study which quantified, qualitatively and quantitatively, the effect of the bed condition.
- This is one of the first experimental studies that investigated the effect the debris mass and orientation on the magnitude of impact forces on structural elements.
- This is the first study that has evaluated the effect of structural mitigation measures (walls) on the hydrodynamic loading on structural elements.
- This study is one of the first to present a critical review and evaluation of the formulas proposed by recent engineering tsunami design guidelines to estimate tsunami loads.

1.5 Dissertation Outline

Chapter 1 presents the research objectives, scope, and novelty of this research program. Chapter 2 details the potential tsunami hazard for Canada and includes a review of the state-of-the-art research in the field of tsunami impact on infrastructure. As part of this chapter, a

discussion is provided on the analogy between tsunami propagation inland and the dam-break wave. It also focuses on the impact of debris carried by tsunami bores on near-shore structures and existing mitigation measures. Finally, lessons learned from recent tsunami events are presented. Chapter 3 discusses the state-of-the-art engineering documents that contain prescriptions to determine tsunami loading and effects. Details on calculating tsunami forces as recommended by the most recent tsunami-resistant design document (FEMA P-646 2012) are also included herein. The experimental setup, instrumentation, scaling considerations, testing program and procedures, debris impact and mitigation elements are presented in Chapter 4. Chapter 5 contains the experimental results, analysis and discussions including: processing of raw experimental data, characteristics of the generated hydraulic bores, and pressure-, base shear force-, base overturning moment- and displacement-time histories experienced by the structural models. The effect of the initial flume bed condition (wet or dry) on the pressures and forces induced on the structural model is also presented. Moreover, the influences of location, height, inclination angle and cross-sectional shape of the mitigation walls on the base shear forces, moments and displacements experienced by the structural models are also discussed. Chapter 6 focuses on a review of recent published tsunami guidelines and a critical comparison with results from the experimental program of this study. In this context, a comparison between the experimental bore-induced pressures and forces on the structural models and those calculated using the most recent tsunami-resistant design guidelines is provided. Finally, conclusions and recommendations for future research derived from the results and discussions of this research work are presented in Chapter 7.

CHAPTER 2

BACKGROUND AND LITERATURE REVIEW

2.1 Introduction

Tsunami is a series of waves generated in a body of water as a result of a sudden disturbance that vertically displaces the water column. The origin of the word stems from the Japanese meaning “harbour waves”. Tsunamis can be generated by earthquakes, landslides, volcanic eruptions, underwater explosions or meteorites; however, the most recent major tsunamis have been generated by subduction zone earthquakes.

The focus of the research presented herein is on the effects of tsunamis on near-shore communities and, specifically, the impact of tsunami-induced bores on structures. Therefore, this literature review focuses on the impact of tsunami bores on structures. The following is a brief description of representative past tsunami damage:

- In 1896, the northeast of Japan, along the Sanriku coast, was impacted by a tsunami that was responsible for more than 20 000 deaths. More than 270 km of the coastline was affected by the ensuing coastal inundation. Financial losses were equivalent to 10% of the Japanese national budget at that time. This tsunami was triggered by the Meiji-Sanriku Earthquake (The Central Disaster Prevention Committee of Cabinet Office,

Government of Japan, 2005). This event provided motivation for people to move away from the shoreline.

- In December 1979, in Tumaco, Ecuador, more than 1, 000 casualties and significant damage resulted from a tsunami triggered by an earthquake that occurred offshore of Columbia and Ecuador. Figure 2.1 illustrates significant damage caused by the tsunami to a residential community.

Figure 2.1 Damage to houses in Tumaco, Ecuador, caused by tsunami on December, 1979 (Tsunami Disasters, n. d.)

Tsunami-reporting also increased by virtue of improved global communications. The high number of deaths is partly due to increases in development of coastal regions followed by increases in population density in these areas. Between 1990 and 2000, 82 tsunamis were reported worldwide exceeding the previous average rate of 57 tsunamis per decade. Ten of those events caused more than 4, 000 deaths each (Tsunami Disasters, n. d.). The following is a brief description of the most destructive tsunamis:

- In 1933, the major Showa-Sanriku Tsunami hit the north-east coast of Japan, resulting in 3,064 deaths; loss of life had decreased relative to previous events due to experience and awareness from previous tsunami events. The large extent of damage was related to the coastal zone topography and bathymetry of the narrow bays present along the shores in these areas. The latter caused particularly large wave heights. After this disaster, to protect life and personal property, the local government of the Iwate Prefecture

constructed a 1,960 m-long breakwater at the entrance of Kamaishi Bay. This was intended to address the problems with the near-shore bathymetry and associated tsunami wave amplification in the area.

- In 1993, the northern Island of Hokkaido, Japan, experienced an earthquake that rattled Okushiri Island and triggered a tsunami that caused large-scale damage and fire. This tsunami was characterized by an early arrival time of the first wave of 3 to 5 minutes after the triggering earthquake. Figures 2.2 a) and b) provide an aerial view and indoor view of the damage caused by the Hokkaido Tsunami to Okushiri Island and American Samoa Island, respectively.

(a) (b)

Figure 2.2 Damage due to tsunamis: **a)** Okushiri Island by Hokkaido Tsunami, 1993 (Science and Nature, n. d.); and **b)** damaged boat inside Pago Community Center, American Samoa Island, 2009 (Tsunamis, n. d.)

- On July 17, 1998, tsunami waves impacted Papua New Guinea's north coast and damaged houses and villages. The death toll exceeded 2, 200 people. Although the tsunami was triggered by a moderate earthquake (magnitude of 7.1 on the Richter scale), the waves were much larger than those generated by similar magnitude earthquakes. This apparent discrepancy between the tsunami wave magnitude and earthquake strength provoked speculation among scientists that there may be other tsunami-generating factors that were triggered by the seismic tremors, such as accompanying submarine landslides or an explosion of gas hydrates. Figure 2.3 demonstrates the damage caused to a coastline community in Papua New Guinea (PMEL, 1998).

Figure 2.3 Damage due to tsunami in Papua New Guinea (July 1998) (PMEL, 1998)

The last decade witnessed three major tsunamis: Indian Ocean 2004, Chile 2010, and Tohoku, Japan 2011. These tsunami events caused massive infrastructure damage, devastating economic consequences, and significant loss of life. They also demonstrated the vulnerability of near-shore infrastructure located within the inundation zone to significant damage from the inland-propagating tsunami bores, highlighting a frequently overlooked fact: tsunamis represent one of the most destructive natural disasters. The following is a detailed description of each of the three above tsunamis:

- On December 26, 2004, a 9.1 magnitude (Richter Scale) subduction earthquake occurred in the Indian Ocean, along the north-western coast of the Indonesian island of Sumatra. In this region, the Indian Ocean Plate is moving towards the east and gradually slides underneath the Burma Micro-Plate at a rate of approximately 60 mm/year (USGS 2006). The earthquake focal depth for this event ranged from 10 to 30 km. The main fault rupture zone was approximately 90 km wide and 1, 200 km long, reaching the Andaman Islands at its northern extremity.

  The earthquake triggered a major tsunami that swept across the Indian Ocean reaching, within hours, India, Thailand, and Sri Lanka, and Somalia and Tanzania in Eastern Africa. However, the most significant damage occurred in Banda Aceh, Indonesia, where the maximum tsunami wave run-up height of 48.8 m was measured in Rhitting, near Banda Aceh (Saatcioglu et al. 2005). Casualties from this disaster

exceeded 174, 500, with 51, 500 people missing and approximately 1.5 million people displaced from their homes. Disaster statistics, conducted by Risk Management Solutions (RMS 2006), indicated that the Island of Sumatra was the most affected, where the tsunami destroyed all infrastructure below an elevation of 10 m along 170 km of the coastline. This low-lying region with relatively high population density does not offer any natural vertical evacuation and this was a factor contributing to the high number of casualties. Surveys performed after the tsunami, for regions located 500 km northeast and 1 600 km northwest from the epicentre of the earthquake (Thailand and Sri Lanka, respectively), emphasized that most of the damage was attributed to tsunami-induced inundation and only negligible damage was attributed to earthquake ground shaking [Ghobarah et al. 2006, Nakano 2010]. Figure 2.4 depicts structural failures due to tsunami bore-induced forces in Thailand and Banda Aceh.

(a) (b)

Figure 2.4 Tsunami-induced damage (Nistor et al., 2006): **a)** column failure in concrete frame, Khao Lak, Thailand; and **b)** punching failure of masonry infill walls, Banda Aceh, Indonesia

- On March 27, 2010, an 8.8 magnitude (Richter Scale) earthquake struck offshore Chile, triggering a major tsunami in the Pacific Ocean. The earthquake was generated along the boundary between the Nazca and South American Plates. These two plates converge at approximately 70 mm/year. The rupture zone had a width of over 100 km and a length of approximately 500 km and was parallel to the central coastline of Chile. The tsunami-induced bore penetrated over 1 km inland in many areas. Lagos et al. (2010) conducted a field survey and noted that the maximum wave height was 11.2 m in the town of

Constitución; while 8.6 m-high waves were measured in Dichato and Tome. A localized maximum run-up of 29 m on a coastal bluff in Constitución was reported by Fritz et al. (2010). Many coastal communities suffered widespread damage; however, the number of casualties attributed to the tsunami was low. Palermo et al. (2013) suggested this was a consequence of two factors: "First, Chile had experienced a major tsunami in 1960, which remains engrained in the memory of the local population. In general, those living along the coast immediately searched for higher ground upon experiencing the earthquake ground shaking. Second, the central coastline of Chile is in close proximity to higher ground providing vertical evacuation". Figure 2.5 illustrates damage sustained by coastal communities along the central coast of Chile.

(a) (b)

Figure 2.5 2010 Chile Tsunami damage (Palermo et al. 2013): **a)** punching failure of masonry infill walls and failure of columns in Pellhue; and **b)** widespread residential destruction in Talcahuano

- On March 11, 2011, a powerful earthquake of magnitude 9.0 (Richer Scale) occurred at a depth of 30 km under the Pacific Ocean, near the northeast coast of Japan. The epicenter of the earthquake was located approximately 129 km northeast of Sendai, Honshu Island, and the subsequent tsunami, which affected the northeastern coast of Japan, arrived approximately 15 minutes after the earthquake, leaving little warning time for many villages and communities. The tsunami swept along the coastline and penetrated inland with local run-up heights of up to 48 m (Chock et al., 2012). This event was responsible for more than 25, 000 deaths and missing people. The Japanese Cabinet Office estimated direct losses of more than $309 billion due to damage to

housing, roads, utilities, and businesses across seven prefectures, making it the most expensive natural disaster on record (EERI, 2011). The tsunami-induced bore displaced, overtopped, and destroyed large structures (e.g. seawalls), which were initially constructed to mitigate the impact of tsunami waves on local communities. Figures 2.6 highlights structural failures as a result of significant hydrodynamic, buoyant and debris impact forces.

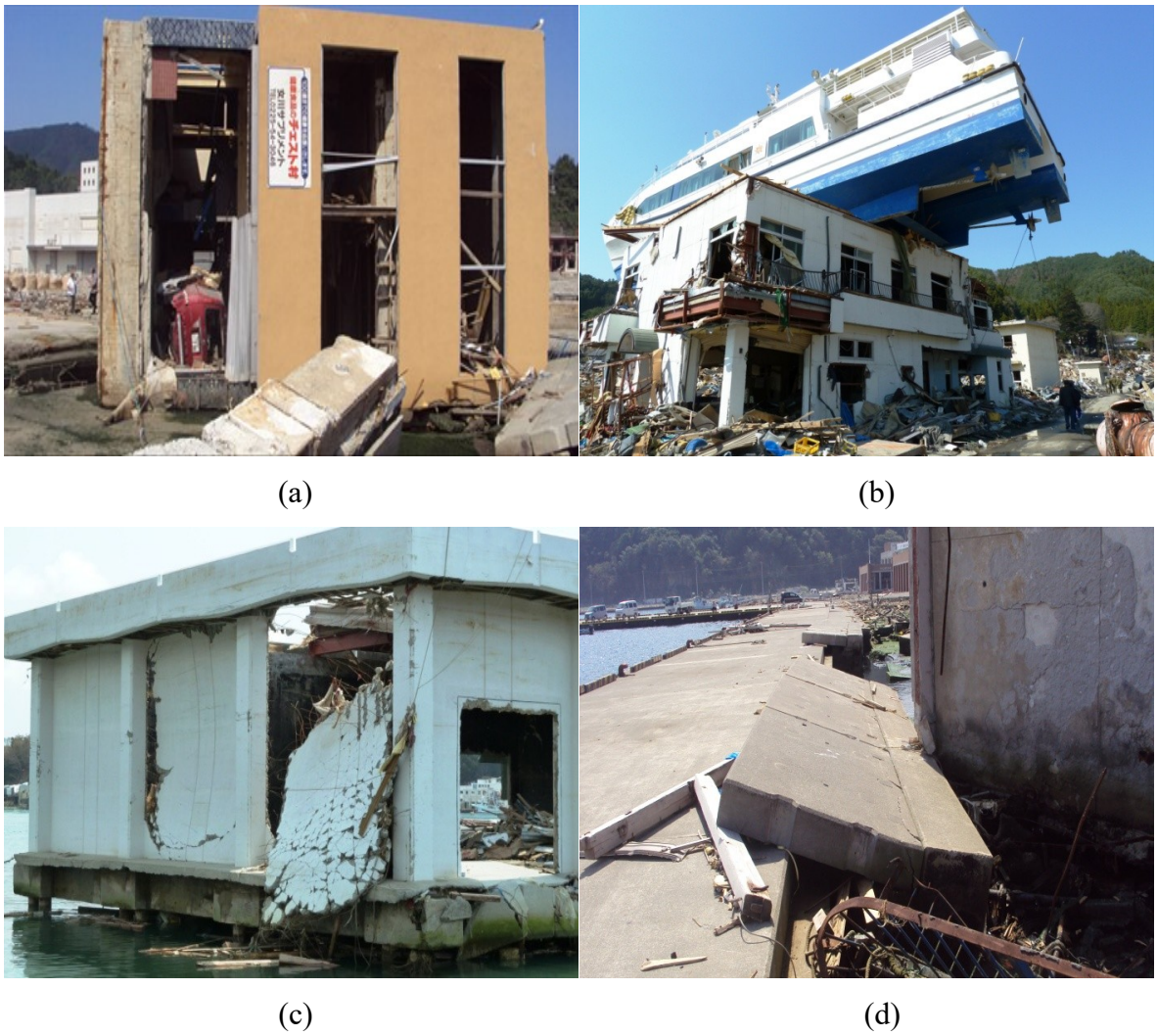

(a) (b)

(c) (d)

Figure 2.6 Impact of 2011 Japan Tsunami on residential and coastal structures (Nistor et al., 2012): **a)** steel structure overturned in Onagawa; **b)** impact loading from large vessel in Otsuchi; **c)** punching failure of fish storage building in Onagawa; and **d)** floating of concrete slabs in Onagawa

Although Japan has a long history of earthquake-generated tsunami events, which provided opportunities to gain experience and develop mitigation strategies, the March 2011 earthquake and subsequent tsunami demonstrated that the current state of the art in disaster prevention and mitigation, mainly for tsunamis, is limited. For the engineering community, regions devastated by tsunamis provide valuable sources of full-scale field data from which lessons can be learnt. Reconnaissance missions (Saatcioglu et al. 2005, Lukkunaprasit and Ruangrassamee 2008, and Nistor et al. 2010) demonstrated that many structures were able to survive the ground shaking of the earthquake, which preceded the tsunami hydraulic bore. However, they were either completely damaged or significantly damaged due to the tsunami inundation. The damaged structures can be categorized into two groups: engineered and non-engineered buildings. Analyses of the former category demonstrated that the structural systems were subjected to loads much higher than what they were designed for. Note that tsunami loads were not defined at that time these structures were constructed. Investigation of surviving buildings confirmed that those structures were able to withstand tsunami event because they were well-designed, well-oriented, and/or because of the existence of low height structural elements (mainly walls) constructed upstream, which reduced the tsunami induced forces (Lukkunaprasit and Ruangrassamee 2008). Figure 2.7 provides photos of buildings that survived the 2004 Indian Ocean Tsunami.

(a) (b)

Figure 2.7 Engineered concrete buildings that survived the 2004 Indian Ocean Tsunami without structural damage (Saatcioglu et al. 2009): **a)** hotel on Phi-Phi Island, Thailand; and **b)** Banda Aceh, Indonesia.

2.2 Tsunami Hazard

Statistics conducted by the Disaster Center (Tsunami Disasters, n. d.) for natural disasters that occurred during the first semester of 2011 demonstrated that tsunami-induced coastal flooding was responsible for five of the ten largest by estimated economic damages, four of the ten largest by number of people killed, and four of the ten largest by number of total people affected. Moreover, more than 95 % of the number of people killed and more than 86 % of the economic losses caused by the largest ten natural disasters in first semester of 2011 were associated with tsunami-induced coastal flooding. Noteworthy is that the 2011 Japan Tsunami caused the worst flood disaster in 2011. These statistics reflect the vulnerability of residential and industrial communities located within inundation zones.

Canada has the longest coastline of any country in the world and it is vulnerable to tsunamis generated in the Pacific, Atlantic and Arctic Oceans. The source of the threat can be either from near or far off-shore tsunamis triggered by tectonic activity. Localized hazards from seismically triggered landslide-generated tsunamis are also a concern for coastal regions of Canada (Mosher, 2009). Recently, meteorological tsunamis have been recognized as a potentially destructive and likely common regional hazard for British Columbia (Thomson et al., 2009). These tsunamis are generated by atmospheric rather than geological phenomena, and are expected to occur randomly rather than having a distinct, localized source of generation. Tsunamis can be generated by volcanic eruptions and asteroid impacts, but at a much lower probability. The Canadian Assessment of Natural Hazard Report (Etkin 2010) cited that:

- A submarine landslide triggered the tsunami in Valdez in 1964. Figure 2.8 displays damage that the tsunami caused in Port Alberni, British Columbia.
- Submarine slope failure generated the Alaska and southern Newfoundland (November 1929) tsunamis. These tsunamis were very destructive locally, but less so as the distance from the slope failure increased.
- In 1958, a large earthquake occurred in Lituya Bay, Alaska, which caused a massive rockslide that displaced the bay water up the shoreline and generated a run-up height of 500 meters: this is the largest wave ever recorded in history. These large waves travelled around the bay for 30 minutes (Miller, 1960).

Figure 2.8 Damage caused by the 1964 Alaska Tsunami at Port Alberni, BC, Canada. (Photo by D. Peregrine, CNN, 2007)

- In 1908, a landslide generated a wave at Notre-Dame-de-la-Salette, Quebec, that killed 33 people.

Tsunamis triggered by landslides are characterized by localized destructive effects with less damage with increasing distance from the location of the landslide.

Finally, tsunamis can be generated by explosions occurring close to a large water body. In 1917, the Halifax Harbour Explosion occurred when the ship Imo collided with the ammunition ship Mont Blanc, causing the latter to explode. This was the largest human-generated explosion in history prior to the Second World War. The explosion generated localized tsunami waves that were responsible for the drowning of approximately 200 people.

The following is a brief discussion of the tsunamigenic sources in the Pacific, Atlantic and Arctic Oceans:

➢ Pacific Ocean:

The Pacific Ocean is considered the source for the most significant tsunami hazard in Canada, from both near-field and far-field sources. A megathrust earthquake along the Cascadia subduction zone has the potential to trigger a tsunami similar to the 2004 Indian Ocean Tsunami. This is the primary tsunami hazard for western Canada. Also, significant are tsunamis from local crustal earthquakes and far-field subduction earthquakes, as well as

local landslide-generated tsunamis. Regularly throughout the Holocene period, megathrust earthquakes impacted the Pacific Coast of North America. More recently, Native American verbal history recounts of shaking that preceded the coastal flooding event between 1690 and 1715 (Ludwin et al. 2005), which was also associated with a damaging tsunami recorded in Japan (Satake et al. 1996). Goldfinger et al. (2010) is the most recent study, based on 80 core samples that were taken from the seabed between Vancouver Island and Cape Mendocino in northern California. The study used coastal marshes and offshore turbidity deposit evidence to conclude the probability of a great earthquake that triggered a destructive tsunami. Previous hazard studies were based on 19 earthquakes with a magnitude of 9 that rattled the region in the past 10, 000 years; the farthest back that core samples are applicable. Those earthquakes have averages of approximately 500 years, with occurrences ranging between 200 to 800 years.

The locations of the samples in the study by Goldfinger et al. (2010) were near the Cascadia subduction zone to examine deposits from submarine landslides triggered by substantial earthquakes. The study found 22 additional earthquakes with approximate magnitude of 8, similar to the 2010 Chile Earthquake. In their investigation, by increasing the number of earthquakes to 41, the average recurrence interval reduced to 240 years. Taking into account the last earthquake of January 1700, the authors concluded that the northwest coast of North America has approximately a 40% chance of experiencing a magnitude 8.0 or larger earthquake in the next 50 years. The Cascadia fault zone is thousands of kilometres long and runs along the northwest coast of North American. This close vicinity increases the tsunami risk to coastal communities due to the very short tsunami wave arrival time, similar to the 2011 Japan Tsunami where time to evacuate was very short, less than 30 minutes in many locations.

In 1960, a tsunami triggered by an earthquake which occurred off the central coast of Chile caused damage to the west coast of Vancouver Island and the Queen Charlotte Islands. The wave height of this tsunami (1.3 m) was smaller than that of the 1964 Alaska Tsunami (2.4 m) due to the significantly longer distance between the source and the impacted region and due to the influence of the orientation of the Chilean fault line on the tsunami propagation direction towards Vancouver Island. Small tsunamis from other distant sources such as Japan, the Kuril Islands, Chile, Mexico, Peru, Indonesia, and the Tonga Islands were

discovered on the British Columbia coast. Eleven tsunamis were recorded between 1994 and 2007 (Stephenson and Rabinovich, 2009). Dunbar et al. (1989), based on tsunami numerical modelling, suggested that additional far sources include Kamchatka and the Aleutian Islands, which can generate tsunamis due to a large subduction earthquake and result in more damage to the coast of British Columbia compared to the one generated by the 1964 Alaska Tsunami.

Another considerable hazard source to the coast of British Columbia and local communities such as the Alberni Inlet arises from tsunamis that are generated by earthquakes elsewhere in the Pacific Ocean (Henry and Murty 1995). In 1964, the Alaska Earthquake with a magnitude of 9.2 (Richter scale) triggered a tsunami that caused significant damage of approximately $10 million in Port Alberni and in the surrounding area of Vancouver Island (Thomson 1981). The British Columbia Provincial Emergency Program stated that a tsunami of such magnitude has a high probability to reoccur (Clague et al. 2006).

Tsunamis that are generated due to subaerial or submarine landslides represent potential sources of hazard and risk. In 1975, a submarine landslide in Kitimat Arm generated a tsunami with a wave height of 8.2 m and caused considerable local damage (Murty 1979). A rock avalanche around the 16th century (Bornhold et al. 2007) at Knight Inlet generated a tsunami that destroyed the First Nations village of Kwalate. Numerical modelling of tsunamis from hypothetical submarine landslides from the delta fore-slope demonstrated that waves several meters in height struck the nearby mainland coast and reached up to 18 m in height in the Gulf Islands of Mayne and Galiano across the Strait (British Columbia), opposite the source region (Rabinovich et al., 2003).

Parts of the low-lying greater Vancouver area are potentially at risk from tsunamis triggered by submarine landslides, specifically on the fore-slope of the Fraser River Delta, which has been identified as unstable by Mosher et al. (1997). Figure 2.9 illustrates potential tsunami sources that threaten Vancouver Island.

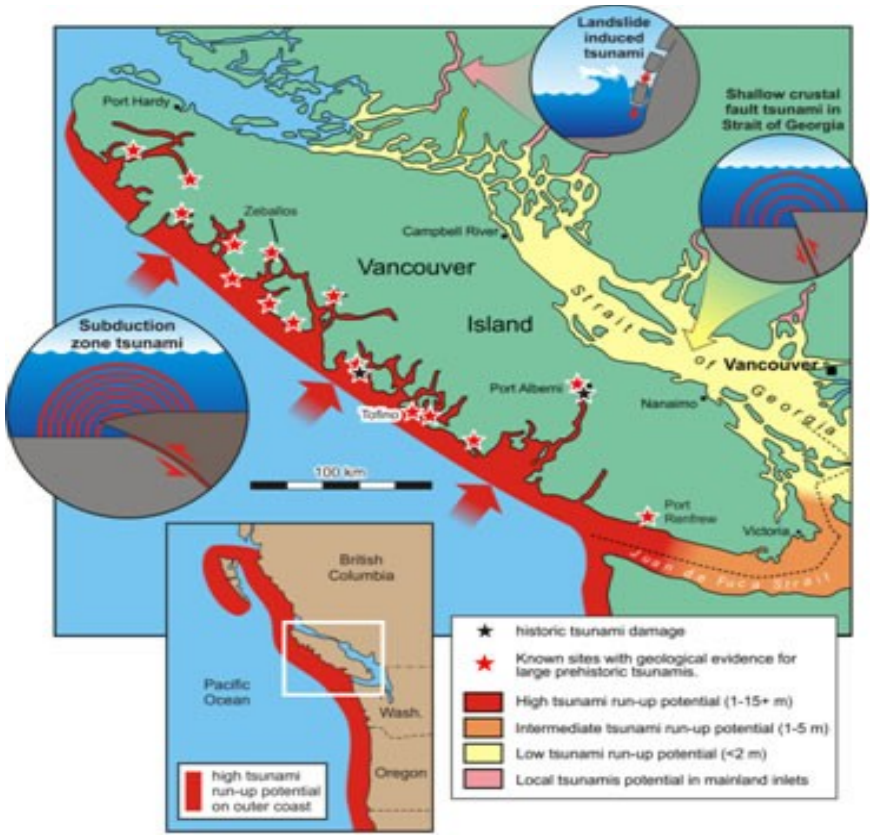

Figure 2.9 Potential tsunami hazards in Southern British Columbia (Clague et al., 2006)

➢ Atlantic Coast of Canada

Tsunami hazard along the Atlantic Coast of Canada is substantially lower than that of the Pacific Coast. There are no active tectonic movements near the coast to trigger tsunamis; however, there is the potential for submarine landslides that can generate local tsunamis, similar to that which occurred in 1929. Historical records reveal that the number of tsunamis along this coast was one fifth of those which affected Canada's west coast (Gustiakov 2009). Unusual water-level fluctuations and flooding of low-lying areas were evident in the harbour of Bonavista, Newfoundland, Canada. Results of tsunami modeling indicated that wave heights greater than 1.5 m could have occurred at several coastal sites in Newfoundland with values of more than 2.5 m in the Bonavista Peninsula (Roger et al., 2009).

In 1929, a landslide generated a tsunami that inundated the Burin Peninsula in southern Newfoundland, with 3 to 8 m-high waves and run-up heights of up to 13 m. This event resulted in 28 fatalities, in addition to economic damage to 12 seafloor-laid telegraph

cables estimated at $400 000 in 1929 dollars (Fine et al., 2005). The submarine landslide was triggered by an earthquake of 7.2 magnitude at the edge of the Grand Banks south of Newfoundland. The recurrence interval for this size of earthquake was predicted to vary between a few hundred to one thousand years; however, not all earthquakes of this size have the potential to generate landslides (Clague et al., 2003).

The area around the St. Lawrence River Estuary is characterized by Quaternary sediments, and moderate seismicity which is concentrated in the Charlevoix seismic zone underlying the estuary. These attributes are the key contributors to having approximately one million people at risk from tsunamis (Poncet et al., 2009). The tsunami waves can be triggered by seismic shaking or landslides due to instability failures along the banks and/or submarine slopes; many of these have evidence of being impacted by a magnitude M7 earthquake which occurred in 1663 (Locat et al., 2003). Numerical simulation of tsunamis generated by earthquakes and landslides indicated that 1-2 m high waves are likely to be associated with local run-up heights of up to 5 m (Poncet et al., 2010).

Importantly, it is believed that the collapse of a large volcanic flank off the Canary Islands represents a far-source tsunami hazard with the potential to generate waves with heights of up to 10-25 m. Such an event would be catastrophic for the Atlantic Coast of North America (Ward and Day, 2001). Recent numerical modelling results of such a tsunami demonstrated the presence of very large, short-period local waves that are strongly dissipated with distance. However, tsunami waves with heights of up to 3 m reaching the east coast of North America still represent a potential hazard (Gisler et al., 2006).

➢ Arctic Coast of Canada

Due to climatic conditions, inaccessibility and extremely low population density, tsunami recordings for the northern Canadian coastline are limited. Recent tide gauge monitoring records indicate that tsunami hazard is likely much lower than the other coastal regions of Canada. Moreover, the presence of extensive sea ice cover does attenuate the energy of tsunami waves. The active seismic fields are the Beaufort Sea and the Baffin Bay area, but tectonic reports reveal that earthquake-generated tsunamis are improbable to occur from any of these two sources. A more recent study hypothesized that a potential tsunami could be triggered by large thrust earthquakes beneath the Mackenzie Delta (Hyndman et al., 2005).

Ruffman and Murty (2006) reported that landslide tsunamis were generated off western Greenland, namely in the Disko Island district. Large mass failure was visible on the front side of the Mackenzie Delta, and considerable mass transport deposit images within shallow sediments of the deep Canada Basin were also identified (Mosher et al., 2010).

Leonard et al. (2010), as part of a Geological Survey of Canada project, presented a summary of geological tsunami sources which could potentially threaten Canadian coasts. The potential tsunami hazards and its triggers are summarized in the map shown in Figure 2.10. Leonard et al. (2010) reported a list of tsunamis triggered by geological sources as shown in Table 2.1.

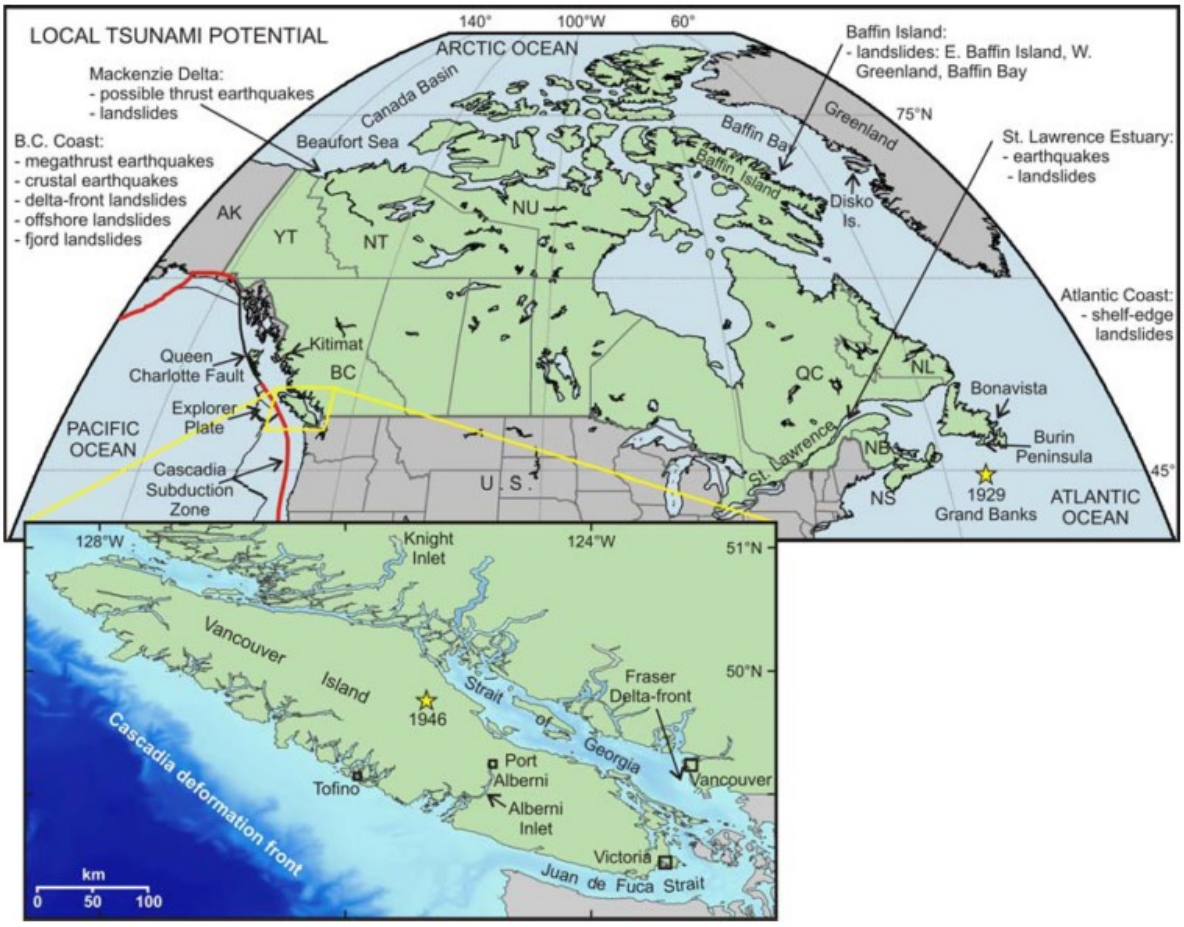

Figure 2.10 Potential tsunami hazards and sources for the Pacific, Arctic and Atlantic coasts of Canada (Leonard et al., 2010)

Table 2.1 Damaging tsunamis (from geological sources) documented in Canada (Leonard et al., 2012)

Date	Source Location	Impact Location (Canada)	Tsunami Source	Earthquake Magnitude	Wave Height (m)	Run-up (m)	Damage	References
COASTAL – WIDESPREAD IMPACT								
Jan 26 1700	Cascadia subduction zone, N. CA – S. BC	W. coast. Esp. W. Vancouver Is. and inlets	Local megathrust earthquake	M-9.0	-5-8; up to 16*	min. 3+	Widespread fatalities; destruction of villages	e.g. Satake et al. 1996; Hutchinson et al. 1997; Cherniawsky et al. 2007
May 22 1960	Southern Chile	W. Vancouver Is. and Queen Charlotte Is. (QCI)	Far-field megathrust earthquake	M 9.5	1.3* (Tofino)	0.1-2.1	Flooding	Wigen 1960; Stephenson et al. 2007 (and reference therein)
Mar 27 1964	Prince William Sound, Alaska	W. Vancouver Is., esp. Port Alberni and QCI	Fa-field megathrust earthquake	M 9.2	2.4* (Tofino); min. 5.2% (PL Alberni)	0.1-8.0	~$10m damage (1964)	Wigen and White 1964; Stephenson et al. 2007 (and references therein)
Nov 18 1929	Grand Banks, off Newfoundland	Burin Peninsula, Newfoundland	Earthquake-triggered landslide	M 7.2	3-8	13	28 fatalities; $400K damage (1929)	e.g., Ruffman 2001; Fine et al. 2005
COASTAL – LOCAL IMPACT								
~16th century	Knight Inlet, BC	Same as source	Rock avalanche	n/a	~2.6#	?	Many fatalities; destruction of village	Bornhold et al. 2007
Jun 23 1046**	Deep Bay, Strait of Georgia, BC	Same as source	Earthquake-triggered submarine landslide	M 7.3	1-2	?	1 fatality; local flooding and damage	Hodgson1946; Murty 1977

Apr 27 1975	Kitimat Arm, BC	Same as source	Submarine landslide	n/a	8.3; 6-11[#]	?	Substantial local damage	Murty 1979; Skvortsow and Bornhold 2007
Nov 03 1994[“]	Skagway, AK	Same as source	Construction-induced submarine landslide	n/a	5-6	9-11	1 fatality; $16-21 million damage to harbour docks	Lander 1995; Kulikov et al. 1996
LAKES/RIVERS – LOCAL IMPACT								
Aug 13 1905	Spences Bridge, Thompson R., BC	Same as source	Riverbank landslide	n/a	4.5-6	22.5	15 fatalities, 20 houses destroyed	Evans 2001; Septer et al. 2007 (and refs therein)
Apr 26 1908	Notre-Dame-de-la-Salette, Lievre R., QC	Same as source	Riverbank landslide	n/a	?	15	27 fatalities,; 12 buildings destroyed	Evans 2001
Jun 23 1946**	Landslide I.K., Mt. Colonel Foster Vancouver Is., BC	Same as source	Earthquake-triggered rock avalance	M 7.3	~29	51	Forest destruction up to 3 km from the lake	Evans 1989
Oct 06 1998	Troitsa Lake, BC	Same as source	Under-water delta-front landslide	n/a	2	?	Damage to boats and wharves	Schwab 1999
Dec 04 2007	Chehalis Lake, BC	Same as source	Landslide	n/a	>10	?	Destruction and damage to campgrounds	Stephenson and Rabinovich 2009

[*] Modelled values for release of 500 years of accumulated strain.

[+] Run-up from tsunami deposits likely lower than actual run-up.

[%] Wave height measured peak-to-trough; other values are wave heights above state of tide.

[#] Modelled values; not observed.

[**] Several tsunamis in lakes and inlets triggered by different landslides set off by the same earthquake.

[“]Not in Canada; included because fjord environment is similar to much of BC coast, and facilities were Canadian-owned.

2.3 Tsunami Waves: Generation and Propagation

Tsunamis are series of successive ocean waves with periods ranging from 5 to 60 minutes; such waves are generated when a large mass of sea water is displaced due to a catastrophic event. Tsunamis can be triggered by an earthquake under the seabed, but they can also be generated by volcanic eruptions, landslides, underwater landslides or meteor and asteroid impacts. Tsunami waves travel towards the shoreline in the form of long waves characterized by extremely low wave steepness. In open ocean (deep water conditions), tsunami wave length can exceed 500 km, while its height can be a meter or less. An example of the presence of a tsunami going unnoticed is the historical Sanriku Tsunami, which struck Honshu, Japan, on June 15, 1896. Fishermen in boats 32 km offshore did not detect the passing tsunami wave due to the fact that the wave height was less than 400 mm (Bryant 2008). These characteristics make tsunami waves difficult to detect offshore, and the significant energy of the tsunami is transported across the ocean without significant damping. As tsunami waves advance toward shorelines and enter shallow water, the wave length decreases while the wave height and steepness increase. The latter change is due to the bottom upslope and friction with the seabed. When the tsunami wave height becomes approximately equal to the water depth, the wave starts to break and continues to advance toward the shore in the form of either a hydraulic bore or a rapid surge. The bore is hydraulically similar to a flood-wave generated by a dam-break. Depending on the coastal topography, the tsunami bore (surge) floods near-shore coastal areas and impacts the infrastructure located in its path.

Tsunami waves differ from wind waves due to their initial long wavelength, relatively small amplitude, and mainly due to their comparatively long period. In addition, unlike wind waves, which have their energy contained mainly near the surface, the kinetic energy of a broken tsunami wave is distributed throughout the entire water depth.

In Open Ocean, tsunami waves have very long wavelengths compared to the water depth. Therefore, shallow water-wave theory has been applied to study and analyze tsunami waves. The shallow-water wave theory is described by the depth-averaged equations of mass and momentum conservation. For simplicity, the one-dimensional wave propagation equations are shown below:

$$\frac{\partial \eta}{\partial t} + \frac{\partial}{\partial x}[(\eta + h)u] = 0 \quad 2.1$$

$$\frac{\partial u}{\partial t} + u\frac{\partial u}{\partial x} + g\frac{\partial \eta}{\partial x} = 0 \quad 2.2$$

Where u is the average-depth horizontal velocity in x-direction, η is the water surface, h is the bottom boundary elevation from a reference datum, g is the gravitational acceleration, x is the horizontal spatial coordinate, and t is the time.

The derivation of the above equations was based on the assumptions that the water is incompressible and inviscid, while surface tension is neglected. Thus, the water depth is small in comparison with the characteristic horizontal length scale of the motion, which results in a hydrostatic pressure field throughout, while the velocity is uniform through the entire water depth.

Past events demonstrated that, depending on the near-shore bathymetry, tsunami waves can break offshore and reach the shoreline and advance inland in the form of a hydraulic bore. Hence, a description of the broken-wave run-up, based on shallow wave theory will be presented hereafter. As waves break, the fluid motion becomes turbulent. Therefore, turbulent closure models based on the Reynolds-averaged Navier Stokes (RANS) equations in three-dimensional flow field are relevant (Iaccarino et al. 2003). Given that the objective of this study is to investigate the interaction and behaviour of bores (broken waves) with near-shore structures, tsunami wave generation and propagation mechanism will not be discussed herein.

2.4 The Analogy between Tsunami Bore and Dam-break

As tsunami waves approach the coast, they transform due to shoaling of the up-sloping near-shore bed; wave amplitude increases while the wavelength decreases. Smaller waves of short periods are generated by soliton fission. The short period waves called fore-runners occur and arrive before the main tsunami waves. For some past tsunami events, witnesses reported the recession of the water at coasts prior to the arrival of the first tsunami wave. This phenomenon was attributed to the tsunami wave first arriving as a trough at the shoreline (Thurairajah 2005). Tsunamis also experience several magnification effects that may lead to the formation of edge waves along the beach. Edge waves mainly exist

shoreward and propagate along the shore; their amplitude is at its maximum at the shoreline and diminishes rapidly while moving in the offshore direction. Bays can also be subject to resonance. Local amplification effects around islands and cliffs can also be significant.

Depending on the near-shore bathymetry, tsunami waves break offshore while approaching the coastline, and further flood the coastal areas in the form of a hydraulic bore or a rapidly rising surge. For the 2011 Japan Tsunami, researchers [Chock (2012), and EERI (2011)] stated that the tsunami had the form of a train of waves offshore and resembled a bore while travelling onshore. Relevant tsunami-bore hydrodynamic characteristics will be discussed in the next section. Murty (1977) documented that a significant amount (up to 90%) of energy loss could be expected for far-field tsunamis. Substantial energy is lost as the tsunami reaches the shore due to refraction, shoaling, bottom friction, Coriolis effect, etc. By assuming that the tsunami energy reaching the shore is dependent upon the energy received at the source, while taking the distance from the shore under consideration, Bryant (2001) provided the maximum inland penetration, x_i , in meters as:

$$x_i = H_s^{0.75} n^{-2} k \qquad 2.3$$

Where H_s is the wave height at the shoreline or the toe of a beach in meters, n is Manning's coefficient (0.015 for flat area, 0.03 for built environment, and 0.07 for tree-lined landscape), and k = 0.06. For H_s = 6.6 m and 10.5 m, with n = 0.015, the maximum inland penetration distances are 825 m and 1, 533 m, respectively.

Figure 2.11 illustrates the effect of the roughness of near-shore regions on the maximum distance of inland penetration of a tsunami.

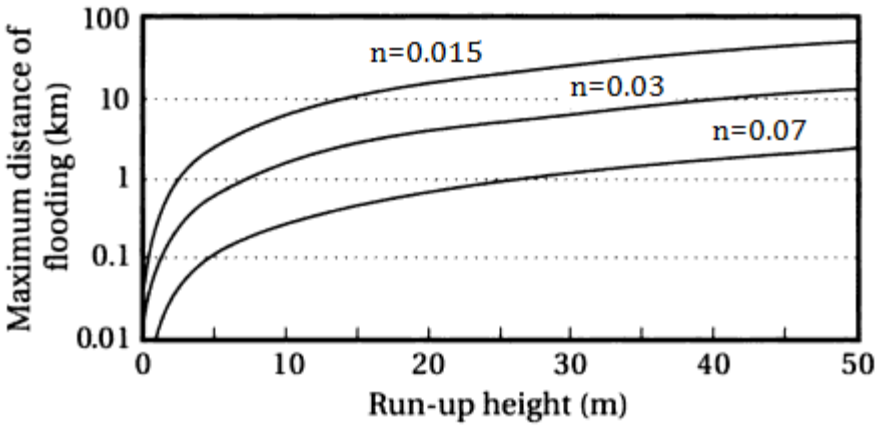

Figure 2.11 Tsunami run-up heights versus inland penetration on flat coastal plain of varying roughness (Bryant, 2001)

The term "dam-break wave" is usually used to refer to the two-dimensional flow generated by the quick removal of a vertical wall impounding a volume of water at rest above a horizontal bed. Dam-break flow analysis has been well investigated, both experimentally and numerically, as part of the dam design and safety analysis in addition to flood plain management (Almeida and Franco, 1994). Ritter (1892) was the pioneer who provided the classical solution based on the approximate Saint-Venant equations. The solution neglected the frictional and turbulent resistance effects; therefore, the simplified analytical solution is not able to accurately describe the actual flow characteristics. Dressler (1954) provided a comparison between experimental data and his previous mathematical results (Dressler, 1952). The experimental data deviated from the theoretical results, indicating that the Chezy resistance function, which is often used in steady flow formulas, is inadequate for highly turbulent flows. Stoker (1957) generalized Ritter's solution for wet-bed initial downstream conditions and arrived at a similar solution. Lauber and Hager (1998) used the shallow water equations with friction slope in the source term to develop an analytical solution.

Chanson (2005 and 2006) used the method of characteristics employing the Saint-Venant equations to analyze the dam-break wave phenomenon, using a wide rectangular channel with a semi-infinite reservoir. He hypothesized that the hydraulic bore generated from breaking tsunami waves is similar to that of a dam-break wave. Based on a simple analytical solution of the dam-break, Chanson derived a simplified, explicit analytical

solution for dam-break flow on a dry horizontal bed. The solution is a function of the bore-front velocity, location and characteristics. As a result, an explicit expression is provided for free-surface profiles of the flow. By analyzing video recordings, which were taken during the 2004 Indian Ocean Tsunami in Phuket Island (Thailand), Chanson estimated the flow depth and velocity. To compare the bore-front profile estimated from video recordings with that of the analytical solution, some assumptions were made: the bore in the video was generated from a 1 m solitary wave that travelled 2 km from the deep water region offshore before the breaking point near the shoreline. However, the solitary wave theory illustrated that the corresponding breaking wave height was 10.5 m with a velocity of 12 m/s. Thus, the location of wave breaking was proposed to be further inland. Therefore, the dam-break solution was assumed with a still water depth d_o = 10.5 m on horizontal bed with and without flow resistance (ideal and real flow resistance: f = 0, and 0.5) and with and without initial velocity (V_o = 0, and 12 m/s). Figure 2.12 provides a comparison between the characteristics of the observed tsunami bore and the bore generated by the dam-break wave on a horizontal plane. The points represent the estimated tsunami height while the dotted line represents the results obtained using the dam-break solution. The graph illustrates good agreement between the actual tsunami-induced bore front profile and the dam-break generated bore.

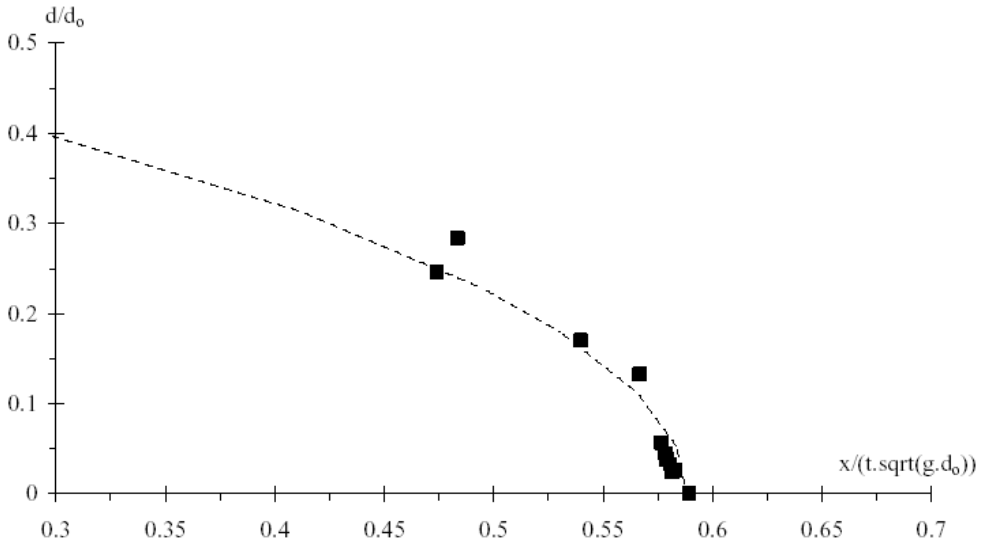

Figure 2.12 Comparison between tsunami-induced bore with dam-break wave (Chanson, 2006)

2.5 Velocity of Tsunami-Induced Bore

Tsunami inundation flow velocity is a significant parameter that is used to estimate the tsunami hydrodynamic loading on structures, and the velocity and associated impact force of floating debris [Matsutomi 1999, Tsutsumi et al. 2000, Iizuka and Matsutomi 2000, Fritz et al. 2006, Jaffe and Gelfenbuam 2007, and Matsutomi et al. 2010]. However, tsunami-bore velocity is difficult to estimate analytically: the bore-front is mathematically represented by a singular point while the velocity is affected by many factors such as the inundation depth, bed slope and bottom friction, and the distance from the shoreline. Therefore, numerical simulation is often used to determine the tsunami-bore velocity. However, various formulae to predict the velocity of hydraulic bores generated by tsunamis have been proposed by several researchers. In this section, a number of the formulae will be presented and their merits and suitability will be subsequently discussed.

- Togashi (1976) proposed the following formula for calculating the bore front velocity u on a dry bed of slope S with friction f at distance x from the shoreline:

$$u = (u_s - Bx)^{1/2} \quad 2.4$$

Where u_s is the velocity at the shoreline, and $B = 2(S + f/a^2)/[(1+a)(1+2a)]$ with $a = 0.5$. Since $u = 0$ at maximum run-up, $x = (Hr - Hs)/S$ at this point.

For S = 0.0025, f = 0.01, Hr = 12 m and Hs = 3 m, the velocity is $u_s = (3.4gh)^{1/2}$. For S = 0.001, f = 0.03, Hr = 6 m and Hs = 2 m, the velocity is $u_s = (16.4gh)^{1/2}$. At x = 10 m from shore, these velocities reduce to $(0.34gh)^{1/2}$ and $(0.88gh)^{1/2}$, respectively.

- Murty (1977) stated that tsunami bore velocity at inundation depth of h (as per Fukui/Mattock) can be estimated by:

$$u = 1.83\sqrt{gh} \quad 2.5$$

- Kirkoz (1983) suggested calculating the up-rush bore velocity of long waves using the energy conversion principle as follows:

$$u = \sqrt{2gh} \quad 2.6$$

- Tsutsumi et al. (2000) conducted field tests focusing on damaged structures due to a tsunami triggered by the Hokkaido Earthquake at Aonae on Okushiri Island, Japan. The tsunami-bore velocity was estimated from the tsunami-induced forces by using Morison's equation. An iron handrail on stairs leading to a 4.5 m high-water barrier was used as a flow surrogate. This handrail consisted of six vertical poles and was parallel to the shoreline (Figure 2.13). All six poles were bent in the direction of the incoming tsunami bore and the bore flow was assumed perpendicular to the handrail. Tsutsumi et al. (2000) estimated the tsunami-bore velocity along two directions of flooding and concluded that the maximum tsunami bore velocity was 10 to 18 m/s along one route and 5 m/s on the second one. The research suggested that the latter velocity was underestimated due to local reflection from the adjacent water barrier.

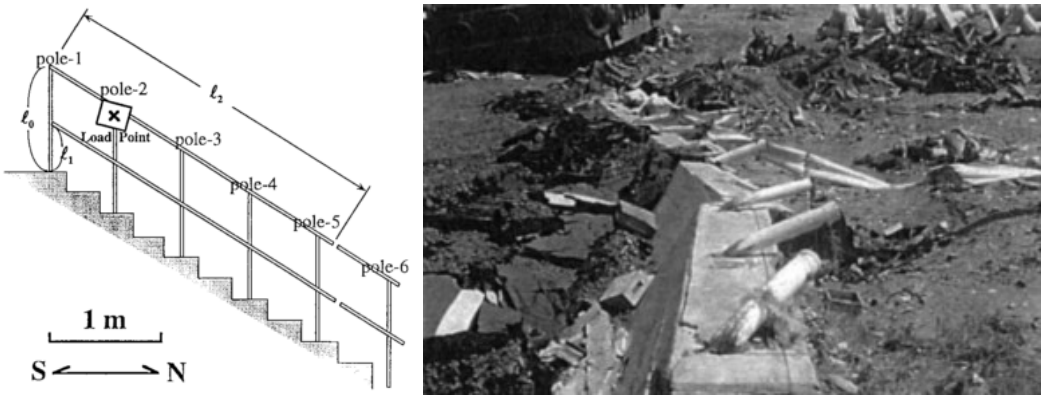

Figure 2.13 Schematic and photograph of guardrail damaged during the Hokkaido Tsunami (Tsutsumi et al., 2000)

- Bryant (2001) proposed calculating the tsunami bore velocity at inundation depth of h for the case without significant bed slope as follows:

$$u = 2.0\sqrt{gh} \qquad 2.7$$

Alternatively:

$$u = H_s^{0.7}(tan\theta)^{0.5}/n \qquad 2.8$$

Where H_s is the wave height at the shoreline, θ is the bed slope, and n is Manning's coefficient (0.015 for flat, 0.03 for built environment, and 0.07 for tree lined landscapes)

- Yeh et al. (2005) recommended using the formula provided by both FEMA-CCM and CCH, which is based on study of Dames and Moore (1980):

$$u = 2\sqrt{gd_s} \qquad 2.9$$

- Matsutomi et al. (2010) investigated the relation between the tsunami inundation depth and the inundation flow velocity using Bernoulli's theorem. They introduced the velocity coefficient (C_v) in the range of 0.58-0.66 (with mean of 0.62) for the square pillar model. The velocity coefficient can be calculated from the following formula:

$$C_v = \frac{u}{\sqrt{2g(h_f - h_r)}} \qquad 2.10$$

Where h_f and h_r are inundation depths at the front and rear of a rectangular building, respectively.

Matsutomi et al. (2010) collected data from recent tsunamis which occurred between 1992-2010 at locations away from the shoreline and as flat as possible. The data presented the inundation flow velocity u as function of the non-dimensional inundation depth h_f/R or h_r/R, where R is the inundation height with reference to the sea level (Figure 2.14). The bore velocity was estimated based on Bernoulli's theorem, under the assumption of a quasi-steady flow:

$$u = \sqrt{2g(h_f - h_r)} \qquad 2.11$$

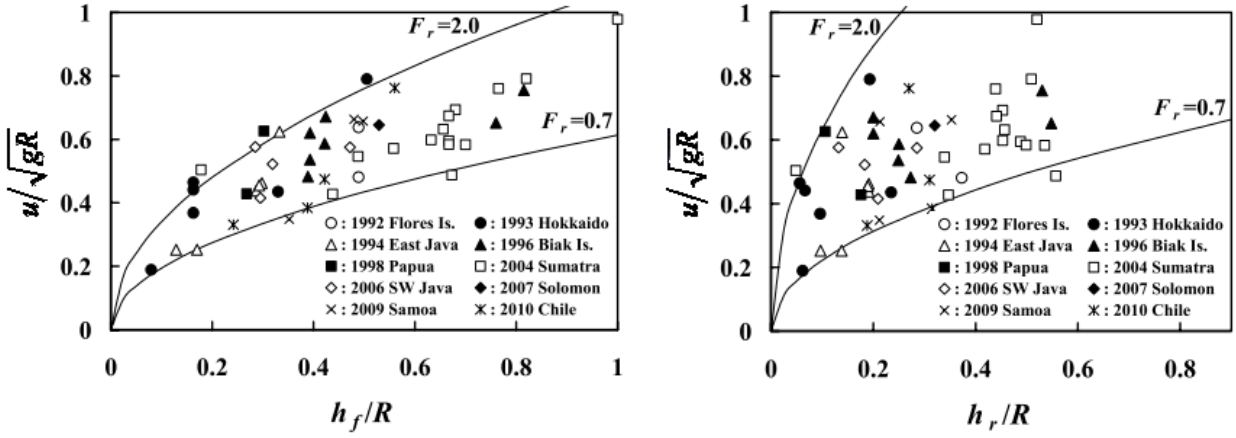

Figure 2.14 Relationship between non-dimensional inundation depths h_f/R or h_r/R and inundation flow velocity (Matsutomi et al., 2010)

The field data indicated that the Froude number, defined as $F_r = u/\sqrt{gh_r}$ where u is estimated from the previous equation, is bounded by values of 0.7 and 2.0. Matsutomi et al. (2010) conducted laboratory experiments under steady-flow conditions. Figure 2.15 shows a plan view of the testing flume. According to the results, the authors recommended, for practical use, $C_v = 0.6$ for very severe damage to the structure. They also recommended the following equations to calculate the tsunami bore velocity used to assess the hydrodynamic force:

$$u = 0.66\sqrt{gh_f} = 1.2\sqrt{gh_r} \quad \text{for the upper bound fluid velocity} \qquad 2.12$$

$$u = 0.36\sqrt{gh_f} = 0.42\sqrt{gh_r} \quad \text{for the lower bound fluid velocity} \qquad 2.13$$

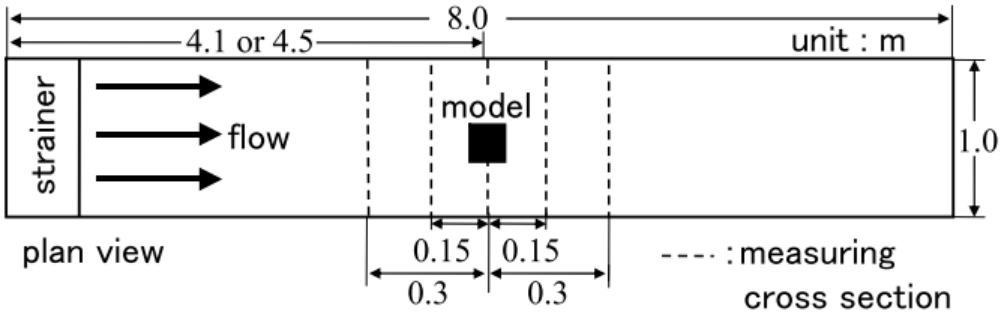

Figure 2.15 Experimental flume and sketch of the building model (Matsutomi et al., 2010)

2.6 Tsunami Loads on Near-shore Structures

Field investigations indicate that, in addition to the drag forces that result from the moving water mass, there are other significant tsunami-induced loads that need to be included in the design of tsunami-resistant structures. These include:

- Hydrostatic Loads
  - Buoyancy force
  - Unbalanced lateral hydrostatic force
  - Residual water surcharge load on floors and walls
  - Hydrostatic surcharge pressure on foundations
- Hydrodynamic Loads
  - Equivalent uniform lateral force

- Overall drag force on buildings
- Drag force on component elements
- Tsunami load on vertical structural elements
- Hydrodynamic load on perforated walls
- Hydrodynamic flow stagnation pressure
- Hydrodynamic surge uplift at horizontal slabs
- Tsunami bore flow entrapped in structural wall-slab recesses
- Debris impact loads

Either alone or in combination, these forces caused structural failures of low- to mid-height buildings or structural components made of all types of materials (EERI 2011). Local element failure shown in Figure 2.16 was found to be caused by lateral and/or debris impact forces, while global structural failure was observed to be caused by lateral forces (sliding and/or overturning due to weak connection to foundation) as shown by Nistor et al. (2005) in Figure 2.17 or progressive collapse.

(a) (b)

Figure 2.16 Damage to structural elements caused by tsunami-waterborne debris: **a)** column failure in reinforced concrete frame, Banda Aceh, Indonesia (Nistor et al., 2005); and **b)** impact failure of precast bearing wall apartment building in Yuriage, Natori, Japan (EERI, 2011)

(a) (b)

Figure 2.17 Damage to reinforced concrete structures caused by tsunamis: **a)** overturning of apartment building, Onagawa, Japan 2011; and **b)** uplift of slabs in Khao Lak, Thailand, 2004 (Saatcioglu et al., 2009)

- Synolakis (1986) investigated the solitary wave run-up on a plane beach and an exact solution was developed. Based on this exact analytical nonlinear solution of tsunami run-up on uniform-slope beach, Yeh (2007) developed the envelope curve of (hu^2) as a function of the ground elevation z and the tsunami maximum inundation depth R as follows:

$$\frac{(hu^2)_{max}}{gR^2} = 0.125 - 0.235\frac{z}{R} + 0.11(\frac{z}{R})^2 \qquad 2.14$$

  Equation 2.14 is based on the assumption of a uniform beach slope, without lateral topography variation, and no friction.

- Asakura et al. (2000) proposed an empirical formula to calculate the maximum tsunami-induced force exerted on a structure by integrating the envelope of the maximum standing-wave pressure. The formula was based on experimental tests of shallow water impacting vertical seawalls. The authors determined that the pressure during wave run-up on a structure can be predicted by measuring the wave run-up in the absence of the structure. The pressure (p_m) was represented by a hydrostatic pressure distribution extending to a height equivalent to three times the measured wave run-up height. During testing, the waves crossed perpendicular to the revetment before

they impacted the seawalls. The testing program consisted of two wave cases: with and without soliton wave break-up. [A soliton is a self-reinforcing solitary wave that maintains its characteristics while it travels at constant speed.] Note that tsunamis usually form as a series of soliton waves. The following formula was proposed to estimate wave pressure without soliton wave break-up:

$$p_m(z) = (3\eta_{max} - z)\rho g \qquad 2.15$$

Where p_m is the maximum tsunami-wave pressure for $0 \leq z/\eta_{max} \leq 3$, z is height of the relevant portion from ground level, g is the gravitational acceleration, η_{max} is the maximum inundation depth and ρ is the mass per unit volume of water. For the case with soliton wave break up, the maximum pressure for $0 \leq z/\eta_{max} \leq 3$ is based on the following formula:

$$p_m(z) = max\left\{\left(5.4 - \frac{4z}{\eta_{max}}\right), 3\left(1 - \frac{z}{\eta_{max}}\right)\right\}\rho g \qquad 2.16$$

- Ohmori et al. (2000) analyzed experimental time history data and assumed that the tsunami force is composed of drag, inertia, impulse and hydraulic force components. They proposed the following formula to estimate the total force induced by tsunami on a structure:

$$F_H = \frac{1}{2}\rho C_D u|u|B\eta + \rho C_M \dot{u} BL\eta + \frac{1}{2}\rho C_S(\theta)u|u|B\eta + \rho g BL\eta \frac{d\eta}{dx} \qquad 2.17$$

Where F_H is the tsunami force; B and L are the width and the length of structure, respectively; C_D is the drag coefficient, which is assumed equal to 2.05; C_M is the mass coefficient assumed equal to 2.19; C_S (θ) is the impact coefficient assumed equal to $3.6tan\theta$, where θ is the wave angle; u is the bore velocity in the direction of wave advancement; $\dot{u}$ is the bore acceleration; and η is the inundation depth.

Iizuka and Matsutomi (2000) proposed a formulation for calculating the force associated with the steady-state flow based on the evaluation of damage experienced by houses due to the Japan Tsunami:

$$F_H = \frac{1}{2}\rho C_D u^2 h_f B_h \qquad 2.18$$

Where F_H is the horizontal sustained force on the structure, C_D is drag coefficient (1.1 to 2.0), u is tsunami bore velocity, h_f is tsunami inundation height in front of a structure, and B_h is the width of the structure. The tsunami bore velocity u is proportional to the square root of tsunami inundation height; therefore F_H is proportional to u squared.

- Ikeno et al. (2001) conducted experiments in a tank that was divided by a sluice gate. A bore was generated using a difference in water level on both sides of the gate (Figure 2.18). The researchers stated that their experiments represented tsunami run-up for two cases: (1) in the deep-water part of a harbour; and (2) inland, after crossing the shoreline. Ikeno et al. (2001) proposed the following formula:

$$p_m(z) = 2.2(a_H - \tfrac{z}{3})\alpha\rho g \qquad 2.19$$

Where p_m is the maximum tsunami wave pressure (for $0 \leq z/a_H \leq 3$ above the surface of still water), a_H is tsunami wave amplitude, and α is the impact coefficient equal to 1.36.

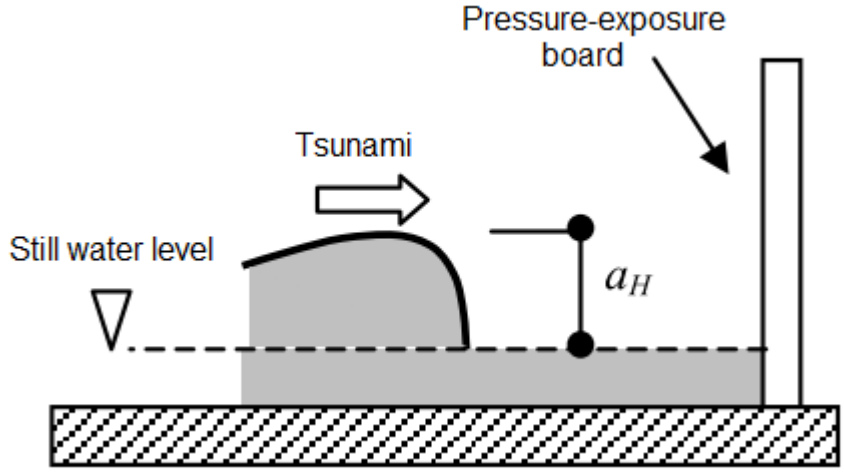

Figure 2.18 Experimental schematic of Ikeno et al. (2000)

Yeh (2006) proposed that the hydrodynamic force induced by quasi-steady flow is a function of the fluid density ρ, flow velocity u**,** and the geometry of the structure as follows:

$$F_d = \tfrac{1}{2} C_D \rho B (hu^2)_{max} \qquad 2.20$$

Where h is the flow depth at location of the structure in the absence of any structure; C_D is the drag coefficient, and, as suggested by FEMA 55 and Coastal Construction

Manual, is 1.2 for cylindrical structures and 2.0 for square or rectangular structures; B is the breadth of the structure; and hu^2 is the momentum flux. At a specific location, the maximum flow velocity u_{max} and maximum bore depth h_{max} do not occur simultaneously, thus $(hu^2)_{max} \neq h_{max}u_{max}^2$.

- Yeh (2007) suggested the use of the maximum momentum flux in the estimation of the hydrodynamic force based on numerical simulations for the case where no structure was present. Yeh proposed that the tsunami hydrodynamic forces be evaluated as a combination of the drag and inertia forces. The latter is particularly important at first impact of the tsunami bore front with the structure. For the surge force due to the bore leading edge impacting a structure, Yeh suggested the use of the formula of Dames and Moore (1980), which was adopted by CCH 2000:

$$F_s = 4.5\,\rho g h^2 \qquad 2.21$$

Where h is the surge height.

- Nakano (2008) followed the Design Guidelines for Tsunami Shelters issued by the task committee under the Japanese Cabinet Office/JCO (2005) and the Standard for Seismic Evaluation of Existing Reinforced Concrete Buildings published by the Japan Building Disaster Prevention Association (2001) to estimate the design tsunami load:

$$q_x(z) = \rho g(3h - z) \qquad \text{for } (0 < z < 3h) \qquad 2.22$$

$$p_x(z) = \rho g(a\eta_{max} - z) \qquad \text{for } (0 < z < a\eta_{max}) \qquad 2.23$$

Where $p_x(z)$ is the design tsunami pressure acting on a structure at level z from the ground level (kN/m^2), ρ is the water density (ton/m^3), g is the gravitation acceleration (m/s^2), h is the design tsunami inundation depth, and z is the distance above the ground level (m). Figure 2.19 illustrates the background of the concept of Eqn. 2.22. This pressure distribution was based on the two-dimensional experimental tests of Asakura et al. (2000). The Japanese Cabinet Office (2005) provided two typical cases for inundation depth and the height of the structure as shown in Figures 2.19 and 2.20.

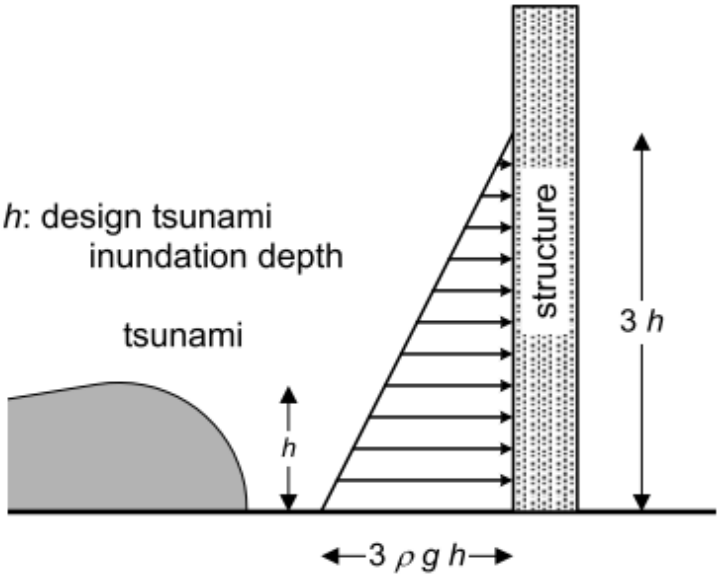

Figure 2.19 Design pressure tsunami distribution (Nakano, 2008)

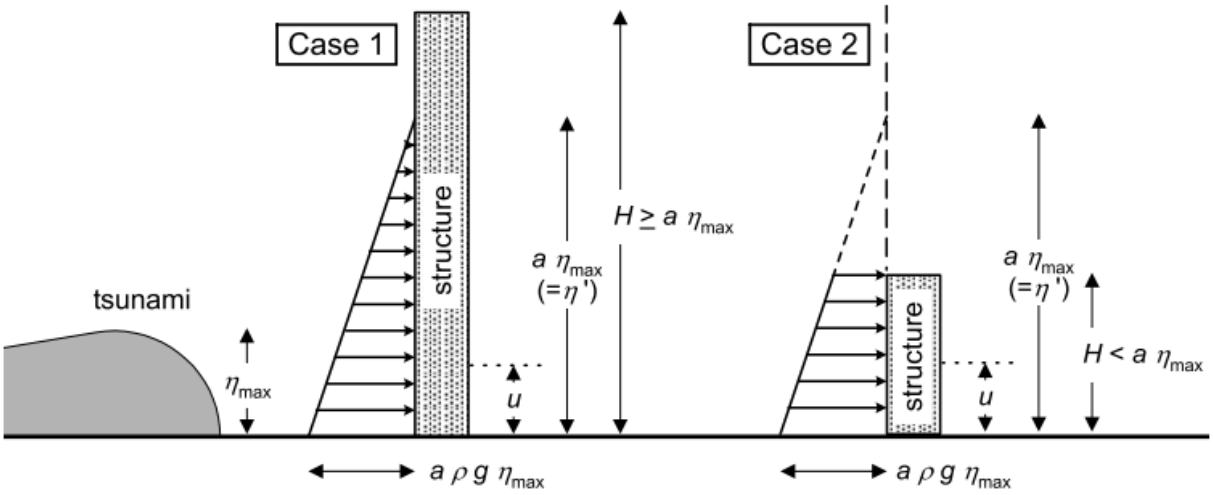

Figure 2.20 Tsunami inundation depth, building height, and tsunami pressure distribution (Nakano, 2008)

Nakano calculated the lateral resistance of damaged structures by considering their modes of failure and equating them to the calculated tsunami force using Eqn. 2.20 to determine the value of a. This coefficient was defined as the ratio between the equivalent water depth to the observed tsunami inundation depth (η_{max}). The observed structures were classified into column-shaped and wall-shaped. Nakano found that the wall-system buildings with $a > 2.5$ did not sustain major damage (excluding the effect

of debris impact), while for $a=2$, it was difficult to differentiate between damaged and survived structures for the column-shaped buildings. Nakano concluded that a value of 3 for coefficient a provided a reasonable limit between damaged and survived structures, but this value was not conservative if the structure was exposed to waterborne debris. The researcher found that structures with an a value greater than 2.5 did not experience major damage, excluding the effect of debris impact. Nakano reported one case for a structure with damage for a = 4, but the damage was the result of debris impact.

- Fujima et al. (2009) conducted a two-dimensional experimental program of tsunami wave impacting a rectangular onshore structural model. They installed the model at different locations from the simulated shoreline (20, 50, 80, 150 cm). The two structural models were represented by a cube with either a width of 10 cm or 20 cm placed parallel to the shore. Figure 2.21 a) shows the experimental set-up and Figure 2.21 b) shows the installation of pressure gauges on the 20 cm wide model. Figure 2.22 provides photos of the bore front impacting the upstream face of the models.

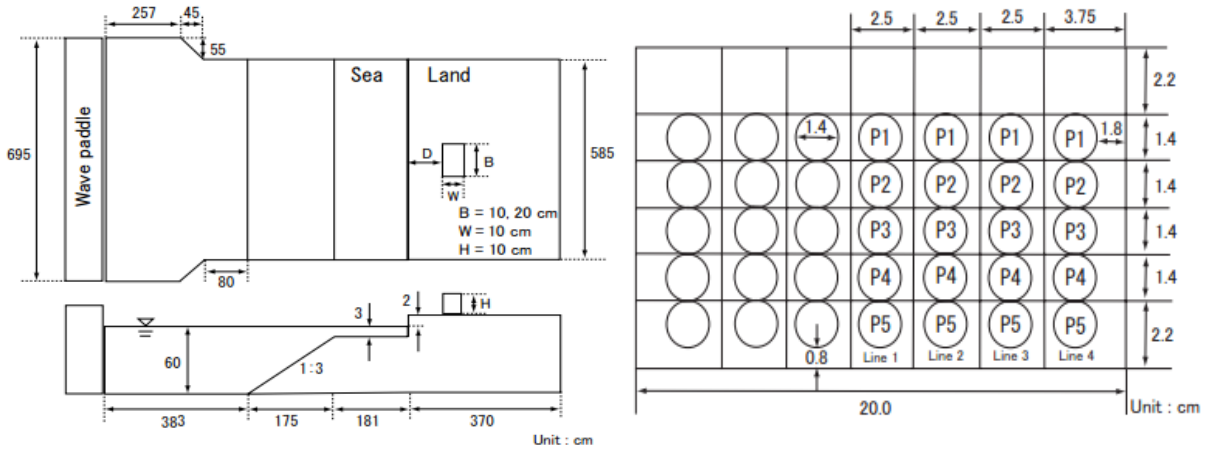

(a) (b)

Figure 2.21 Physical model of Fujima et al. (2009): **a)** experimental setup; and **b)** location of pressure gauges on the structural model

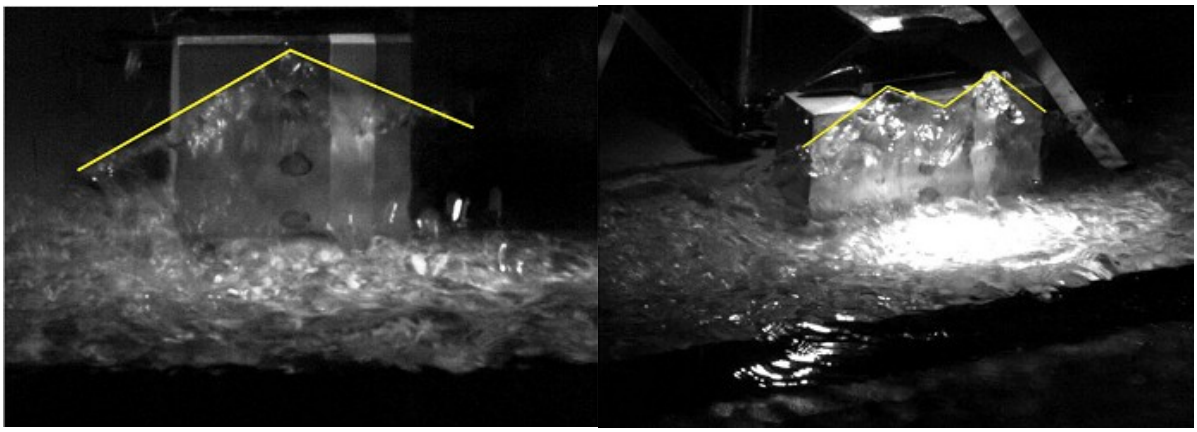

(a) (b)

Figure 2.22 Splashing on the upstream face of the models (Fujima et al., 2009): **a)** 10 cm wide model; and **b)** 20 cm wide model

The authors (Fujima et al., 2009) studied the pressure exerted on the 20 cm wide model using relatively small amplitude waves to avoid overtopping the model. They also measured the total horizontal force acting on the model using a load cell. The average pressure and force recorded from five repeated tests are shown in Figure 2.23. The figure illustrates that the maximum force occurred after the maximum recorded pressure. The authors attributed this to the gap between the lowest pressure sensor and the flume bed. In the research reported by Al-Faesly et al. (2012), the lowest pressure sensor was located sufficiently close to the flume bed to capture the first arrival of the bore front, thus the force and pressure recordings commenced simultaneously.

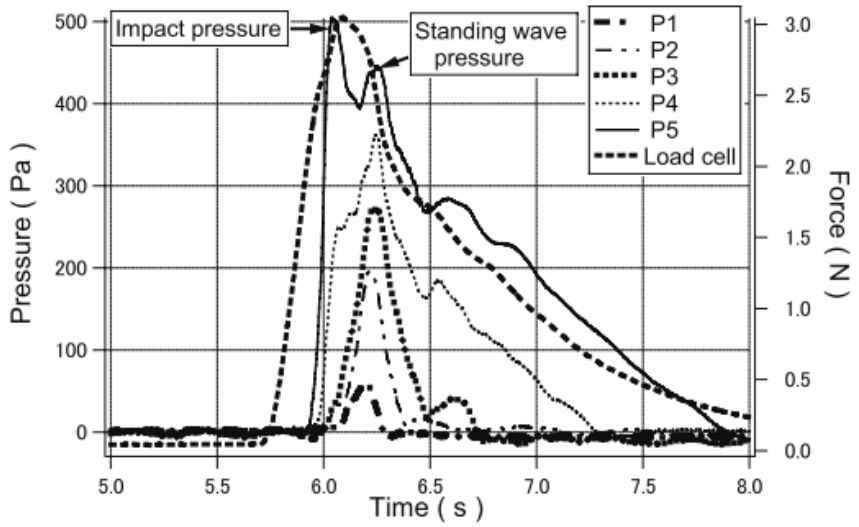

Figure 2.23 Pressure- and force-time histories at centerline for the 20 cm wide model (Fujima et al., 2009)

Fujima et al. also discovered a time lag between the pressure sensor readings, both vertically and horizontally (in height and width directions). The authors assumed that this variation was related to the irregularity of the wave and to the complexity of the wave-structure interaction. This type of variation did not appear in the experimental study of Al-Faesly et al. (2012). Fujima et al. investigated the effect of the distance between the structure and the shoreline on the maximum recorded force, and suggested using the following formulas to calculate the maximum tsunami-induced force on structures:

$$F_m = \begin{cases} 1.3\rho B h_{im} u_{im}^2 & for\ ({}^{h_{im}}/_{D}) < 0.05 \\ 3.3\rho g h_{im}^2 B & for\ ({}^{h_{im}}/_{D}) > 0.05 \end{cases} \qquad 2.24$$

Where h_{im} is the maximum inundation depth at the location of the structure and D is the distance between the structure and the shoreline. They suggested using Morrison's equation to calculate the tsunami wave force with C_D=*2.0* and C_M =*1.0:*

$$F_m = \left\{ \frac{1}{2} C_D \rho B h_i u_i^2 + C_M \rho B W h_i \frac{\partial u_i}{\partial t} \right\}_m \qquad 2.25$$

Fujima et al. (2009) presented a non-dimensional comparison between their experimental data and that estimated using Asakura's formula (Asakura et al., 2000); the results are shown in Figure 2.24.

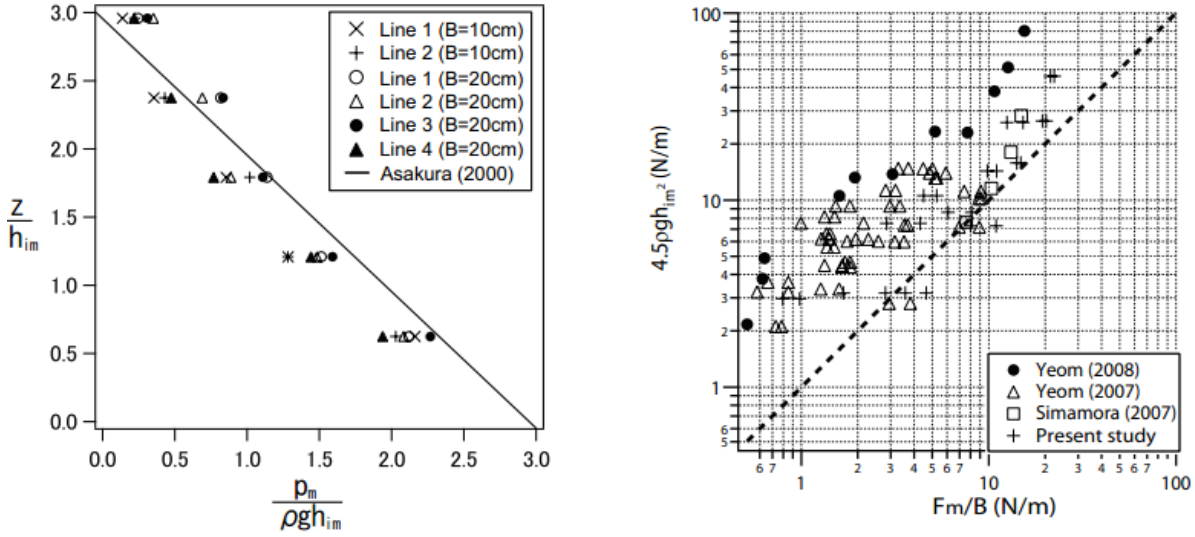

(a) (b)

Figure 2.24 Comparison of experimental data with Asakura's formula (Fujima et al., 2009): **a)** non-dimensional relationship between the maximum pressure (p_m) and measurement height (z), h_i is the inundation height; and **b)** measured versus estimated wave force by Asakura's formula

The majority of previous research focused on the forces or the coefficient of the drag for a specific structural element, such as walls [Ramsden and Raichlen 1990, Yeh 2007, Arikawa 2009]. Predominantly, the researchers either measured the breaking wave force on a structural elemental model [Ramsden 1996, Yim et al. 2008, and Arikawa 2009] or the surge flow advancing on a sloped beach [Ramsden and Raichlen 1990, Chanson et al. 2000, Mohammed 2008, and Lukkunaprasit et al. 2009]. In both cases, still water was present upstream of the model, which does not typically represent a tsunami bore crossing the shoreline and flooding the inland.

2.7 Impact of Waterborne Debris

Past events highlighted that tsunami flooding carries substantial amounts and varying sizes of debris, such as wooden logs, components of damaged buildings, shipping containers, fishing boats, and cars. Such debris may collide with structures located in the path of the

tsunami-induced bores. The magnitude of these impact forces can be large enough to cause significant or even catastrophic damage to the structures. Thus, it is essential to investigate the mechanism of impact loading due to debris and the dynamic response of infrastructure subjected to the dynamic impact of waterborne debris. However, it is difficult to estimate the debris impact force accurately. Review of past studies on the estimation of the debris impact force on near-shore structures is the focus of this section.

There are three basic approaches to estimate the maximum impact force on structures and they are based on three parameters: debris mass, debris velocity, and a third parameter whose selection varies depending on the approach followed. The following are the three approaches based on the selection of the third parameter:

1. **Work-energy** was proposed in the Highway Bridge Design Specification which was published by the National Association of Australian State Road Authorities (NAASRA 1990). This approach is based on the work done by the change in kinetic energy ($0.5mu^2$) as follows;

   $$F_{imax} = \frac{mu_o^2}{S} \qquad 2.26$$

   Where m is the debris mass; u_o is the debris velocity at the time of impact; and S is the debris stopping distance, obtained from the distance the debris travels from the point of contact with the target until the debris comes to rest ($u=0$). NAASRA suggested different values based on the structure stiffness only; that is, shorter stopping distance for stiffer targets.

2. **Impulse-momentum** was suggested by the Federal Emergency Management Agency (FEMA 1995) and the U.S. Army Corps of Engineers (1995), which uses the debris stopping time:

   $$F_{imax} = \frac{mu_o}{t_i} \qquad 2.27$$

   Where t_i is the impact duration, which is equal to the time between the initial contact of the debris with the structure and the maximum impact force. There is significant uncertainty in evaluating the duration of impact. Moreover, this equation provides the average force, not the maximum. To determine the maximum impact force, the force

must be estimated as a function of time. Although this function is expected to be sinusoidal in shape, a linear rise of force with time is typically used as the simplest approach suggested by Haehnel and Daly (2002).

3. **Contact stiffness** is recommended in the 2nd edition of the LRFD Bridge Design Specifications, which is published by the American Association of State Highways and Transportation Officials (AASHTO, 1998) as follows:

$$F_V = 8.15\, u \sqrt{DWT} \qquad 2.28$$

Where *DWT* is the dead-weight tonnage of the debris. The name of this approach indicates that it is based on the effective contact stiffness of the impact to estimate the maximum force.

The following is a list of recent studies performed by several researchers to better understand and estimate the debris impact force and the parameters affecting the magnitude:

- Matsutomi (1999) conducted large-scale debris (wood log) impact testing in air and another set with small-scale debris in a channel with the purpose to develop a practical formula to estimate the impact force of driftwood on structures. The author reported that the impact of debris in air is significantly different from that occurring in water due to the water mass surrounding the debris prior to impact, which is referred to as the "added-mass effect" or "virtual mass". Matsutomi used the test data from the small-scale experiments to compensate for the added-mass effect. Based on the simplified elasto-plastic theory, the author derived an analytical formula to calculate the impact force based on the following formula:

$$\frac{F_I}{\gamma_w D^2 L} = 1.6 C_M \left(\frac{u}{\sqrt{gD}}\right)^{1.2} \left(\frac{\sigma_f}{\gamma_w L}\right)^{0.4} \qquad 2.29$$

Where F_I is the debris impact force; γ_w is the specific weight of water; *D* and *L* are the debris diameter and length, respectively; C_M is the added-mass coefficient, which has a value of 1.7 for surge and 1.9 for common flow; u is the debris velocity at impact; and σ_f is the compressive strength parallel to grain of the wood. Although Eqn. 2.29 is based on a comprehensive experimental study with significant laboratory data, it is of

limited use due to the scale of the testing and the use of only cylindrical-shaped log debris.

- Ikeno et al. (2001) investigated the behaviour of timber drifted by tsunami flooding and the associated impact force with an impermeable vertical seawall. They illustrated that the impact force was identical, regardless of the shape of the drifted body, for the same momentum of the drifted body. Moreover, Ikeno et al. (2003) discussed the impact forces of drifted timber logs due to run up of tsunami on land. From these results, the wave force due to run-up of tsunami was determined to be larger than that due to a non-run-up tsunami. The laboratory tests of Ikeno et al. (2001 and 2003) investigated the impact-force of waterborne debris other than logs, but they were performed in a narrow two-dimensional flume where the flow was restrained at the seawall, which is not representative of actual tsunami events. The following empirical formula was derived based on data from small-scale experiments, approximately 1:100:

$$\frac{F}{gm} = SC_m \left(\frac{u}{\sqrt{g\sqrt{DL}}} \right)^{2.5} \qquad 2.30$$

  Where S is a constant equal to 20 for bore flow; m is the mass of debris; and C_m is the added mass coefficient with a value of 0.5 regardless of the shape of the debris, based on impact with an impermeable wall [this was adopted from Matsutomi's results (1999)]. Ikeno et al. (2003) suggested that S = 5 and C_m = 0.8 for spherical-shaped debris and C_m = 1.5 ~ 2.0 for cylindrical- and square-shaped logs. The values of C_m were suggested to be less than one as a result of the impermeable wall. [The impermeable wall causes significant flow reflection which leads to reduced debris impact forces.]

- Haehnel and Daly (2002) investigated experimentally the maximum impact force that floodplain structures may be exposed to by floating, wooden debris. They performed experiments in a small flume using reduced-scale logs placed in steady flow conditions, and prototype logs placed in a large towing basin. The authors studied the effect of impact geometry and construction material of the structure on the magnitude

of the debris impact force. The authors determined that the material of the structural model had no effect on the magnitude of the maximum impact force. The debris impact was modeled using a single-degree-of-freedom model as shown in Figure 2.25 in which m is the mass, k is the stiffness, ξ is the damping coefficient, and u is the velocity, while the subscripts are s is for the structure, l for the log debris, and t for the local point of impact.

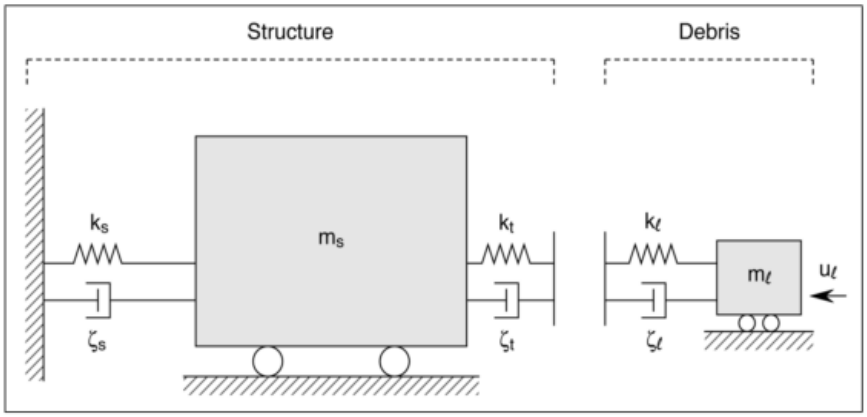

Figure 2.25 Debris-structure impact modelled as a single-degree-of-freedom model (Haehnel and Daly, 2002)

Haehnel and Daly (2002) assumed a rigid structure, as structure stiffness is much higher than that for the debris. The descriptive equation for the system illustrated in Figure 2.25 is as follows:

$$m_l\ddot{x} + \hat{k}x = 0 \qquad 2.31$$

Where $\hat{k}$ is the effective contact stiffness (resulting from contributions of both the structure and the debris). The variable $\hat{k}$ is challenging to calculate as it is a function of the displacement of the structure and the impact period. x is the summation of the compression penetration depth of the target and the debris during impact and rebound, where the dot notation indicates the time derivative of x. Based on the linear relationship between the penetration depth and the impact force ($F = \hat{k}x$), the authors provided the following equation as the solution to Eqn. 2.31:

$$F_I = u_l\sqrt{\hat{k}m_l} \quad 2.32$$

Where F_I is the maximum impact force as a function of the impact velocity multiplied by the square root of the product of the effective contact stiffness and the debris mass. This approach is based on a large mass and stiffness for the structure, which leads to a relatively stiff structure. Thus, this approach produces relatively large error when applied to light structures with shallow foundations. Note that in these experiments the water in the towing basin was stationary; consequentially the effect of added-mass on the structure was not considered. In an actual tsunami, the moving water that carries the debris and, in turn, the debris impacts the structure at the same time (inertial effects are exerted on both the water and the structure).

- SEI/ASCE Standard 7-02 is based on the impulse-momentum concept, which defines the impulse of a force acting for an infinitesimal time step, set equal to the change in linear momentum:

$$I = \int_0^\tau F dt = d(mu);\ \tau \to 0 \quad 2.33$$

Where I is the impulse, F is the impact force, m is the debris mass, u is the debris velocity, and t is time.

This document provided the following equation to estimate the debris impact force:

$$F = \frac{\pi\ m\ u\ C_I\ C_o\ C_D\ C_B\ R_{max}}{2\Delta t} \quad 2.34$$

Where m is the debris mass, u is the impact velocity of the debris, C_I is the importance coefficient, Co is the orientation coefficient, C_D is the depth coefficient, C_B is the blockage coefficient, R_{max} is the maximum response ratio for impulsive load, and Δt is the impact duration (recommended to be taken as 0.03s). Table 2.2 provides impact durations recommended by FEMA 55 and CCH 2000. The proposed C coefficients were based on non-peer-reviewed results of experimental testing and on engineering judgment.

Review of the available formulas reflects uncertainty of the present understanding

and quantification of the debris-impact force. Equation 2.34 contains five coefficients with values based only on engineering judgement, which presents the major difficulty of this quantification process.

Table 2.2 Ranges of impact duration suggested by FEMA 2005 and CCH 2000

Construction Material	Duration of Impact Δt (seconds)		
	FEMA 55 - 2005		CCH 2000
	Wall	Pile	
Wood	0.7 – 1.1	0.5 – 1.0	1.0
Steel	NA	0.2 – 0.4	0.5
Reinforced concrete	0.2 – 0.4	0.3 – 0.6	0.1
Concrete masonry	0.3 – 0.6	0.3 – 0.6	NA

NA – Not Applicable

- Yeh (2006) used the algorithm presented by Carrier et al. (2003) to reformulate the exact solution of the one-dimensional, nonlinear shallow-water wave theory that was provided by Shen and Meyer (1963). The solution was based on the assumption of a uniformly sloping beach with no lateral variation in topography of friction. Yeh presented a formula to estimate the maximum incident bore velocity, which occurs at the leading edge of a tsunami bore, as a function of the ground elevation at the point of interest (z) and the maximum inundation depth (R):

$$u_{max} = \sqrt{2gR(1 - \frac{z}{R})} \qquad 2.35$$

Substituting u_{max} from Eqn. 2.35 as the water-borne debris velocity to estimate the impact force would result in an overestimation of the debris impact force. Considering that u_{max} occurs at the bore leading edge where the water depth is very small, and the fact that the debris requires a certain water depth to float, Peregrine and Williams (2001) provided equations for temporal and spatial variations in flow velocity *u* and depth *h* for incident bore run-up onto a uniformly sloping beach. Yeh (2007) modified

the equations by including the beach slope (θ) and the elevation of the point of interest (z):

$$\eta = \frac{1}{36\tau^2}(2\sqrt{2}\tau - \tau^2 - 2\xi)^2 \qquad 2.36$$

$$v = \frac{1}{3\tau}(\tau - \sqrt{2}\tau^2 + \sqrt{2}\xi) \qquad 2.37$$

Where: $\eta = \frac{h}{R}$, $v = \frac{u}{\sqrt{2gR}}$, $\tau = t\tan\theta\sqrt{\frac{g}{R}}$, and $\xi = \frac{z}{R}$, t is the time (= 0 when the bore crosses the shoreline), and θ is the beach slope.

- Yeh (2007) stated that, "for a given tsunami penetration, the incident-bore formation should yield the maximum flow velocity; gradual flooding of non-breaking tsunami should result in slower flow velocities". By combining Eqns. 2.36 and 2.37 and eliminating τ, the graph in Figure 2.26 was developed, which provides the maximum flow velocity at a given location for a given flow depth.

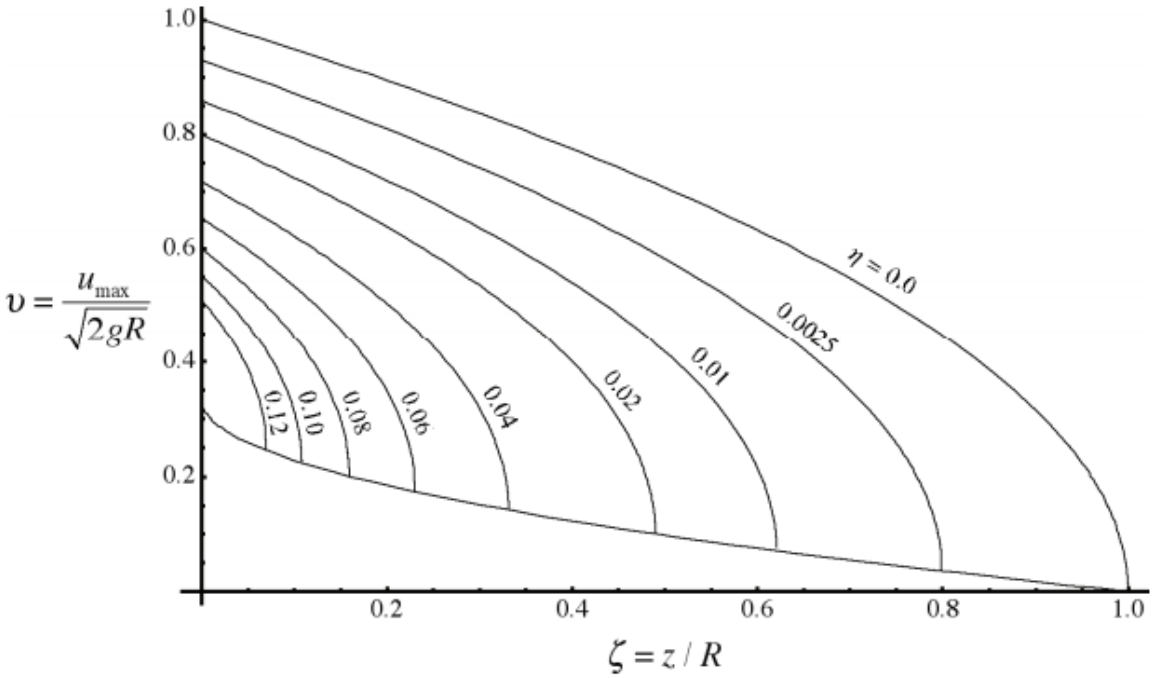

Figure 2.26 Maximum flow velocity for a given flow depth and ground elevation (Yeh, 2007)

FEMA P-646 recommended Eqn.2.35 and Figure 2.26 to estimate the debris impact force. Moreover, where numerical models are used to determine the maximum flow velocity u_{max}, FEMA P-646 prescribes that u_{max} should be at least 80% of that estimated from Eqn. 2.35 or Figure 2.26.

- Matsutomi et al. (2008) conducted laboratory experiments to understand the behaviour of floating bodies at the front of a surge and the basic characteristics of flow with floating bodies. The flume was 300 mm wide, 500 mm high and 11, 000 mm long, with glass side walls and a steel bed. The impounding gate was installed 5, 000 mm upstream from the end of the flume. The parameters studied were: impounding water level (220, 250, and 300 mm), length of debris (18, 54, and 108 mm), and the void ratio e (0.4, 0.6, and 0.8). The authors used video recordings from the top and the side of the flume to investigate the behavior of the floating bodies. The floating bodies were square in section with a side of 18 mm. The researchers used three void ratios *e*; the ratio of net flume-bed area which is not covered by floating bodies to flume-bed area (*e* = 1- net area occupied by floating bodies/flume bed area where floating bodies were arranged). Matsutomi (2009) recorded the debris weight change with time in a sequence of 1, 3, 5, 10, 30, 60, and 90 minutes. The results demonstrated that the mass was constant after 60 minutes. Matsutomi et al. (2009) determined that the velocity of the debris was less than the bore velocity. The study also resulted in the following:
    - The authors were able to determine the following parameters: inundation depth, moving velocity, surge front velocity and vertical section area of the accumulating region with the void ratio for different test cases.
    - The inundation depth increased as the impounding depth increased or the void ratio decreased.
    - The surge front propagation velocity was greater than the moving velocity of the debris in 25 of the 27 cases.
    - Both the moving velocity of the debris and the surge front propagation velocity increased as the impounding depth or the void ratio increased.

- A model was presented to calculate the surge front velocity and moving velocity as functions of the density of the fluid and floating bodies, stored and inundation depths, void ratio and friction factor between the body and the flume bed.
- The authors concluded that the surge with floating bodies behaves like a bore (flow velocity > moving velocity of the debris).

- Yeom et al. (2009) analyzed the impact of a shipping container drifted by tsunami run-up using a drift impact-coupled model. Numerical simulation was conducted using LS-DYNA Software and the results were compared against laboratory experiments of scale 1:75. Satisfactory agreement was observed between the full-scale numerical simulation and the small-scale experimental data.
- Hiraishi et al. (2010) conducted an experimental program to investigate the impact force caused by timber debris on a jacket-type structure. The testing involved a pier model with a 1.2 m diameter (scale of 1:10) and uniform flow velocity that varied from 0.6 to 1.3 m/s. The drifting timber was 10 m long and 1 m in diameter. The initial direction of the debris was either 0˚ or 90˚. Hiraishi et al. (2010) used the formulas provided by Sogabe et al. (1981) to estimate the debris impact force. Figure 2.27 illustrates the experimentally measured impact force against those estimated. The authors concluded that the impact force depended on the debris velocity and mass. The study did not include the effect of debris orientation or the influence of bore depth on the resulting impact force. In addition, only one size and shape of debris was used in the experiments.

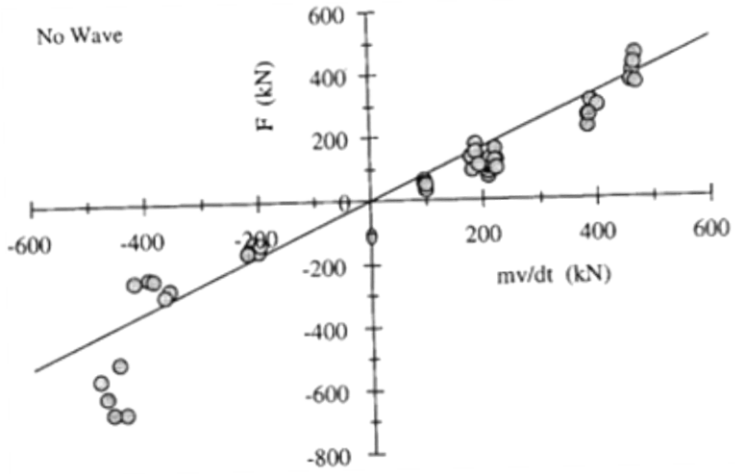

Figure 2.27 Variation of measured and expected maximum forces (Hiraishi et al., 2010)

2.8 Tsunami Countermeasures

Coastal communities on a global scale are witnessing an increase in frequency and magnitude of costal hazards, vulnerability, and the impact of climate change. The associated risk from coastal hazards such as severe storms, tsunami inundation, flooding and environmental degradation is also increasing. Therefore, a need exists to develop more resilient coastal communities that have the capacity to withstand the impacts of hazards. There is considerable evidence to suggest that coastal forests can reduce the force, depth and velocity of a tsunami bore, reducing damage to property and reducing loss of life. Many anecdotes, field surveys, and scientific studies in countries affected by the 2004 Indian Ocean Tsunami (Indonesia, Japan, Malaysia, Maldives, Myanmar, Sri Lanka, and Thailand) provide a connection between areas with the highest levels of damage and the absence of coastal forests [Forbes and Broadhead 2008, and Hettiarachchi 2009)].

Therefore, it is important for coastal development planning to consider the context of overall coastal hazards, such as tsunamis. However, there is a low probability of an extreme tsunami event taking place (similar to that of the 2004 Indian Ocean Tsunami or 2011 Tohoku, Japan Tsunami). Countermeasures should be adopted in coastal zones susceptible to tsunamis and/or other coastal hazards that are accompanied by high waves and high inundation. These countermeasures can be broadly classified into two main categories:

- **Promoting successful evacuation from tsunamis**

  Countermeasures included in this category are: early warning systems, public warning systems, and hazard and inundation maps.

- **Mitigating tsunami impact**

  Countermeasures in this category include:

  1. Construction of man-made structures for protection: breakwaters, dikes and revetments, etc…
  2. The effective utilization of natural coastal ecosystems: Coral Reefs, Sand Dunes and Coastal Vegetation (Mangrove Forests)
  3. Tsunami Resistant Buildings and Infrastructure

Based on the location of and function in protecting the coast, physical interventions to mitigate tsunami can be classified as follows:

a) Reduce the impacts of tsunami waves prior to reaching the shoreline. (e.g. Tsunami Breakwaters, and Coral Reefs)
b) Protect the coastal zone by preventing the inland movement of tsunami waves. (e.g. Tsunami Dike, and Sand Dunes)
c) Mitigate the severe impacts of tsunami waves on entry to the shoreline. (e.g. Tsunami Dikes, Revetments, and Mangrove Forests)

In this study, the function of the physical intervention stated above in (c) was investigated with low-height structural elements (mitigation walls). The influence of the configuration of the mitigation walls (height, inclination angle, cross-section, and location) on the magnitude of base shear forces, base overturning moments and pressures was investigated.

2.9 Engineering Lessons from Recent Tsunamis

Past tsunamis demonstrated that their behavior is quite different from that of other coastal hazards such as storms. Hence, tsunami effects cannot be inferred from the effects generated by wind waves and storm surges. Even though major tsunamis are rare events, the danger

they pose and the associated extreme consequences dictates that structural design of buildings in tsunami-prone regions is critical.

Following a number of recent major tsunamis that were responsible for the loss of many lives and major infrastructure damage, engineering associations and research centers sent teams of experts into the affected areas to evaluate the performance of infrastructure. In addition, these teams attempted to develop new strategies for mitigating the impact of future tsunamis.

Following the 2004 Indian Ocean Tsunami, a Japanese team of researchers from the Research Center for Disaster Reduction Systems (RCDRS 2005) performed a reconnaissance visit in the region of southwest Thailand, a well-known tourist destination located approximately 500 km from the tsunami-generation area. This area has many well-designed buildings that were constructed to high standards. The team reported that due to the offshore bathymetry, the tsunami wave height varied between 4 and 11 m. The team reported that permanent damage to civil infrastructure (bridges and roads) was limited to seafront structures. However, private residences and businesses in low-lying areas were also badly damaged. The team concluded that most of the well-designed reinforced concrete buildings with proper foundations survived the incoming tsunami waves. The percentage of well-designed buildings which survived the tsunami impact was greater than that of elevated buildings which allowed water to flow underneath or through. It was also documented that, in some places (*e.g.* Kata-Karon area of Phuket), where residential and commercial structures were set back behind a sand dune, damage was limited due to the dune dramatically reducing flow velocity. Note that the sand dunes were overtopped by the tsunami bore. It was stated that, “damage was limited to direct flooding and did not convey that kind of impact-related structural damage that was seen elsewhere” (RCDRS 2005). In Patong Beach, a low-height seawall deflected the tsunami bore run up and thus reduced the forces on seafront buildings, which suffered only minor non-structural damage (Figure 2.28).

Figure 2.28 Pedestrian opening in the Patong Beach seawall (RCDRS, 2005)

Debris-structure impact was a significant factor in the observed damage. Therefore, identifying the potential debris in a tsunami risk zone is essential.

Nistor et al. (2006) presented findings from a reconnaissance mission to Thailand and Indonesia to investigate the effects of the 2004 Indian Ocean Tsunami on infrastructure. Both engineered (mostly reinforced concrete) and non-engineered buildings, in which concrete block or clay brick masonry infill walls were used as non-structural elements, were studied. The researchers stated that structural damage resulted from either impulsive pressure of breaking waves at the shore or the dynamic pressure inland due to the movement of the bore. Saatcioglu et al. (2006) used the empirical formula (Eqn. 2.38) that was developed by Goda (1985) to estimate the impulsive pressure of breaking waves:

$$p_{max} = \frac{\pi \gamma c H_w}{4g\tau} \qquad 2.38$$

Where γ is the specific gravity of seawater (kN/m^3), c is the wave celerity (m/s), τ is the impact duration (0.2 s), and H_w is the water height in meters. This formula was developed to estimate the breaking wave pressure on coastal structures at the shoreline, hence using it for near-shore infrastructure resulted in significant overestimates. Hiroi (1919) suggested a simple expression to estimate the uniform dynamic pressure as a function of water specific gravity and water height (Figure 2.29):

$$p = 1.5\gamma H_w \qquad 2.39$$

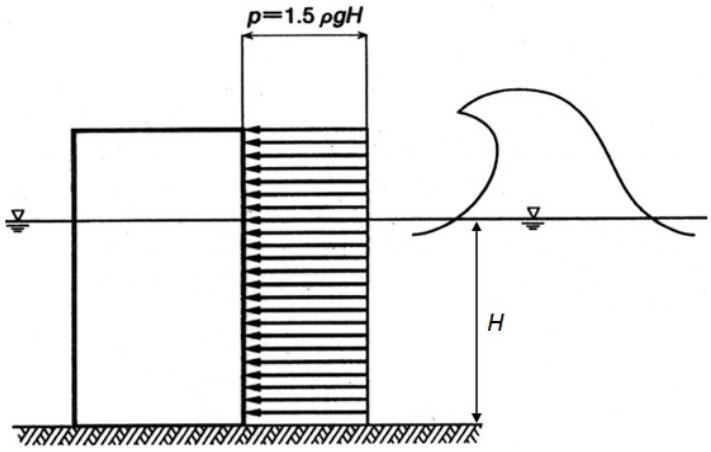

Figure 2.29 Dynamic breaking wave pressure assumed by Hiroi (1919)

Saatcioglu et al. (2006) compared the hydrodynamic tsunami pressure produced from Eqn. 2.38 with the design wind pressure based on the National Building Code of Canada (1995) for a building located in the City of Vancouver, Canada. The study demonstrated that the tsunami pressure on the first-floor level was approximately 26 times higher than the design wind pressure. Saatcioglu et al. (2006) investigated the performance of different types of construction: timber-framed structures, unreinforced masonry walls, and engineered and non-engineered reinforced concrete structures. Figure 2.30 and Figure 2.31 provide samples of the structural damage observed in Phi Phi Island (Thailand) and Banda Aceh (Indonesia), respectively. The displacement of entire structures and punching failure in masonry walls illustrated the large lateral force exerted on the buildings due to the tsunami bore while moving inland.

The researchers concluded that designing buildings for earthquake may not be sufficient to ensure proper capacity to resist tsunami loading. Moreover, near-shore structures should have properly anchored foundations to resist the significant uplift and lateral forces. Despite the impossibility of assuring structural safety in the event of another disaster of the same magnitude, practical implementation of knowledge gained from past tsunamis could considerably reduce the loss of lives and structural damage in the future.

(a) (b)

Figure 2.30 Damage to non-engineered reinforced concrete buildings, Phi Phi Island, Thailand (Saatcioglu et al., 2006): **a)** punching failure in masonry wall; and **b)** column failure due to debris impact

(a) (b)

Figure 2.31 Destruction of residential community of timber structures in Banda Aceh, Indonesia (Saatcioglu et al., 2006)

Expensive and costly efforts are in progress in Japan to secure protection from tsunamis for coastal communities and populations living near the sea. These measures include building suitable structures; using disaster prevention training; and having well-designed, tested tsunami warning systems. Seawalls are another method that has been tested and proven doubtful due to its inability to protect. More than 185 people died on Okushiri Island due to a 1993 tsunami, despite the presence of 4.5 m-high seawall that was erected to shield the Aonae Peninsula. There is debate to the efficiency of such a wall given the cost to build and the obstructed view of the sea. Currently, several countries around the Indian

Ocean are deciding whether to allow reconstruction on the coast, which structures to rebuild and relocate, and how to rebuild to minimize human and material losses during future tsunamis.

In summary, tsunami behaviour is quite distinct from other coastal hazards such as storm waves. Previous tsunamis have shown that the reasons leading to structural failures of near-shore buildings can be categorized into three groups: 1) loading due to hydrodynamic forces, 2) loading due to the impact force induced by water-born objects, and 3) foundation undermining due to scour and foundation failure. Tsunami-induced structural failure due to foundation damage is out of the scope of this current study. Therefore, the effects of tsunami on structural foundations such as scouring and erosion will not be discussed.

2.10 Discussion

Many historical natural disasters have been associated with tsunamis impacting coastal communities. The result has been the loss of hundreds of thousands of lives and massive economic consequences. The last decade witnessed four major tsunamis out of which two held the record of the most deadly and costly natural disaster in human history, respectively. Canada, the country having the world's longest coastline, is vulnerable to tsunamis that may be triggered in any of the three surrounding oceans. The Canadian Assessment of Natural Hazard Report of 2010 (Etkin, 2010) reported that the Cascadia subduction fault along the western seaboard of British Columbia is considered to be the largest tsunami hazard to Canada's coastal communities. Past tsunamis that occurred in Canada were generated due to different triggers: earthquakes, landslides, and massive ammunition explosions. Although some of the past tsunamis generated by landslides or explosions were limited and generated, though extreme, only local effects, they were responsible for the loss of lives and resulted in significant economic consequences. Canada is one of the countries that participate in the Pacific Tsunami Warning System. The 2011 Japan Tsunami demonstrated that a long warning time is not always available between the tsunami generation and the actual tsunami inundation. This is particularly true for near-shore generated tsunamis such as near-shore subduction earthquake-induced tsunamis.

Tsunami has the appearance of a series of waves most often triggered by a submarine earthquake. Tsunami waves move very fast in deep water with negligible loss of energy.

Depending on the near-shore bathymetry, tsunami waves may either flood the shoreline in the form of a rapidly rising tide or break off-shore and flood the shoreline in the form of a rapidly advancing hydraulic bore. Past tsunami events illustrated that the induced bore is characterised by high turbulence and high velocity, in addition to carrying floating debris. Therefore, using wave force formulae to estimate tsunami-induced forces on near-shore structures is inaccurate. Reconnaissance visits to regions affected by tsunamis illustrated that different forces with very high magnitude and at different bore propagation stages were exerted on near-shore structures.

This survey of the existing literature highlighted that tsunami-induced coastal inland flooding is a complex process marred by significant uncertainty. Different formulas proposed by several researchers were suggested to estimate the tsunami bore velocity [Murty 1977, Kirkoz 1983, Matsutomi 1999, Tsutsumi et al. 2000, Iizuka and Matsutomi 2000, Shuto et al. 2007], the bore-induced forces [Asakura et al. 2000, Iizuka and Matsutomi 2000, Ikeno et al. 2001, Yeh 2006, and Fujima et al. 2009], and the debris impact force [Sogabe et al. 1981, Matsutomi 1999, Ikeno et al. 2001, and Haehnel and Daly 2002]. The variations of the results using the proposed formulas leads to two findings: the complexity and difficulty of using results of laboratory model tests to suggest accurate formulas for real scale loading; and the lack of correct estimations of tsunami-induced loads on near-shore structures. Noteworthy is that the vertical and the horizontal distribution of the bore pressure around a structure during tsunami inundation are not fully understood. Moreover, the impact force caused by waterborne debris is found to be one of the main factors leading to significant damage or progressive collapse failure of near-shore infrastructure. This force is not well-understood as the magnitude depends on many parameters (e.g. mass, size or shape, velocity, etc. of the debris in addition to the bore characteristics). Past tsunamis demonstrated that the vast majority of non-engineered infrastructures were incapable of sustaining significant tsunami inundation due to the extreme hydrodynamic and impact forces. However, some structures survived the tsunami inundation due to the presence of a tsunami wall located seaward of those structures.

Very few studies are directly related to the problem of tsunami-induced forces on near-shore structures. In the present study, structural models of different cross-sectional shape were impacted with experimentally simulated tsunami bores. The bores were

generated from three impounding water levels, whose release in the form of a dam break wave similar to the tsunami-induced bores resulted in three inundation depths at the location of the structures. Furthermore, in this experimental study, the probability of debris orientation on impact was investigated both qualitatively and quantitatively. Review of previous work reveals uncertainty of the present understanding of debris impact forces. The literature review brought to light the fact that each approach has a parameter that is challenging to estimate accurately.

In conclusion, the literature review has highlighted the following deficiencies:

- Tsunami-induced bores can flood wide swaths of coastal regions and exert extreme hydrodynamic and debris impact forces on near-shore infrastructure.
- Critical infrastructure, including buildings designated as tsunami shelters (for general near-source tsunami and for the cases when horizontal evacuation is not an option), located in tsunami hazard regions need to be designed to withstand tsunami-induced forces.
- There is no one specific formula that can be used to compute each type of tsunami load with reasonable accuracy.
- Some structures survived tsunami inundation due to the existence of a natural obstacle (dune, coastal forest, and mangroves) or man-made structures located in the space between the structures and the shoreline.
- There is a need for detailed research aimed at better understanding the tsunami-structure interaction by quantifying the pressure distribution, forces, and overturning moments imposed on structures.
- Tsunami-induced bores transport floating debris which causes significant damage to near-shore infrastructure: to date, no specific formula providing a reasonable estimate is available.
- The relationship between bore characteristics (depth and velocity) and magnitude of the induced forces on structures is not well understood.

CHAPTER 3

REVIEW OF TSUNAMI LOADING

3.1 Introduction

Life safety through properly designed infrastructure is the main priority of the engineering design community. Safety can be achieved by taking into account, in the design process, all probable load types and combinations that a structure must sustain during its service life. This requires an understanding of the loads imposed on near-shore structures during tsunami events. Tsunami is a rare event and only few design documents are currently available, offering limited guidance for design engineers.

The focus of this chapter is to collate and present relevant information available in engineering design documents for estimating the design-tsunami loads for building structures located in areas prone to tsunami, taking into consideration that infrastructure safety could be achieved through a combination of policy and design. Policies cover areas of strategy, planning, warning and other associated measures. These are out of the scope of this study and thus will not be discussed herein. This chapter presents a brief description of the evolution of research related to tsunami-induced forces on near-shore structures, followed by a discussion of tsunami loads presented in recent engineering design documents. Finally, tsunami load components, formulas to estimate the individual forces, and tsunami load combinations applicable in the structural design process of near-shore buildings will be

presented. This chapter ends with a critical discussion of previous research and currently available engineering guidelines.

3.2 Tsunami-Induced Forces on Near-shore Structures

The earliest study on tsunami loading was completed by Cumberbatch (1960). The researcher investigated mathematically the impact of a two-dimensional water wedge on a wall. In the study, the effect of the gravity forces was neglected as the impact occurs over a very short time interval. Cumberbatch considered the impact of irrotational flow and formulated the problem in terms of a velocity potential which satisfies Laplace's equation for any time $t > 0$, satisfying the Bernoulli equation at any point. Far from the wall, the flow must approach the initial wedge condition of uniform flow and must satisfy free surface dynamic and kinematic boundary conditions. Cumberbatch introduced two solutions that are valid over a large distance from and near to the wall. Then these two solutions were matched to provide a complete solution to the problem.

Fukui et al. (1963) carried out an experimental investigation on the behavior of tsunami-bores and the forces induced by tsunamis on dikes. The authors used two different water tanks, one large and one small in sizes to study scale effects.

Cross (1967) considered Cumberbatch's solution for the initial water wedge shape, which resulted in two simultaneous ordinary first-order differential equations. The numerical integration of those equations over the wall generates the force per unit width as follows:

$$\frac{F_u}{\rho u^2 h} = \frac{1}{tan\theta} \int_0^{\lambda_w} C_p \left\{1 - \frac{\lambda^2}{\lambda_w^2}\right\} d\lambda \qquad 3.1$$

Where θ is the angle of the water surface as the surge advances toward the wall, λ is a similarity variable to solve the problem independently of time. To calculate the total force in a dimensionless form, Cross integrated the pressure along the wall for one side of the wedge from λ=0 to λ=λ_w.

Cross defined the right side of the above equation as C_F, force coefficient, a term which is used to evaluate the tsunami surge-induced force:

$$C_F = \frac{F_u}{\rho u^2 h} \qquad 3.2$$

As Eqn. 3.1 suggests, C_F is a function of the angle of water surface θ. The total force generated by the momentum and hydrodynamic pressure in the case of steady flow is:

$$F = 0.5\,\rho h^2 + \rho u^2 h \qquad 3.3$$

Exchanging the second term with that from Eqn. 3.2 to determine the force resulting from the flow approaching a wall, as opposed to steady flow, one obtains:

$$F = 0.5\,\rho h^2 + C_F \rho u^2 h \qquad 3.4$$

Cross (1967) used Cumberbatch's work to evaluate the force coefficient C_F and found that when the surge is flat, C_F *=1.0,* and when θ *= 50˚ - 72˚,* C_F can be calculated from the following formula:

$$C_F = (tan\,\theta)^{1.2} + 1 \qquad 3.5$$

Cross (1967) developed an expression to describe the surge front in which it was assumed that hydraulic, frictional, inertia and gravitational forces shape the surge tip. Cross's assumptions included a uniform horizontal flow velocity throughout the tip region and that both the velocity and acceleration of the bore front are known in advance. Cross's expression for the bore-tip shape advancing on dry-bed is as follows:

$$x = \frac{H}{b} - \frac{u^2}{C^2 b^2} \ln\left\{1 + \frac{C^2 b}{u^2} h\right\} \qquad 3.6$$

Where x is the distance from the beginning of the bore tip, u is the bore velocity, H is the bore height, C is Chezy resistance coefficient, $b = \frac{1}{g}\frac{du}{dt} - S$, and S is the bed slope. For a horizontal bed (zero slope) with the assumption of a constant bore velocity, the previous formula can be rewritten in the following form:

$$h = \frac{u}{C}\sqrt{2x} \qquad 3.7$$

Ramsden (1990) measured experimentally the forces induced by broken solitary waves on a vertical wall. The incident bore depth was varied from 24 to 49 mm and the

celerity from 750 to 1260 mm/s. During the reflection of bores and steep solitary waves at the wall, strong vertical accelerations caused the maximum force to occur before and after the maximum run-up for steep solitary waves and bores, respectively. The researcher noted that the maximum force varied from five to seven times the hydrostatic force, and that this maximum force occurred after the maximum run-up was observed.

Asakura et al. (2002), Ikeno et al. (2001), Iizuka and Matsutomi (2000), Ohmori et al. (2000), Yeh (2006), Fujima et al. (2009), and Nakano (2010) investigated tsunami-induced forces on structures and their proposed approaches were previously described in Chapter 2, Section 2.6.

3.3 Tsunami Loads in Current Engineering Codes

The purpose of a construction design code is to establish the minimum acceptable requirements necessary for protecting public health, safety, and welfare in the built environment. However, this is not necessarily the case for tsunami impact. The following section is a brief description of the most well-known construction codes and engineering design guidelines that provide some instructions pertaining to tsunami loads. A comparison between the available formulas will be presented and discussed in Chapter 7 (Section 7.2).

3.3.1 The City and County of Honolulu Building Code (CCH) (2000)

The City and County of Honolulu Building Code (CCH 2000) Article 11 provides regulations for flood hazard districts. Flood-proofing and structural requirements are provided for coastal flood water design including the effects of tsunamis. This document includes guidance on force components that should be considered in the design of structures, which are based on the work of Dames and Moore (1981) and is assumed to be applicable to tsunami waves. The magnitude of bore velocity is assumed to be equal in magnitude to the bore depth, and scour around foundations is determined from the distance from the shoreline and the soil type at the location of the structure. Offered in this code are formulae to estimate forces affecting building via coastal flooding. These forces include buoyant, surge, drag, and hydrostatic forces, as well as the impact force produced by waterborne debris.

CCH (2000) provides formulas similar to those cited in the previous section for the hydrostatic force, buoyant force, hydrodynamic force, surge force, and impact force. CCH

(2000) assumes that the debris velocity before impact is U_b and it drops to zero after impact (during a very short time). Therefore, the following approximation was used:

$$F_I = \frac{31U}{\Delta t} \quad 3.8$$

3.3.2 American Society of Civil Engineers Standard ASCE/SEI 24-05 (2005)

The American Society of Civil Engineers/Structural Engineering Institute Standard 24-05 (ASCE/SEI 24-05) Flood Resistant Design and Construction Standard provides minimum requirements for flood-resistant design and construction of structures located in flood hazard areas. Flood hazard topics include: basic requirements, high risk areas, coastal high areas, and coastal zones. This standard complies with the US Federal Emergency Management Agency (FEMA) and the National Flood Insurance Program (NFIP) flood plain management requirements. This standard was also referenced by the International Building Code (2006). ASCE 24-05 refers to ASCE7-05 for flood loads including hydrostatic, hydrodynamic, wave loads, debris impact loads, and load combination.

3.3.3 Federal Emergency Management Agency FEMA P-55 (2011)

The Federal Emergency Management Agency (FEMA) issued the fourth edition of the Coastal Construction Manual known as FEMA P-55 (2011). This manual contains instructions to design and construct structures located in coastal regions which are under the threat of damage due to a natural disaster (e.g. hurricane, earthquake, flood, etc.). Chapter 8 includes formulations related to site-specific loads, including: snow, floods, tsunamis, wind, tornados, and earthquakes, in addition to load combinations. The flood loads include estimates for flood depth, wave setup, wave height, flood velocity, hydrostatic loads, breaking-wave loads on piles and walls, and debris impact loads. FEMA P-55 treats tsunami as an extreme flood event with high flow velocity based on the study of Dames and Moore (1981). This document suggests that tsunami loads can be calculated similarly to other flood loads as the physical processes are similar but the scale is different. Based on the study of Tsunami Engineering by Camfield (1980), FEMA P-55 states that tsunami propagates inland in one of two forms: as a rapidly rising tide or a bore-like broken wave. The buoyant and hydrostatic forces resulting from the first form are the main cause of structural damage to

buildings, while the hydrodynamic forces are largely responsible for damage resulting by the latter form.

3.3.4 Structural Design Method of Buildings for Tsunami Resistance (SMBTR) (2005)

In 2000, the Building Technology Research Institute - The Building Center of Japan issued engineering guidelines for tsunami loads and structural design of tsunami refuge buildings. A structural design method was proposed for tsunami refuge structures based on literature survey of experimental studies of tsunami loads on coastal structures (Asakura et al. 2000, Ohmori et al. 2000, Iizuka and Matsutomi 2000, and Ikeno et al. 2001). This document includes formulations for loads applied to near-shore structures resulting from tsunamis. The maximum tsunami force is based on a hydrostatic pressure distribution extending vertically to $3h$, where h is the water depth at the structure measured from the base of the structure. The corresponding pressure at the base of the wall is set equal to $3\rho gh$. The resulting base shear force is effectively 9 times the equivalent hydrostatic force for the same water depth. SMBTR also provides guidance on the effect of buoyancy and load combinations with other types of forces.

In 2005, the method was revised with minor changes, which were published as the Structural Design Method of Buildings for Tsunami Resistance (SMBTR). The method was verified by applying it to a few buildings that were damaged during the 2004 Indian Ocean Tsunami. The following equation was proposed to calculate the tsunami wave pressure:

$$q_z = g\rho(3\eta - z) \qquad 3.9$$

Where q_z is the tsunami wave pressure in the direction of flow (kN/m^2), z is the height of the relevant portion from ground level ($0 \leq z \leq 3h$) in meters. Figure 3.1 illustrates the tsunami pressure estimated from Eqn. 3.9.

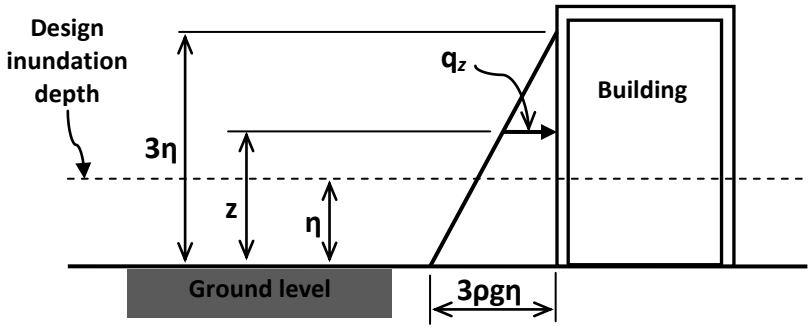

Figure 3.1 Tsunami wave pressure in the flow direction (SMBTR, 2005)

SMBTR (2005) calculates the tsunami wave force on structures by integration of the previous formula as follows:

$$Q_z = \frac{1}{2} g\rho B\{(6\eta z_2 - z_2^2) - (6\eta z_1 - z_1^2)\} \quad 3.10$$

Where Q_z is the tsunami wave force in the direction of flow (kN), B is the width of the structural element (m), z_1 is the minimum height of the pressure-exposed surface ($0 \leq z_1 \leq z_2$) in m, and z_2 is the maximum height of pressure-exposed surface ($z_1 \leq z_2 \leq 3h$) in m as shown in Figure 3.2

SMBTR (2005) suggests that the tsunami wave force can be reduced based on the presence of obstacles surrounding the structure. Furthermore, the buoyant force is determined from Eqn. 3.20.

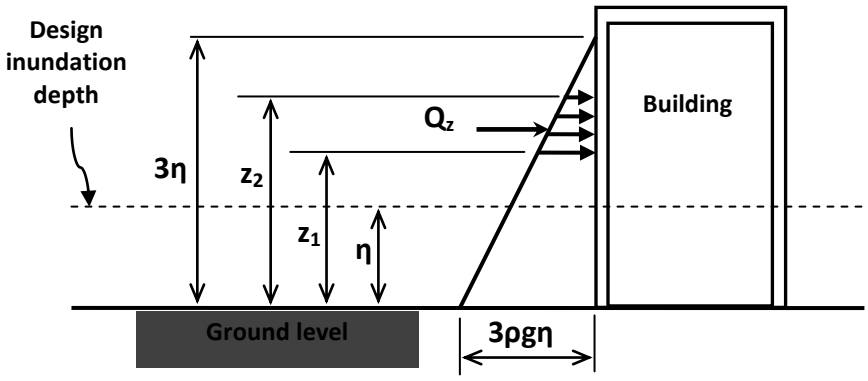

Figure 3.2 Tsunami wave force in the flow direction (SMBTR, 2005)

3.3.5 Federal Emergency Management Agency FEMA P-646 (2012)

The Federal Emergency Management Agency (FEMA) published the second edition of the Guidelines for Design of Structures for Vertical Evacuation from Tsunamis, known as FEMA P-646 (2012). This document represents the state-of-the-art engineering document that provides provisions to calculate tsunami loads on structures. The objective of FEMA P-646 was to develop guidance to design a structure to be earthquake and tsunami-resistant. Chapter 6 contains prescriptions for estimating tsunami-induced force components and for structural design criteria.

There are a number of force components that results from tsunamis; these include the following:

- Hydrostatic forces developing from standing or slowly-moving flow around the structure;
- Buoyant forces caused by the displaced volume of water;
- Hydrodynamic forces surfacing from moderate-to-high-velocity water flow around the structure;
- Impulsive forces arising from the leading edge of the water surge as it hits the structure;
- Debris impact forces caused by floating debris; and
- Damming of waterborne debris due to the accumulation of debris on the upstream side of the structure; this results in additional drag forces.

Taken into consideration with these forces is an uplift force applied on the raised floors of a structure that is submerged.

The following formula is suggested by FEMA-P646 to estimate the hydrodynamic force. The force is a function of the fluid density, flow velocity, and structure geometry. This force results from the pressure generated by the moving water mass and the drag generated by the water flow around the structure and/or its components. These equations were used to calculate the hydrodynamic forces induced on the structural models in this experimental study and were compared with those experimentally measured:

$$F_d = 0.5\rho_s C_d B(hu^2)_{max} \quad 3.11$$

$$(hu^2)_{max} = gR^2\left\{0.125 - 0.235\frac{z}{R} + 0.11\left(\frac{z}{R}\right)^2\right\} \quad 3.12$$

FEMA P-646 recommends setting the density of the fluid $\rho_s = 1100\ \mathrm{kg/m^3}$ to account for the presence of sediment and small debris. C_d is the drag coefficient which depends on the shape, orientation, and size of the structure, and FEMA P-646 recommends a conservative value of 2.0; B is the breadth of the structure in the plane normal to the flow direction; hu^2 is the momentum flux per unit mass per unit width; g is the gravitational acceleration; R is the design run-up elevation (taken as 1.3 times the maximum run-up from the tsunami hazard map or from numerical simulation of tsunami propagation), and z is the ground elevation at the location of the structure.

3.3.6 American Society of Civil Engineers Standard ASCE/SEI 7-10 (2010)

The American Society of Civil Engineers Standard ASCE 7-10 Minimum Design Loads for Buildings and Other Structures provides general requirements for structural design, including forces arising from floods and waves on specific types of structural elements. The standard also covers important definitions that relate to flood areas or coastal high-hazard areas associated with tides, storm surges, riverine flooding, seiches or tsunamis. Chapter 5 of ASCE 7-10 contains formulas to calculate wave loads and breaking wave loads on piles and walls. The formulas simply convert hydrodynamic loads into equivalent hydrostatic forces, provided the flow velocity does not exceed 3.05 m/s; otherwise, basic concepts of fluid dynamics are required. ASCE 7 defines the hydrodynamic load during flooding based on the flow velocity into two categories. When the flow velocity does not exceed 3.05 m/s (10 ft/s), equivalent hydrostatic loads are determined, after increasing the Design Flood Elevation (DFE) by an equivalent surcharge depth d_h, as follows:

$$d_h = \frac{av^2}{2g} \quad 3.13$$

Where v is the average flow velocity, a is the coefficient of drag or shape factor ≥ 1.25, and g is the gravitational acceleration.

This equivalent surcharge depth d_h is added to the DFE to calculate the hydrostatic pressure and applied to the vertical projected area of the structure which is perpendicular to

the flow direction, while other surfaces parallel to flow direction are subjected to DFE only. ASCE 7 provides formulas to estimate breaking wave loads on piles and walls. However, for debris impact force, no guidance is provided except to consider it as concentrated force acting at the most critical location in a structure at or below DFE. No formulations, however, are prescribed. This document does not specifically contain a set of formulations for tsunami loads.

3.4 Tsunami-Induced Force Components

Depending on the nearshore bathymetry, tsunami waves tend to break offshore and advance onto the shoreline as a hydraulic bore or as a surge. Wave-breaking is often in the form of a plunging-type breaker in which the entire wave front collapses and overturns. The current research focuses on the tsunami induced force components on near-shore structures, thus wave-break forces were excluded herein. The following provides a description of the tsunami hydraulic forces and other associated forces observed during past tsunamis.

3.4.1 Hydrostatic force

The hydrostatic force occurs when standing or slowly moving water comes in contact with a structural component. The pressure (force) acts perpendicular to the surface of the component. Since the interior of a structure may not flood immediately, the hydrostatic force arises due to a differential in water depth on opposite sides of the structural component (e.g. an external wall). In the case of short width components (e.g. columns in framed structure with no partitions), water can quickly fill the space around the column and alleviate the hydrostatic force. Conversely, when the structure or component has significant width, similar to seawalls, the water levels will be considerably different on the both sides and result in significant hydrostatic forces. FEMA P-646 recommends evaluating this force for individual wall panels in watertight structures. The following equation is used to estimate the hydrostatic force:

$$F_h = p_c A_w = \frac{1}{2}\rho_s g b h_{max}^2 \qquad 3.14$$

where p_c is the hydrostatic pressure, A_w is the wetted area of the wall, ρ_s is the fluid density including entrained sediment and debris (1100 kg/m^3), g is the gravitational acceleration, b

is the width of the wall, h_{max} is the maximum water height above the base of the wall at the location of the structure. When the water height exceeds the wall height ($h_{max} > h_w$), the hydrostatic force is calculated using the following formula:

$$F_h = p_c A_w = \rho_s g b h_w (h_{max} - \frac{h_w}{2}) \quad 3.15$$

Here, h_{max} is the vertical difference between the design tsunami inundation depth (R) and the wall base elevation, which can be calculated as follows:

$$h_{max} = 1.3R^* - z_w = R - z_w \quad 3.16$$

where R^* is the maximum inundation depth, and z_w is the wall base elevation.

FEMA P-646 recommends evaluating R^* using a detailed numerical simulation model and to address uncertainty in the magnitude, FEMA suggests an increase of 30 %. Figure 3.3 shows the hydrostatic pressure distribution and resultant force assumed by FEMA P-646.

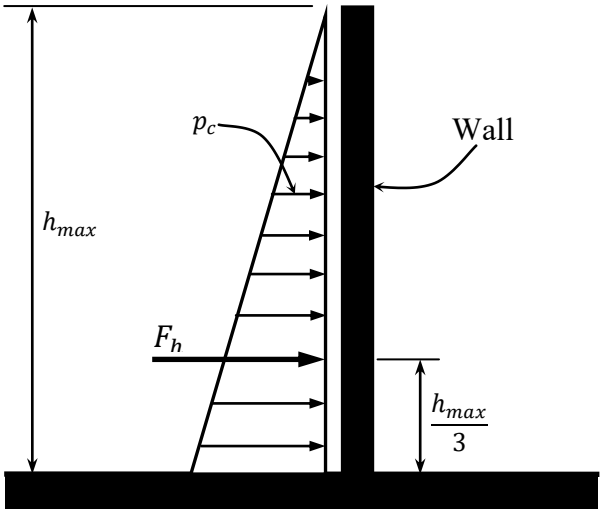

Figure 3.3 Hydrostatic force distribution and location of resultant (FEMA P-646, 2012)

The City and County of Honolulu Building Code (CCH, 2000) provides the following to calculate tsunami hydrostatic force:

$$F_{HS} = \frac{1}{2}\rho g \left(d_S + \frac{u_p^2}{2g}\right)^2 \quad 3.17$$

where ρ is the sea water density, g is the gravitational acceleration, d_S is the inundation depth and u_p is the normal component of velocity against a wall.

3.4.2 Hydrodynamic force

When a tsunami bore propagates inland with moderate to high velocity, the structure as a whole and the individual structural components are subjected to hydrodynamic forces. These forces are caused by a combination of lateral pressure and friction from the moving mass of water around the structure. FEMA P-646 proposes a uniform hydrodynamic pressure distribution over the inundated height of the structure as shown in Figure 3.4. Hydrodynamic forces depend on the fluid density, flow velocity and the structure geometry. FEMA P-646 provides the following equation to calculate the hydrodynamic force:

$$F_d = \frac{1}{2}\rho_s C_d B (hu^2)_{max} \qquad 3.18$$

where B is the width of the structure or the component in the plane perpendicular to the flow direction, C_d is the drag coefficient, h is the flow depth, and u is the flow velocity at the location of the structure.

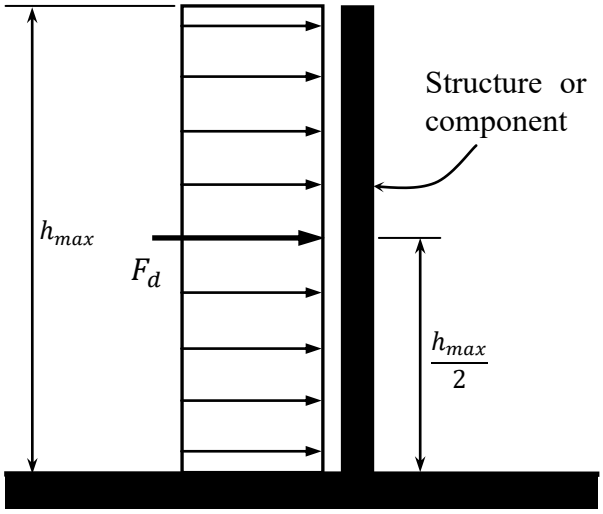

Figure 3.4 Hydrodynamic pressure distribution and resultant force (FEMA P-646, 2012)

The drag coefficient C_d depends on the geometry of the structure: CCH and FEMA P-55 recommend 1.0 and 1.2 for circular piles, respectively, while for rectangular piles, CCH, FEMA P-55, and FEMA P-646 recommend a value of 2.0.

Equation 3.18 is similar to that provided by FEMA P-55 and CCH 2000 ($F_d = \frac{1}{2}\rho C_d A u^2$) with very simple modifications to the momentum flux $(hu^2)_{max}$. As shown in Section 5.1.2 of this thesis, the maximum bore velocity is typically recorded at the front of the bore when the bore depth is small, while lower velocities are associated with the quasi-steady flow phase. Therefore, to predict the momentum flux, FEMA P-646 suggests referring to existing data or running a detailed numerical simulation with a very fine mesh resolution (< 5 m) to minimize error in the estimation of the momentum flux.

Based on Yeh (2007), FEMA P-646 provides the following formula (additional details are included in Section 2.5) to estimate the momentum flux:

$$(hu^2)_{max} = gR^2\left\{0.125 - 0.235\frac{z}{R} + 0.11\left(\frac{z}{R}\right)^2\right\} \quad 3.19$$

Where the parameters have the same definitions as previously cited and where R is the design inundation depth ($R = 1.3R^*$). This formula is based on one-dimensional nonlinear shallow-water theory with the assumptions of a uniform beach slope with no lateral topographical variation and no friction. FEMA P-646 suggests that Eqn. 3.19 be used for: (1) preliminary design; (2) approximate design in the absence of other modelling information; and (3) to evaluate the accuracy of numerical simulation results.

Although numerical simulations for tsunami run-up have advanced in recent years, calculating the bore velocity is not achieved with the same accuracy. As stated in Section 2.5, the bore velocity, a critical element in the prediction of the hydrodynamic force, is the one parameter generating significant disagreement among researchers. FEMA P646 recommends that the flow momentum should not be less than 80 % of that calculated from Eqn. 3.19.

3.4.3 Buoyant forces

Buoyant forces are vertical hydrostatic forces that act through the centroid of the displaced volume of water on a structure or structural component under conditions of partial or total submergence. The buoyant force equals the weight of the water that is displaced. This force is resisted by the weight of the components and any other forces working in the direction of gravity. Past reconnaissance trips [Nistor et al. 2006, Saatcioglu et al. 2006, Palermo et al.

2011, and Chock et al., 2012] reported the role of this force in the damage of light structures (wooden structures and empty tanks) and structural components (precast slabs). Buoyant forces can be estimated using the following equation:

$$F_b = \rho g V \qquad 3.20$$

Where V is the volume of displaced water due to the existence of a structure (Figure 3.5). The depth of displaced water is h_{max}, which is calculated from Eqn. 3.16. The fluid density according to FEMA P-646 can be taken as ρ_s=1100 kg/m^3, while CCH 2000 recommends simply using the water density of 1000 kg/m^3.

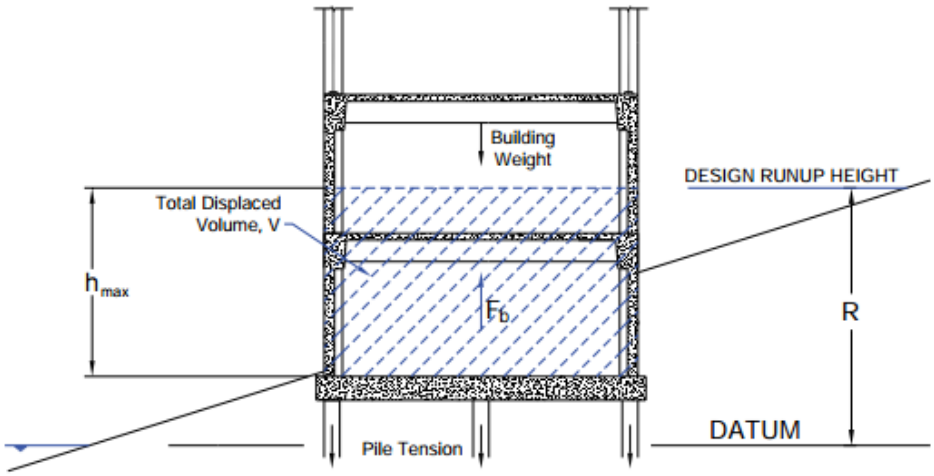

Figure 3.5 Buoyancy forces on structure with watertight lower floors (FEMA P-646, 2012)

3.4.4 Uplift forces on elevated floors

When the tsunami inundation depth is equal to the story level/s, uplift forces will act on the submerged level/s. Therefore, these floors must be designed to resist uplift forces due to buoyancy and hydrodynamic forces. Additional buoyant force arises from the extra water volume that is displaced due to air trapped underneath floor systems. Furthermore, exterior walls at the upper floor levels preventing ingress of water increase the buoyant forces (Figure 3.6).

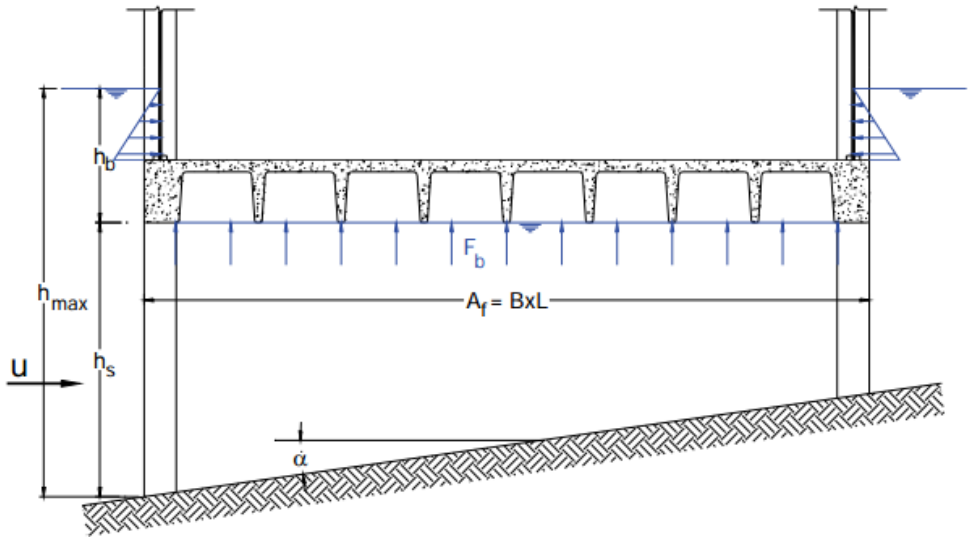

Figure 3.6 Uplift forces on the floor systems (FEMA P-646, 2012)

The total uplift force acting on floor systems can be estimated from the following formula:

$$F_b = \rho_s g A_f h_b \qquad 3.21$$

Where h_b is the height of water displaced by the floor system including entrapped air.

In addition to this uplift force, and under the condition of rapid inundation, hydrodynamic forces can impose vertical forces on floor slabs. The presence of vertical structural elements (walls and columns) in a building will act as terminators to tsunami flowing through the building. The flow will run-up on such elements and impose uplift forces on floor slabs immediately in front of the obstruction. FEMA P-646 provides the following formula to calculate the uplift force:

$$F_u = \frac{1}{2}\rho_s C_u A_f u_v^2 \qquad 3.22$$

Where C_u is a coefficient taken equal to 3.0, A_f is the area of the floor panel, u_v is the vertical velocity of the flow or rate of rise adopted from API (American Petroleum Institute, 1993). For sloping topography below the building, the vertical velocity can be estimated from Eqn. 3.23; otherwise a detailed hydrodynamic investigation should be conducted:

$$u_v = u \tan \alpha \quad (3.23)$$

Where u is the horizontal flow velocity, and α is the average slope of the ground at the location of the structure. Figure 2.25 can be used to evaluate u by replacing d/R with h_s/R, where h_s is the elevation of the floor as shown in Figure 3.6.

3.4.5 Impulsive (Surge) forces

Impulsive forces are generated by the leading edge of the tsunami-induced flow on a structure. The estimation of this tsunami force component has a high degree of uncertainty due to the complexity of tsunami-induced bore-structure interaction and lack of detailed experiments. Based on a study by Dames and Moore (1980), CCH 2000 recommended the following equation:

$$F_s = 4.5\, \rho g h^2 \quad (3.24)$$

Where F_s is the total surge force per unit width of wall and h is the surge height.

The surge force calculated from the Eqn. 3.24 acts at a distance h above the base of the wall. This equation should be used only when the wall height is equal to, or greater than, $3h$. Otherwise the surge forces should be calculated using an appropriate combination of hydrostatic and drag force for each specific situation.

FEMA P-646 was based on studies of Ramsden (1993) and Arnason (2005) in which a maximum overshoot of approximately 1.5 times the subsequent hydrodynamic force was observed. In those studies, the overshoot appeared in the case of wet-bed conditions for a surge and it was attributed to the relatively mild slope of the front profile of the water surface. This is in contradiction with studies of Chanson (2006) and Nouri (2008), and data collected in this present study, in which the overshoot (spike) was evident for dry-bed conditions.

FEMA P-646 recommended that a conservative value be given to the impulsive force, equal to 1.5 times the hydrodynamic force that is estimated from Eqn. 3.25:

$$F_s = 1.5 F_d \quad (3.25)$$

FEMA P-646 suggests applying this force on structural members with significant width (structural walls) at the leading edge of the tsunami bore, while hydrodynamic forces will be applied on all members that have already been passed by the leading edge (Figure 3.7).

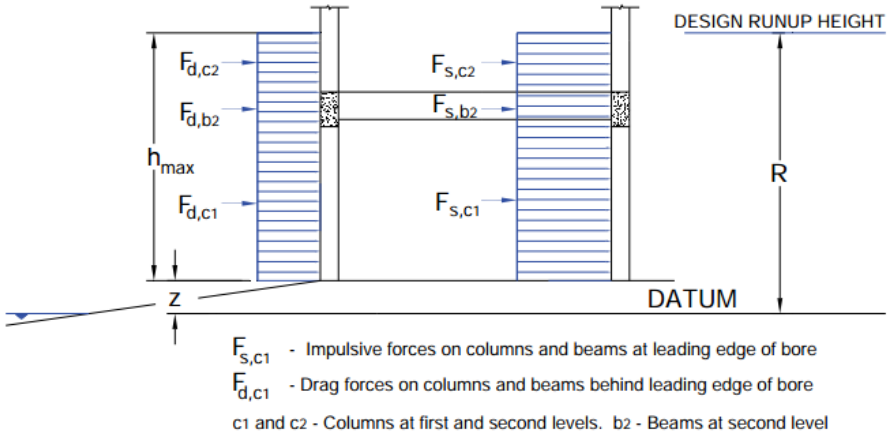

Figure 3.7 Hydrodynamic impulsive and drag forces on components of a building subjected to inundation by a tsunami bore (FEMA P-646, 2012)

3.4.6 Debris impact forces

Waterborne debris in tsunami-prone areas possess special features, such as rapid out-bursting, impacting, rushing and depositing, and ultimately damaging structural elements. The hydrodynamic loading due to flow and the impact force of the debris often act simultaneously. Past tsunamis showed that the debris type depends on the characteristics and land use of the coastal area - in ports and fishing coasts, debris are usually boats and/or shipping containers; while in residential areas, debris consists of floating construction materials (e.g. timber logs, champers, cars, etc). Thus, the debris field is characterized by a wide variety of sizes with different shapes, masses, and orientations during a tsunami event.

The impact force of floating debris carried by tsunami-induced bores (e.g., driftwood, automobiles, shipping containers, boats, and buildings) can result in significant damage or even collapse of entire structures. As previously noted (Section 2.7), there are three approaches to estimate the debris impact force. FEMA P-646 used the formulation proposed by Haehnel and Daly (2002), which was based on the effective stiffness approach,

and introduced the hydrodynamic mass parameter c, and an importance factor of 1.3 as suggested by ASCE 7-10 for debris impact on Risk Category IV structures as follows:

$$F_{max} = 1.3u_{max}\sqrt{km_d(1+c)} \qquad 3.26$$

Where u_{max} is the maximum bore velocity carrying the debris at the site, with the conservative assumption that the debris moves at same flow velocity. In the case where debris is rolling along the ground, the debris velocity may be taken as 50 % of flow velocity; k is the effective combined stiffness of the debris and the impacted structural element; m_d is the debris mass; and

c is the hydrodynamic mass coefficient which represents the influence of water surrounding the debris. The value of the hydrodynamic coefficient depends on the size, shape, and orientation of the debris with respect to the flow direction.

This force is assumed to act locally on a single structural element at the elevation of the water surface as shown in Figure 3.8. Debris impact force should be evaluated considering the location of the structure and the surrounding area. For most coastal communities, floating debris would mainly consist of logs and construction elements. For large ports, fishing harbours, and industrial locations, the expected debris are shipping containers and/or boats.

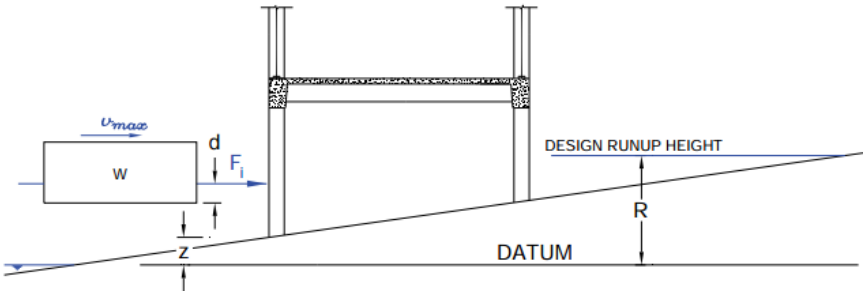

Figure 3.8 Impact force due to waterborne debris (FEMA P-646, 2012)

As shown above, Eqn. 3.26 requires the mass and stiffness of the debris. FEMA P-646 provides the following values for common waterborne debris (Table 3.1), for other types of debris these factors must be derived.

FEMA P-646 recommends that the debris velocity be obtained from a numerical simulation with a fine grid for more accurate results, although this velocity will be less accurate than the predicted inundation depth. Moreover, FEMA P-646 adopts the flow velocity formula (Eqn. 2.35) derived by Yeh (2007) that was described in Section 3.4.2. Figure 2.26 was also adopted to determine the maximum flow velocity (to be equal to the debris velocity) based on the debris-drift/inundation depth ratio and ground elevation. It is important to emphasise that this approach was based on the analytical solution of tsunami run-up with the following assumptions: uniformly sloping beach, with no lateral topographical variation, and no friction. The first two conditions are rarely satisfied; while the third is an ideal case. Thus, the flow velocities estimated from this method are expected to be higher than the actual velocities. FEMA P-646 (2012) advises that u_{max} should not be taken less than 80 % of that estimated from Eqn. 2.35 or Figure 2.26. The debris drift d can be estimated from the following formula:

$$d = \frac{W}{\rho_s g A_f} \tag{3.27}$$

Where W is the debris weight, and A_f is the cross-sectional area parallel to the water surface.

Table 3.1 Mass, hydrodynamic mass coefficient, and stiffness of waterborne debris (FEMA P-646, 2012)

Type of Debris	Mass (m) in kg	Hydrodynamic Mass Coefficient (c)	Debris Stiffness (k_d) in N/m
Lumber or wood log – oriented longitudinally	450	0	2.4×10^6
20 ft Standard Shipping Container - oriented longitudinally	2200 (empty)	0.30	85×10^6
20 ft Standard Shipping Container - oriented transverse to flow	2200 (empty)	1.00	80×10^6
20 ft Heavy Shipping Container - oriented longitudinally	2400 (empty)	0.30	93×10^6
20 ft Heavy Shipping Container - oriented transverse to flow	2400 (empty)	1.00	87×10^6
40 ft Standard Shipping Container - oriented longitudinally	3800 (empty)	0.20	60×10^6
40 ft Standard Shipping Container - oriented transverse to flow	3800 (empty)	1.00	40×10^6

3.4.7 Debris damming

Depending on the location of the structure, partitioning of the seaward-elevation, debris size, surrounding obstacles, and usage of coastal area, debris may accumulate resulting in an increase in the building breadth subjected to hydrodynamic forces. As the distance between adjacent buildings and/or the spans between columns may be less than the size of potential debris, the probability of debris-damming forces imposed on the structures during tsunami events rises. FEMA P-646 modified Eqn. 3.11 to consider debris damming forces as follows:

$$F_{dm} = \frac{1}{2}\rho_s C_d B_d (hu^2)_{max} \qquad 3.28$$

Where B_d is the breadth of the debris dam and C_d is taken equal to 2.0.

As the damming force F_{dm} results from flow blocking by the accumulation of debris, this force should be assumed as uniformly distributed over the width B_d. FEMA P-646 (2012) suggests that the damming width B_d should be at least 12 m (40 ft) or more; this limit represents the size of a shipping container or a mass of floating lumber. The debris damming effect should be evaluated at different locations for the structure to determine the worst effect.

3.4.8 Additional gravity loads

In addition to loads described, FEMA P-646 prescribes an extra gravity load resulting from water retained on elevated floors as illustrated in Figure 3.9. The volume of retained water depends on its height h_r which can be deduced by subtracting the floor level from the maximum inundation depth.

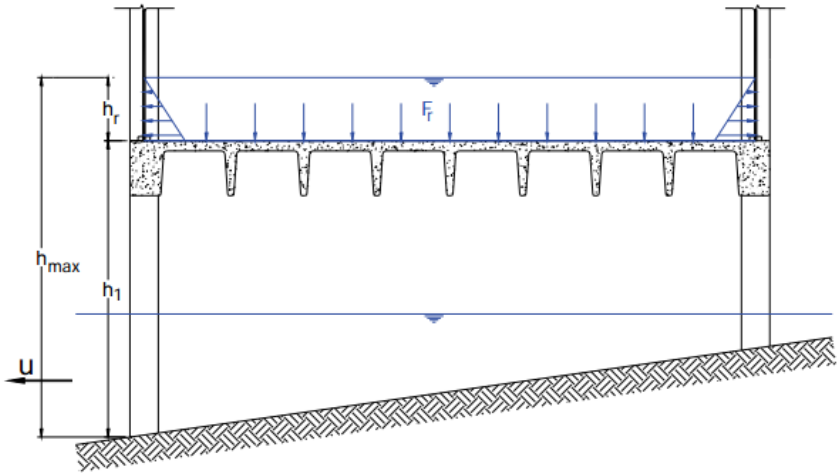

Figure 3.9 Extra gravity loads on elevated floors imposed by retained water (FEMA P-646, 2012)

Given that tsunamis represent a credible hazard for near-shore structures, and to address uncertainty accompanied with determining tsunami loads, FEMA P-646 (2012) recommends the following when using the formulas listed above:

1. Tsunami bore fluid consist of 10% sediment concentration and the density is assumed to be approximately 1.1 times the density of freshwater ($\rho_s = 1100\ kg/m^3$).

2. Tsunami design maximum inundation depth is increased by 30% ($R = 1.3R^*$) to recognize the variability in local tsunami run-up height due to onshore topographic characteristics and uncertainty in numerical modeling of tsunami inundation.
3. Tsunami bore velocity, depth, and momentum flux should not be taken less than 80% of the values determined from the analytical solution (Figure 2.26, Equations 2.35 and 3.19, respectively).

As the inundation parameters (R and u) are produced from detailed site-specific numerical simulation models, the above assumptions were implemented due to the uncertainty in the onshore tsunami inundation modeling results.

3.5 Loading Combinations

Tsunami-induced force components (hydrostatic, hydrodynamic, impulsive, buoyant, and debris impact) do not occur concurrently, and they do not affect a specific structure or individual structural elements at the same time. Thus, appropriate combinations of these components, taking into consideration the type and location of the structural element, are required to ensure an economic and safe structure. The load combinations substantially affect the magnitude of the resultant tsunami-forces and consequently the structural design. Although the load combinations for flood-induced surges are well recognized in engineering standards, the literature review highlighted that proposed tsunami-load combinations require further enhancements and should be integrated into engineering guidelines and building design codes. As previously stated, tsunami-induced bore differs from flood surge (e.g. inundation depth and flow velocity); therefore, load combinations for flood surge are not suitable for tsunami-induced bore. This section describes tsunami loading combinations proposed in the literature:

Dias et al. (2005) proposed two load combinations called ‘point of impact/ not submerged’ (when the static and dynamic loads act in a single direction) and ‘post-submergence/submerged’ (when only a net dynamic force is effective) as shown in Figure 3.10. These load combinations are described for two situations: (i) the instant the tsunami-bore impacts the structure; and (ii) when the whole structure is inundated, and are presented as follows:

Point of Impact:

F_d (on walls facing shoreline) + F_s (on walls facing shoreline)

Post-submergence/Submerged:

F_d (on walls facing shoreline) + F_b (on submerged section of the structure)

Where F_s is defined as the hydrostatic force; F_d is the hydrodynamic force; and $F_b = \gamma V$ is the buoyant force, with γ the unit weight of sea water and V the volume of the submerged section of the structure.

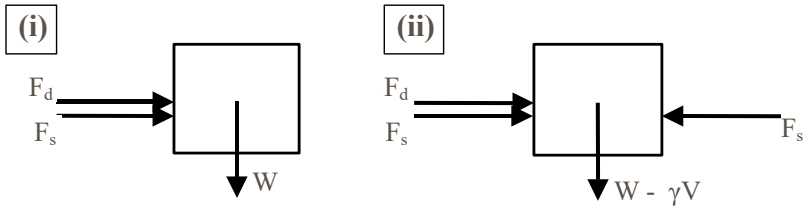

Figure 3.10 Loading combinations: **i)** point of impact; and **ii)** post-submergence (Dias et al., 2005)

Nouri et al. (2007) proposed load combinations based on modifications of the two cases proposed by Dias et al. (2005) as shown in Figure 3.11. The proposed load combinations by Nouri et al. (2007) follow a consistent format as the above combinations:

Columns:

F_s (on front row of columns only) + F_i (on one critical column in the front row only), or

F_d (on all columns) + F_i (on one critical column only)

Solid (wall) foundation (perpendicular to flow direction):

F_s (on walls facing shoreline) + F_i (on one corner), or

F_d (on walls facing shoreline) + F_i (on one corner) + F_b (on submerged section of the structure)

Where; F_s, F_i, F_d, and F_b refer to the surge force on walls and columns, debris impact force, hydrodynamic force and buoyant force, respectively. Figure 3.11 is a schematic drawing for the load combinations proposed by Nouri et al. (2007).

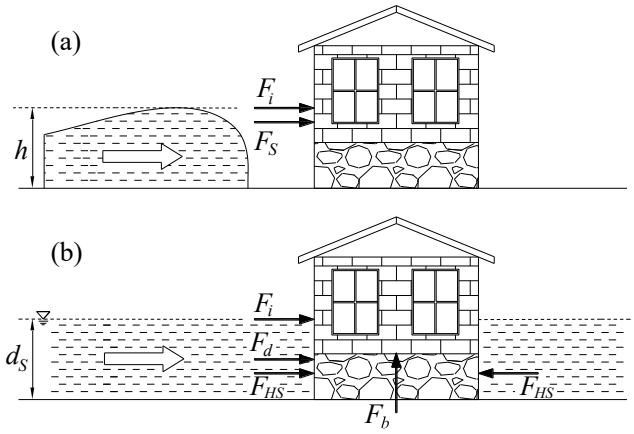

Figure 3.11 Proposed loading conditions: **a)** point of impact; and **b)** post-impact (Nouri et al., 2007)

FEMA P-55 (2011) provides the following flood load combinations for structural design in coastal zones. While these combinations cannot be directly applied for tsunami load, they can, however, be used as guidance. Flood load combinations for two types of foundations: piles or open foundations, and solid walls in flood hazard zones and coastal high hazard zones are presented as follows:

Pile or Open Foundation in Zone V or Coastal A Zone:

Greater of F_{brkp} or F_{dyn} (on front row of piles only) + F_{dyn} (on all other piles) + F_i (on one pile only)

Solid (perimeter Wall) Foundation:

Greater of F_{brkp} or F_{dyn} + F_i (on one corner)

Where $F_{brkp}, F_{brkw}, F_i, and\ F_{dyn}$ are the breaking force on pile, breaking force on wall, impact force, and hydrodynamic force, respectively.

For additional guidance on designing for tsunami forces and load combinations, FEMA P-55 refers to the Guidelines for Design of Structures for Vertical Evacuation from Tsunami (FEMA P-646).

FEMA P-646 (2012) proposes two combination strategies: combinations on overall structure and combinations on individual structural components.

Combinations on overall structure:

$(F_b + F_u)$: The buoyant and hydrodynamic uplift forces affect the overturning resistance and should be considered in all load combinations.

F_s: The impulsive force is caused by the leading edge and should be applied sequentially to all structural components, but not concurrently.

F_d: The drag force acts on all structural components which were passed by the flow leading edge. Thus the total hydrodynamic force on a structure is the summation of the impulsive forces on the elements at the leading edge and the drag forces on the previously submerged elements behind the leading edge. The worst case will likely occur when the leading edge reaches the last row of vertical components in the building frame (Figure 3.12).

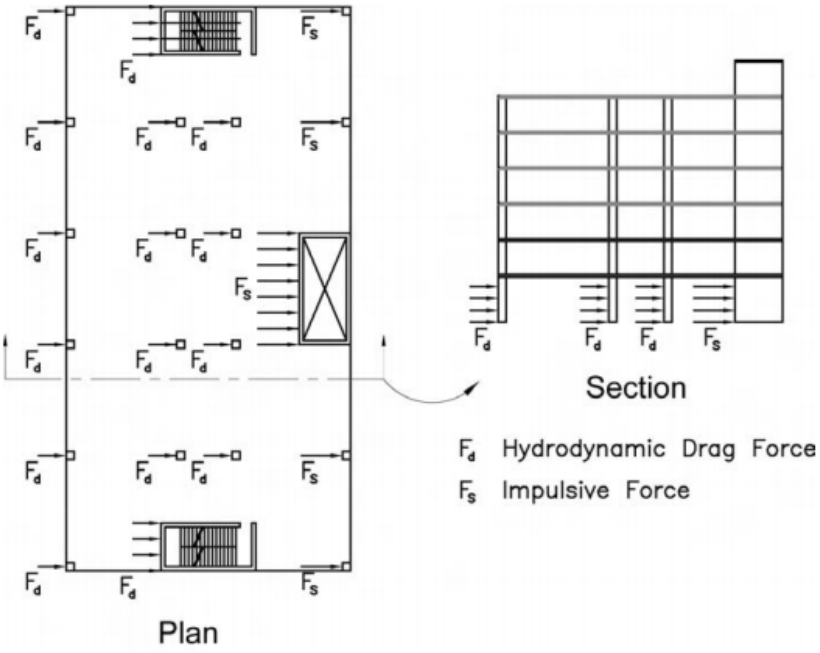

Figure 3.12 Combination of impulsive and drag forces applied to a typical building (FEMA P-646, 2012)

F_i: Debris impact force can be combined with the hydrodynamic force F_d but not with the impulsive force F_s; large floating debris are not carried by the bore leading edge. Due to the low probability of more than one impact occurring at any point in time, only one impact force should be considered. The impact force in combination

with other tsunami forces, except impulsive force, will be resisted by both individual structural components and the overall structure.

F_{dm}: Debris damming forces increase the area of the structure projected to the direction of the bore flow. Consequently, the hydrodynamic forces increase in magnitude. This force should be applied at the most critical location on a structure, while the hydrodynamic forces act on all other structural components as shown in Figure 3.13.

F_r: Water retained forces should be applied independently from the lateral tsunami forces against the floor systems.

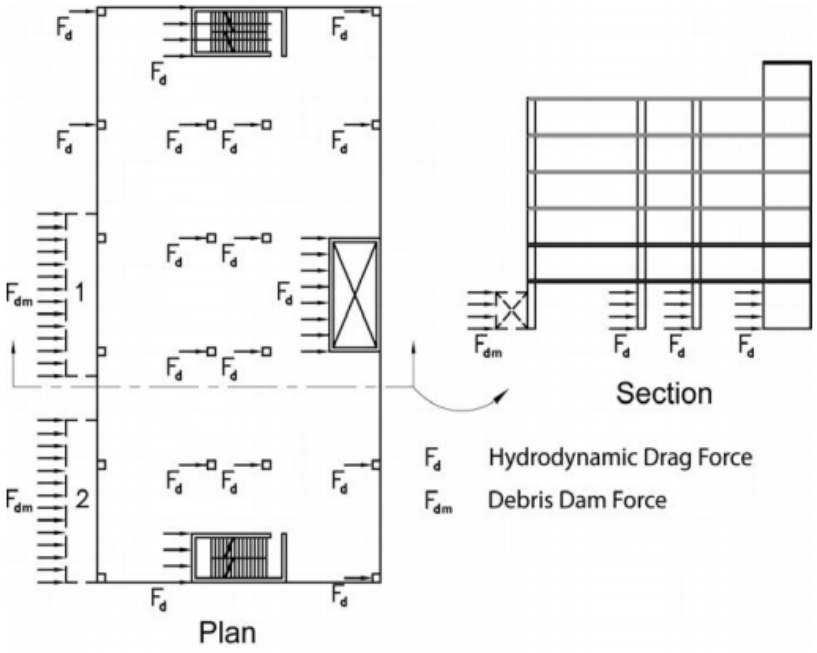

Figure 3.13 Combination of debris damming and drag forces applied to a typical building (FEMA P-646, 2012)

Combinations on individual components:

This combination is proposed in two categories depending upon the direction of the forces: horizontal (lateral) and vertical.

- **Lateral forces**: effect on structural components: columns, walls, and beams.

  F_s: Impulsive force applies to the component due to leading edge.

$F_d + F_i$: Hydrodynamic force and debris impact force apply to the component at most critical section.

F_{dm}: Debris damming force applies to the component representing the worst load condition to the member with 40 ft as minimum debris width.

F_h: Hydrostatic pressure force applies on walls surrounding watertight areas of a structure.

- **Vertical forces**: effect on floor framing components.

  F_b: Buoyancy force applies to submerged floor components including the effects of entrapped air and upturned beams or walls.

  F_u: Hydrodynamic uplift force applies to floor systems for flow velocity at a depth equal to the soffit of the floor system.

  Slabs, beams, and connections must be designed for maximum uplift condition: the maximum uplift force should be combined with 90% of dead load and zero live load.

  F_r: Water retained forces should be combined with 100% dead load.

Based on the Commentary of ASCE/SEI 7-10, Minimum Design Loads for Buildings and Other Structures (ASCE, 2010), FEMA P-646 (2012) has proposed Strength Design Load Combinations and suggests using those combinations in addition to load combinations available in current building design codes. The resulting tsunami loads acting on a structural member (T_s) should be combined with gravity load effects according to the following combinations:

$$1.2D + 1.0T_s + 1.0\ L_{REF} + 0.25\ L \qquad 3.29$$

$$0.9D + 1.0\ T_s \qquad 3.30$$

Where D is the dead load, T_s is the tsunami load, L_{REF} is the live load in a refuge area, and L is the live load outside of a refuge area. Note that the above load combinations are specific for tsunami refuge structures.

In the Strength Design Load Combinations the tsunami load factor is equal to one due to three reasons: the expected tsunami hazard level corresponds to the Maximum

Considered Tsunami (MCT) with a 2475-year return period, the 30% increase applied to the maximum inundation depth to recognize uncertainty, and only elastic response is considered for design of tsunami forces.

ASCE7-10 specification recommends that the design strength of structures, components and foundations that are exposed to fluid (for buildings in flood zone) should be designed with strength equal or be greater than the effects of the factored loads according to the following load combinations:

$$1.4(D + F) \tag{3.31}$$

$$1.2(D + F + T) + 1.6(L + H) + 0.5(L_r \text{ or } S \text{ or } R) \tag{3.32}$$

Where D = dead load, F = load due to fluid with well-defined pressure and maximum heights,

T = self-straining force, L = live load, H = load due to earth pressure and ground water pressure, L_r = roof live load, S = snow load, and R = rain load.

3.6 Discussion

The earliest studies on hydraulic bore-induced forces on structural elements date back to the 1960s (Cumberbatch (1960), Fukui et al. (1963), Cross (1967)), and followed by others more recently (Ramsden (1990), Asakura et al. (2002), and Ikeno et al. (2001)). Although four decades have passed from the pioneering studies, the hydraulic bore-induced forces on structures are still not well understood. This issue may be justified mainly by two reasons: (1) the bore propagation inland and its interaction with structures are very complex processes; and (2) large tsunamis are relatively rare events and for the most part occur at active seismological regions that are located close to a large body of water. Thus, to date, there is no engineering design code that contains a detailed description of tsunami-induced forces; few building codes/standards and engineering guidelines provide primitive instructions. The last decade witnessed four mega tsunamis that caused significant loss of life and economic consequences. Those events raised public awareness on tsunami and motivated researchers around the world to investigate tsunami mitigation. In this chapter,

five of the most recent engineering codes/standards and guidelines were presented with brief descriptions for each.

Although there is some similarity between the physical processes of tsunami inundation and other floods, the scale of tsunami inundation is significantly different and the run-up elevation is much greater. Most of the existing guidelines [CCH 2000, ASCE 24-05, ASCE 7-10, and FEMA P-55] provide flood load prescriptions to be used for tsunami bore-induced forces, which give inappropriate estimations for tsunami loads. The need for improved tsunami load characterization has been brought to light due to the number of lives lost and significant economic impact as a result of four mega tsunamis that inundated coastal communities during the last decade. FEMA P-646 and SMBTR are the only two guidelines that provide prescriptions specifically for tsunami loads. A comparison between the tsunami-forces determined by two guidelines revealed the uncertain nature of tsunami load prediction, and points to the need for additional research [Al-Faesly et al. (2012) and (2011)].

This work focuses on tsunami-induced forces exerted on structures that lie inland at some distance from the shoreline. Wave-breaking forces imposed directly on structures are not considered in this research study. Recall that tsunami waves break off-shore and propagate inland in the form of a bore or a surge. As a tsunami bore advances inland and impacts structures in its propagation path, different forces are imposed on the structure: hydrostatic, hydrodynamic, impulsive (surge), buoyant, uplift on elevated floors, debris impact, and debris damming. The magnitude of those forces is a function of the inundation depth and flow velocity at the location of the structure, structural shape, type or mass of floating debris and objects existing in the area surrounding the structure. Among these forces, only the hydrostatic and buoyant forces have similar approaches in all guidelines, while the other forces are not consistently calculated. Considering that these forces do not affect a specific structure concurrently, the combination of the forces to be used in structural design should follow a rational approach. FEMA P-646 (2012) presents the most recent combinations that are based on the lessons learned from past tsunamis.

CHAPTER 4

EXPERIMENTAL PROGRAM

4.1 Introduction

As a result of recent tsunami events and the vulnerability of structures as documented in previous chapters, a comprehensive interdisciplinary experimental program was jointly initiated by the Department of Civil Engineering at the University of Ottawa and the Ocean, Coastal and River Engineering (OCRE) at the National Research Council (NRC) in Ottawa, Canada. The experimental component of this program involved a simple test setup to generate tsunami-induced bores that impacted two structural models. This simulated tsunami-induced bore was an abstraction of natural processes in which the cross-sectional area, bottom slope, and friction characteristics can vary in both time and space. The number of parameters is extensive thus a systematic variation of the bore characteristics was not possible in these laboratory experiments. The objectives of this testing program was to provide a better understanding of the impact of tsunami-induced bores on onshore infrastructure, and to investigate the associated forces.

Within the experimental program several proposed mitigation strategies were investigated by installing various low-lying wall configurations in an attempt to reduce tsunami hydrodynamic loading. The testing simulated the impact on the structural models

due to hydraulic bores, similar to those generated by a broken tsunami wave advancing onshore. During testing, force-, moment-, lateral displacement-, acceleration-, bore depth- and velocity-time histories were recorded. Three impounding water depths were used: 550, 850, and 1150 mm, which generated maximum inundation depths (h_{imax}) at the location of the structural models of 250, 350, and 450 mm, respectively. These inundation depths correspond to the case where no structural model was installed in the flume. Figure 4.1 provides a flow chart of the experimental testing components.

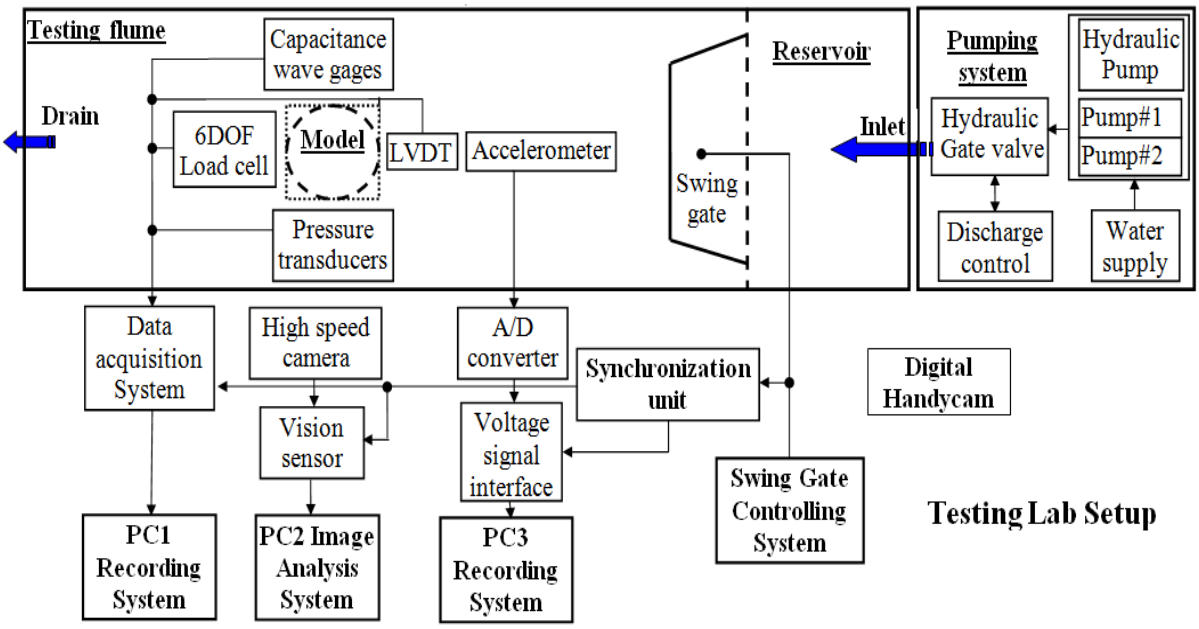

Figure 4.1 Flow chart of experimental testing components

The following provides details of the testing facility, structural models, instrumentation, mitigation walls, and testing procedure and program.

4.2 Scaling Principles and Considerations

To satisfy scaling for physical hydraulic modeling, similarity of motion and similarity of forces should be maintained. In free-surface flow investigations (including dam-break wave and tsunami bore) the gravity effect is usually dominant and scaling is performed using Froude similitude (Hughes 1993). Where the same fluid is used in both the model and the prototype, distortions are introduced by effects other than gravity (i.e. viscosity and surface

tension) - this results in scale effects. As the tsunami bore propagates inland, bed friction opposes the flow motion. Modeling flow resistance is challenging due to the geometric similarity of roughness (height and spacing) not being sufficient (Chanson 1999). Therefore, to ensure an undistorted Froude scaling model, the model resistance should be similar to that in the field (prototype). This requires the following condition to be satisfied:

$$f_R = \frac{f_P}{f_M} = 1.0 \qquad 4.1$$

Where f_R is the Darcy friction ratio, and $f_P \; and \; f_M$ are the Darcy friction factors of the prototype and model, respectively.

Video image recordings from the 2004 Indian Ocean Tsunami and 2011 Tohoku, Japan Tsunami illustrate that the tsunami bore front is characterized by:

a) High turbulence: This requires the simulated flow in the model be turbulent as well, which means that the modeled tsunami bore should have Reynolds number (Re_M) of $5000 < Re_M \leqq 10000$.

b) Significant air entrainment: The scale effects in terms of air bubble entrainment ("white water") may take place for a geometric similarity ($L_R = \frac{L_P}{L_M}$) of $L_R = 10 \; to \; 20$ coupled with Froude scaling principles to achieve the air entrainment flow condition (Wood 1991 and Chanson 1997).

c) High content of sediment and debris: Scaling of both the sediment movement and the fluid motion poses a significant challenge for movable-bed hydraulic models and makes modeling the actual tsunami flow (three-phase: water-sediment-air entrainment) a hydraulic phenomenon difficult to model at full scale.

In conclusion, physical modeling of tsunami bores is challenging. At present, all previous researchers [Arikawa (2009), Lukkunaprasit et al. (2009), Yeom et al. (2009), Nistor et al. (2008), Matsutomi et al. (2008), Palermo et al. (2007), Arnason (2005), Ikeno and Tanaka (2003), Haehnel and Dally (2002), Ikeno et al. (2001), Asakura et al. (2000), Lauber and Hager (1998), Ramsden (1996)] used the same approach as the one used in the present thesis in terms of simulating hydraulic bores, without considering the entrainment of sediment.

Based on that and to minimize scaling effects, the experiments were carried out in a large, high-discharge flume with a relatively large structural model with a scale factor 1:5.

4.3 Scaling Effects

Lauber and Hager (1998) conducted an experimental study on turbulent bores in a smooth rectangular channel with variable bed slope of up to 45 degrees. The authors reported that scale effects due to air entrained in a smooth prismatic and rectangular channel are insignificant, provided the reservoir depth is $h_o \geq 300\ mm$. With the exception of the wave front, the flow is governed by the Froude similarity law. The authors also indicated that the non-dimensional separation time of the wall/gate impounding the water should be smaller than ($t * \sqrt{g/h_o} = \sqrt{2}$), where g is the gravitational acceleration, h_o is the reservoir depth, and t is time. To satisfy this condition for the impounding water depths used in the testing program in this study, the swinging-gate separation time was required to be equal to or less than 0.335 s, 0.416 s, and 0.484 s for the 550, 850, and 1150 mm impounding depths, respectively. The gate fully opened in 0.32 s for the 550 mm impounding depth and in 0.28 s and 0.026 s for the two other higher impounding depths of 850 and 1150 mm, respectively.

4.4 Other sources of error and uncertainty

The systematic and random errors, δ, lead to uncertainties when conducting measurements ($X_{Measured}$). Thus, the true value of the actual measurements (X_{Real}) can be expressed as:

$$X_{Real} = X_{Measured} \mp \delta \qquad 5.21$$

Where X is any measured variable in the experiment and δ is the total error of the measurement. Systematic errors can occur due to temporal drifts in the instrumentation during testing due to errors in calibration of the instrumentation, or to changes in the experimental environment. Systematic errors are often difficult to determine and cannot be eliminated by averaging a number of experimental trials with the same conditions. Random errors are intrinsically unpredictable and may cause a scatter about the exact value of a measured variable. The interpretation of the instrumental reading, fluctuations in the instrument measurements, or environmental interference in the measurement process represent all sources of random errors. These errors may be estimated depending on the

measurement methodology. All test series of this study were conducted in a closed laboratory environment with approximately constant temperature, humidity, and wind conditions. At the same time, the recording equipment used (water level gauges, dynamometer, pressure transducers) were calibrated and checked periodically to ensure that data were recorded with consistent precision. However, in the present study, potential errors could have occurred due to errors in:

- Bore profile measurements by the water level gauges
- Pressure measurements by the differential pressure transducers
- Base shear force and base overturning moments measured by the dynamometer
- PIV analysis of the bore velocity

Errors due to the water level gauges were reduced by taking the following measures:

1. Calibrating the water level gauges by moving the probes vertically in exact intervals (100 mm) while keeping the water level stationary
2. Re-zeroing the gauges frequently to ensure that reading of the gauges was accurate
3. Using three probe lengths for the different bore depths at different sections
4. Deploying three pairs of water level gauges at several sections upstream and downstream from the model
5. Using a high sampling frequency to capture a precise bore profile
6. Monitoring the targeted impounding water depth in the reservoir with a fixed scale on the sidewall of the flume to compare against Water Level Gauge WG1 prior to each test

Pressure transducers were calibrated twice. For the first calibration procedure, the fluid used was air in a Honeywell pressure calibration device. An acrylic cylinder with 120 mm diameter and 1800 mm height was used in the second calibration. Although water was used in the second calibration, the calibration stage did not change.

The calibration of the dynamometer was performed based on the table of volt to force factors provided by the manufacturer. To ensure accurate base shear force readings when using the dynamometer, a load cell was used to apply a known force to the model and then compared to two recordings. The periodic calibration returned invariably accurate readings. For the base overturning moments, the dynamometer was loaded with a known

force at a specific elevation from the base of the model and, subsequently, the calculated moment was compared with the moment recorded by the dynamometer along both flow and transverse directions.

The errors from camera measurements were due to both random errors and systematic optical imaging errors. The random errors occurred due to the analysis technique used to process the recorded images. In the case of bore velocity tests, as described in Section 4.11.1.2, an adjustment of the distance traveled by the seeding particles was performed using the bore depth-time history. In the case of the debris impact tests, the debris velocity was adjusted for the debris orientation angle.

Despite inherent errors when conducting experimental modeling in hydraulic engineering, the corrections and adjustments described above were implemented to minimize errors in the recorded data.

4.5 Limitations of the experimental tests

Tsunami is a complex and multi-faceted phenomena. Wave impact on coastal areas is complex and difficult to assess. Since this experimental program a pioneering study, more complex aspects of tsunami-induced coastal inundation were not considered. These include: the presence of a sloped shore, return flow, and influence of other adjacent structures on the flow. The follows is a brief discussion for each of these aspects:

- Up-sloping onshore coastal topography causes the advancing tsunami-induced bores to lose energy. Thus, a bore advancing on an up-sloping shore generally reduces its depth and velocity compared to a bore propagating over a horizontal plane. However, in the case of coastal plains, such as in the City of Banda Aceh in Indonesia during the 2004 Indian Ocean Tsunami or in the Sendai plain in Tohoku during the 2011 Japan Tsunami, overland flow conditions were very similar to that in the present experiment program.
- Depending on the nearshore bathymetry, tsunami waves break offshore and advance inland in the form of hydraulic bores. The leading edge of the bore has high flow velocity and depth. While propagating inland, the bore loses energy mainly due to topographical features (upslope) and due to bottom friction. After reaching its

maximum penetration inland, water flows back into the ocean. During this stage, flow-structure interaction occurs; however, forces induced on the structures in this case are generally lower in magnitude at this point than those occurring during the propagation stage since flow velocity during this stage is usually significantly lower, particularly for flat coastal plains. As this study aims to quantify the maximum (critical) forces induced on the near-shore structures, and due to size limitation of the testing facility, the testing program of the present study did not include the backflow stage. Furthermore, previous tsunami events illustrated that significant damage to near-shore structures occurred primarily during the inland bore propagation and less damage was the result of the backflow phase.

- One of the objectives of this study was to quantify the design loads (pressures, forces and moments) resulting from tsunami-induced bores on structures. To achieve this objective, and to investigate various testing configurations, involved multiple repetitions of testing. Furthermore, the mode of failure and/or the characteristics of damage to the structures were not in the scope of present investigation. A comprehensive comparison between the results of the different tests required the use the same undamaged structural models. Therefore, the structural models used in this study were designed to withstand the bore-induced forces and the debris impact forces. As previously discussed, the impoundment depth of 1150 mm was excluded from the test series for assessing the debris impact force to protect the structural models from damage.
- The influence of upstream obstructions on the loading on the structures was investigated by Nouri et al. (2010). Therefore, effort in study was directed towards investigating the effect of mitigation walls with different geometric parameters (height, inclination angle, shape, and location).

4.6 Flume Description

The experimental program was conducted in a stainless steel High Discharge Flume (HDF) at CHC-NRC. The flume dimensions are: 14.56 m long, 2.70 m wide, and 1.20 m deep. A partition was installed at mid-width of the flume to reduce the active width to 1.35 m for the

testing section. The flume is equipped with a hydraulic variable pitch pump that has a maximum discharge rate of 1.7 m^3/s. The intake system was outfitted with a hydraulic butterfly valve for accurate control of the inflow discharge such that the desired impounding water depths could be achieved. A swinging gate was installed at the upstream end of the flume ensuring that 25.5 m^3 of water could be impounded behind the gate for the maximum impoundment depth of 1150 mm. The gate was fitted with a hinge at the top end and, in turn, was connected to the top sides of the flume. A locking mechanism was installed on the gate 0.15 m above the flume bed as shown in Figure 4.2.

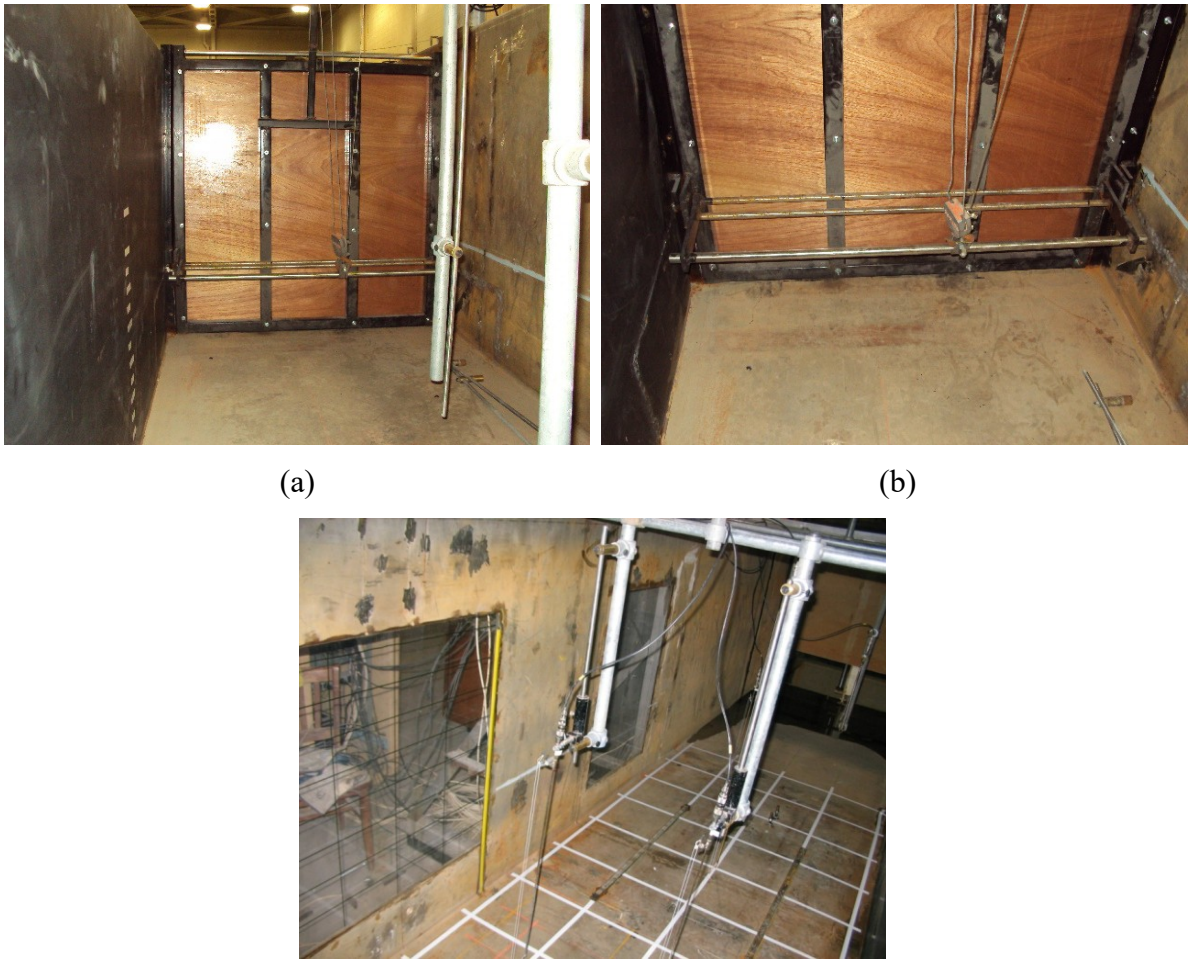

(a) (b)

(c)

Figure 4.2 Flume features: **a)** swinging gate; **b)** locking system; and **c)** side windows

The gate consists of square steel hollow sections of 50.8 × 50.8 mm (2" x 2"), which were welded to form a steel frame to support a 19 mm-thick plywood sheet. The plywood

was fastened to the steel sections to form the face of the swinging gate. Rubber seals were installed on the side edges of the gate; while a rubber strip was installed on the lower edge of the gate on the upstream face to control leakage. However, a very thin trace of water was able to leak beneath the gate during testing. An electric winch with a capacity of 225 kg was attached to the locking system of the gate to control the opening. Counter weights and the hydrostatic pressure of the water were used to rapidly open the gate. The gate opening mechanism was synchronized with the data acquisition system and a high-speed digital camera. The structural models were installed downstream from the gate to ensure that the simulated tsunami bore was fully developed and to allow visual observation of the bore-structure interaction through the windows located on the sidewalls of the flume. A sluice gate, located at the downstream end of the flume was used to control the water level during the re-zeroing of the water level gauges. A vertical drain positioned behind the sluice gate directed the water into the reservoir located underneath the flume. Two square-shaped glass windows are located on the side of the flume to visually observe the flow. The flume is positioned horizontally, and the slope of the flume cannot be modified. Figure 4.3 provides a photo of the flume during testing.

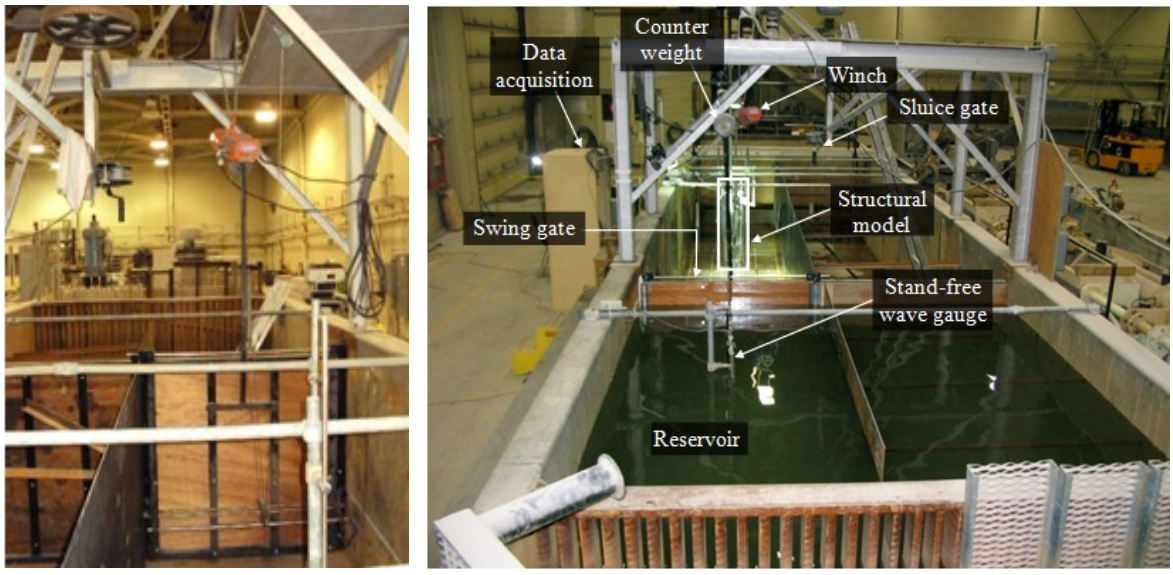

(a) (b)

Figure 4.3 High Discharge Flume at CHC-NRC Ottawa and experimental setup: **a)** upstream view, empty reservoir; and **b)** downstream view, reservoir filled with water

4.7 Structural Models

In this study, two structural models, one with a square and the other with a circular cross section were fabricated from acrylic sheets and an acrylic cylinder, respectively. Both models were 1.0 m in height with a 305 mm outside cross-sectional dimension. The wall thickness of the circular structure was 9 mm, while the square model was fabricated with 6.3 mm-thick walls. Figure 4.4 provides photos of the fabrication stages of the models in the workshop of the Faculty of Engineering. The models were connected to a six-degree of freedom (6 DOF) high frequency load cell (dynamometer) which was bolted to the bottom plate of the flume: this allowed direct recording of the base shear force- and overturning moment-time histories. Two aluminum frames were built to connect the structural models at the base to the load cell. These frames were manufactured so that the models could be rotated about their vertical axis. The rotation of the model was intended to measure the pressures-time histories around the perimeter of the models using a number of pressure transducers installed on a vertical line on both the circular and square structures (Figure 4.5).

(a) (b)

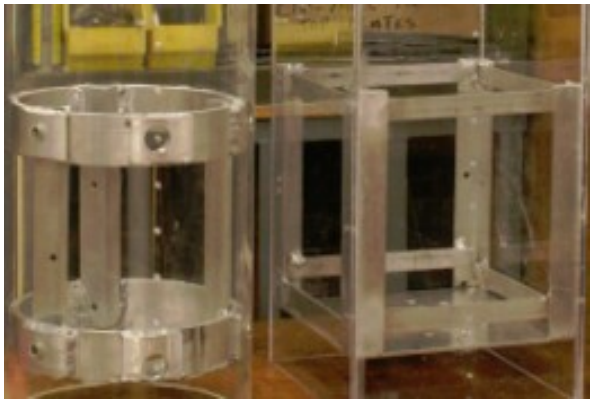

(c)

Figure 4.4 Fabrication of the structural models: **a)** circular model; **b)** aluminum frame for the circular model; and **c)** aluminum frames connected to the models

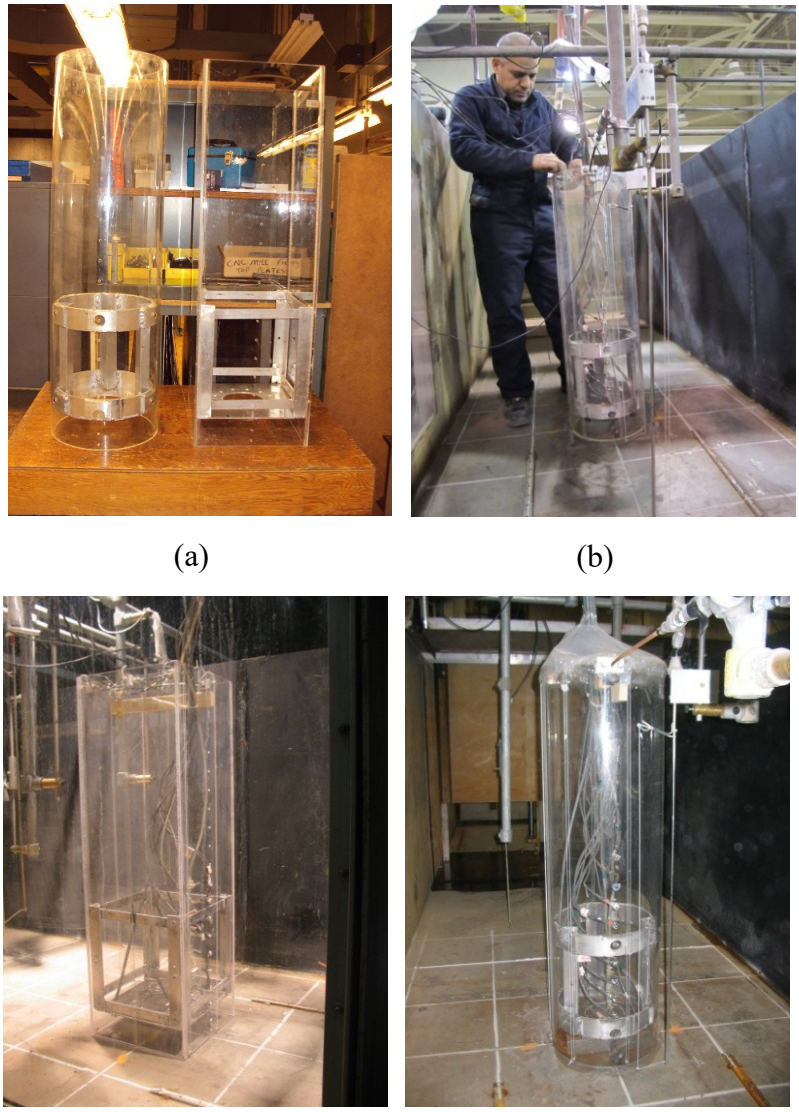

(a) (b)

(c) (d)

Figure 4.5 Structural models: **a)** models prepared in the workshop; **b)** installation of circular model in the flume; **c)** square model installed; and **d)** circular model installed

A gap of approximately 4-5 mm was present between the base of the models and the flume floor as a result of the connection to the dynamometer. This gap was filled with flexible silicon to prevent water infiltrating inside the models. Figure 4.6 (a) provides a schematic diagram of the structural model with the instrumentation installed on the model.

4.8 Instrumentation

A number of sensors were used in the test program to record the characteristics of the hydrodynamic pressure, water level on the faces of the structures, and the response of the structural models. The dynamometer recorded base translational forces and base overturning moments about two axes (longitudinal and transverse, with respect to the direction of the flow). An accelerometer was installed at the top edge of the structural models to record the longitudinal acceleration. The lateral displacements of the top edge of the structural models were recorded by a linear variable differential transducer (LVDT) with a maximum capacity of 50 mm (Figure 4.6 (b)). Thirteen capacitance water level gauges were employed during testing to record the bore depth-time histories along the flume and around the models.

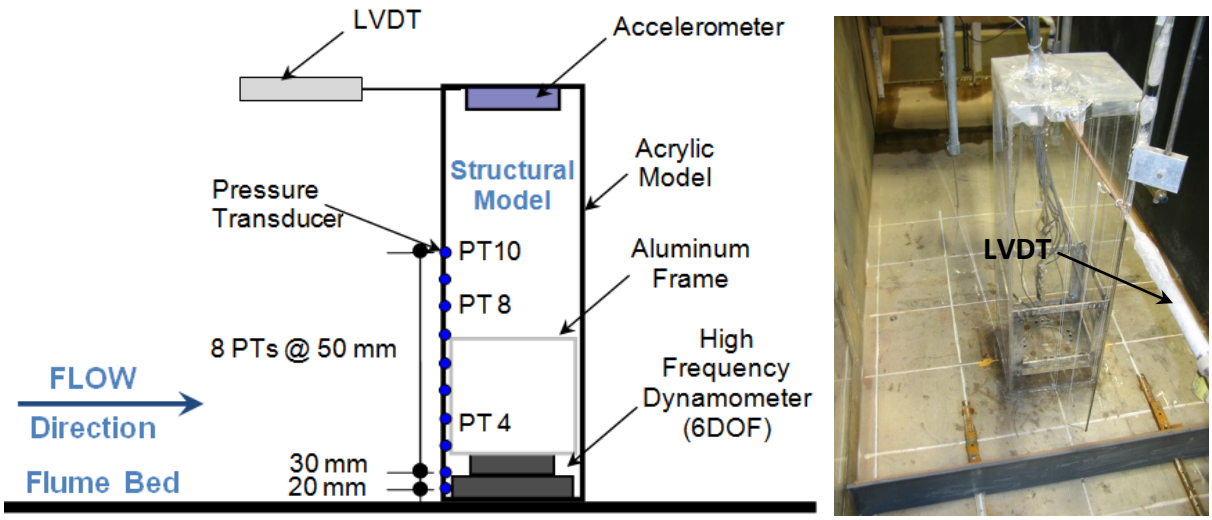

(a) (b)

Figure 4.6 Square structural model: **a)** instrumentation on the structural model; and **b)** covering of the top opening of the model to protect instrumentation from water

4.8.1 Water level gauges

Two groups of capacitance water level gauges [Akamina Model WP-AO-V02–03, Akamina Technologies, Ottawa, Ontario, Canada] were used during testing to record the bore depth-time histories. The first group consisted of eight stand-free probes of different lengths, which were installed along the flume; one of them was installed in the reservoir (1.25 m upstream of the swinging gate) and used to control the impounding water depth. Another water level gauge was installed at 2.77 m downstream from the swinging gate and the other

six gauges were installed in pairs at 3.92, 4.92, and 5.92 m downstream from the gate. The second pair was located at the position of the structural models. This arrangement was followed in the sets of tests aimed at investigating the bore characteristics (when there was no model installed in the flume). In other sets of tests with the structural model in the flume, the second pair of water level gauges was removed and replaced with another group of water level gauges that were attached directly to the models.

The second group of water level gauges were installed directly on the structural models: four on the circular model and five on the square model. Figure 4.7 shows the location of these sensors for both models. Section 5.1.1 will demonstrate that this group provided more accurate data on the water level near the faces of the structure in comparison to the free-standing water level gauges placed further away from the surface of the models.

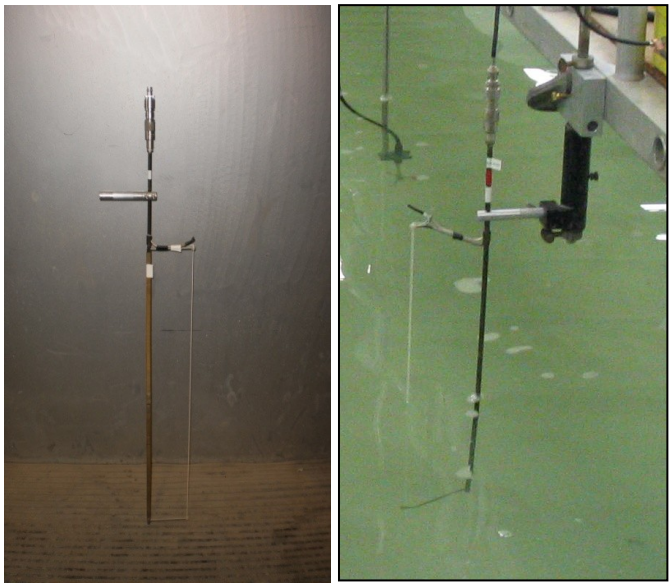

(a)

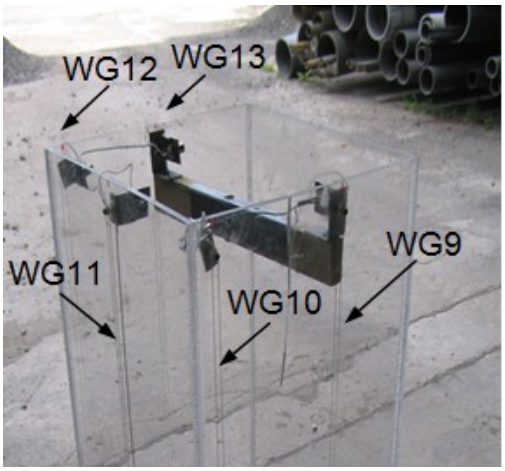

(b)

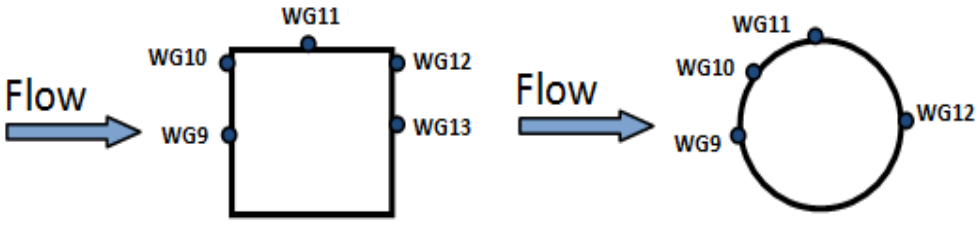

(c)

Figure 4.7 Water level gauges: **a)** stand-free gauge model; **b)** gauges attached to the square model; and **c)** drawing of water level gauges attached to the structural models

The water level gauges used in this study provided highly accurate measurements of bore depth, owing, in part, to a precise calibration procedure. The calibration process was conducted for each gauge from the first group separately; while for the second group, it was implemented for all gauges concurrently, using a large cylinder filled with water. Through the calibration of each water level gauge, the water surface was changed to five different levels which resulted in five correlation points (between the water depth and the voltage signal) on the calibration line. Water levels were measured with an acceptable tolerance of less than 0.05%, which led to errors of less than 0.5 mm in the 1.0 m probe length. The distribution of the free-standing sensors is provided in Figure 4.8. The top drawing provides the top view of the flume and the location of the water level gages along the flume width. The bottom drawing provides an elevation view along the flume with the designations of the gauges.

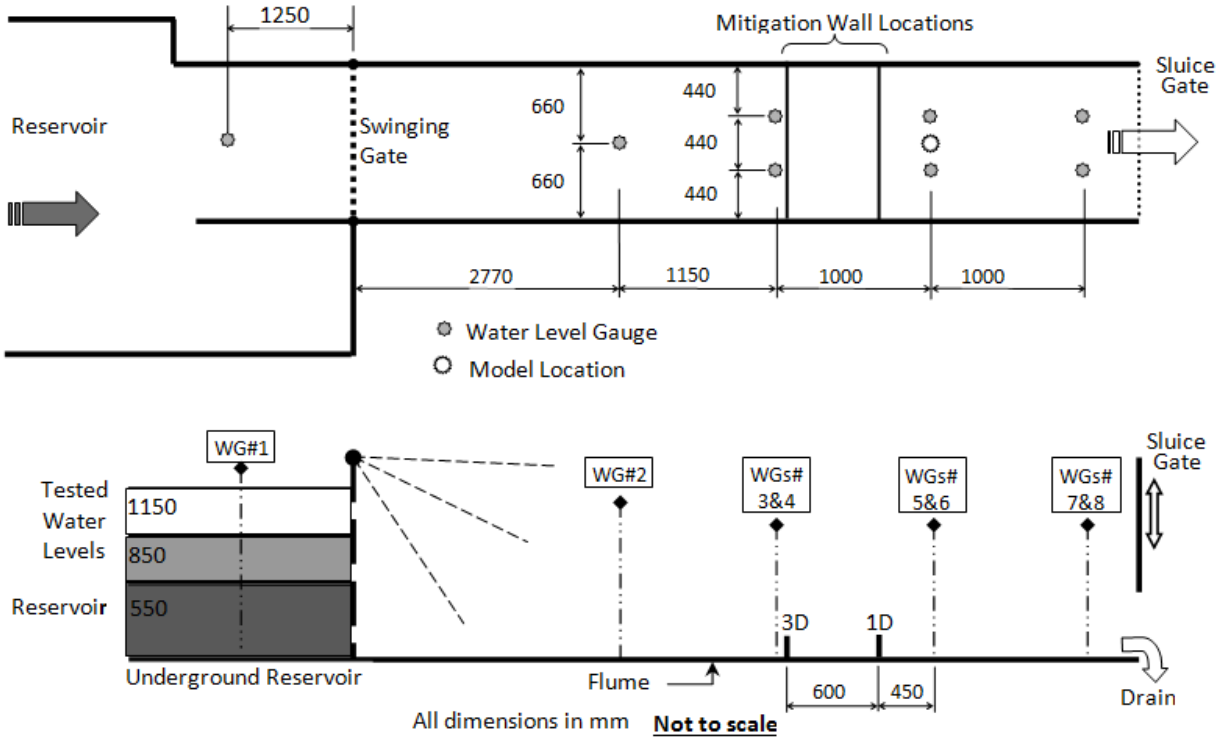

Figure 4.8 Schematic of the experimental setup with location of water level gauges and mitigation walls

After each calibration process, the water level gauges were re-installed at their positions in the flume and a re-zeroing process was implemented. The re-zeroing requests

define a specific water depth in the flume to the data acquisition system. This was achieved by closing the sluice gate at the end of the flume and filling the reservoir and the flume with water to a specific depth. At each re-zeroing process, a five minute time period was implemented under which this approximately constant water depth was maintained and then that particular water depth was sent to the data recording system. Figure 4.9 provides data of eight water level gauges through the re-zeroing process at 550 mm water depth.

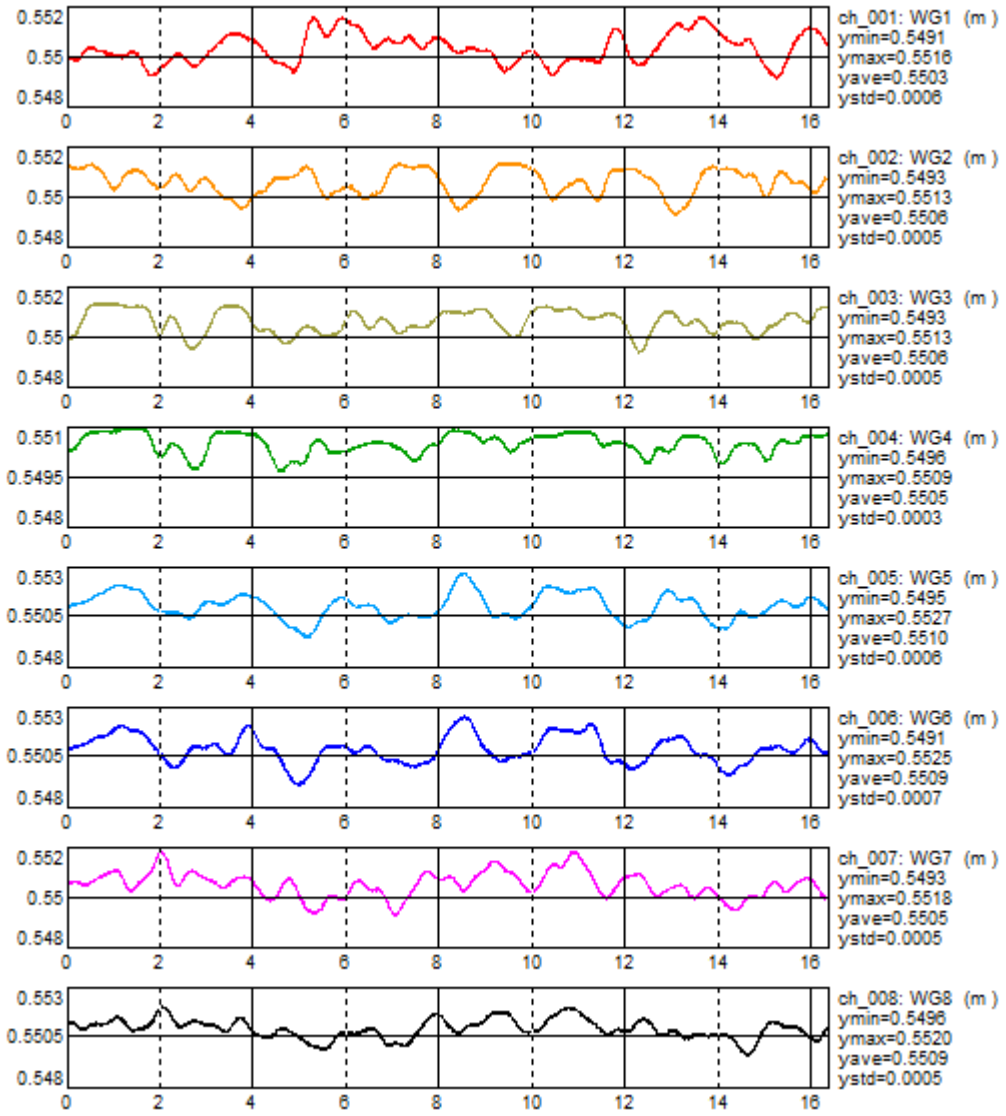

Figure 4.9 Re-zeroing of the stand-free water level gauges using 550 mm water depth

4.8.2 Pressure transducers

Ten differential pressure transducers (PTs) were installed on a vertical line at mid-width on the upstream face of the models. The lowest pressure transducer (PT1) was installed 20 mm above the flume bed, while the subsequent transducer (PT2) was positioned 50 mm above the flume bed. The remaining PTs were equally spaced vertically at 50 mm intervals. Figure 4.10 provides upstream and side view photos of the installed PTs. The PTs were placed flush with the surface of the models to reduce additional turbulence during the impact with the hydraulic bores. The sensors have a measuring capacity of 69 kPa (10 Psi), and it was ensured that the pressures recorded were less than the capacity. Prior to testing, the sensors were calibrated using an air-pressure calibration device. Thereafter, a column of water in a graded cylinder was used to calibrate the sensors; the results of both methods were similar.

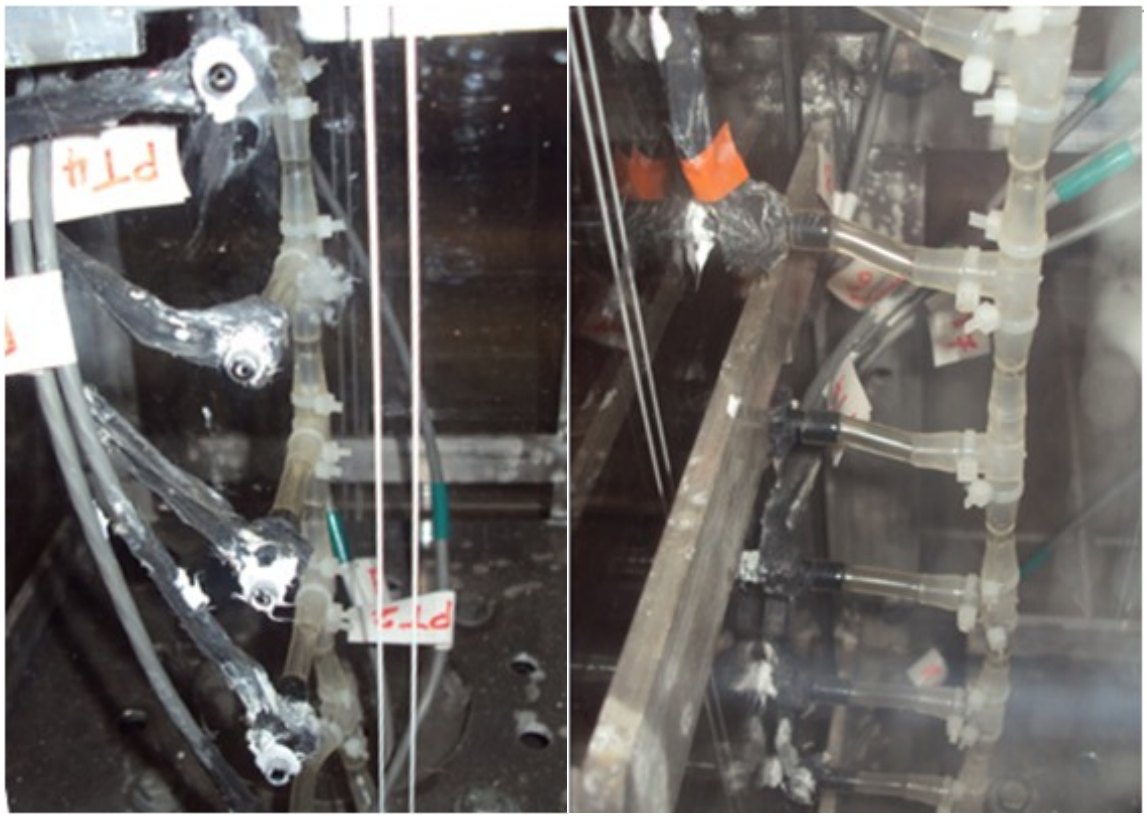

(a) (b)

Figure 4.10 Pressure transducers installed in the models: **a)** upstream view; and **b)** side view

4.8.3 Dynamometer

The high frequency, six-degree of freedom dynamometer [MC6 Series, Advanced Mechanical Technology Inc. (AMTI), Toronto, Ontario, Canada] was used to measure the forces and moments experienced by the structural models. The MC6 incorporates strain gauges and four precision elements to isolate and measure applied loads in the form of orthogonal forces and bending moment components: F_x, F_y, F_z, M_x, M_y, and M_z. Similar to other strain gauge transducers, the MC6 requires bridge excitation and signal amplification (Figure 4.11 (a)). High-gain amplifier device was connected to the dynamometer to provide excitation and amplification for multiple channels. The amplifier processes the signals from the dynamometer and provides output suitable for the data acquisition.

The maximum standard capacity for the vertical force (F_z) is 4500 N and for the horizontal forces (F_x and F_y) is 2250 N. The maximum moment capacities are 170 Nm for M_z and 340 Nm for M_x and M_y. The dynamometer has a 152.4 mm square, top-mounting surface equipped with threaded inserts. Four screws were used to attach the aluminum frame of the structural models to the dynamometer. Four bolts were welded to the flume bed to fasten the dynamometer a distance of 4.92 m from the swinging gate. The location of the model was determined based on two factors: (1) to coincide with the location where the simulated tsunami bore is fully developed; and (2) adjacent to the glass windows located on the sides of the flume to enable visual monitoring of the bore-structure interaction. A reference load cell was calibrated with five predefined forces and then used to calibrate the forces and moment readings of the MC6 (Figure 4.11 (b)). This calibration was performed before each set of tests.

(a) (b)

Figure 4.11 Dynamometer and reference load cell: **a)** dynamometer MC6; and **b)** reference load cell

4.8.4 Accelerometer

A uniaxial accelerometer with $2g$-capacity was installed at top of the models to monitor the acceleration of the structural models in the flow direction. The accelerometer was installed such that positive acceleration corresponded to the flow direction (Figure 4.12). The accelerometer was calibrated before performing each set of tests.

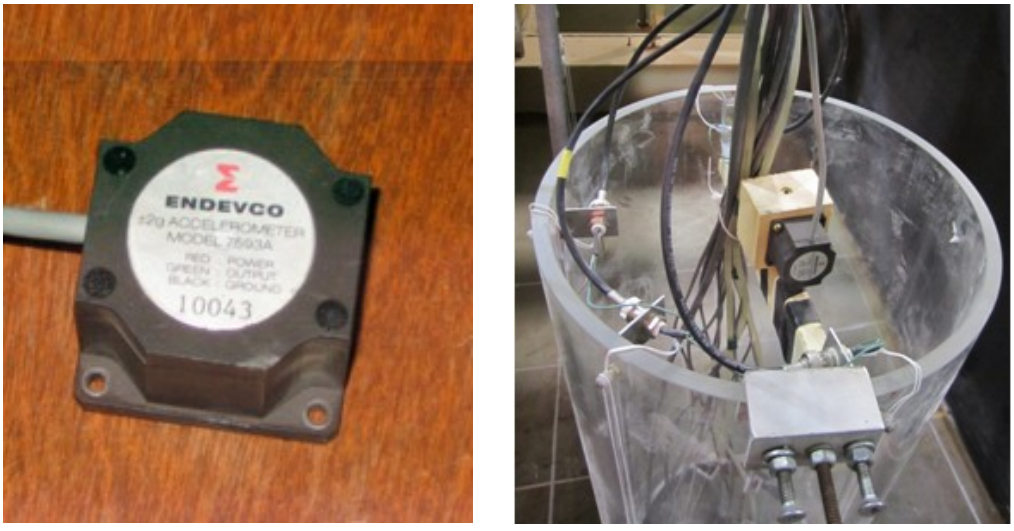

(a) (b)

Figure 4.12 Accelerometer: **a)** the device; and **b)** installed on the circular model

4.8.5 Linear variable displacement transducer

A single Linear Variable Displacement Transducer (LVDT) with a capacity of 50 mm was used to record the lateral displacement of the structural models. The sensor was installed at 1.0 m above the flume bed and 0.8 m upstream from the face of the model. The latter distance was required to avoid sensor damage due to high splashing occurring during the tests, particularly with the larger impounding water depth. The LVDT was supported with a steel frame and was connected to the upstream face of the model through a 7 mm threaded steel bar. The end of the bar was attached to the model firmly with an inverted u-shape clamp to ensure that the LVDT recorded displacements in the direction of the flow and opposite to the flow (Figure 4.13). The LVDT was calibrated between each group of tests and re-zeroed daily. Before each re-zeroing process, the LVDT was installed at the mid-range position. This ensured that there was sufficient displacement capacity in both directions of response.

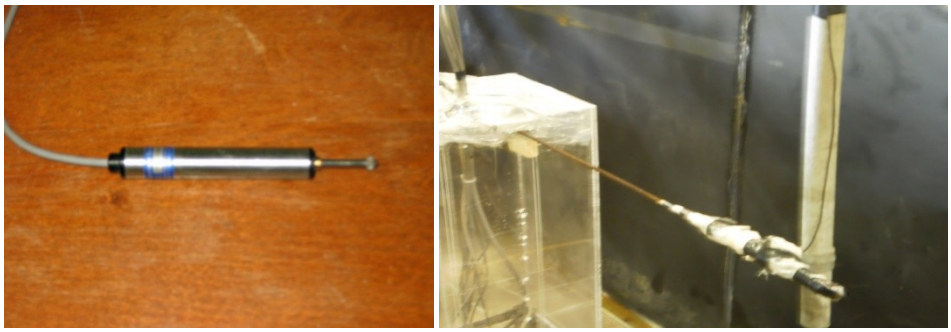

(a) (b)

Figure 4.13 LVDT to measure the lateral displacements induced in the models: **a)** the device; and **b)** installed in the flume

4.8.6 High-Speed Digital Video-Camera

A RedLake slow motion high-speed digital camera was used to capture videos (Figure 4.14). The camera was connected to a vision sensor card that was installed in a desktop included in the image analysis system. This camera has the capacity to capture 10,000 fps with shutter speed up to 1/5000 s. In this experimental program, different capturing rates were used depending upon the test group and the position of the camera. A grid of 300 mm x 300 mm was painted on the flume bed along a 3.0 m length section (2.0 m upstream from the model location and 1.0 m downstream) as shown in Figure 4.15. The gridlines were used as

reference markers in tracking the bore front advancing downstream. The camera was installed at a height of 2.4 m from the flume bed, directly over the location of the structural models.

(a) (b)

Figure 4.14 RedLake high-speed digital camera installed 2.4 m above the structural model: **a)** top view; and **b)** side view

Figure 4.15 Grid spacing of 300 mm x 300 mm marked on the flume bed

The video capturing using the high-speed camera demands high intensity light spanning the target location. However, high intensity light caused reflection in the video, particularly for the tests where the turbulent water surface contained substantial air-entrainment. Therefore, numerous video capturing trials were conducted that included a study of the camera settings (shutter time, exposure time, capturing speed, etc.), capturing angle, and light source arrangement. Hence, the still frames presented in this thesis represent the best videos captured with the least reflection.

4.9 Data Acquisition

A 32-digital channel data acquisition system with analog to digital convertor was connected to more than 30 sensors, which were used in the experiments. The voltage signals received from the sensors were converted to digital format and saved in binary data files (DAC files). These data files contain headers including definition of the project and type of sensors used, sampling frequency, testing-time-date, description, and any comments collected during the tests. The data files collected were all referenced by following a specific procedure so that they could be synced with each other in time. GEDAP, a software package developed at the Ocean, Coastal and River Engineering of NRC, Ottawa, was used to control the data acquisition system. This software permitted the following tasks: saving test configurations, sensor calibration and re-zeroing, sampling frequency and test sampling time period, synchronization of data collected with the high-speed videos, and saving the test data files. Signals from the transducers were routed through a signal convertor to the data acquisition card (National Instruments Inc. model 6031E) housed inside a desktop. The data acquisition card (Figure 4.16) had 16-bit resolution, and a maximum sampling frequency of 100 kHz.

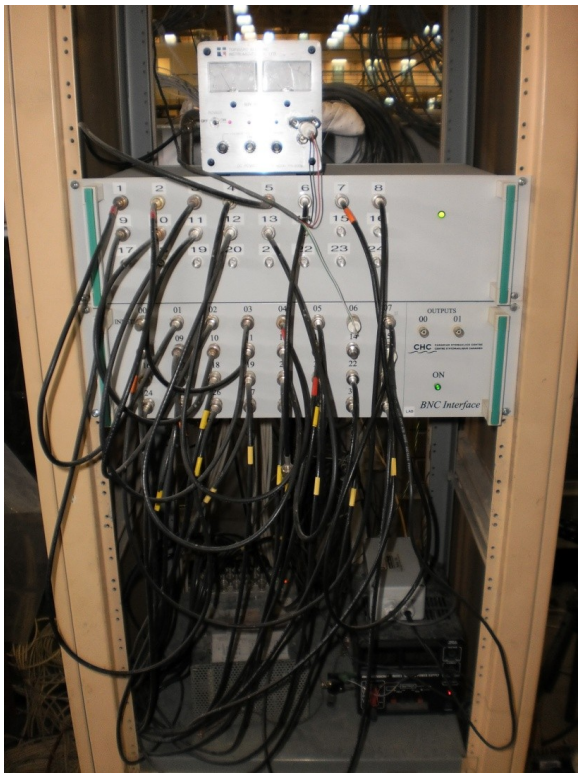

Figure 4.16 Digital data acquisition system with sensors connected to PC

4.10 Mitigation Walls

Different coastal structures, such as bulkheads, seawalls, and/or breakwaters, are used to protect shoreline regions from the effect of waves and rising water levels. Geotexiles, quarry rock, reinforced concrete or a combination of these materials is used to construct such coastal structures. Structure type, size and materials are dependent on the estimation of the loading, water levels, probability of occurrence of loading, material availability, and local geotechnical conditions. Construction of any protection structure may limit beach access and be intrusive to the shoreline views. For example, reinforced concrete walls can withstand larger wave forces than soil revetments or stone bulkheads. Moreover, they can be cast in any recommended geometric shape.

For this research program, low-height walls were investigated as a means to reduce the impulsive force induced by the impact of the leading edge of a tsunami bore. Thus, the forces and moments induced on structures located landward of the mitigation wall must be considered in the design of these structures. Such protection walls are not necessarily

designed to prevent flooding of the area behind the wall. However, they would be designed to dissipate a significant portion of the tsunami bore energy on near-shore structures and to ensure, even when overtopped, additional time for the evacuation of inhabitants living in the vicinity. Furthermore, the tsunami wave front propagates onshore either as a bore or a surge and often carries debris, such as logs, shipping containers or fishing boats. As observed during past tsunami events, such debris imposes high impact loads and adds to the destructive power of the tsunami. To reduce part of the tsunami bore energy, the author of this research program is proposing low-height, high-stiffness structural walls located upstream from the structures to serve as mitigation strategies against the tsunami bore-induced forces and tsunami-driven debris fields.

Movable multi-slope mitigation walls were fabricated to investigate the effect of the height, vertical angle, cross-sectional shape, and location of the wall on the forces imposed on the structural models. The effect of mitigation wall height was examined by using 100 and 150 mm wall heights with front faces angled at 45˚ (inclined wall) and 90˚ (vertical wall) with respect to the flume bed for both wall heights. These walls were constructed from 19 mm-thick plywood and were painted with different color patterns to be easily identified in the video recordings. The influence of cross-sectional shape of the mitigation walls on the efficiency of decreasing the induced forces on the structural models was explored with two additional walls: a Wave Return Wall of 100 mm height; and a curved cross-sectional wall of 150 mm height. The Wave Return Wall was constructed based on provisions described in the Handbook of Coastal Engineering (Herbich 2000). The curved wall was prepared by cutting an acrylic cylinder with a 320 mm outside diameter and 19 mm thickness. Details of the mitigation walls are shown in Figure 4.17. The effect of each wall was examined for the three impounding water depths (550, 850, and 1150 mm). The walls were installed at two different locations relative to the structural model: 305 mm (1 ft), and 915 mm (3ft) upstream from the model, referred to as 1D and 3D, respectively. Figure 4.18 is a photo of the mitigation walls used in the tests.

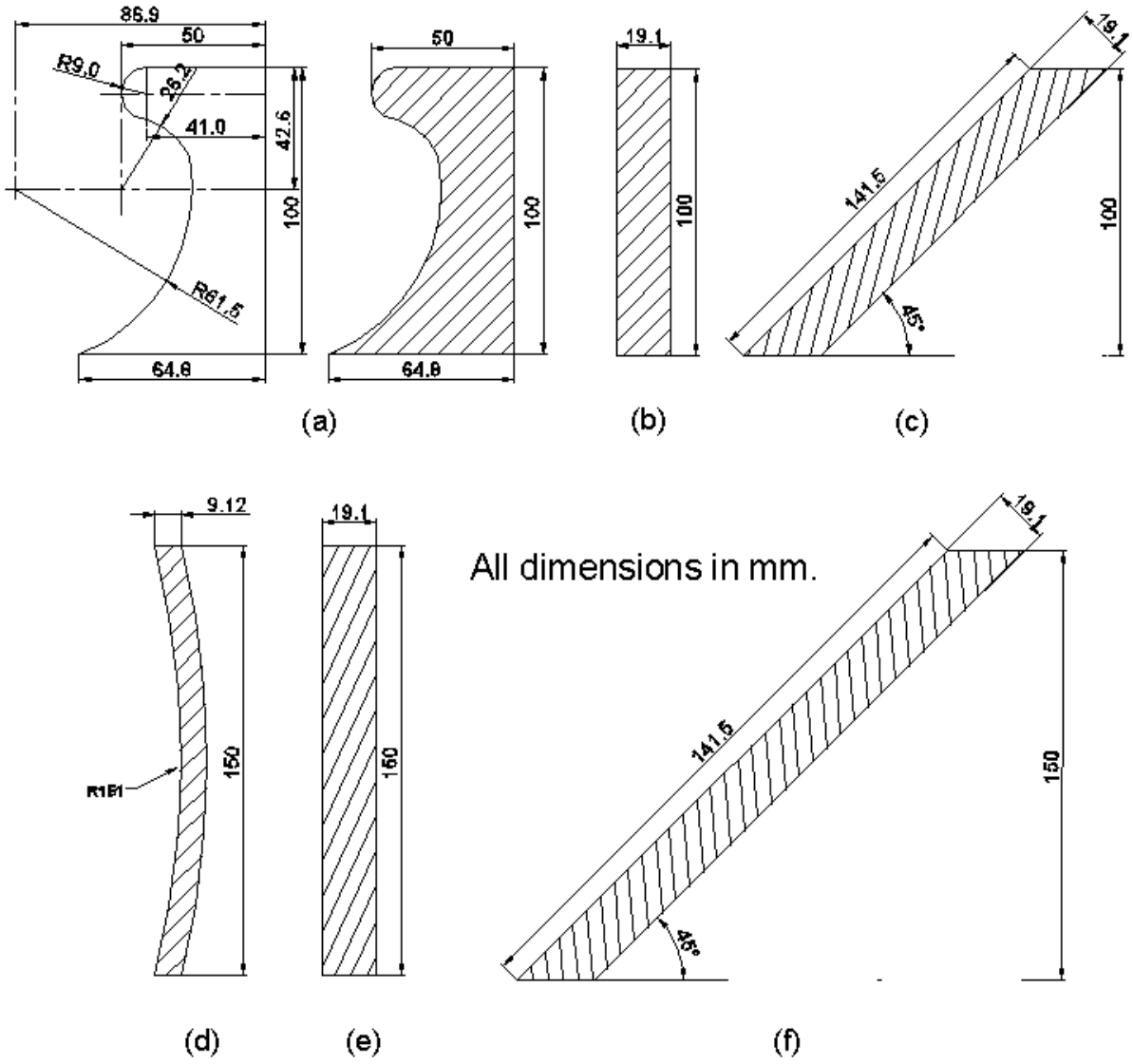

Figure 4.17 Details of mitigation walls: **a)** Wave Return Wall; **b)** 100 mm vertical wall; **c)** 100 mm-45˚ inclined wall; **d)** curved wall; **e)** 150 mm vertical wall; and **f)** 150 mm-45˚ inclined wall

Figure 4.18 Photo of mitigation walls

4.11 Wooden Debris

Several cases were documented from previous tsunamis (Tohoku 2011 and Indian Ocean 2004) in which significant damage or progressive collapse occurred as a consequence of debris impact. Broken tsunamis waves which occur in the form of highly turbulent hydraulic bores often carry various forms of floating bodies. This floating debris include a wide variety of shapes, sizes and masses, and consist of driftwood, boats, cars, timber, and construction members or materials from damaged structures located in the advancing tsunami bore path. Field reconnaissance visits to tsunami-affected zones conducted by engineering teams reported that near-shore buildings suffered significant structural damage (including complete collapse) caused by the direct impact of floating debris. Thus, a proper estimation of the debris impact force imposed on the structure is one of the most significant tasks to be considered for the design of tsunami-resistant near-shore buildings. This estimation requires the investigation of the effects of debris-mass, -shape, and velocity. To

date, in the available literature, the debris velocity has been assumed to be equal to the bore flow velocity. Tsunami debris impact depends many complex factors such as, but not limited to: debris-shape, -mass, -location (related to both the structure and the shoreline), inundation depth, and flow velocity. These factors significantly influence the magnitude of the resulting impact forces. Therefore, proposing a specific formula that can provide a precise estimation of the debris impact force is a challenging task. The literature provides three approaches to estimate the debris impact force. Each approach consists of at least one factor that involves considerable uncertainty in assessing its value. This demonstrates the uncertainties of the present understanding of floating debris-induced impact forces. This study aims to better understand the impact force resulting from the interaction of floating bodies carried by the bore front with a near-shore structure. The study investigated the effects of debris-mass, -shape, -orientation, and -eccentricity from the center of a circular structural model. These factors were explored with two impounding water depths: 550 mm and 850 mm. The bore flow was recorded with a digital high-speed camera (up to 10,000 fps). Three, prism-shaped wooden debris were individually used in the experimental program. The debris was prepared from a wooden log of 76.2 x 76.2 mm (3" x 3") cross section. The debris were cut into lengths of 490 mm and 916 mm: these lengths were selected to produce two masses of approximately one and two kilograms as shown in Figure 4.19.

The logs were waterproofed with epoxy; therefore their masses remained constant despite the extended water contact during the repetition of numerous tests. The debris were marked with cross lines at 100 mm intervals to be easily recognized in the high-speed video recordings and to allow a reliable estimate the debris' velocity (see Figure 4.19 (b)). Figure 4.19 (c) shows a sketch of the debris dimensions. The debris dimensions and masses were: 76.2 x 76.2 x 490 mm (1.088 kg); 76.2 x 76.2 x 916 mm (2.191 kg); and 76.2 x 152.4 x 490 mm (2.258 kg). They were designated as "1kg", "2kg1P", and "2kg2P", respectively. The debris were attached to ropes to prevent them from being carried into the reservoir of the flume. The ropes were sufficiently long to allow the debris to impact the structural model freely.

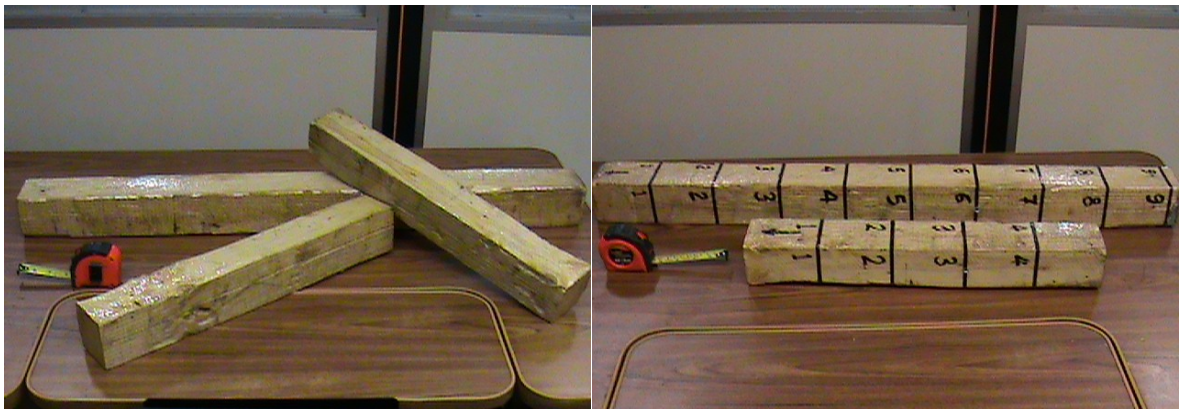

(a) (b)

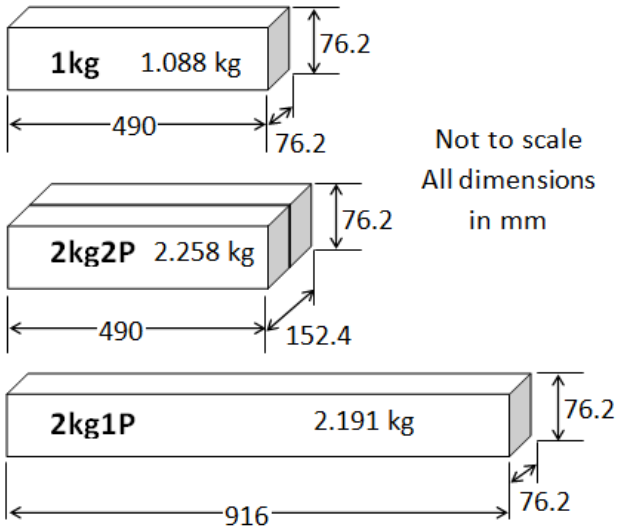

(c)

Figure 4.19 Wooden debris used in the experimental program: **a)** coated with waterproof; **b)** marking used for the high-speed videos; and **c)** sketch of debris dimensions

A sample of the debris with dimensions of 76.2 x 76.2 x 310 mm was tested with a Universal Testing Machine under compression stress. Figure 4.20 displays the force-displacement response. The effective stiffness was estimated from the slope of the tangent line of this response, and was determined to be approximately 69 N/mm. Given the softening in the initial response, the tangent line was based on the linear segment of the loading branch.

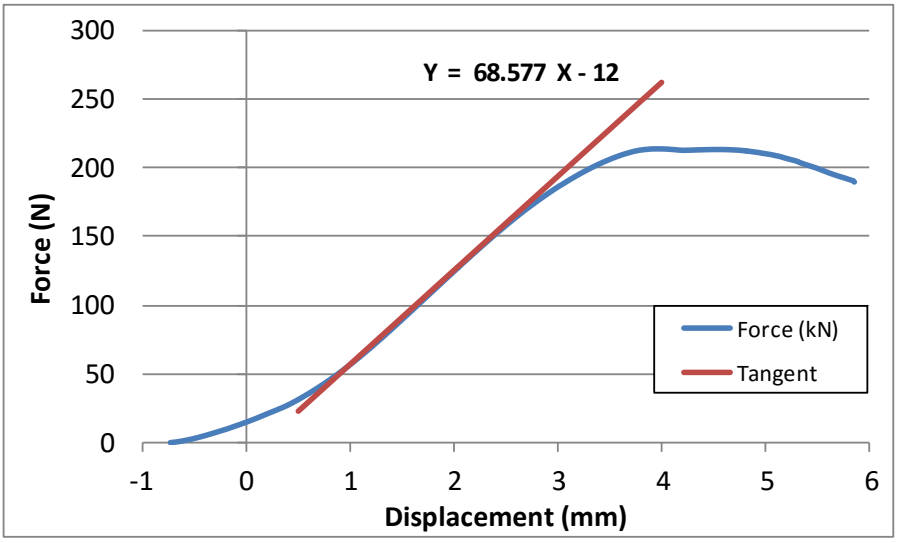

Figure 4.20 Force-displacement response from compression test of a sample wooden debris

4.12 Testing Program

The experimental program involved tests with and without the structural models positioned in the flume, and with different setup configurations. During a 30-month period (December 2009 to May 2012) more than 550 tests were conducted in the stainless steel flume at the National Research council Canada (NRC), Ocean, Coastal and River Engineering (OCRE) in Ottawa. The dam-break technique was used to generate the tsunami-like hydraulic bores by releasing water impounded behind a rapidly-opening swinging gate. The gate opening mechanism relied on the pull-force of an electric winch in addition to the hydrostatic pressure of the impounded water. Initially, several tests with different impoundment depths were conducted to find the minimum impoundment depth that satisfied the condition of the non-dimensional gate opening time ($t * \sqrt{g/h_o} = \sqrt{2}$). As discussed in Chapter 3, to generate a dam-break wave, the gate opening time should be sufficiently short to allow the separation of the gate from the body of the impounded water. The minimum depth was found to be 450 mm, while the maximum depth was limited by the physical depth of the High Discharge Flume, which is 1200 mm. The selection of the three impoundment depths of 550 mm, 850 mm and 1150 mm, was chosen to generate three different inundation depths at the location of the structural models. Based on the testing program, these tests were categorized into four main groups:

1. Hydraulic bore characteristic tests;
2. Bore-structural model interaction tests;
3. Waterborne debris impact tests; and
4. Mitigation wall influence tests.

Note that all the tests were repeated three times to ensure repeatability. The following are brief descriptions of the objectives for each test group. Appendix A provides a table listing all the tests conducted as part of this study.

4.12.1 Hydraulic-bore characteristic tests

Eight, free-standing water level gauges were deployed longitudinally along the flume in addition to a grid painted on the flume bed to monitor the bore flow advancing along the flume (Note: no structural model was installed in these tests). A high-speed video digital camera, in addition to two digital regular video cameras, was used to estimate the bore flow velocity. The data collected from these tests was used to investigate the following elements:

- The hydraulic bore characteristics for three different maximum inundation depths;
- Estimation of the bore front velocity using two measuring techniques;
- Estimation of the bore velocity-time history using Particle Tracking Velocimetry (PTV);
- Investigation of the bores depth- velocity relationship; and
- Critical review of existing bore velocity formulas available in the literature.

4.12.2 Bore-structural model interaction tests

In this group of tests, two structural models were each installed 4.92 m downstream of the swinging gate. Sets of tests were conducted in which the circular and square structural models were impacted with hydraulic bores of different inundation depths, similar to those generated by broken tsunami waves. The bores were generated from three different impounding water depths: 550, 850, and 1150 mm. The vertical distribution of the pressure-time history around the models was recorded by rotating the structural models around their central vertical axis. The pressure transducers on the circular model were rotated at angles of 0˚, 30˚, 60˚, 90˚, 120˚, 150˚, and 180˚ from the initial position which was facing the incoming bore; while the square model was rotated at angles of 0˚, 90˚, and 180˚ from the

same initial position. The angles were measured clockwise from the flume longitudinal centerline. During these tests, in addition to the pressures, forces, moments, accelerations, and displacements experienced by the structural models were also recorded. The time-history of the flow depth around the models was recorded by water level gauges installed directly on the surface of the model. [Note that this is the first study to provide such experimental data.] The data analysis from these tests focused on the pressure distribution generated around the model in two directions (radial and circumferential for the circular model; and upstream, downstream and side faces for the square model). The data depicted the presence of three main segments in the pressure-time history, namely: impulsive, run-up and quasi-steady flow stages. The analysis further focused on:

- Studying the bore-structure interaction and recording the time-histories of: base shear forces, base overturning moments, pressures at different levels around the models, displacements, and accelerations induced on the models during the test.
- Investigating the vertical and horizontal pressure distribution around the two models at different flow stages and for different inundation depths.
- Integrating the pressure recorded around the models and comparing the results with the longitudinal and transverse total base shear force-time histories that were recorded during testing with the dynamometer.
- Using the results from the previous step to identify the magnitude of the hydrodynamic force components during the run-up and quasi-steady flow states.
- Evaluating current formulas in the literature to estimate the hydrodynamic forces imposed by tsunami on the structural elements.
- Assessing the effect of initial flume bed conditions on the forces and pressures exerted on the structural model.

4.12.3 Waterborne debris impact tests

Post-tsunami field reconnaissance visits to tsunami-affected zones highlighted that impact forces caused by waterborne debris on near-shore structures was a major contributor to collapse of structures or significant structural damage. Therefore, one of the objectives of

the present study was to investigate debris impacts on structures. Three wooden debris of different masses and shape were placed into two inundation depths to impact the circular structural model. The results of these tests were used to investigate the influence of the following parameters on the magnitude of the impact force:

- Debris mass;
- Debris orientation;
- Debris shape (slenderness ratio);
- Debris eccentricity from the center of the structural model; and
- Inundation depth.

Finally, the most recent published formulas for debris impact force were verified against the experimental data.

4.12.4 Tests on the influence of mitigation walls

These tests involved installing low-elevation walls upstream of the structural model to reduce the bore-induced forces on the structural model. The walls had two different heights (100 and 150 mm), different vertical angles of the front face (45˚ and 90˚ with the horizontal flume bed), various cross-sectional shapes (flat, curved, and a Wave Return Wall that had compound circular curves), and were installed upstream of the structural at two different locations (305 mm and 915 mm from the model). During these tests, the time-histories of: base shear forces, base overturning moments, pressures, displacements, and accelerations induced on the structural model, in addition to the flow depth, were recorded. The models were rotated around their central vertical axis to record the pressure distribution. Data collected from this test group focused on:

- The effect of the mitigation walls on the pressure distribution-time histories around the model.
- The influence of the following wall characteristics on the effectiveness of force reduction:
  - Wall location relative to the model,
  - Wall height relative to the inundation depth,
  - Wall vertical face inclination angles of 45˚ and 90˚, and
  - Wall cross-section: flat, curved, and Wave Return Wall.

Based on the experimental data recorded and the discussion on the influence of the mitigation wall, recommendations were presented for the most efficient combination of the wall parameters (i.e., height, location, vertical inclination angle, and cross-section) that would result in a significant reduction in the forces experienced by the structural model.

4.13 Testing Procedures

4.13.1 Testing Procedure for Investigating Bore Characteristics

Two sets of tests were conducted in the absence of the structural model in the flume with the aim of recording the bore depth- and velocity-time histories at the location of the model (4.92 m downstream from the swinging gate). The following two sections describe the testing procedure for each set of these tests.

4.13.1.1 Bore depth-time history

First, the swinging gate was closed tightly followed by starting the hydraulic pumps. Based on the targeted impoundment depth, the flow discharge from the underground tank to the upstream reservoir was controlled by a butterfly hydraulic valve. The three impounding depths (550, 850, and 1150 mm) were used to generate tsunami bores. Numerous initial trials were conducted to find the appropriate discharge required to maintain the water depth in the reservoir approximately constant for each impounding water depth. Before the water depth in the reservoir reached the targeted impoundment depth, the data acquisition and the regular cameras were triggered to start recording data. At the desired water depth, the swinging gate was rapidly opened and the high-speed camera was simultaneously triggered. The flow drained at the downstream end of the flume through an opening into the underground tank. After the bore attained the quasi-steady flow state (at the model location), the test was terminated and the hydraulic pumps, the data recording, and cameras were turned off. Eight, stand-free water-level gauges were deployed along the flume to record the bore depth-time histories of the flow at different locations as shown in Figure 4.8. The probes of the water level gauges had different lengths (2 - 1 m, 4 - 0.8 m, and 2 - 0.65 m) to reduce their reading errors. The bore depth-time histories at the reservoir and seven sections throughout the flume for the three impounding depths, as well as the bore front velocities at the model location were recorded.

4.13.1.2 Bore velocity-time history

Tests were repeated three times for each impounding water depth to ensure repeatability of the recorded data. For the bore depth-time history tests, the eight free-standing water level gauges were positioned along the flume; while for the bore velocity test, the four gauges located between the swinging gate and the model location were removed. This was implemented for two reasons: avoid impacting of the suspended seeding tracers with the probes, and to eliminate additional turbulence that may be caused by these gauges. The bore velocity was estimated using a particle tracking velocimetry (PTV) technique. The bore was seeded with square pieces of paper with an approximate 30 mm side dimension. Two transverse wooden bars extending across the width of the flume were used as reference markers, and were installed 150 mm upstream and downstream from the model location at a height of 480 mm from the flume bed. A water level gauge was installed at the model location to record the time-history of the bore depth. The high speed digital video camera was installed at the model location at a height of 2.4 m above the flume bed. Given that the seed particles were near the surface of the flow, a correction for the distance travelled by the paper relative to the side makers was required. Figures 4.21 (a) and (b) provide a photo and a sketch of the test setup, respectively; while Figure 4.22 (a) and (b) provides two pictures from the side angle before and during the test. Figure 4.22 (c) and (d) display still frames from the high-speed video recording of a bore-velocity test with one of the seed papers crossing beneath the reference bars. In this case, the bore was generated from a 550 mm impounding depth.

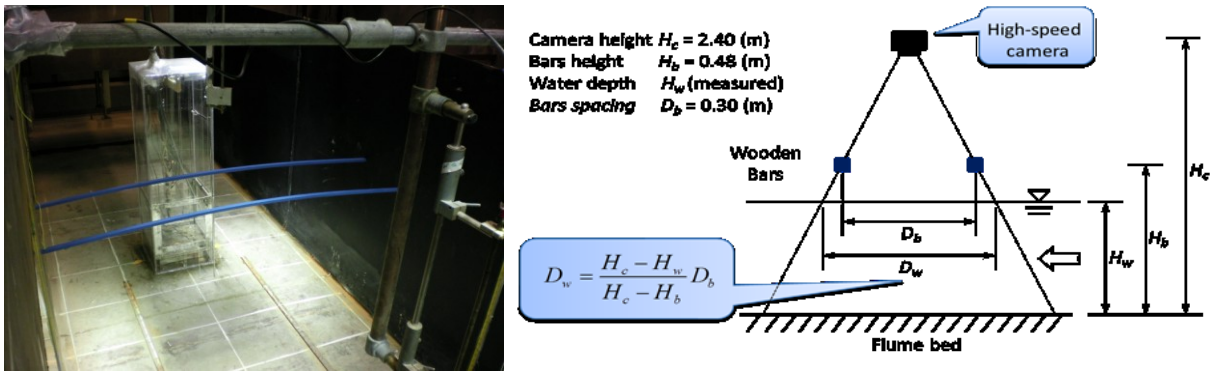

(a) (b)

Figure 4.21 Bore-velocity tests lab preparation: **a)** reference bars; and **b)** spatial referencing correlation

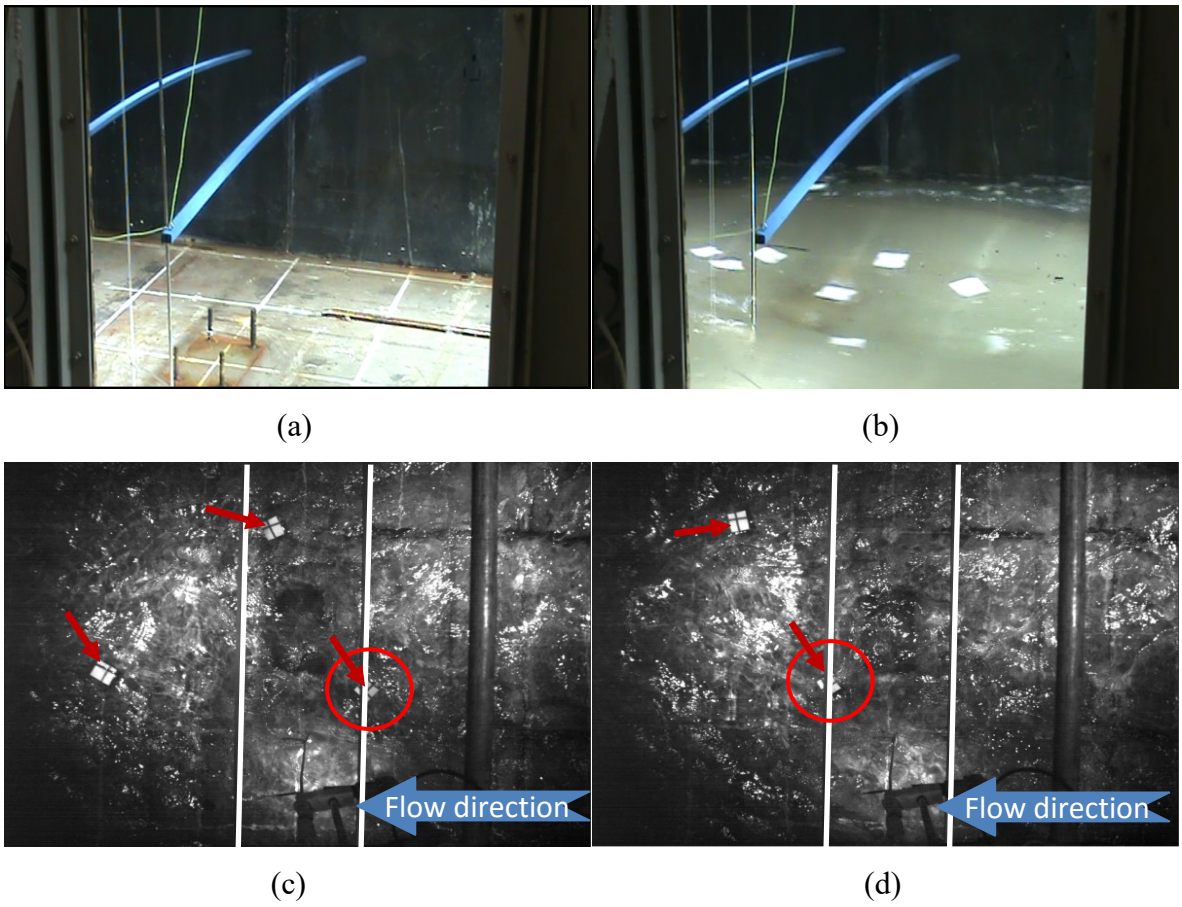

Figure 4.22 Bore-velocity tests: **a)** side view before starting the test; **b)** side view during the test and the seed tracers crossing beneath reference bars; **c)** seed tracers crossing beneath the 1st reference bar; and **d)** seed tracers crossing beneath the 2nd reference bar

4.13.2 Testing Procedure for Bore-Induced Forces

In these tests, the structural models were each installed at 4.92 m downstream from the swinging gate. The models were equipped with water gauges placed on their surface; therefore, gauges WG5 and WG6 were removed in this testing group. The models were impacted with three impoundment depths and the base shear force- and base overturning moment-time histories (both longitudinally and transversely) were recorded. The pressure-time histories around the models were recorded as well as the acceleration- and lateral displacement-time histories of the structural models. As previously discussed, the gap (5 mm) between the base of the model and the flume bed was filled with flexible material

(silicon) to prevent infiltration of water. Also, the top opening of the models were covered with plastic sheets to protect the sensors from water due to splashing.

4.13.3 Testing Procedure for Debris Impact

The circular model was impacted with waterborne debris. Two impoundment depths (550 mm and 850 mm) were used to generate the hydraulic bores, while the 1150 mm depth was not used for these tests due to the concern of impact damage to the structural model. Only water-level gauges WG1, WG7, and WG8 were used during these tests; while the remainder were removed to protect from damage. The influence of the initial location of the debris was investigated by selecting four initial locations: 1.75 m, 2.25 m, 2.75 m and 3.25 m upstream from the structural model.

After closing the swinging gate, and before turning on the water pump, the wooden debris was placed at the centerline of the flume at one of the pre-defined distances upstream from the structural model. The debris primarily was laid down on the flume floor oriented longitudinally with the flow direction as shown in Figure 4.23. For each test, it was ensured that the debris would float freely downstream. Then, the water pumps were turned on and the gate was opened when the targeted water impoundment depth was achieved. After the debris impacted the model, the pumps were shut down and the test was terminated.

(a) (b)

Figure 4.23 Initial position of debris on the flume: **a)** downstream view; and **b)** upstream view

Two digital video cameras were deployed to capture videos for the tests. One of the cameras, facing downstream, was installed above the swinging gate, while the other camera

was installed outside the flume and perpendicular to the side window. Figure 4.24 presents still frames from the videos recorded by those cameras for tests of 2kg1P and 2kg2P debris floating in the hydraulic bore generated by the 850 mm impounding water.

(a) (b)

Figure 4.24 Debris floating in the bore flow during the test with 850 mm impounding depth: a) downstream view for 2kg2P; and b) side view for 2kg1P

4.13.4 Testing Procedure for Mitigation Wall Effects

Six mitigation walls were individually installed upstream from the structural model and subjected with bores generated from the three impounding water depths. Each mitigation wall was installed at two locations: distances of one diameter (1D) and three diameters (3D) of the circular structural model upstream from the model as shown in Figure 4.25. The walls were installed across the entire flume width. The flow depth-time histories upstream and downstream from the walls were recorded. Similar steps to those employed for the debris tests were used, with the exception that the mitigation walls were fastened to the flume bed.

(a) (b)

Figure 4.25 Mitigation walls installed upstream from the square model: a) 150 mm-45˚ inclined wall at 1D; and b) 150 mm vertical wall at 3D

4.14 Similarity between Field Tsunami Bores and Experimental Conditions

Tsunami waves differ from wind-generated waves. Generally, tsunami waves tend of be similar to solitary waves propagating in shallow waters. The solitary wave maintains its form in shallow water due to the even distribution of the kinetic energy throughout the water depth, and thus, most of its energy is conserved during propagation. Video recordings from past tsunami events show that, depending on the near-shore bathymetry, tsunami waves may break offshore when the near-shore slope is mild or in the presence of fringing reefs and advance in the form of rapidly-advancing hydraulic bores (high-speed surge). In some cases, particularly when the slope of the near-shore bathymetry is steep, tsunami-induced coastal inundation can take in the form of a rapid surge. The present study focuses on tsunami-induced hydraulic bores. An inland tsunami has the potential to generate a significant bore height, potentially reaching more than twice its initial height as it approaches the shore (Bryant 2008). In laboratory conditions, the sudden and rapid opening of the swinging gate generates a perfect dam-break wave, which is created by the sudden free collapse of the lateral side of a standing body of water. The hydraulic bore generated is very similar to that generated from broken tsunami waves. In the laboratory, the flume bed is smooth and horizontal, thus the bore conserves most of its energy as it impacts the structural models.

This study investigated the influence of several parameters and hence employed different test configurations, which required repeated runs to ensure repeatability. Although the two structural models were designed to sustain the bore-induced forces, the 1150 mm impoundment depth was excluded during the debris impact testing to protect the models from damage.

Hudson et al. (1979) investigated the bore-structure interaction for an impervious structure. The study highlighted factors which influence the magnitude of the pressures induced on the structure investigated:

a) Bore depth at the structure location, angle of approach, seaward bottom friction and slope, and structure reflective characteristics; and
b) Concentration of entrained air in the water as the bore strikes the front face of the structure

These factors make it extremely challenging to ensure that scale effects are eliminated and to develop accurate empirical loading formulas. However, laboratory tests of tsunami effects on structures have gained significant attention from the scientific community even though scale limitations exist. The laboratory testing is able to provide physical information of the tsunami impact mechanisms.

CHAPTER 5

EXPERIMENTAL RESULTS, ANALYSIS AND DISCUSSION

5.1 Processing of Raw Experimental Data – GEDAP Software Package

The Ocean, Coastal and River Engineering of National Research Council of Canada developed a data processing software system known as "GEDAP" (which is derived from General Experiment Control, Data Acquisition, Data Analysis and Plotting Package). The software pre-processes, organizes and analyzes laboratory data, and provides real-time experiment control and data acquirement functions. GEDAP software package has several modules (e.g. data manipulation, data analysis, statistical analysis, etc). GEDAP is capable of handling large amounts of data in the form of binary files. Although this format cannot easily be edited and/or displayed, it is much more efficient than other formats (i.e. ASCII code) for numerical analysis and it requires less than half as much disk space (Miles, 1997). Figure 5.1 shows a block diagram of the components of the GEDAP software.

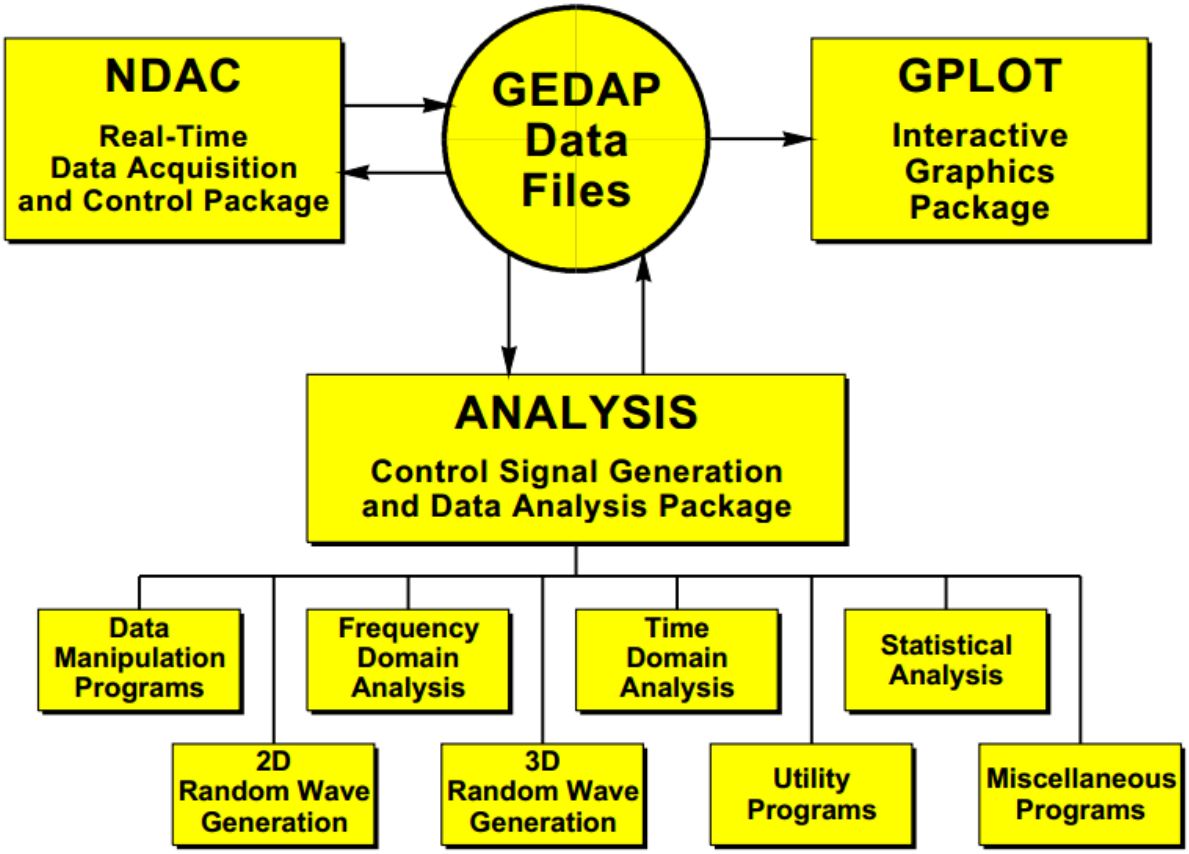

Figure 5.1 Block diagram of the GEDAP system (Miles, 1997)

Fast Fourier Transform (FFT) is one of the tools offered in GEDAP through a subroutine called "FILT_FFT" which employs a rectangular band pass filter to filter the time series signal. This filter removes all data in the signal that occurs at frequencies out of an operator-specified frequency range. This range is defined by two limit frequencies: the lowest and the highest frequencies. An inverse of FFT is then used to obtain the filtered output signal. The input signal may contain any number of points. If necessary, FILT_FFT performs cubic spline interpolation to resample the signal to a larger number of points for compatibility with FFT operations. FILT_FFT removes the mean value of the input signal prior to applying the filter. The original mean value can also be added to the filtered output signal as an option. FILT_FFT does not remove any trends other than the mean value. In some cases, it may be necessary to use program "TREND2" to remove linear or quadratic trends from the data prior to filtering.

Program “PEAKS” performs peak detection on a time series signal Y(t). Program PEAKS is designed mainly for use with force or pressure signals resulting from wave, debris or ice impacts with a structure. A peak is detected whenever a local maximum of the signal Y(t) exceeds the local minimum on each side of it by a threshold level YT, which is chosen by the user. YT has the same units as the input signal. The main purpose of this peak amplitude threshold is to prevent small ripples resulting from noise in the signal from being counted as valid peaks. Thus, increasing the value of YT will reduce the number of peaks detected. If the user enters a value of 0.0 for the amplitude threshold, then a default value is set for YT = 0.01 * the standard deviation of the input signal. In some cases, peaks that are too close together in time cannot be considered to be independent. In order to handle this situation, program PEAKS also allows the user to specify the minimum time permitted between two peaks. If any two peaks are closer together than the specified time period in seconds then the smaller peak is discarded and the larger peak is retained. In such option, no two peaks in the resulting set will be closer together than the specified period. Increasing the value of the period will reduce the number of peaks detected and will also usually make the resulting set of peaks more statistically independent. To retain all detected peaks in the data, no minimum period were imposed (0.0).

After processing the analysis of the data in the GEDAP system, GEDAP includes subroutines that enable researchers to transform the data files to ASCII code files. The ASCII code files can be easily opened with Excel of MS-Office software to continue the analysis and display process.

A sample of raw data for bore depth-time history along the flume captured by eight stand-free water depth gauges are displayed in Figure 5.2.

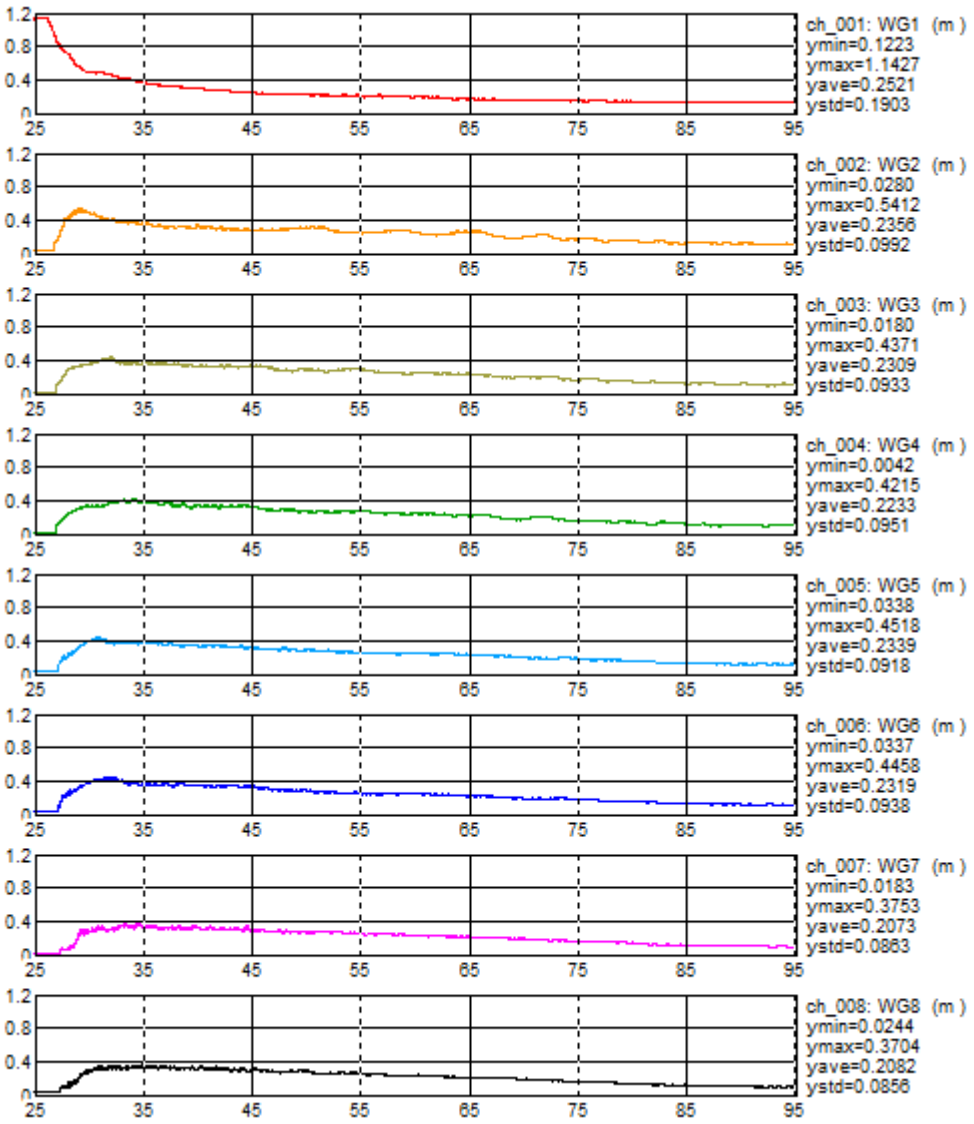

Figure 5.2 Sample of raw data of the bore water level-time history generated by 1150 mm impounding depth (vertical axis is the water depth in meters and x-axis is time in seconds)

5.2 Characteristics of the Hydraulic Bore

Tsunami bore front can be characterized by four categories: (1) bore front on a flat dry bed, (2) bore front propagating on very shallow water, (3) bore front with rolling head propagating in medium water depth, and (4) bore front similar to undular bore, without breaking (Nakamura 1973). One of the objectives of this study is to quantify the forces associated with tsunami-induced bores on near-shore structures. Therefore, the first

category mentioned above is of most interest to this study. Ritter (1892), Nakamura (1973), and Chanson (2001) indicated that tsunami bore of this category is essentially identical to the bore generated from a perfect dam-break wave. Therefore, the dam-break analogy was utilized in the current experimental program by impounding a water volume behind a rapidly opening swinging gate. When the water reached the target height specified for a test run, the gate rapidly opened.

Two sets of preliminary tests were performed to study the dam break-induced bore characteristics by estimating the bore velocity and recording the bore depth-time histories. To estimate the bore velocity, the first set of tests was completed without the structural model installed in the flume. The high-speed camera was installed above the location reserved for the structural models to capture the plan view of the bore while advancing downstream of the swinging gate.

5.2.1 Bore depth-time history

- Without the structural model

Eight capacitance water level gauges were deployed longitudinal in the flume to measure the flow depth-time history during the tests. Figure 5.3 illustrates the arrangement of these water level gauges. One of the gauges (WG1) was installed in the water reservoir, 1.25 m upstream from the swinging gate to record the impounding water level-time-history.

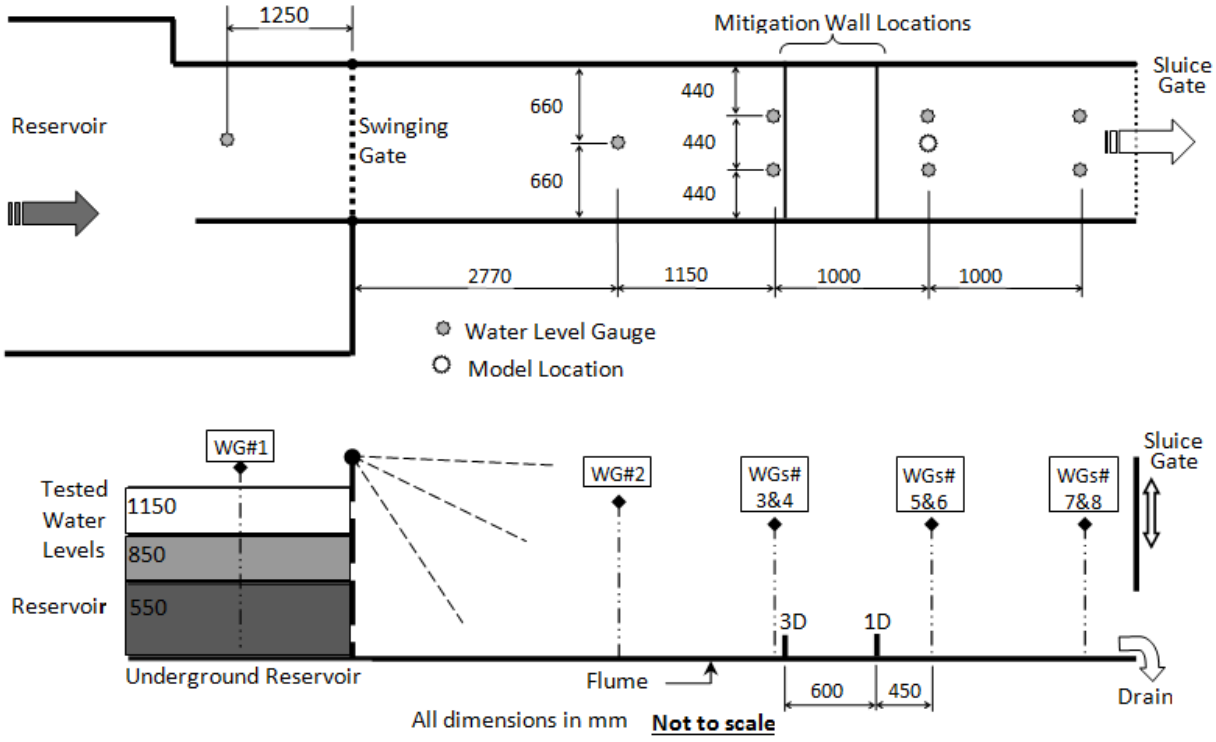

Figure 5.3 Schematic of the experimental setup with location of water level gauges and mitigation walls

Another water level gauge (WG2) was installed 2.77 m downstream of the gate along the flume centerline, while the remaining six gauges (WG3 - WG8) were installed in pairs on three rows located at 3.92, 4.92, and 5.92 m downstream from the swinging gate. The paired gauges were installed equally spaced across the flume width. The middle pair was located at the location reserved for the structural models (4.92 m downstream from the swinging gate). This water level gauge arrangement was used when no structural model was installed in the flume to monitor the bore profile and to estimate the bore front velocity. The gauges of the middle pair (WG5 and WG6) were further removed as the two structural models were equipped with gauges attached to their front, lateral and back to directly measure the time-history of the flow depth around the models. Sample time-histories of the bore depth generated from the 850 mm impounding water level are presented in Figure 5.4.

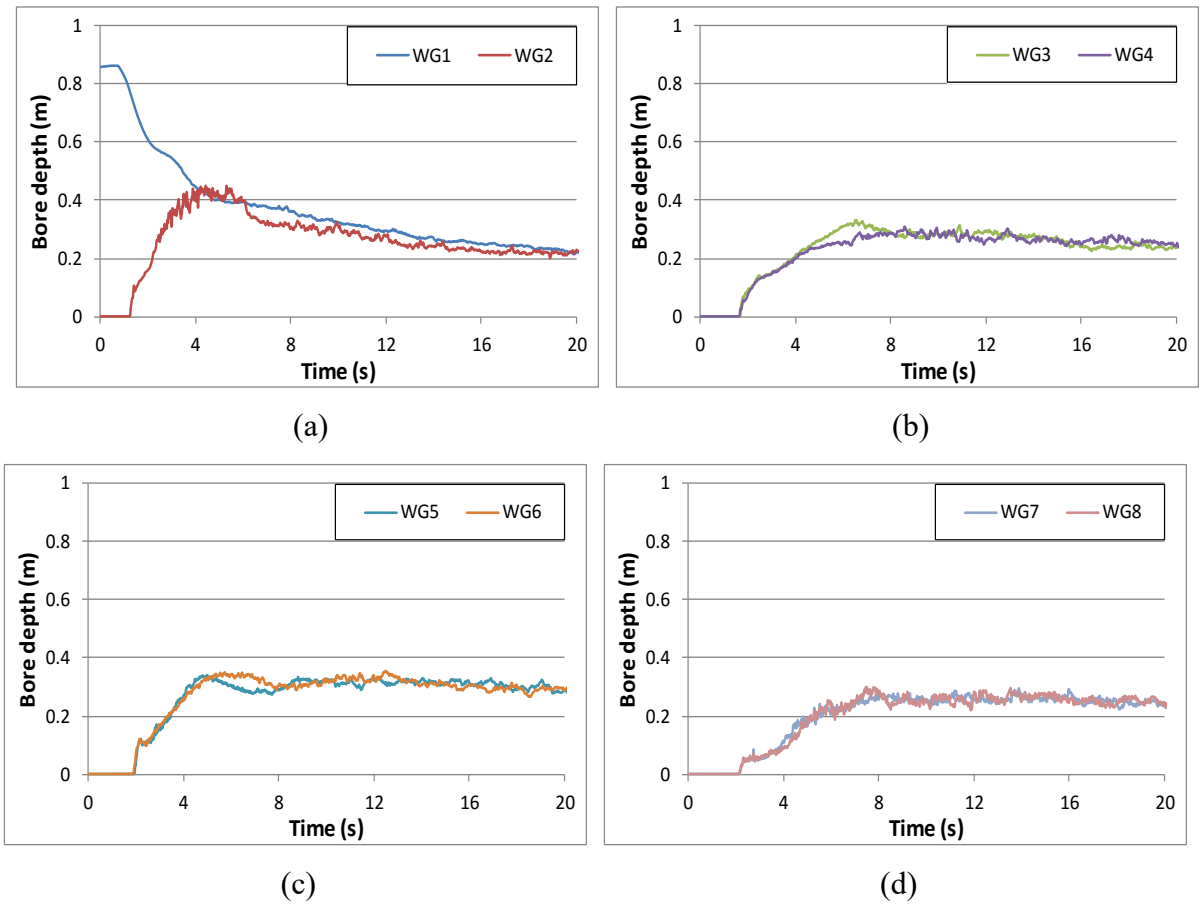

Figure 5.4 Bore depth-time histories at different water level gauges along the flume produced from the impounding depth of 850 mm in the absence of the structural model in the flume

The test was repeated three times for each impounding water depth to investigate the bore profile consistency and ensure repeatability of the data recorded. The relative differences in the records of each pair of water level gauges on the same row were compared using the least square method and were found to be less than 10%. The largest difference was at 2.07 m downstream from the gate where cross-waves had a negligible effect. Figure 5.5 shows a sample of the data collected from repeating tests. The tests were generated from 550 mm impounding water depth in the absence of the structural model. The water level gauge WG6 was at the model location, while the WG8 was 1 m behind the model location.

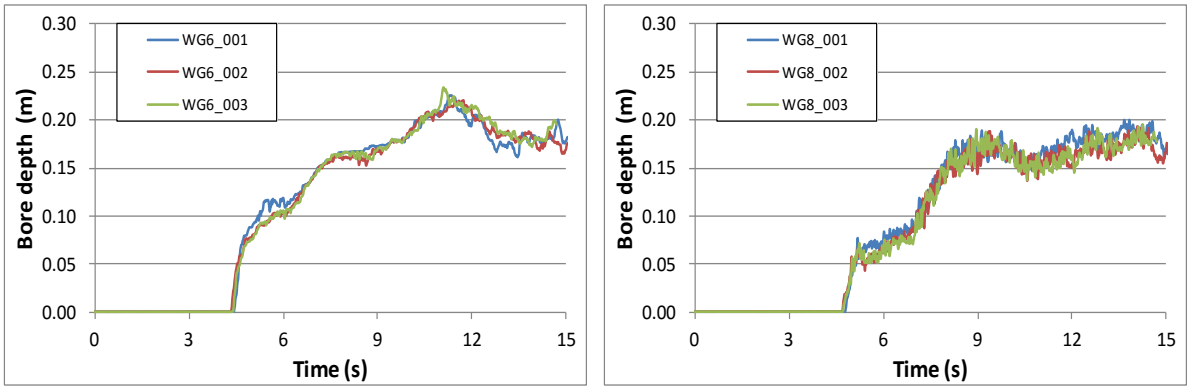

(a) (b)

Figure 5.5 Bore depth-time histories for three repeated tests generated with the 550 mm impoundment water depth: **a)** at model location; and **b)** 1 m behind the model location

- With structural models

The two structural models were (individually) installed at 4.92 m downstream from the swinging gate (measured from the center of the models) and were subjected to a series of bore impact tests. Figure 5.6 (a) and (b) provide the bore depth-time histories recorded by the water level gauges installed on and around the square and circular models, respectively, for an impounding water depth of 850 mm. For comparison, the data recorded by a water level gauge that was placed at the center of the structural models from a companion test, in which the model was not installed in the flume, is also shown in Figure 5.6. For the square model, data recorded by the two gauges located on the upstream face of the model (WG9 and WG10) recorded an abrupt increase in bore depth, followed by a sustained, higher water depth on the front face of the model. The slope of the initial rise in bore depth for the square model is larger than that for the circular model. After the maximum run-up was recorded, the bore depth decreased to approximately 600 mm for both of the models. The histories of the other three attached water level gauges (on the side and back faces of the square model) were less than that recorded in the case when the structural model was not installed. For the test with the circular model, although WG9 and WG10 have a similar trend to the test with the square model, the rise time to peak run-up depth was larger and the maximum run-up (peak bore depth) was approximately 75 mm less than that recorded with the square model. This is due to the reduced aerodynamic shape of the square column compared to the circular

for which water flows more smoothly around the column. Furthermore, the maximum run-up bore-depth was sustained for a longer time than that in case of the square model. During this time, the other water level gauges, particularly those located on the downstream face, indicated very low water levels. As the flow redirects around both sides of the models, the bore depth on the upstream face decreases while on the sides and back faces of the models it increases. The effect of model geometry is evident through a comparison of the time histories recorded by water level gauge WG11, which was placed on the side face of the models. With the square model, the bore depth-time history of WG11 was nearly similar to that on the downstream face (WG12 and WG13); however, WG11 recorded flow depth that was between the recordings for WG9 and WG12 (upstream and downstream faces) for the circular model. The flow depth-time histories recorded in the absence of the structural models were similar to the time-histories recorded by the downstream gauges in the presence of the structural models. However, the rise times while the structural models were present were shorter than they were in the absence of the models. This resulted from the obstruction of flow due to the presence of the model.

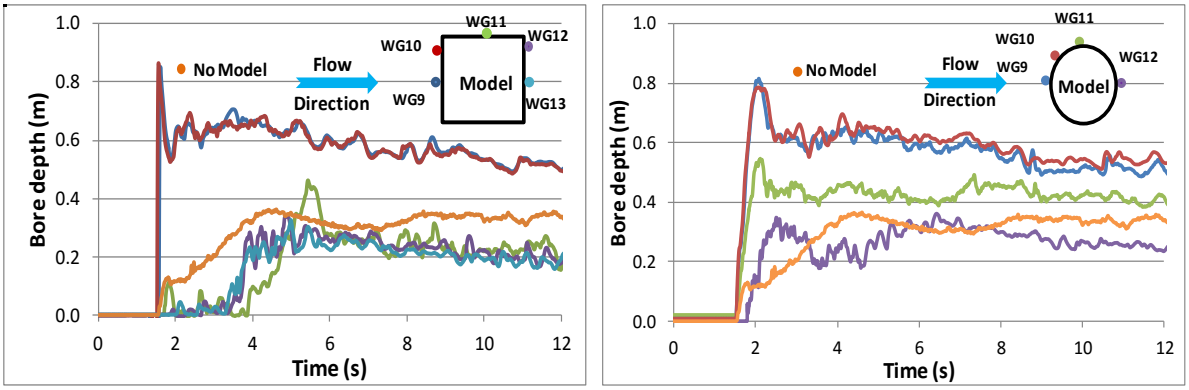

Figure 5.6 Bore depth-time histories around the structural models generated from the 850 mm impounding water depth: **a)** square model; and **b)** circular model

Visual observations and video recordings demonstrated that subsequent to the initial impact of the bore with the structural models, the flow was characterized by high turbulence and rapid fluctuations in its free surface. By the end of this stage, the maximum run-up force was recorded. Thereafter, the flow continued to pass around the lateral sides of the model. At that instant, an increase in bore depths was recorded by the water level gauges located on the

sides and back face of the models. Figure 5.6 also indicates that during the quasi-steady flow, the bore depth on the upstream face was approximately 2.5 times larger than that recorded by the side and back water level gauges for the square model, while it was found to be 1.25 and 2.5 times, respectively, for the circular model.

5.2.2 Bore velocity-time history

The bore-induced hydrodynamic forces are proportional to the square of the flow velocity. Therefore, errors in estimating the flow velocity lead to either under- or over-estimation of the hydrodynamic force. Thus, to quantify bore velocity, three techniques were explored in this experimental program. Note that two of these investigated methods are applicable to the calculation of the bore front velocity only and were not used to capture the bore velocity under quasi-steady flow conditions. The first method used six water level gauges in three successive pairs. The pairs were each spaced longitudinally at a distance of one meter with the second row positioned at the location of the structural models. The one meter distance was selected to minimize the effect of the wake generated by the upstream gauge on the subsequent downstream pair. The bore velocity was then estimated using the time for the bore to reach a specific depth at successive pairs of gauges. Those specific depths were 30, 40, 50, and 60 mm, which enabled the calculation of the bore front velocity. Figure 5.7 (a) shows the bore front velocity for the three impounding water depths. Each point represents the average velocity of three repeated tests with the same impoundment depth. The results reveal that as the impounding water depth is increased, which corresponds to an increase in the maximum inundation depth at the location of the structural model as is shown in Figure 5.7 (a), the bore front velocity increased. For example, for the 40 mm bore front depth, the estimated bore front velocities at the model location were 2.65, 4.0, and 5.08 m/s for the 550, 850, 1150 mm impounding water depths, respectively. Therefore, the velocity under quasi-steady flow conditions (near constant bore depth) would increase as the bore depth at the location of the structure increases. This is in agreement with results shown in Figure 5.7 (b).

Figure 5.7 (b) presents the bore front velocity gradient, along a one-meter distance centered at the location of the structural model for the 550 mm impounding water depth. As the bore depth at the location of the model used to calculate the velocity increased, there was

a gradual decrease in the bore front velocity. For example, for the 550 mm impounding water depth, as the bore depth increased from 30 to 60 mm, the bore front velocity decreased from 2.75 to 2.24 m/s, with decreasing intervals of 0.24, 0.17, and 0.1 m/s per each 10 mm increase in bore depth. The decrease in velocity was attributed to a decrease in the difference in head between the initial impounding water depth in the reservoir and the bore depth at the location of the structure. Similar trends were observed for the 850 mm and 1150 mm impoundment depths: the bore velocity dropped from 4.37 to 3.77 m/s and from 5.22 to 4.55 m/s, respectively, for an increase of 30 mm in bore depth (30 mm to 60 mm). These results are in good agreement with previous studies (Carrier et al. 2003 and Yeh 2006) that have also demonstrated that at a specific location the bore front, which typically is characterized by the lowest bore depth, has the highest bore velocity.

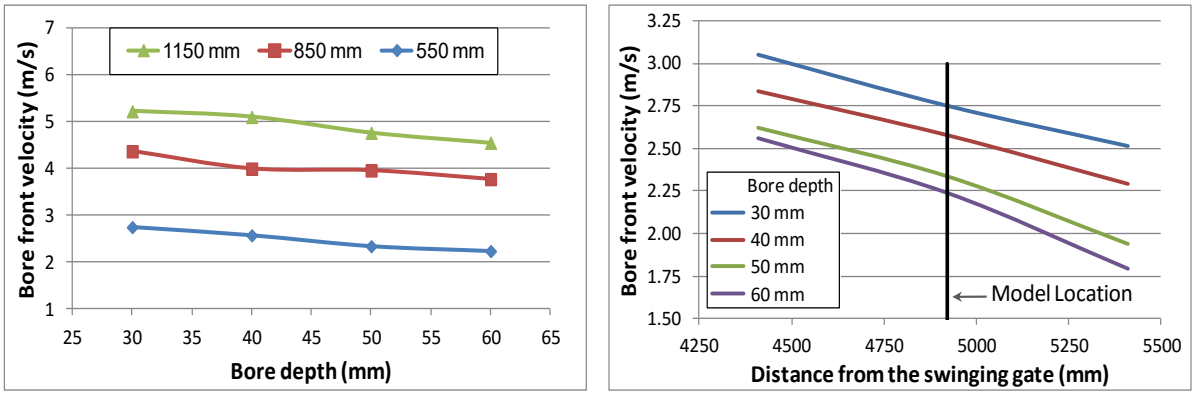

(a) (b)

Figure 5.7 Calculated bore velocity: **a)** at the location of the model; **b)** along the flume corresponding to a bore due to the 550 mm impounding water depth

Furthermore, Figure 5.7 (b) also shows that the rate of change in the flow velocity decreases as the bore front depth increases. The drops in velocities from the 30 mm to the 60 mm bore depth at the location of the structural model were 19%, 14%, and 12% for the 550, 850, and 1150 mm impounding water depths, respectively.

The second technique used to quantify the bore front velocity involved tracking the bore with a high-speed digital video camera. A 300 mm x 300 mm grid was painted on the flume bed to video-track the advancement of the bore front. The high-speed digital camera was installed 2.4 m above the floor of the flume precisely above the planned location of the

models. Using the time sequence of the video recordings (Figure 5.8) and the measured distance between the transverse grid lines, the bore front velocity at different sections along the flume was calculated.

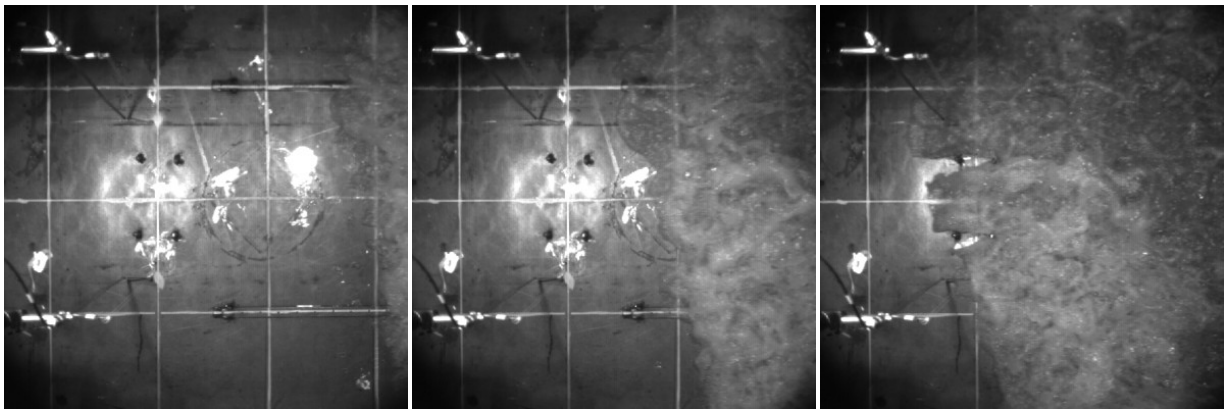

(a) t = 2.134 s (b) t = 2.208 s (c) t = 2.283 s

Figure 5.8 Advancing bore front crossing the gridlines on the flume bed from for 850 mm impounding water depth

The velocity that was calculated between two adjacent grid lines was assumed to represent the average velocity for that segment. The videos captured a 1.5 m length along the flume. The results of this technique are shown in Figure 5.9. The bore-front velocities at the location of the model were 2.99 m/s, 4.37 m/s, and 5.64 m/s for the 550 mm, 850 mm, and 1150 mm impounding water depths, respectively. The velocities predicted from the water level gauges corresponding to the 30 mm bore depth were 2.75 m/s, 4.04 m/s, and 5.22 m/s, respectively. The bore front velocities estimated from high-speed videos were slightly higher due to the smaller bore front depths.

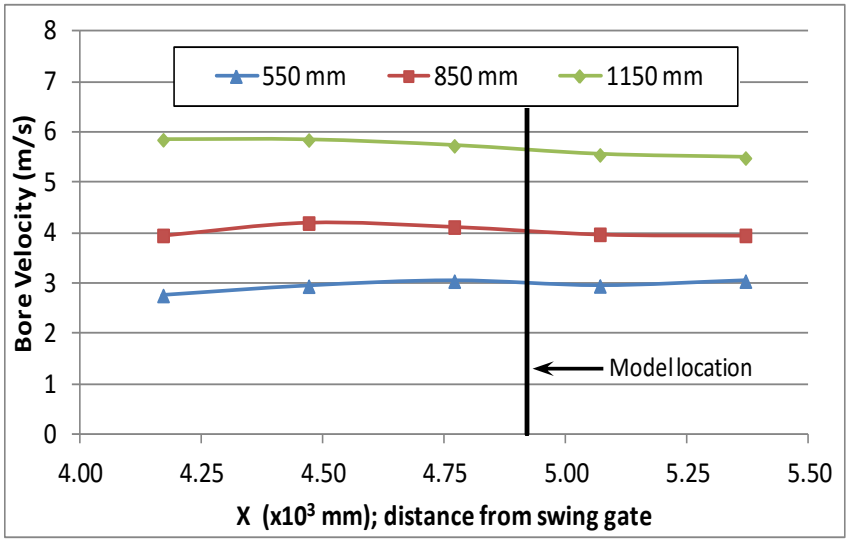

Figure 5.9 Bore front velocities for three impoundment depths

Although the bore front velocities estimated from the high-speed video recording were slightly higher than those obtained using the procedure involving the water level gauges, differences were reasonable as the former technique captured the bore velocity earlier and the bore depth was slightly smaller than in the latter technique.

Figure 5.10 shows the bore depth- and bore velocity-time histories for the three impounding water depths of 550, 850 and 1150 mm. The results presented in this figure were recorded from the tests described in Section 4.11.1.2 (Page 118). The bore depth was recorded by a water level gauge (WG4), which was installed at the model location (midway between the reference bars as shown in Figure 3-b). In Figure 5.10, t = 0 s represents the instant the swinging gate opened and the hydraulic bore was generated. The bore front reached the model location after 1.520, 1.191 and 0.970 s for impounding water depths of 550, 850 1150 mm, respectively. The bore depth- and bore velocity-time-histories for the three impounding water depths demonstrated a similar trend. The quasi-steady flow appeared during the period from 10 s to 20 s for both the 550 mm and 850 mm impounding depths, while for 1150 mm impoundment it was recorded between 7 s to 11 s. The bore front velocities (which were the highest recorded velocities in each test) at the model location were 3.03, 4.2 and 5.02 m/s, while the quasi-steady flow velocities were 1.54, 2.19 and 2.39 m/s for the impounding water depths 550, 850 and 1150 mm, respectively. The maximum bore flow depths at the model location were 211, 292 and 344 mm for the impounding water

depths 550, 850 and 1150 mm, respectively. These bore velocities and bore depths were used in this study with the prescriptions from the design guidelines previously presented to estimate the force components. Note that although the velocities were determined relative to the flow surface, given the significant vertical exchange of momentum within the water column due to turbulence, it is assumed that they are relatively uniform for the entire flow depth. Figure 5.10 (a), (b), and (c) reveal that, as the impounding water depth increased the slope of the leading edge of the bore also increased. The figure suggests that as the impounding water depth increased the bore velocity for both its front and the subsequent quasi-steady flow portion have also increased. For a specific impounding water depth, the velocity is a maximum at the leading edge of the bore front, and as the bore depth increases and then reaches a quasi-steady state flow level, the velocity gradually decreases. The rate of change in the velocity decreases as the bore depth attains the steady flow level.

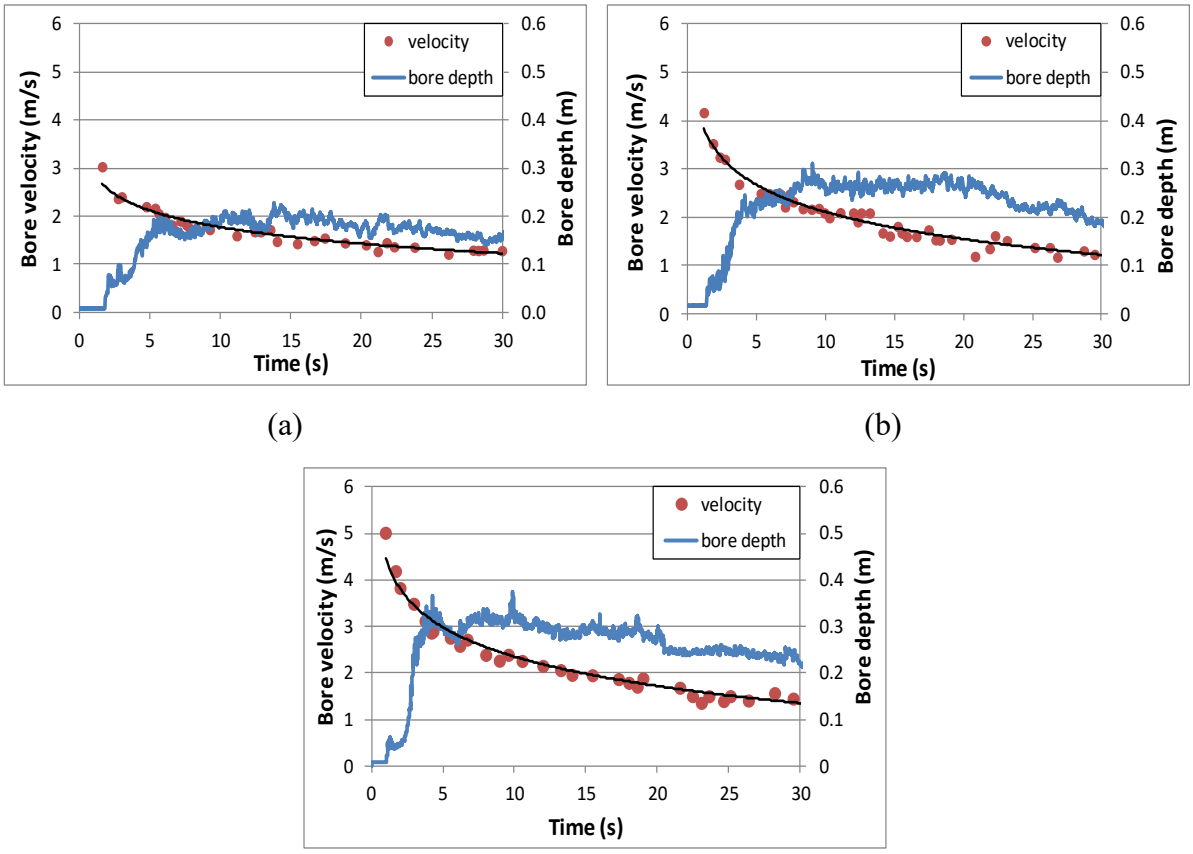

Figure 5.10 Bore depth- and bore velocity-time histories generated by impounding depths of: **a)** 550 mm; **b)** 850 mm; and **c)** 1150 mm

Froude and Reynolds numbers were calculated for the three water impoundment depths for the tests without the model installed in the flume. The recorded flow depths and estimated velocities at the model location were used to calculate the Froude and Reynolds numbers. Figure 5.11 (a) illustrates that the Froude number for the flow resulting from the three impoundment depths deduced from approximately 2 to 1,5 after 5 seconds from arrival of the bore. Conversely, the time-history of the Reynolds number proportionally increases with the increment in the impounding water depth during the run-up flow states. The time history of the calculated Reynolds number is shown in Figure 5.11 (b). In contrast with Figure 5.11 (a), the Reynolds number for the three impounding water depths are similar for the leading edge of the bore front, but differs significantly immediately thereafter and the difference becomes less in the quasi-steady flow state. As the impoundment water depth increased, the Reynolds number increased proportionally for the bore front and run-up flow states.

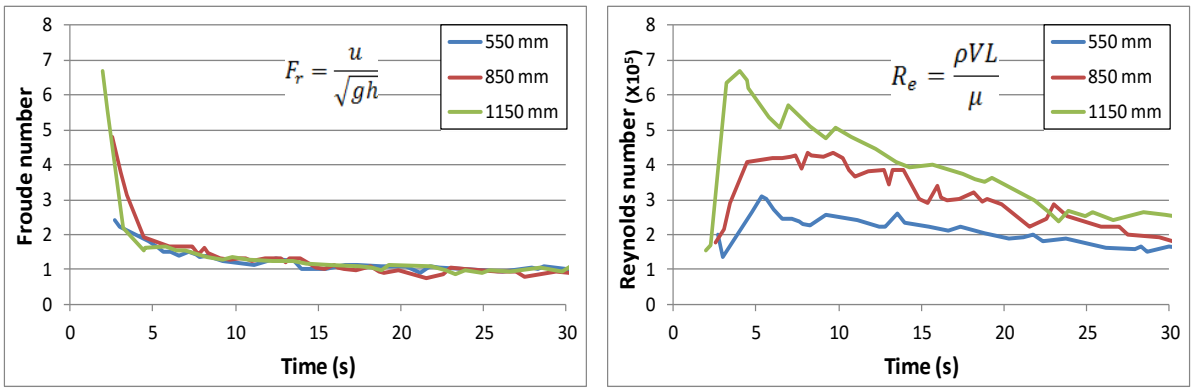

(a) (b)

Figure 5.11 Froude and Reynolds numbers-time histories for the bore flow: **a)** Froude number; and **b)** Reynolds number

The analysis of the data indicated that, as the impounding water depth increased, the generated bore traveled at higher velocity. In any single test, the velocity was found to peak at the bore front when the bore depth was at a minimum, and as the bore depth subsequently increased, the corresponding velocity decreased. The bore velocity continued to reduce until the flow reached a quasi-steady state condition.

5.2.3 Available bore velocity formulas

Current predictions of tsunami-induced bore velocities are uncertain as demonstrated by the various formulae proposed in the literature and their comparison with field data obtained from processing of video-recordings taken during the 2011 Japan Tsunami (Chock et al. 2012). Figure 5.12 provides bore velocities using formulae from: CCH (2000), FEMA 55 (2000), Bryant (2001), Murty (1977), Iizuka and Matsutomi (2000), and Shen and Meyer (1963).

For the range of bore depths considered, FEMA 55 offers an upper bound. The City and County of Honolulu Building Code (CCH 2000) provides a lower bound for bore depths not exceeding 6 m, while Bryant (2001) provides the lower bound velocity for bore depths greater than 6 m. For a bore depth of 6 m, the predicted velocity varies from 6 m/s according to the City and County of Honolulu Building Code (CCH 2000) to 15.3 m/s using Shen and Meyer (1963) (which was adopted by FEMA P-646 2008). Note that bore velocities estimated by these formulae correspond to the quasi-steady flow state as a function of the maximum inundation depth; hence, an increase in the inundation depth results in an increase in bore velocity.

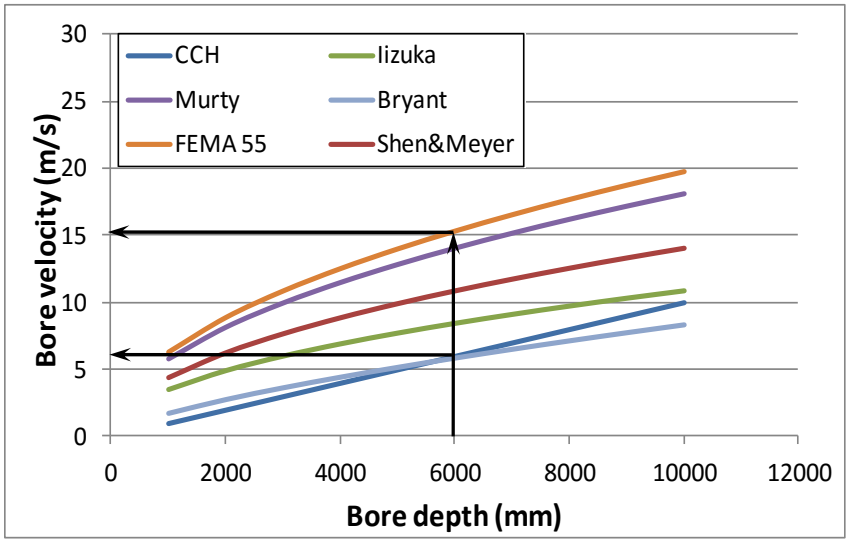

Figure 5.12 Tsunami-induced bore velocities calculated using formulae from current literature

As mentioned in Section 2.5, different tsunami-bore velocity estimation formulae were proposed by several researchers. These formulae were used to estimate tsunami bore

velocity for steady flow conditions, using the maximum tsunami inundation depth. Figure 5.12 illustrates the differences between the results of those formulas. For example, for 6 m maximum inundation depth, the lowest estimated bore velocity is 6 m/s while the highest is 15.3 m/s. Given that the magnitude of the hydrodynamic force is proportional to the square of the bore velocity, errors in estimating the bore velocity will reflect exponentially in the calculation of the hydrodynamic force. As explained in Section 5.2.2, two techniques were used to estimate the bore velocity experimentally. Although the bore velocities determined using the two techniques were in agreement, they represented the bore-front and not the velocities corresponding to the quasi-steady state portion of the flow. To determine these particular bore velocities, additional tests were conducted using a Particle Tracking Velocimetry (PTV) technique for the three impounding water depths. The results of this technique (PTV) were presented in Figure 5.10.

5.3 Bore-Structure Interaction

5.3.1 Bore-induced pressures

For a better understanding of the hydraulic bore pressure distribution on structures due to impacting hydraulic bores, ten pressure transducers were installed along a vertical line on the surface the structural models. The bore pressure-time-histories induced on the structural models at different sides (for the square structure) or horizontal angles (for the circular structure) and at different elevations (20, 50, 100, 150, 200, 250, 300, 350, 400, and 450 mm) from the flume bed, were recorded for the three impounding water depths in the reservoir located upstream from the gate (550, 850 and 1150 mm). The following sections provide a concise summary of the data recorded and processed.

5.3.1.1 Square model

The pressure-time histories induced by the advancing bore on the square model are shown in Figure 5.13 (a, c, and e). These pressures were generated by the rapid release of the 550, 850, and 1150 mm impounding water depths, respectively, under wet-bed flume conditions. For all cases, the highest recorded pressures corresponded to the lowest-located pressure sensors and the pressure decreased for the sensors located higher on the face of the structure. As shown in Figure 5.13, the time histories of sensors P1, P2, P3, P4, and P5 located at

elevations of 20, 50, 100, 150, and 200 mm, respectively, from the flume floor demonstrated an abrupt rise in pressure following the instant the bore front impacts the model. Then the pressure decreases gradually to the quasi-steady hydrodynamic pressure as shown in Figure 5.13 (b, d, and f). Note that the origin of the time histories is shifted by 0.25 s to allow the identification of data from each pressure transducer. The pressure transducers located at higher elevations on the column (PT6 to PT10) recorded lower pressures compared to the pressure transducers (PT1 to PT5) placed in the lower elevation of the column. Due to the direct impact of the bore-front, with small depth and very high velocity, on the upstream face of the structural model; a discontinuity of bore velocity is released locally. This new situation has to be adopted quickly and progressively by the following flow. The bore-front redirected as an upward jet on the upstream face of the model which generating negative pressures were recorded by some of the upper pressure transducers (PT6, PT7, and PT10). This loading process has been noticed previously in experimental study carried out by Lafeber et al. (2012) and in numerical simulation implemented by St-Germain et al. (2014).

As the response of the lower level pressure transducers approached the quasi-steady hydrodynamic pressure state, the pressure of the upper level sensors began to increase. Predominantly at this time, the maximum run-up force was recorded by the dynamometer. However, for dry-bed flume conditions, the maximum force was recorded coincidently with the impulsive pressure corresponding to the first impact between the bore and the structural model.

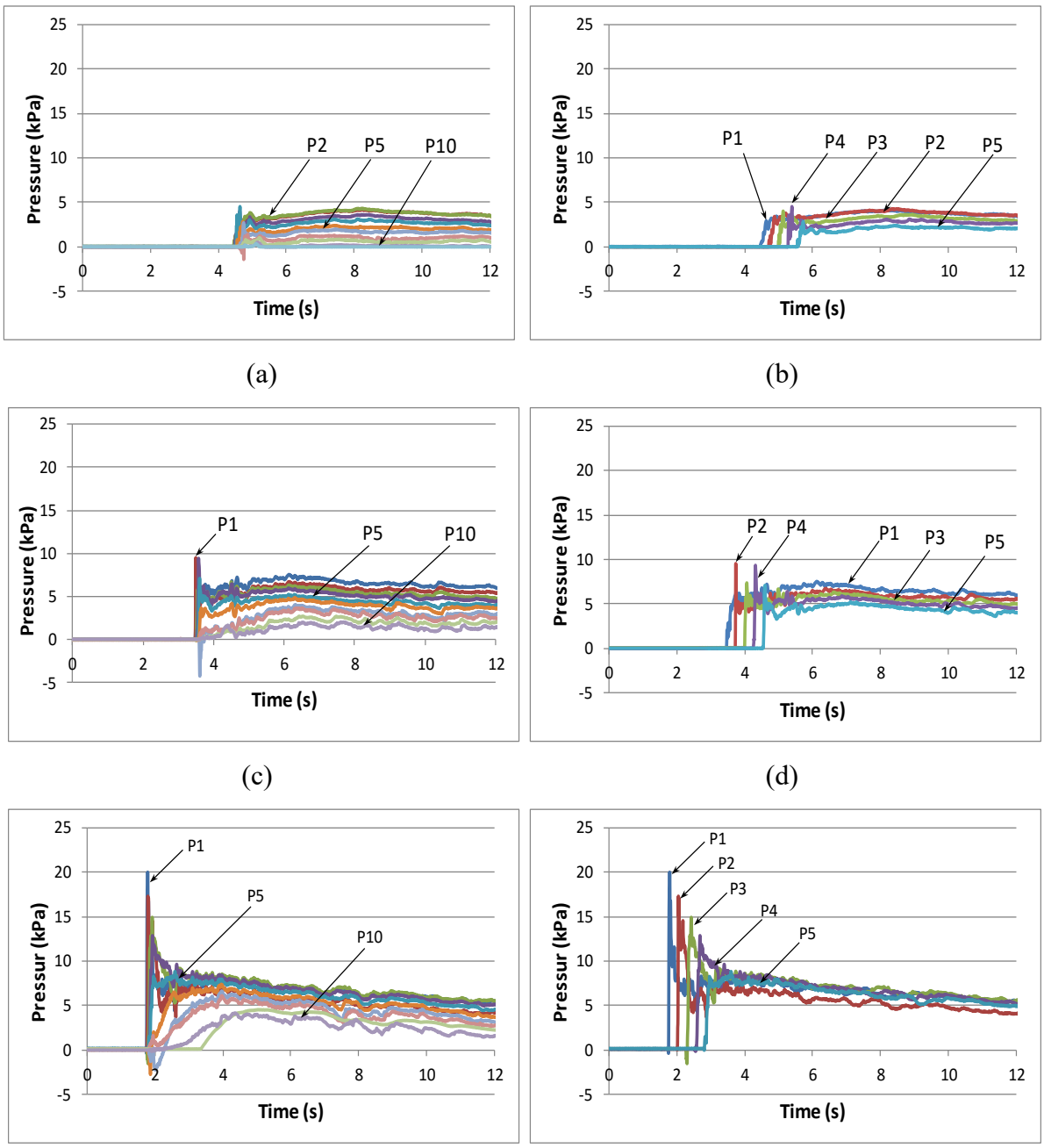

Figure 5.13 Bore pressure-time histories induced on the upstream face of the square model: **a)** all pressure sensors with 550 mm impoundment level; **b)** Sensors P1 to P5 with 550 impoundment level; **c)** all pressure sensors with 850 mm impoundment level; **d)** Sensors P1 to P5 with 850 impoundment level; **e)** all pressure sensors with 1150 mm impoundment level; and **f)** Sensors P1 to P5 with 1150 impoundment level

5.3.1.2 Pressure around square model

The pressure-time histories induced on the upstream, side and back faces of the square model were captured for the three impounding water depths. Figure 5.14 (a, b and c) shows the time histories of the pressure induced by the hydraulic bore generated from 850 mm impounding depth on the front, side and back which was designated as: 850_NW_SQ_0R, 850_NW_SQ_90R, and 850_NW_SQ_180R, respectively. The test name notation included the following elements in their numbering/lettering string: impoundment water depth in mm _ mitigation wall type _ structural model type _ rotation angle for the model. Thus, 850_NW_SQ_0R refers to 850 mm impoundment water depth, no mitigation wall installed, square structural model installed, and zero-degree rotation of the model (which means the pressure transducers were facing upstream). The pressure variation on the upstream side of the model was recorded by all pressure sensors (PT1 – PT10). The pressure-time history can be distinguished into three flow states: impulsive, run-up and quasi-steady states. Maximum pressure throughout the test was recorded on this upstream side of the model during the impulsive flow state (9.45 kPa) as illustrated in Figure 5.14 (a). The time history the pressure induced on the side face demonstrated a gradual increase to its maximum peak, which coincided with maximum run-up acting on the upstream face. Pressure variations were evident for the five lowest sensors (PT1 – PT5 which were located up to 200 mm above the flume floor), while the rest of sensors recorded no pressures as shown in Figure 5.14 (b). Sensor PT5 recorded pressures for 3 second duration only, which was during the run-up flow state, with peak of 1 kPa. In contrast, the pressure-time histories of the downstream side, Figure 5.14 (c), illustrates that pressure was recorded by the five lowest sensors (PT1 – PT5), however the fluctuation in their records were less than that noticed on the side face. Further the pressures recorded by (PT3 – PT5) were last for a shorter duration than that on the side face of the model.

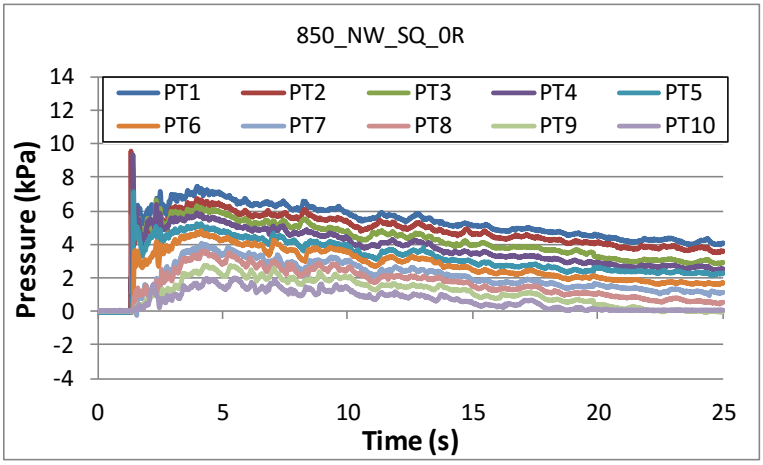

(a)

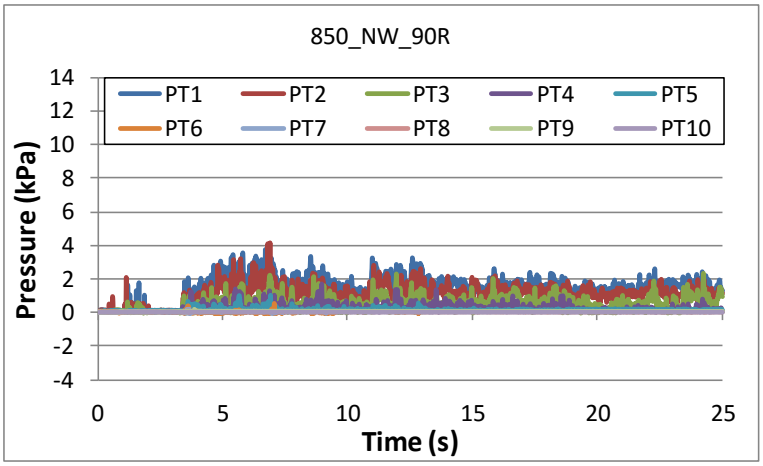

(b)

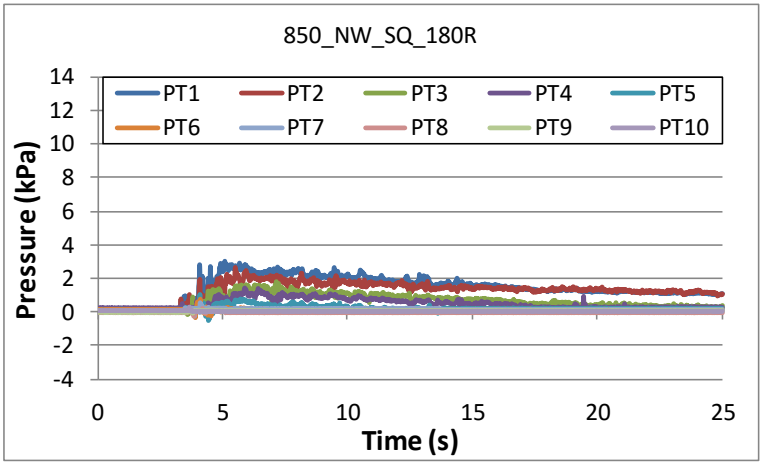

(c)

Figure 5.14 Bore pressure-time histories induced on square model: **a)** upstream face, **b)** side face, and **c)** downstream face.

5.3.1.3 Circular model

The time histories of the pressure induced on the circular model by the hydraulic bore generated from the three impounding water depths are presented in Figure 5.15. A comparison between this figure and Figure 5.13 shows, in general, similar trends of the time-history of the bore pressures despite differences in the geometry of the structures. However, the streamlined shape of the circular model affected the duration of the impulsive pressure that was recorded by the lowest five sensors (Figure 5.15 (b), (d), and (f)). The curvature of the circular model allows the redirection of the flow around the model, resulting in shorter impulsive pressure durations. A comparison between Figures 5.13 (b, d, and f) and 5.15 (b, d, and f) reveals that although the impulsive pressure recorded by lowest placed pressure transducer (PT1) has a smaller magnitude for the circular model, all other sensors recorded slightly higher impulsive pressures than in the case of the square model. This was most likely the result of the pressure transducers being installed at the midline of the upstream face of the models, which would be the points tangential to the bore leading edge. Due to the curvature of the outside surface of the circular model, the pressure differences are not uniform around the upstream half of the circular model. In other words, the pressures measured on this upstream face of the circular column corresponding to the first bore impact are significantly higher than the pressures exerted on the other verticals of the upstream face situated at an angle from that vertical initially impacted by the bore. This is in contrast to the square model where the pressures on the front face of the structure are uniform over the entire width of its front face. As a result, the base shear force exerted on the square model was always higher than that recorded for the circular model for the same impounding water depth and other testing conditions.

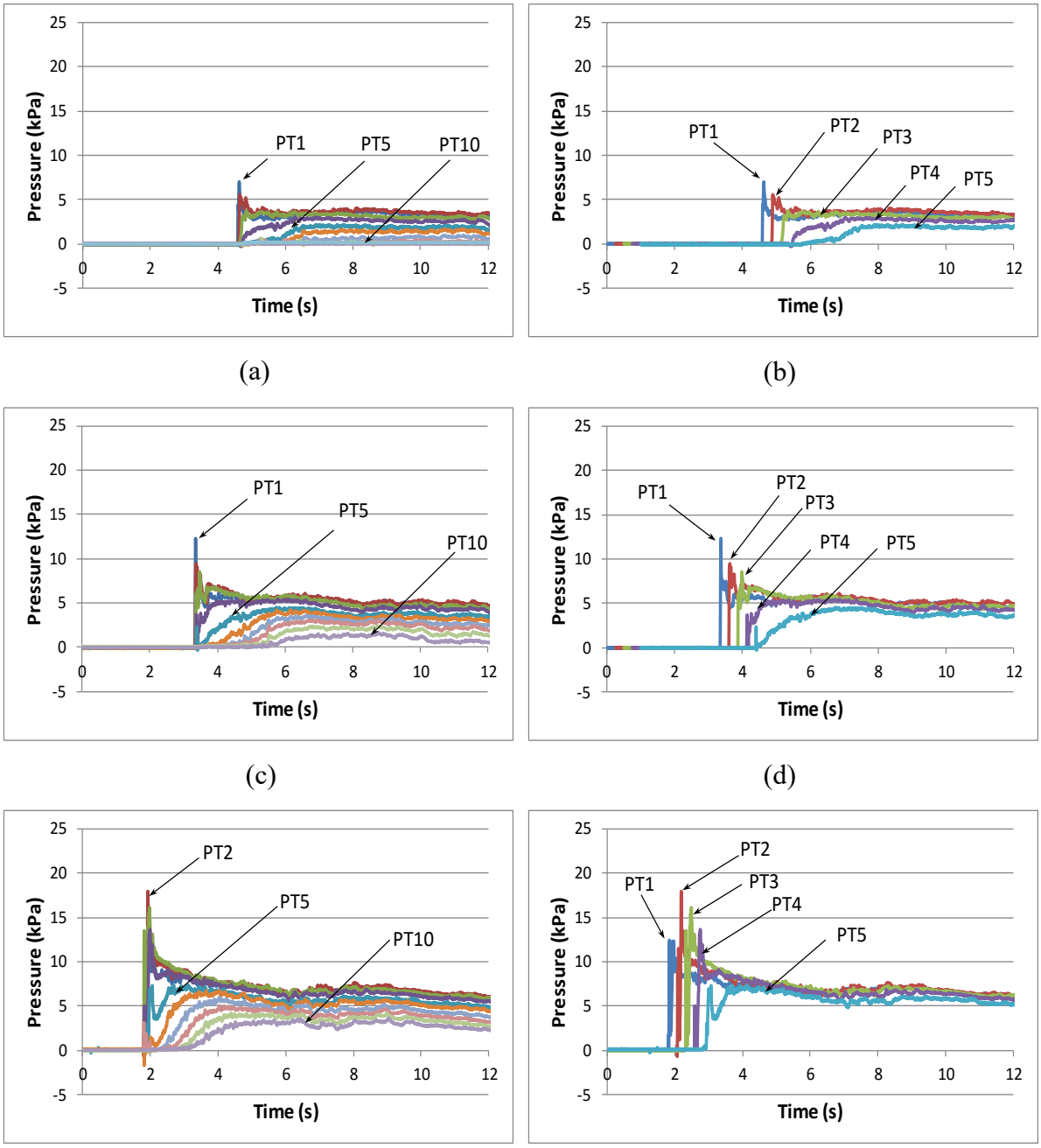

Figure 5.15 Bore pressure-time histories induced on circular model: **a)** all pressure sensors with 550 mm impoundment level; **b)** Sensors P1 to P5 with 550 impoundment level; **c)** all pressure sensors with 850 mm impoundment level; **d)** Sensors P1 to P5 with 850 impoundment level; **e)** all pressure sensors with 1150 mm impoundment level; and **f)** Sensors P1 to P5 with 1150 impoundment level

5.3.1.4 Pressure around circular model

The time history of the pressure induced and measured around the circular model was obtained for several positions of the model which was rotated (about its central vertical axis) by 30˚, 60˚, 90˚, 120˚, 150˚, and 180˚ as indicated in Figure 5.16. Three impounding water depths were used to generate hydraulic bores which impacted the model for each model's position.

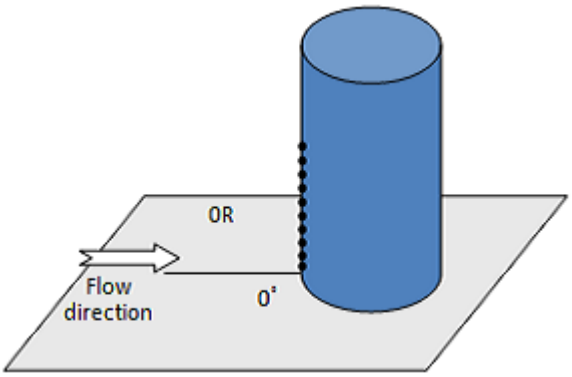

(a)

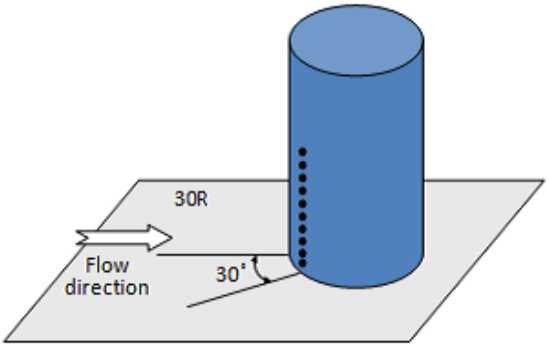

(b)

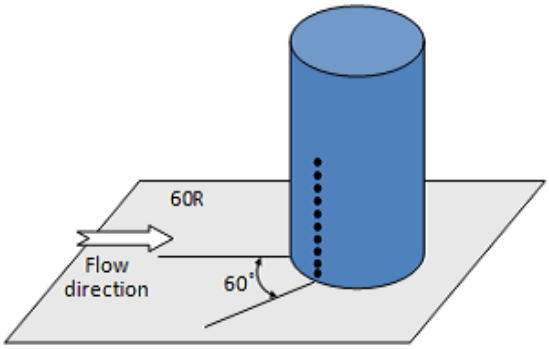

(c)

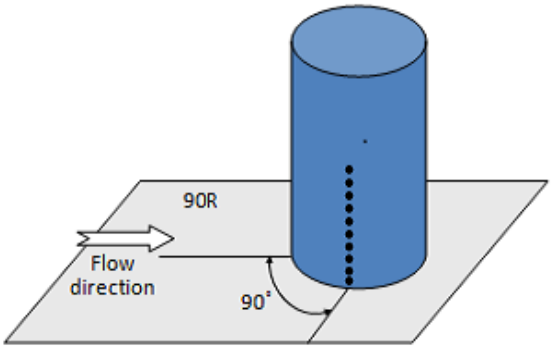

(d)

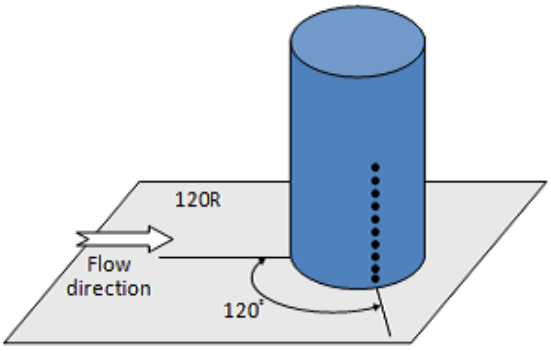

(e)

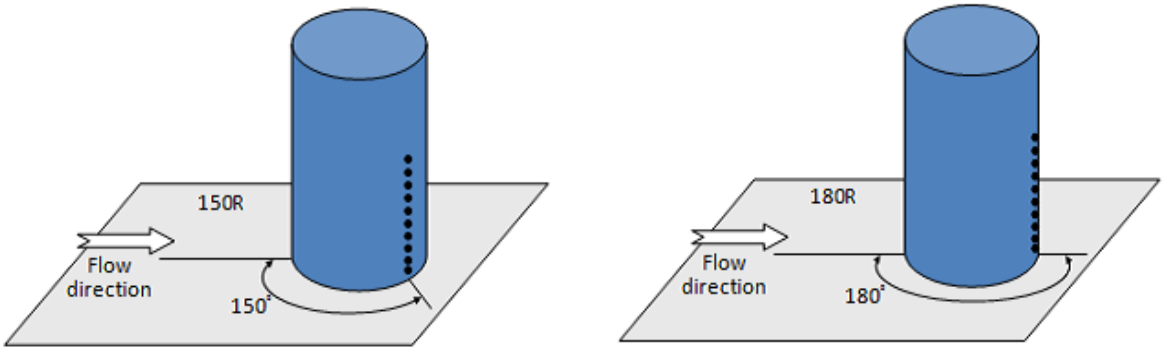

(f) (g)

Figure 5.16 Circular model rotated to record the pressure-time history around its surface: **a)** 0˚; **b)** 30˚; **c)** 60˚; **d)** 90˚; **e)** 120˚; **f)** 150˚; and **g)** 180˚

Figure 5.17 displays the pressure-time histories captured by the three pressure transducers nearest to the flume bed; the pressures recorded by the other sensors were negligible (or zero when the rotation angle of the model was greater than 60˚). The pressures presented were induced by the hydraulic bore generated from the 550 mm impounding water depth. No mitigation wall was installed in these tests. Several observations are made with respect to the pressure-time-histories:

- High impulsive pressures of 7 kPa and 4.5 kPa were recorded at 0˚ and 30˚ angles, respectively. The recorded pressure is inversely proportional with the elevation of the sensor. This pressure segment was not observed for rotation angles greater than 60˚ (Figure 5.17 (a), (b), and (c)).
- Largest impulsive pressure was recorded when pressure transducers were positioned at 0˚; while the lowest pressure was recorded at 60˚ (Figure 5.17 (a), and (c)).
- Negative impulsive pressures were recorded when the transducers were placed at 90˚. Positive pressures were recorded when the flow began to build up on the upstream face of the model: however, the magnitudes were negligible, Figure 5.17 (c).
- Slight decrease in the recorded pressures by all transducers at 30˚ in comparison with that of 0˚ particularly for the run-up and quasi-steady flow states (Figure 5.17 (a), and (b)).

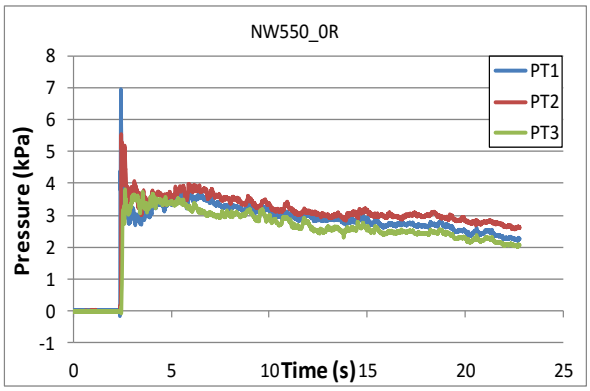
NW550_0R
PT1
PT2
PT3
Pressure (kPa)
Time (s)

(a)

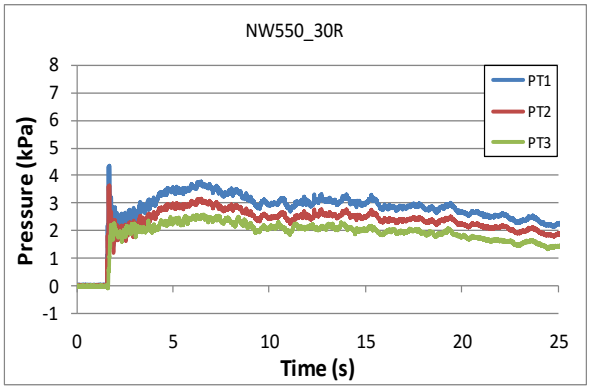
NW550_30R
PT1
PT2
PT3
Pressure (kPa)
Time (s)

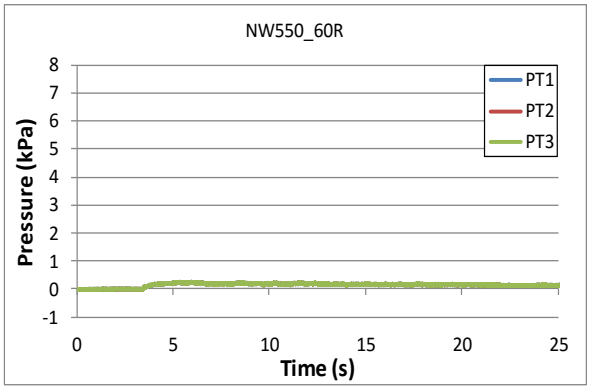
NW550_60R
PT1
PT2
PT3
Pressure (kPa)
Time (s)

(b)

(c)

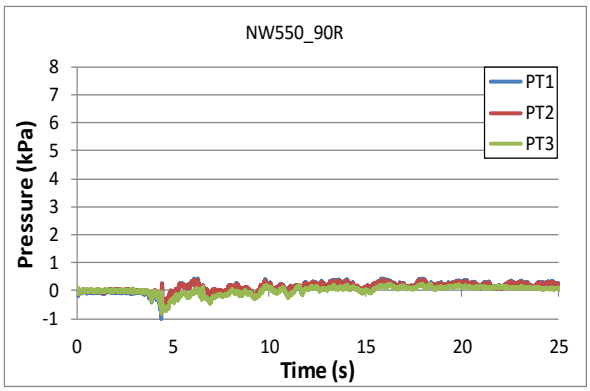
NW550_90R
PT1
PT2
PT3
Pressure (kPa)
Time (s)

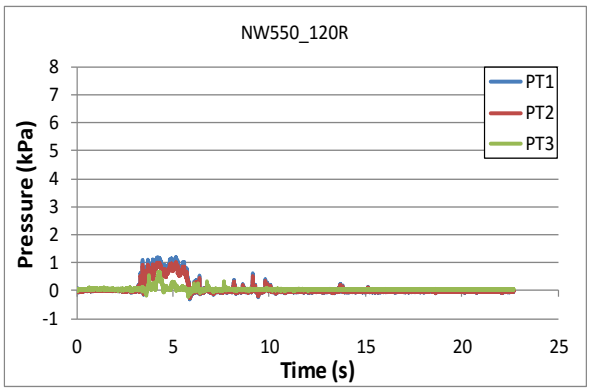
NW550_120R
PT1
PT2
PT3
Pressure (kPa)
Time (s)

(d)

(e)

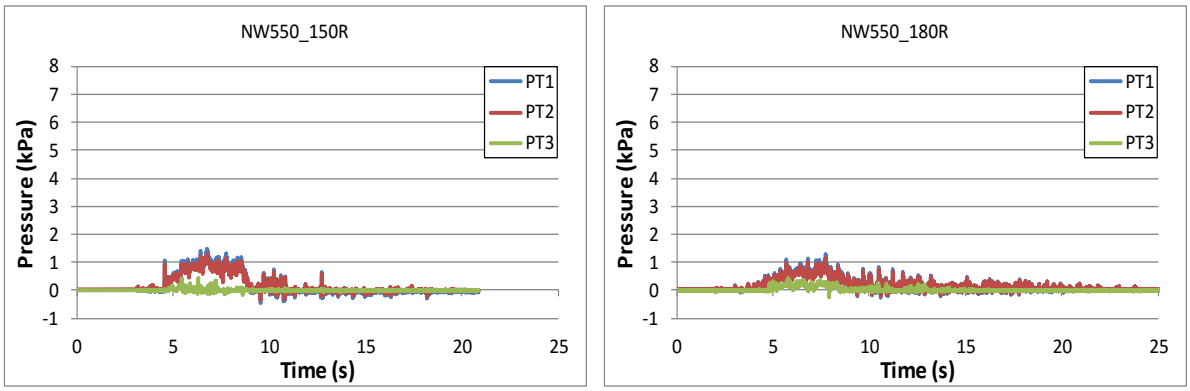

(f) (g)

Figure 5.17 Bore pressure-time histories induced around the circular model from hydraulic bore generated by 550 mm impounding water depth: **a)** 0˚; **b)** 30˚; **c)** 60˚; **d)** 90˚; **e)** 120˚; **f)** 150˚; and **g)** 180˚

The vertical distribution of the bore-induced pressure for each rotation angle was plotted for the three flow segments characterizing three different flow phases: the impulsive phase, the run-up phase, and the quasi-steady phase (Figure 5.18). The hydrostatic pressure distribution for the three flow phases (IHS, RHS, and QHS, respectively) were plotted as well. Several observations can be made as follows:

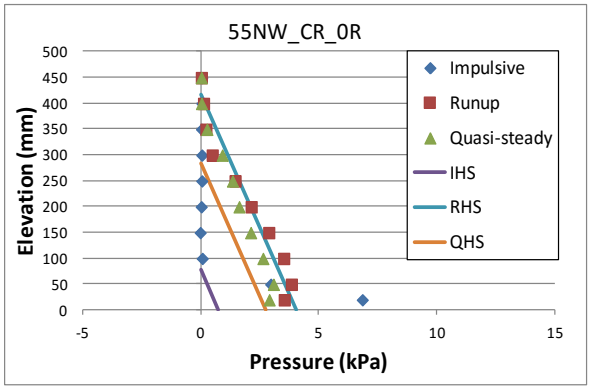

(a)

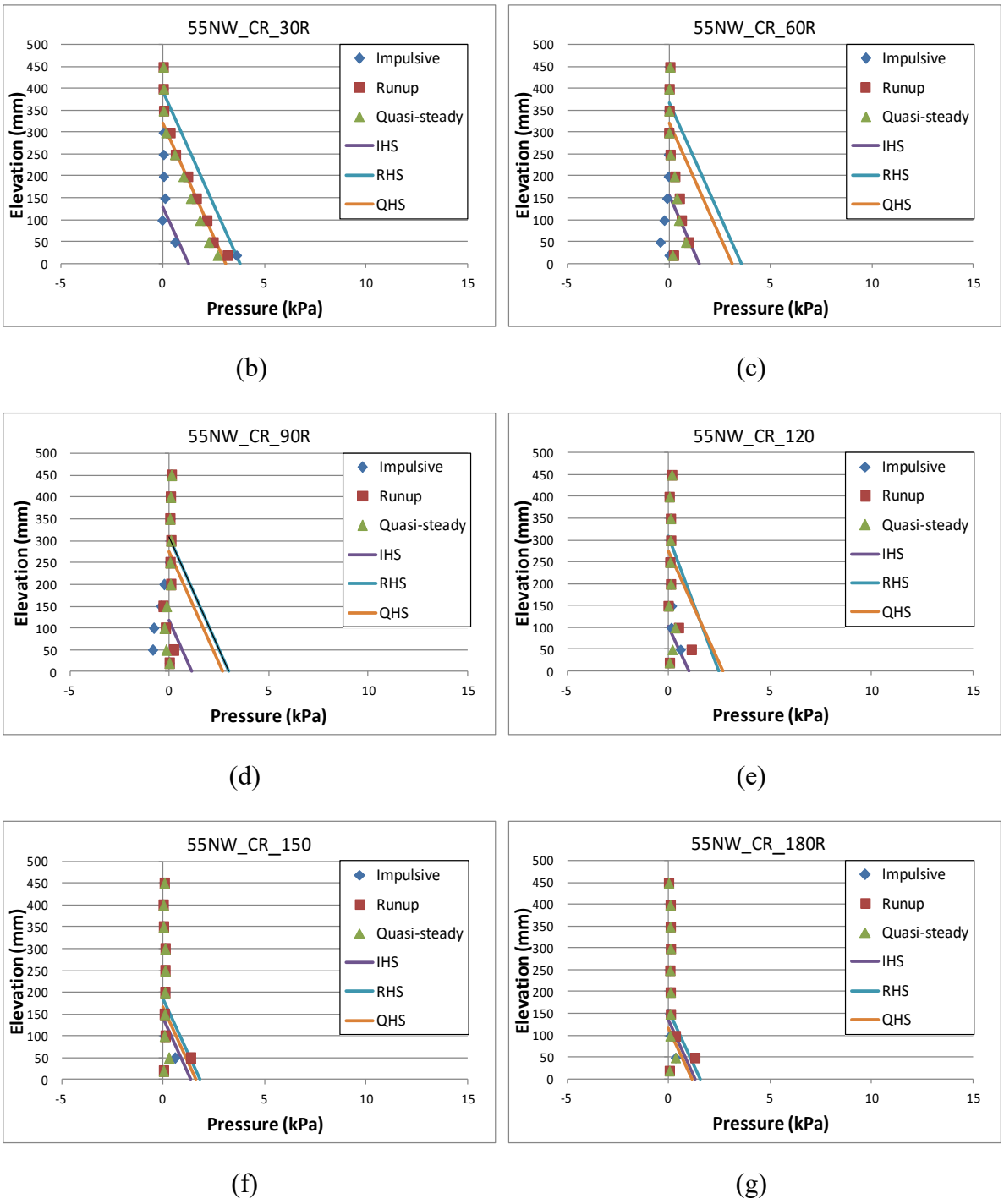

Figure 5.18 Vertical distribution of bore-induced pressure around the circular model for three flow phases: impulsive, run-up, and quasi-steady generated from 550 mm impounding water depth in comparison with the HydroStatic pressure (lines: IHS, RHS, QHS): **a)** 0˚; **b)** 30˚; **c)** 60˚; **d)** 90˚; **e)** 120˚; **f)** 150˚; and **g)** 180˚

- Impulsive flow phase: highest pressure recorded by the sensor nearest (20 mm) to the flume bed (PT1) at the center of the upstream face of the model (0˚ rotation). Approximately 44% reduction was recorded at 30˚ relative to that at 0˚. For both angles of 0˚ and 30˚, the impulsive pressure was the maximum pressure recorded throughout the test. The pressures recorded during testing for the other angles were less than 10% of that recorded at the 0˚ angle. For this flow phase, the pressure variation was evident on the model up to 100 mm height (PT1, PT2, and PT3) for 0˚, 30˚, 120˚, 150˚, and 180˚, and up to a height of 200 mm for 60˚ and 90˚.
- A hydrostatic pressure distribution satisfactorily captured the pressures for both the run-up and quasi-steady flow phases.

Figure 5.19 (a) shows the vertical distribution of the impulsive pressure imposed around the model. Similar to the corresponding graph for the pressure distribution from the bore generated by the 1150 mm impounding water depth, the highest impulsive pressure was recorded by PT1 (20 mm above the flume bed) when pressure transducers were set at the 0˚ and then 30˚ angles. These maxima were about half the magnitude of that recorded for the 1150 mm impoundment-induced bores.

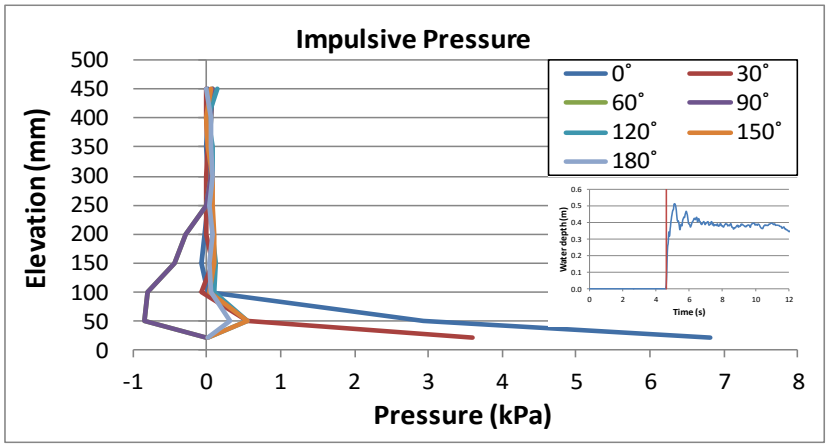

(a)

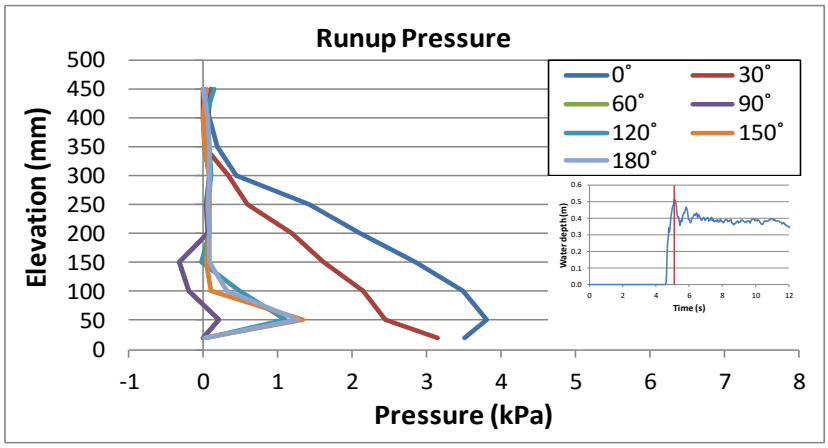

(b)

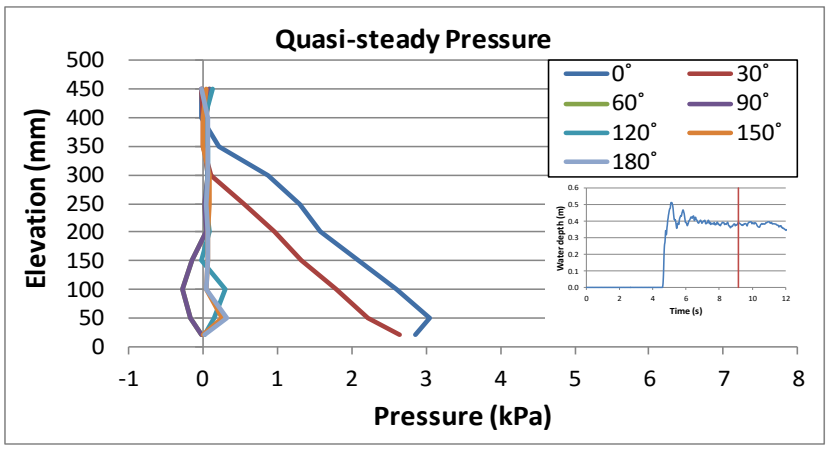

(c)

Figure 5.19 Vertical distribution of the bore-induced pressure around the circular model generated by 550 mm impounding water depth: **a)** impulsive; **b)** run-up; and **c)** quasi-steady

Another difference is that, in the case of the 1150 mm impoundment-induced bores, the maximum pressure was recorded by the PT2 (located at 50 mm above flume bed). The positive impulsive pressure was recorded up to a height of 100 mm on the circular model – for the case with the 1150 mm impoundment-induced bore the pressure was recorded up to a height of 250 mm. Suction pressures for this flow phase were only recorded when the transducers were located at an angle of 90˚.

The pressure distribution around the circular model at four elevations: 20, 100, 250, and 400 mm, are presented in Figure 5.20. Three flow states for the 550 mm impounding water depth are illustrated: impulsive, run-up, and quasi-steady. A polar coordinate system was used considering the circular cross-section of the structural model. The radial coordinates represent the pressure: -4 kPa at the center and 16 kPa at outer rim of the circle (maximum). The angular coordinates represent the angle around the model with zero corresponding to the upstream centerline of the flume. Figure 5.20 (a) reveals that maximum pressure is recorded at the lowest measuring level (20 mm) on the upstream face of the model (zero angular coordinate) at the impulsive flow state. Figure 5.20 (b) shows the pressures were recorded at 100 mm of elevation between the model rotation angles (φ) of 60˚ to 300˚, which corresponds to the segment of the structure facing the flow. The maximum pressure of 4 kPa recorded at this elevation was during the run-up flow state. At this elevation, the pressure distribution during the quasi-steady flow was slightly less than that during the run-up flow state. The impulsive pressure at this elevation and above is zero due to swallow flow depth at the bore front.

The pressure induced on the circular model at 250 mm of elevation is demonstrated in Figure 5.20 (c). At this elevation, pressures were induced on the model between angles of 330˚ and 30˚ during the quasi-steady flow state; while no pressure was recorded during the impulsive and run-up flow states. No pressure was recorded on the model at an elevation of 400 mm during the three flow states for the hydraulic bore generated by 550 mm impounding depth. Responses for the pressure distribution around the circular model induced by hydraulic bores generated by 850 and 1150 mm impounding depths are available in Appendix B.

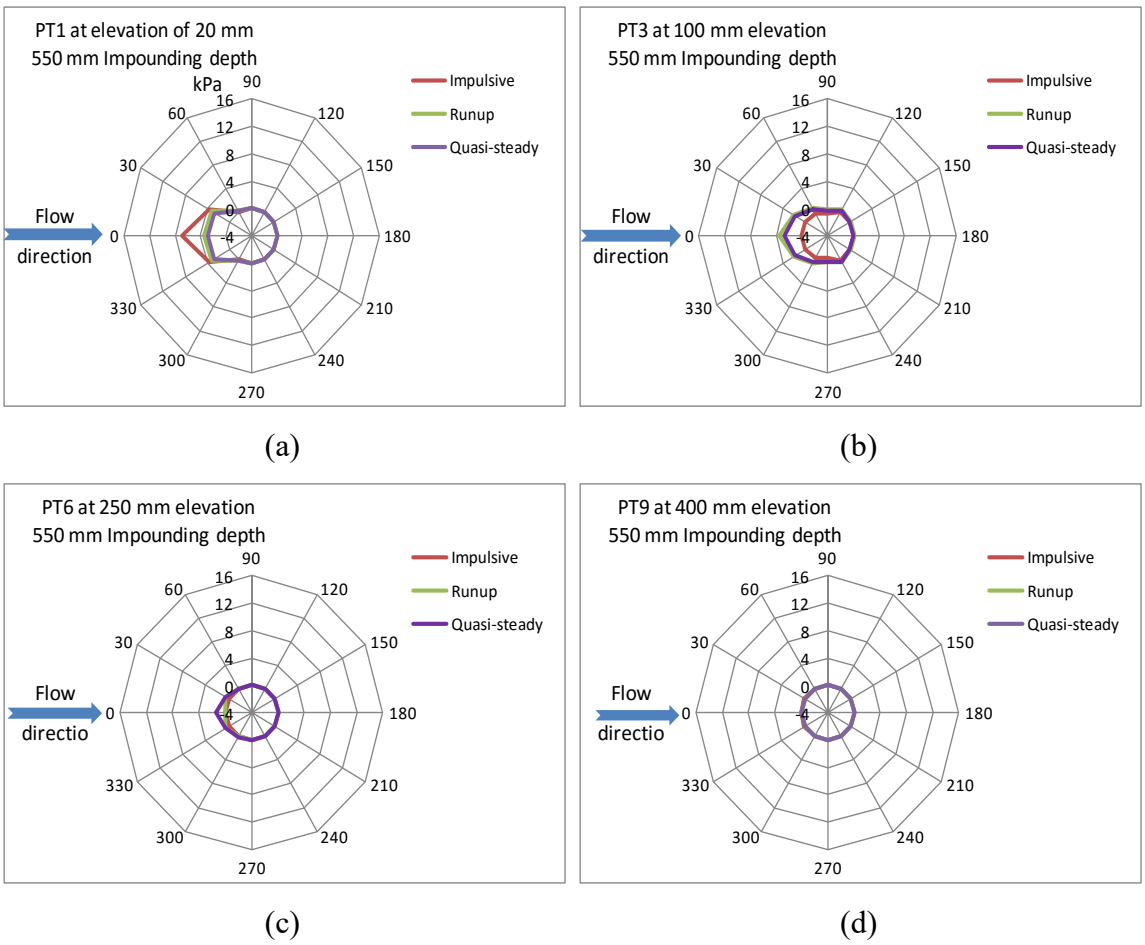

Figure 5.20 Pressure distribution around the circular model for three flow phases generated from 550 impounding water depth recorded at four elevations: **a)** 20 mm, **b)** 100 mm, **c)** 250 mm, and **d)** 400 mm

The experimental data illustrates that the pressures induced on the structural model are inversely proportional to the elevation of the pressure transducer from the flume bed. In this case, the maximum pressure was typically recorded by the lowest pressure transducer PT1. However, for a number of tests with the circular model - particularly when the impounding water depths were 850 mm or 1150 mm - the maximum pressure was recorded by PT2 or PT3. Based on hydrodynamics of flow around structures of different shapes, the difference is due to the cross-sectional shape of the structural models. The flat upstream surface of the square model is perpendicular to the flow direction and allows the build-up of water on the front face, leading to an increase in pressure. The circular model, with its curved surface,

results in smoother flow redirected on both of its sides, thereby reducing pressures on its surface compared to the square model.

The pressure-time history is also influenced by the initial flume bed condition: dry or wet. For identically-generated bores (similar impoundment water depth), when the flume bed was initially dry, a spike in pressure was recorded by the lower pressure sensors, while this was not observed for the wet flume bed. The influence of the bed condition (wet or dry) will be discussed in detail in Section 5.3.3.

5.3.2 Bore-Induced Forces and Moments

A series of tests were performed with different impounding water depths to investigate the bore-induced base shear forces and overturning moments on the two structural models. The models were installed 4.92 m downstream of the swinging gate. The hydraulic-induced forces and moments imposed on the two structural models in the direction and transverse to the flow were recorded using a 6 DOF dynamometer. The base shear force- and overturning moment-time histories induced on the two structural models by the three impounding water levels are discussed in the following sections.

5.3.2.1 Square model

Typical time history of the forces in longitudinal direction is characterized by four distinct segments (Figure 5.21). The first represents the impulsive force that arises from the impact of the leading edge of the bore. This is the shortest segment (0.05 s to 0.12 s) in the force-time history recording. Subsequently, the bore depth increases and water begins to build-up on the upstream face of the model due to flow obstruction, resulting in the second force segment. This force has previously been referred to as the run-up force or the transient hydrodynamic force. For most tests, this phase lasted for approximately 2 s to 3 s. This segment was marked by significant oscillations due to the high flow turbulence, and during this stage, the maximum force was also recorded. As the bore was redirected around the lateral sides of the model, a decrease in the force was observed in the time-history. This descending branch represents the third segment, which lasted between 3 s and 8 s. The final segment corresponds to the quasi-steady state flow phase and is described as the near-constant force response, known as the quasi-steady hydrodynamic force. The duration of this

segment varied relative to the maximum impounding water depth – longer duration for higher impoundment depths. The force-time histories shown in Figure 5.22 (a) correspond to the base shear forces in the longitudinal direction (in flow direction) induced on the square model. The forces were recorded for three impounding water depths: 550 mm, 850 mm, and 1150 mm, all for wet-bed conditions. Figure 5.22 (b) displays the base overturning moment arising from the longitudinal force imposed on the square model for the three impounding water depths.

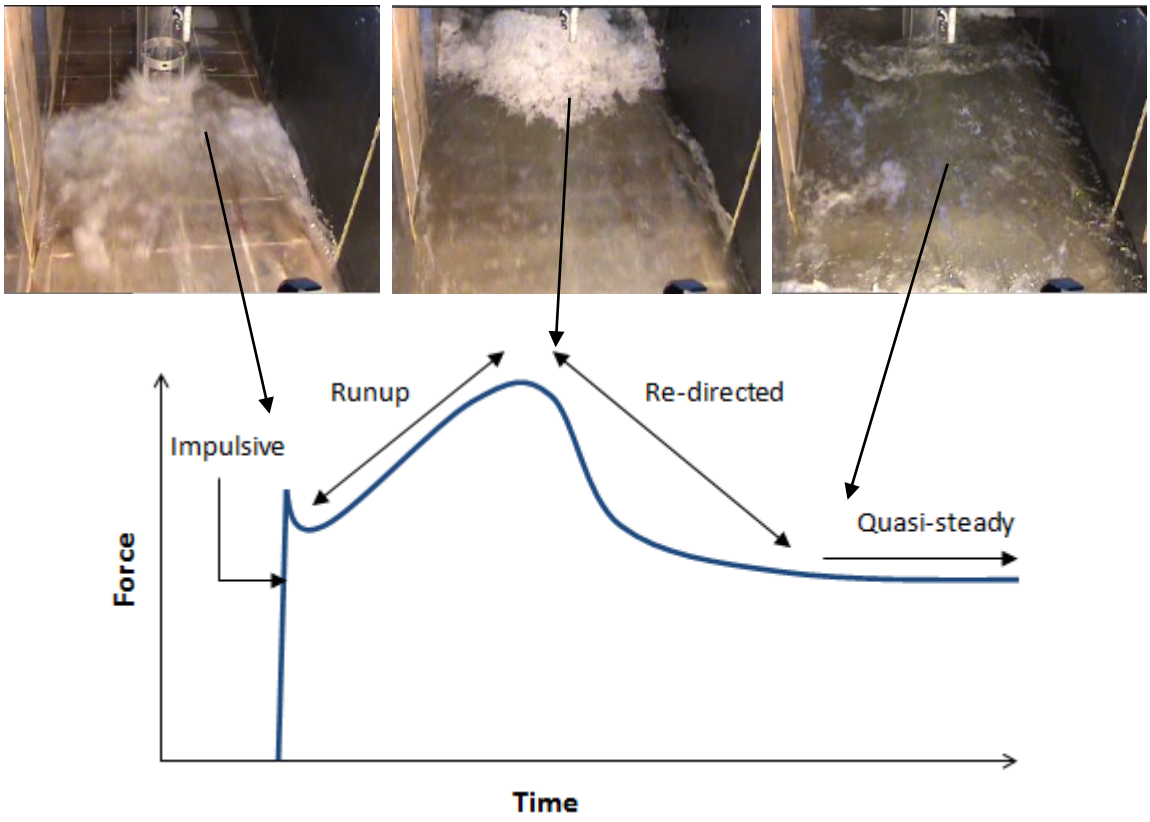

Figure 5.21 Typical Schematic of the components of the longitudinal force-time history (wet-bed condition) induced on the models

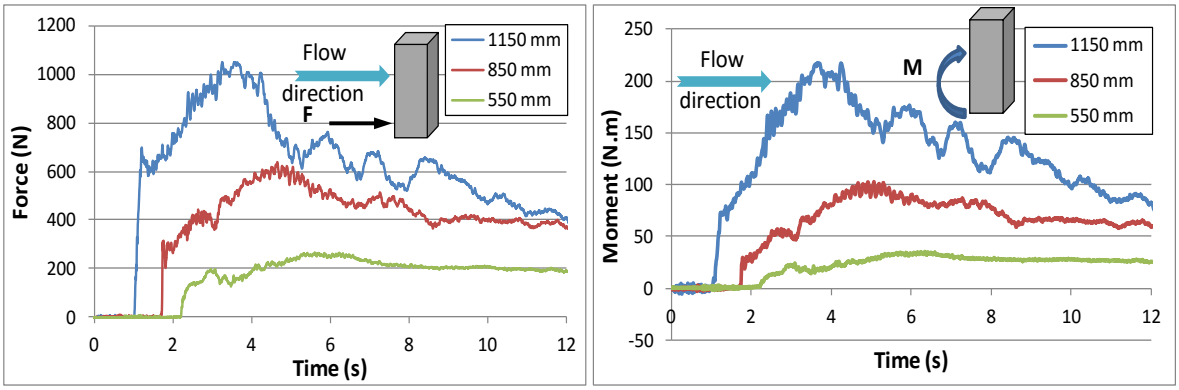

(a) (b)

Figure 5.22 Longitudinal base force- and overturning moment-time histories induced on the square model: **a)** longitudinal base force; and **b)** overturning moment

The transverse base force- and overturning moment-time histories induced on the square model for the three impoundment depths are presented in Figure 5.23.

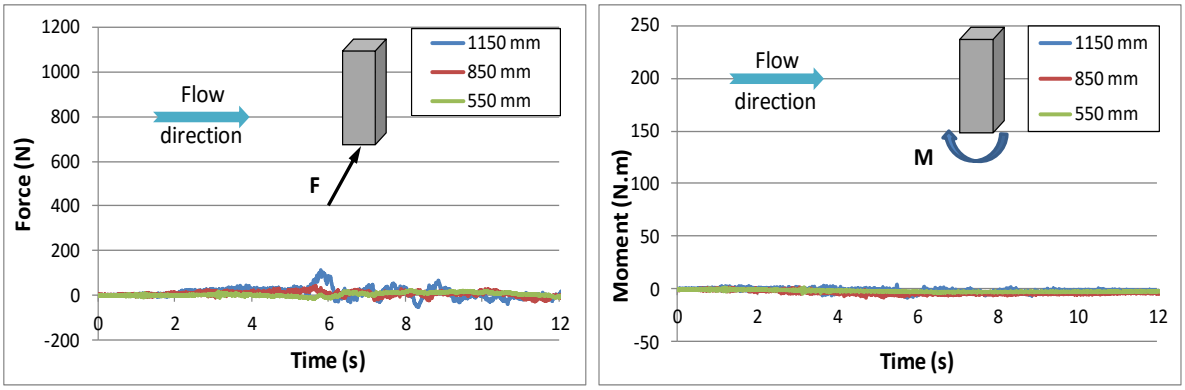

(a) (b)

Figure 5.23 Transverse base force- and overturning moment-time histories induced on the square model: **a)** transverse base force; and **b)** overturning moment

5.3.2.2 Forces on square model

The square model was rotated by 90˚ and 180˚ from the initial position in which the pressure transducers were facing the incoming flow. The longitudinal and transverse forces induced on the models were recorded and compared with those calculated by integrating the pressure field measured with the transducers on the upstream and side faces of the square model.

5.3.2.3 Circular model

The longitudinal forces induced on the circular model are shown in Figure 5.24 (a). The base shear force in the flow-direction generated from the three impounding depths demonstrated similar trends in the time histories, i.e., the same four force segments that were observed for the square model are also present in the time-history of the force exerted on the circular column. However, the magnitudes were lower in comparison with the corresponding forces recorded for the square model for similar impounding water depths. On the average, runup and impulsive forces induced on circular model were approximately 40 - 50% of those observed on square model (Figure 5.24 (a)).

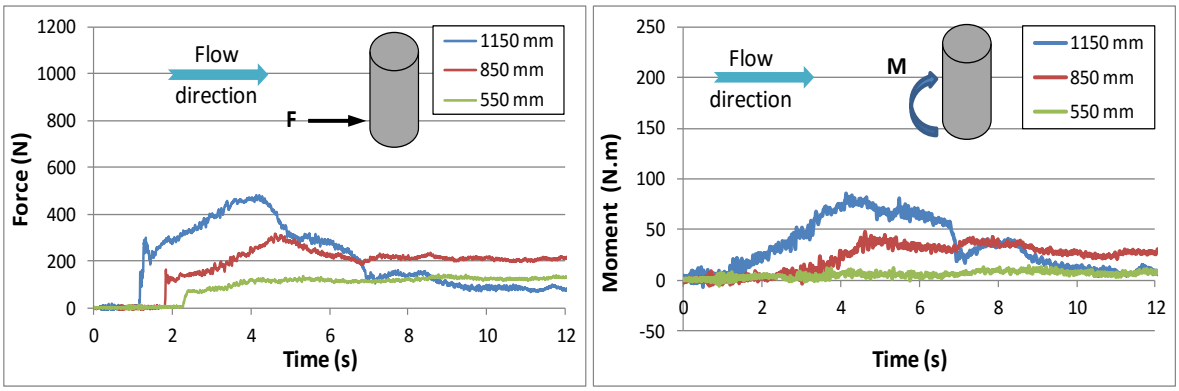

(a) (b)

Figure 5.24 Longitudinal base force- and overturning moment-time histories induced on the circular model: **a)** longitudinal base force; and **b)** overturning moment

However, unlike the force time-histories, the trends observed in the moment-time histories for the circular model (Figure 5.24 (a)) differ from those recoded for the square model (Figure 5.22 (a)). A notable difference is evident during the impulsive flow phase. Steep gradients were observed for the moments induced on the square model; whereas the circular model experienced a more gradual gradient up to the run-up phase. This difference is attributed to the curved surface of the circular model. Furthermore, the larger force magnitude recorded for the square structure over the same period of time accentuated the steeper gradient of the moments. This infers that for equivalent cross-sectional dimensions, the overturning demand of circular structures is lower than for square-shaped structures.

Figure 5.25 (a) illustrates that the transverse base shear force on the circular model was characterized by slightly higher forces than those recorded in the case of the square

model. This difference can be attributed to the vortex shedding which fluctuates periodically on the lateral and back sides of the circular column. For the circular model, the transverse force was approximately 25% of that induced in the flow direction; while for the square model, the transverse force did not exceed 5% of the force in the flow direction. In general, though, the transverse forces induced on the models are relatively small in comparison with the force in the flow direction. This suggests that the effect of the transversal flow circulation was minimal for this experimental program.

The time-histories of the overturning moment induced on the circular model by the transverse forces are shown in Figure 5.25 (b). The same fluctuation in the time histories of the transverse base shear force reflected in the moment-time histories. The maximum transverse moments are less than 25% of the corresponding maximum moments in the longitudinal direction for the same impoundment depth.

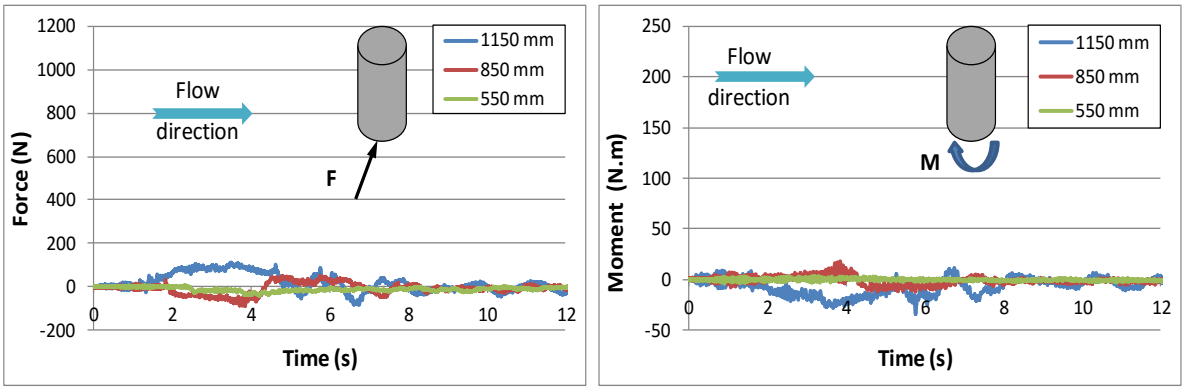

(a) (b)

Figure 5.25 Transverse base force- and overturning moment-time histories induced on the circular model: **a)** transverse base force; and **b)** overturning moment

5.3.2.4 Forces around circular model

The circular model was rotated to 180˚ in 30˚ intervals around its central vertical axis. The pressure transducers, therefore, were able to measure the pressures around the model (as explained in Section 5.3.1.4). The integration of the pressures over the tributary area of each sensor for each rotation angle and for the three impoundment depths was conducted to obtain the total force acting on the structure. The tributary area corresponding to each pressure transducer is bounded by two vertical lines and two horizontal arcs as shown in

Figure 5.26. The integration limits for the two vertical lines are set at angles of -15˚ to +15˚, while the zero reference is the line connecting the center of the model to the pressure transducers. The horizontal arcs are set at the mid distance between adjacent transducers.

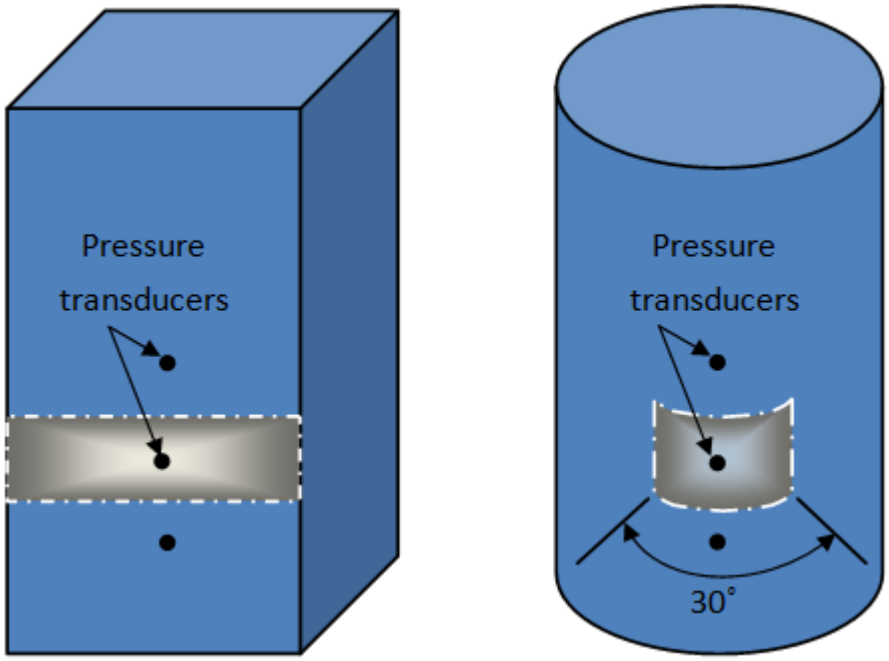

(a) (b)

Figure 5.26 Integration limits for the force calculation from the pressure measurements: **a)** square model; and **b)** circular model

The upper horizontal limit (arc) was always limited by the instantaneous bore depth recorded at the surface of the model by Water Gauge WG7. The summation of the calculated forces (pressure integration) at each rotation angle resulted in the total force induced on the model at that angle (angle measured between the flume centerline and the radial line passing through the pressure sensors). Figure 5.27 shows the force induced around the circular model impacted by hydraulic bore generated from the 550 mm impounding depth. The forces denoted as F-0, F-30 ... and F-180 correspond to the angles of 0˚, 30˚... and 180˚, respectively. The smallest magnitude in the component forces corresponds to the area at the 60˚ angle; while, as expected, the largest magnitude was recorded for the tributary areas corresponding to the 0˚ angle (directly facing the upstream direction).

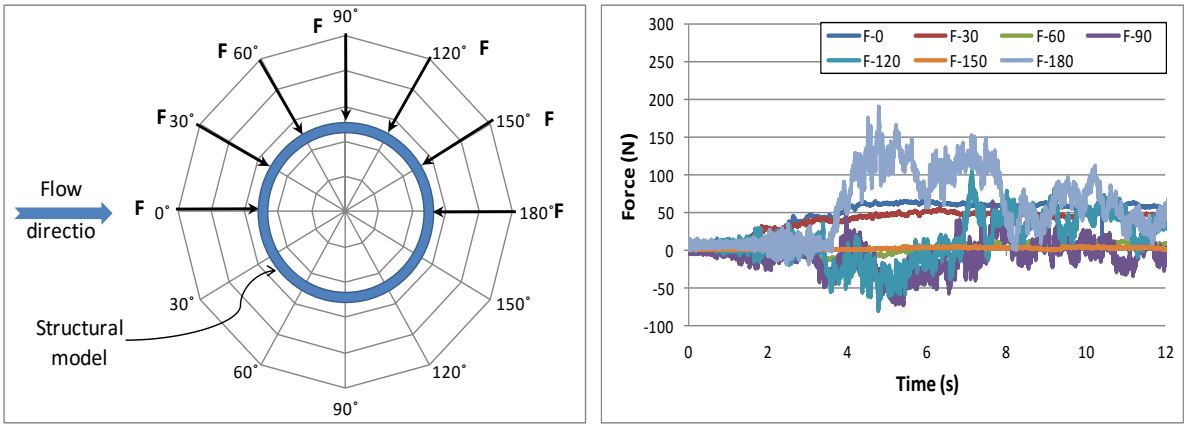

(a) (b)

Figure 5.27 Forces induced around the circular model: **a)** force designations and their influence points; and **b)** time histories of the integrated forces from recorded pressures

The forces induced around the circular model were divided into two components: longitudinal and transverse forces. Assuming flow symmetry, the longitudinal force components were calculated and summed and compared with the total base shear force as recorded by the 6-DOF dynamometer as shown in Figure 5.28.

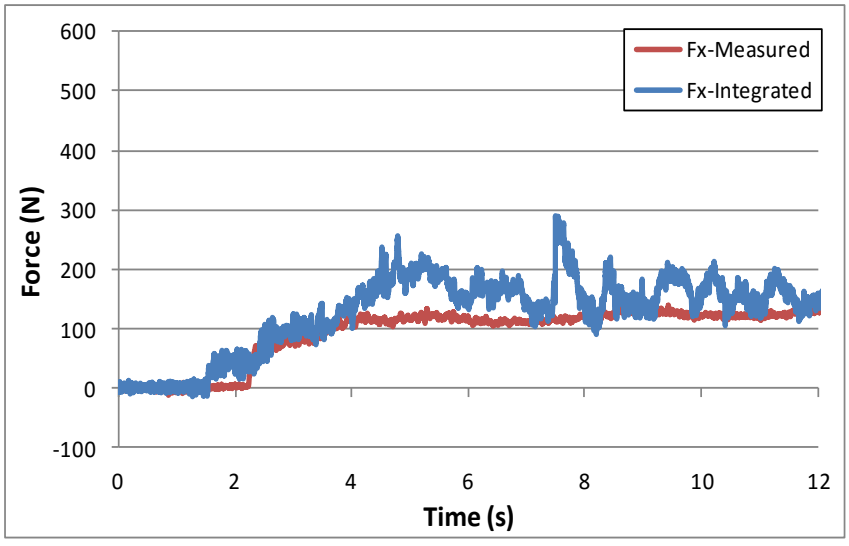

Figure 5.28 Time-histories of the total measured and integrated longitudinal base forces on the circular model

Using an identical approach, the summation of the transverse components was compared with the total transverse base shear force recorded by the dynamometer (Figure 5.29). Depending on the flow phase, both the integrated longitudinal and transverse forces were either in agreement or demonstrated some differences with the corresponding measured forces. These differences were expected due to the fact that flow on both sides of the model is not fully symmetric, particularly given the highly turbulent flow. The results of the integration could be improved by: (1) increasing the number of angular sectors over which the sensors are rotated, thus reducing the tributary areas and the associated approximation that the pressure is constant over the tributary area; and (2) instrumenting the entire surface of the model with pressure transducers.

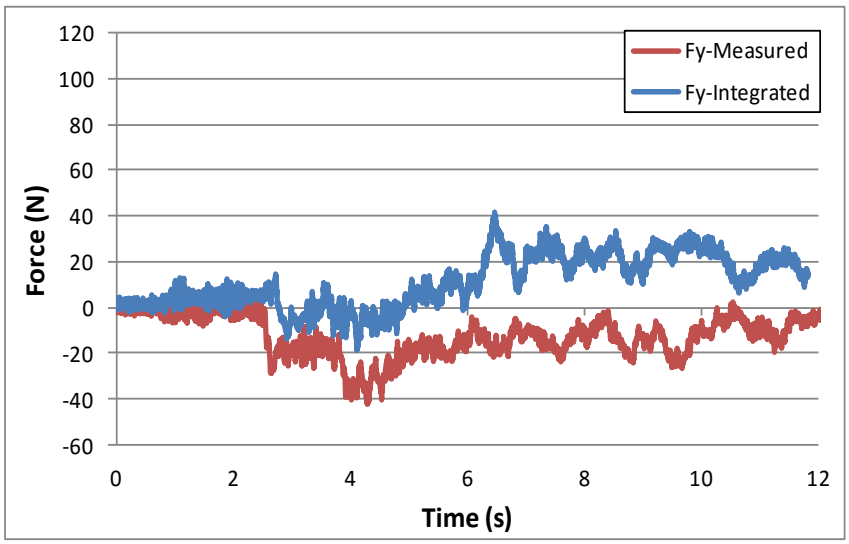

Figure 5.29 Time histories of the total measured and integrated transverse base forces on the circular model

5.3.2.5 Bore-induced moments on the models

The time series of the overturning moments experienced by the models from the hydraulic flow generated by the three impounding water depths are shown in Figure 5.22 (b) and 5.24 (b). As expected and shown in Figure 5.22 (b), the general pattern in the variation of the magnitude of moments induced on the square model is similar to those observed in the forces that generated the moments. However, the force-time history for the 1150 impounding depth reveals a temporary drop in force after the initial impact of the leading edge of the bore, whereas the magnitude of the moment shows a continuous increase. It is

probable that while the resultant force demonstrated a temporary drop in magnitude, the height of the resultant force relative to the base increased. This phenomenon would result in an increase in the base moment.

Although the overturning moment-time histories of the square model were similar to the force-time histories, the same was not observed for the circular model (Figure 5.24 (b)). The overturning moment increased gradually to a maximum which corresponded to the maximum run-up force. It is probable that the force spike is generated by the impact of a very thin bore front at the base of the column. Therefore, although the impact force is significant, the distance of the force with respect to the location of the dynamometer is very small; hence the absence of a significant spike in the moment at this particular instant. The transverse overturning moment in the circular model was also slightly different to that observed with the square model for the same impoundment depth (Figure 5.23 (b) and 5.25 (b)). The maximum transverse moment recorded for the circular model was 36 Nm for the 1150 mm impounding water depth, while for the square model it was negligible (fluctuated between 0 and 5 Nm). However, the magnitude was small compared to the magnitude of the longitudinal moment.

5.3.3 Effect of Initial Flume Bottom Condition

As previously stated tsunamis are a series of waves which, depending on the nearshore bathymetry, can either advance in the form of a surge or break off-shore and propagate inland in the form of turbulent hydraulic bores. Reconnaissance visits to tsunami impacted regions in the Tohoku region (St-Germain et al., 2014) revealed that structures that had a pond between them and the incoming waves suffered marginal damage. This is in contrast with nearby structures in the same region without a shielding pond to the incoming bore. This motivated the author of this study to investigate the effects of the flume bed condition on the forces induced on the two structural models.

For the current experimental set-up, although rubber water stoppers were used around the frame of the swinging gate, leakage of water was evident across the gate. Therefore, the first run of the daily testing were considered dry although, for some tests, small areas of water pools were present along the side walls of the flume. Thus, experiments were performed with a virtually dry bed condition (Figures 5.30 (a) and (c)). However,

subsequent to the first run, due to the difficulty in completely drying the downstream section of the test channel between runs, most experiments were performed with wet bed condition as a thin water layer. For these tests, a film of water of a few millimetres remained on the flume bed from previous tests as shown in Figures 5.30 (b) and (d). Consequently, the dry condition was typically associated with the first test in the day and/or when a sufficient time between runs allowed for the flume bed to dry. The effect of the initial flume bed condition was investigated for these two conditions (dry and wet). The following sections discuss the influence of these two bed conditions on the bore depth-, bore pressure-, and force-time histories.

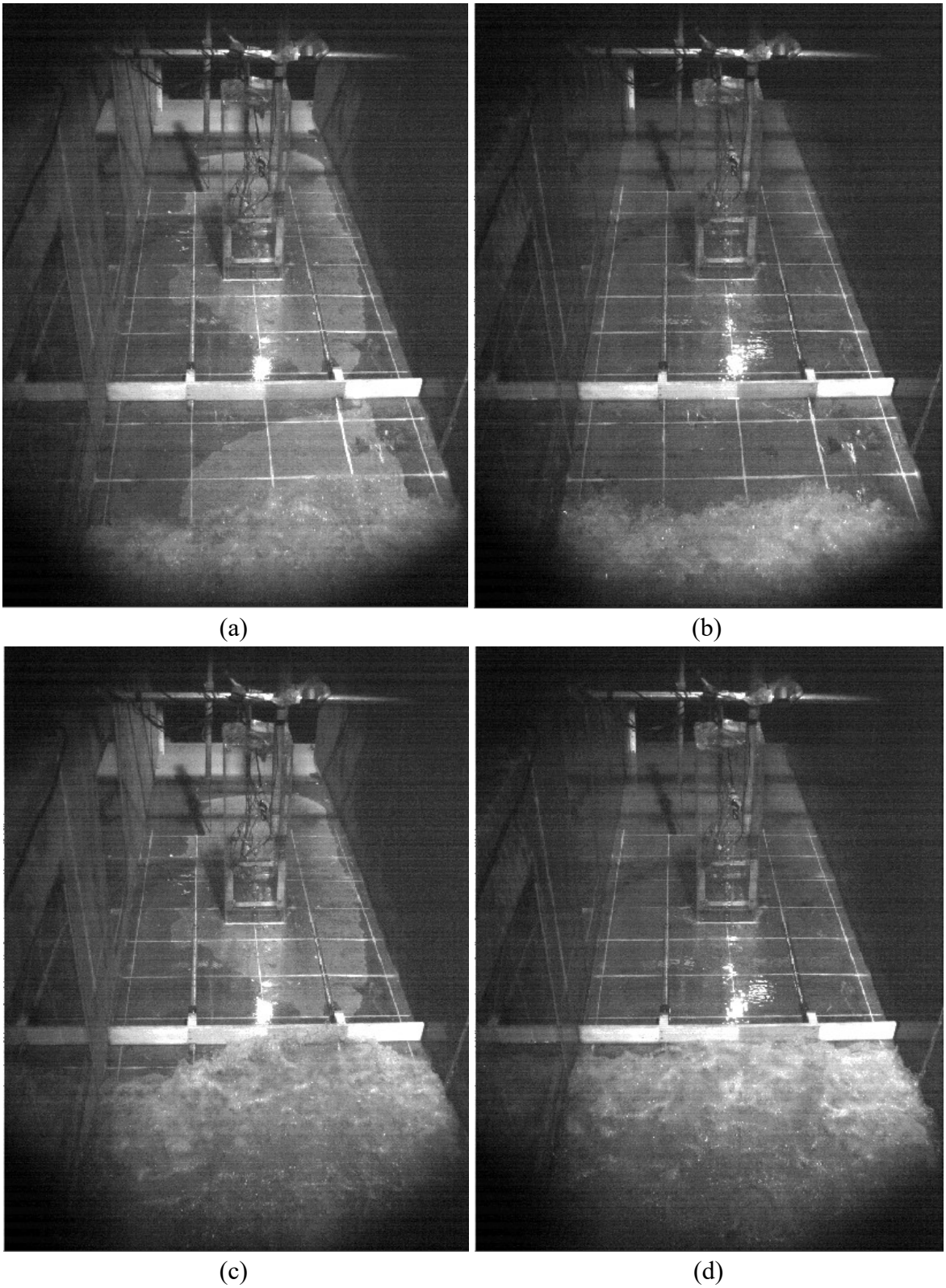

Figure 5.30 Photographs of bore-front generated from 550 mm impounding depth propagating over quasi-dry bed ((**a**) and (**c**)) and wet bed ((**b**) and (**d**))

5.3.3.1 Bore depth-time history

Figure 5.31 shows the bore depth-time histories generated from the 550 mm impounding water depth. These series were recorded by Water Level Gauge WG9 which was attached to the square model at midpoint on the upstream face (Figure 4.6). Figure 5.31 reveals that the bore surface in dry-bed condition has a slightly steeper slope during the run-up phase (between 5.3 and 8.8 seconds). The maximum inundation depth recorded in both cases were similar, however the maximum magnitude was recorded later in the case of the dry bed. The effect of the flume bed condition on the bore depth-time histories manifests itself only prior to attaining the maximum inundation depth. The maximum run-up depth was recorded immediately after the leading edge of the bore impacted the model (about 0.25 s) for the wet-bed condition, while the maximum inundation was observed after approximately 2.5 s for the dry-bed condition. The bore depth-time histories are similar for both conditions after the maximum inundation depth was attained for both conditions.

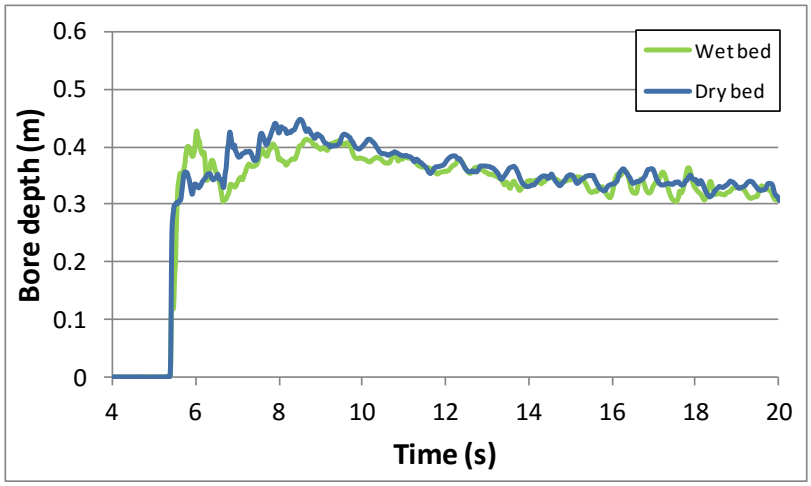

Figure 5.31 Bore depth-time histories generated from the 550 mm impounding water depth

5.3.3.2 Bore-induced pressure

The pressure-time histories recorded on the upstream face of the square structural model were recorded for the two initial flume bed conditions: dry and wet. Figure 5.32 shows the pressures for a bore generated by the 550 mm impounding water depth. The bore front reached the square model at 3.184 s, with the origin of the time axis set at the opening of the gate. The maximum water level recorded by WG9 was 0.45 m and occurred at 7.5 s.

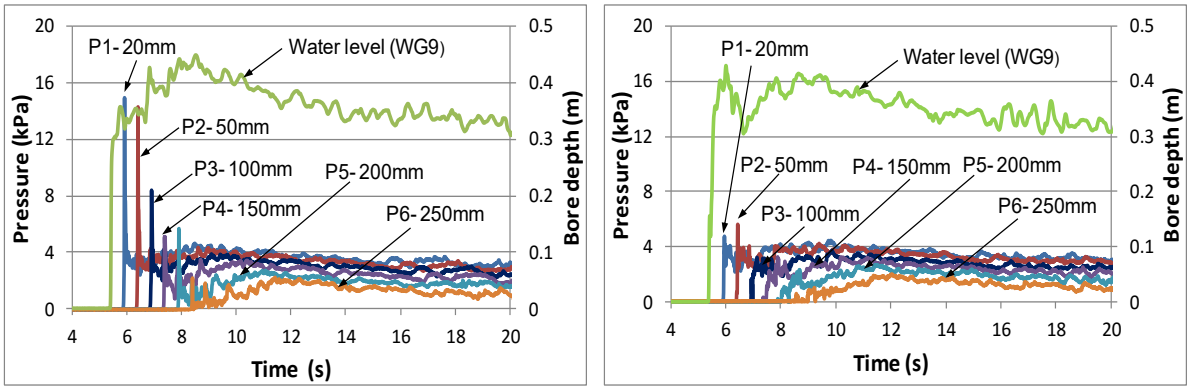

Figure 5.32 Pressure-time histories induced on square model by 550 mm impounding water depths: **a)** dry-bed condition; and **b)** wet-bed condition

The pressure-time histories shown in Figure 5.32 show a distinctive peak at initial impact of the bore front and the structural model for the dry-bed condition. Beyond the initial impulsive pressures observed for all impoundment depths, the pressure-time histories for the dry- and wet-bed conditions are similar. Árnason et al. (2009) obtained similar results for the wet-bed condition; however his testing program were only conducted on dry-bed conditions. Beyond the initial impulsive pressures, the pressure-time histories have large fluctuations whose amplitudes increase with the impoundment depth. These fluctuations are the result of strong turbulence and air entrainment in this region, after the initial impact of the bore front and before the run-up flow state, which led to the formation of the wake downstream from the model.

Hattori et al. (1994) conducted an experimental investigation on the impact of waves breaking directly on vertical walls. The study highlighted that the larger the amount of air entrained in the impinging wave, the lower the magnitude and compression time of the impulsive pressures. Peregrine (2003) also studied the impact of breaking waves on vertical walls and observed that the entrained air provided cushioning effect on the impulsive pressures. Thus, the absence of the initial impulsive spikes in the pressure-time histories for the wet-bed condition is attributed to the following: for the wet-bed condition, the small film of water (few millimeters in depth) on the flume bed provides resistance to propagation of the bore. This resistance to flow and the resulting decrease in the bore-front velocity have been reported by Jánosi et al. (2004) and Leal et al. (2006). Furthermore, it is probable that,

as the bore advanced downstream, additional turbulence is generated through the transfer of momentum from the advancing bore-front to the downstream still-water layer. Consequently, this would generate higher concentration of entrained air in the bore-front that, in turn, inhibits impulsive pressures at initial impact. This is supported by the still images of the tests captured with a high-speed video camera (Figure 5.30).This suggested increase in the concentration of entrained air within the bore-front is evident for the wet-bed conditions.

5.3.3.3 Bore-induced force

Figure 5.33 presents the force-time histories for two tests conducted with the square model and impacted with hydraulic bore generated by the 550 mm impounding water depth. The tests were conducted using the same configuration and testing conditions of the previous ones, with the exception of the flume bed condition. The maximum recorded force under dry-bed conditions was the impulsive force, *Fi*, of 404 N at 4.395 s. During these tests, the maximum pressure was recorded by the pressure transducer located at 20 mm above the flume bed (PT1) of 14.95 kPa. The rise times for the impulsive force and pressure were 0.03 s and 0.015 s, respectively.

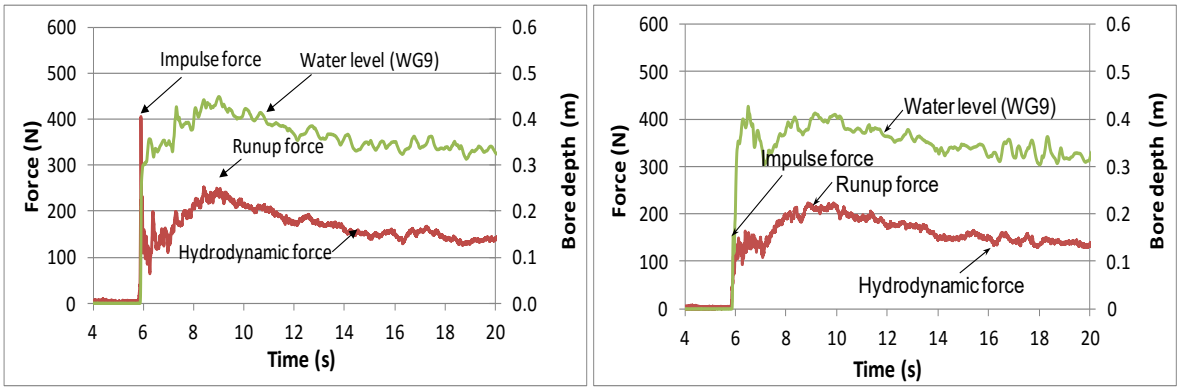

Figure 5.33 Time histories of bore depth and base shear force on the square model by bore due to the 550 mm impounding water depth: **a)** dry-bed condition; and **b)** wet-bed condition

The impulsive pressure for the dry-bed condition was much higher than that recorded for the wet-bed condition. As a result, the time history of the force induced on the model for

the dry-bed condition showed a distinctive impulsive force. Furthermore, Figure 5.33 shows that the impulsive force for the dry-bed condition was recorded 0.080s earlier than that recorded for the wet-bed condition. This difference in time is most likely due to the water film on the flume bed, which increased the resistance to downstream flow propagation and hence slowed the advancement of the bore front.

5.4 Performance of Mitigation Walls

Mitigation walls with different configurations were installed upstream from the two structural models. The forces, moments, pressures, and lateral displacements experienced by the models in the presence of the mitigation walls were captured. The effects of the wall configurations on the measured responses are discussed in the following sections. The tests were named as follows: MM-IMPD-WALTYP-WLOC-RTAG-###, where these symbols refer to:

- MM is the structural model type: SQ for square model and CR for the circular model
- IMPD is the water impoundment depth: 55, 85, and 115 for the 550, 850, and 1150 mm depths, respectively. The zero was removed to shorten the file name
- WALTYPE is the wall type as follows:
    - 10W45 is a 100 mm hig flat wall with 45˚ inclination angle
    - 10W90 is a 100 mm high flat vertical wall with 90˚ inclination angle
    - 10WAR is a 100 mm high wave return wall
    - 15W45 is a 150 mm high flat wall with 45˚ inclination angle
    - 15W90 is a 150 mm high flat vertical wall with 90˚ inclination angle
    - 15ARW is a 150 mm high curved vertical wall
- WLOC is the location of the wall: 1D and 3D for 305 and 915 mm upstream from the structural model location
- RTAG is the rotation angle of the structural model about its vertical axis: 0, 90, and 180 for the square model, and 0˚, 30˚, 60˚, 90˚, 120˚, 150˚, and 180˚ for the circular model
- ### is a three-digit number generated by the data acquisition system which represents the repetition sequence of the test

For example, the acronym *CR-55WH-10W90-1D-0R-001* refers to the test with the circular model impacted with hydraulic bore generated by the 550 mm impoundment water depth, with the 100 mm high vertical mitigation wall installed at 1D upstream from the structural model; the model is placed at the zero rotation angle (pressure transducers are facing upstream), and this is the first test in this series.

5.4.1 Influence of wall location

Two positions for the mitigation walls with respect to the location of the structural models were investigated: 305 mm and 915 mm upstream from the models, designated as 1D and 3D, respectively, where D represents the cross-sectional dimension of the model (side length of the square model or diameter of the circular model). Figure 5.34 shows the time histories of the base shear forces and overturning moments experienced by the square model due to the bore resulting from the 550 mm impounding water depth for three test configurations: without mitigation wall, and 150 mm high curved wall placed at 1D and at 3D, respectively.

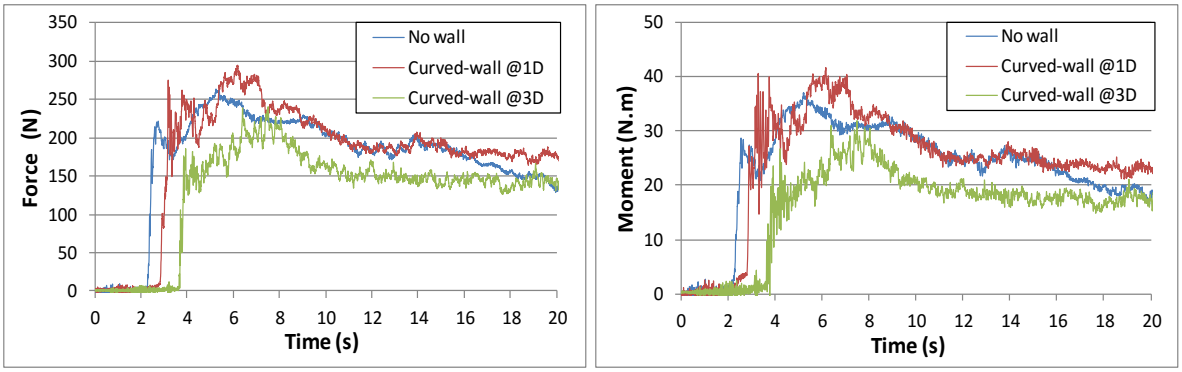

(a) (b)

Figure 5.34 Time histories of the square model subjected to a bore generated by the 550 mm impounding water depth with 150 mm-high curved wall installed at 1D and 3D: **a)** base shear force; and **b)** base overturning moment

As shown in Figure 5.34, the curved mitigation wall placed at 3D reduced the magnitude of both the base shear force and overturning moment in the direction of the flow; while the same wall placed at 1D upstream from the model resulted in a slight increase in both the force and the moment. The reduction in the force and the overturning moment for the former were 20% relative to the test without the mitigation wall. To investigate the consistency of this protective effect, due to the presence of mitigation walls, in the form of a

reduction in the force and overturning moment, several mitigation walls with different cross-sectional shapes were further investigated. A set of tests for the circular model were executed with the 45˚ inclined plane mitigation wall of 100 mm height (denoted as 10W45 rather than 100W45 to shortening the data file name). Similarly, the mitigation wall was placed at 1D and 3D upstream from the circular model. Figure 5.35 provides the results from the 1150 mm impounding water depth including for the case where no mitigation wall was installed, which serves as the reference case.

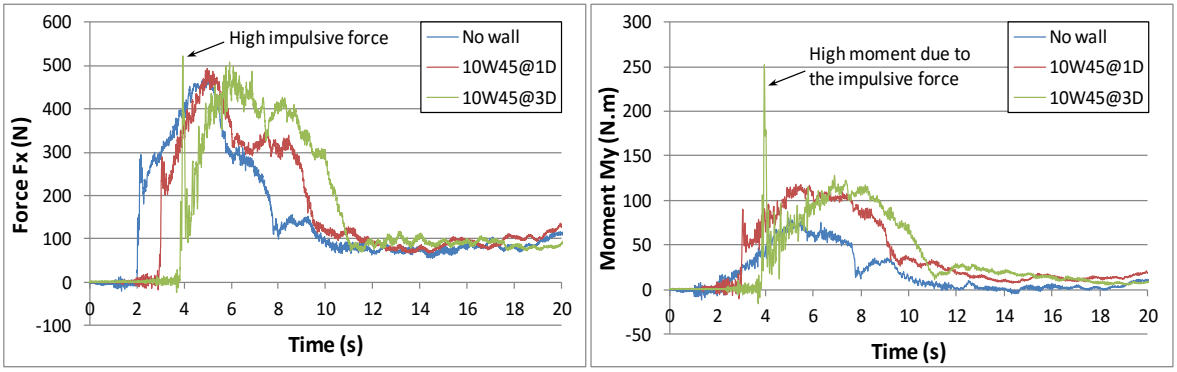

(a) (b)

Figure 5.35 Time histories of the circular model subjected to a bore generated by the 1150 mm impounding water depth with 100 mm-high, 45˚ inclined plane wall installed at 1D and 3D: **a)** base shear force; and **b)** base overturning moment

Mitigation walls located at a distance of 3D upstream of the structure resulted in larger impulsive forces and base overturning moments than the same wall positioned at 1D. Observations noted during testing showed that the bore front impacted the structural wall at a higher elevation as a result of the flow being redirected at an angle due to the wall inclination and distance to the mitigation wall. These results are contradictory to those with the curved wall due to the difference in cross-sectional shape. In the case when the curved wall was deployed, the bore front bounced upstream after the first impact with the mitigation wall. Hence, this reflected flow decreased the speed of on the subsequent flow, causing at the same time a reduction in the impulsive forces imposed on the structural model. This highlights that proper physical modelling of tsunami mitigation strategies are critical prior to implementing any measures.

Figure 5.36 illustrates the effect of the 100 mm-height vertical wall installed upstream from the circular model on the forces and moments induced by the hydraulic bore generated from the 850 mm impounding water depth. The presence of the vertical wall at 1D slightly decreased the maximum force but increased the overturning moment. The latter was the result of the mitigation wall redirecting the flow at a higher elevation on the model, effectively increasing the arm of the force more significantly than the decrease in the force magnitude. It is also evident that the duration of the run-up force was longer than the case without the mitigation wall. Contrary to this, the same wall at 3D increased the base shear force, but reduced the overturning moment.

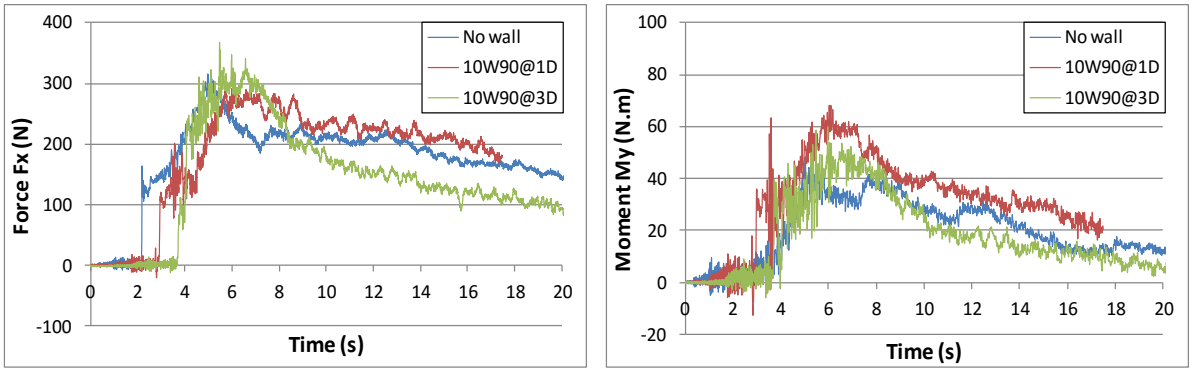

(a) (b)

Figure 5.36 Time histories of the circular model subjected to a bore generated by the 850 mm impounding water depth with 100 mm-high, vertical plane wall installed at 1D and 3D: **a)** base shear force; and **b)** base overturning moment

To explain this phenomenon, Figure 5.37 provides still frames from high-speed video recordings of two tests for the circular model impacted with hydraulic bore generated from 550 mm impounding water depth. These tests were conducted under similar testing conditions and configurations with the exception of the mitigation wall which was installed at a distance of 1D in one test and at 3D in the other. The frames in Figure 5.37 (a), (c), (e), and (g) relate to the test with the mitigation wall located at 1D; while the frames in Figure 5.37 (b), (d), (f), and (h) relate to the test with the mitigation wall located at 3D. The mitigation wall located at 3D is not shown in the photos given that it lies upstream from the side windows of the flume. For the mitigation wall at 3D, the large distance between the wall and the structural model allows the bore front to plunge to the flume bed and impact the

model near its base. Conversely, for the mitigation wall located at 1D, the bore front impacts the model prior to it having the space to plunge to the flume bed. Furthermore, the mitigation wall located at 3D results in a delay in time for the flow to reach the structural model. In addition, the presence of the mitigation wall increased the flow turbulence. Consequently, the entrained air increases in the flow, which contributes to a reduction in the force induced on the structural model.

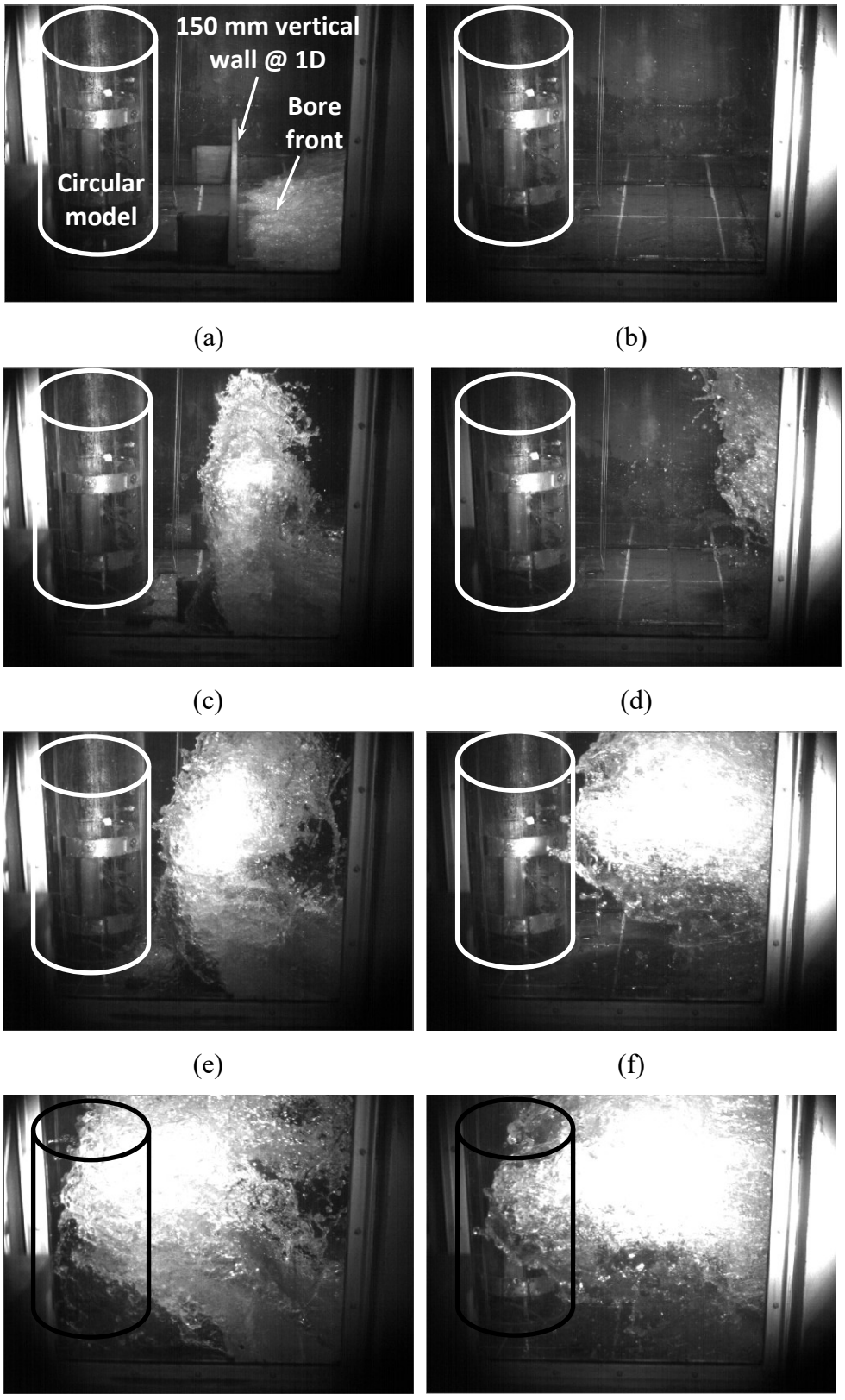
150 mm vertical wall @ 1D
Bore front
Circular model
(a)
(b)
(c)
(d)
(e)
(f)
(g)
(h)

Figure 5.37 Still frames from high-speed video recordings for the bore generated from the 550 mm impounding water depth for the circular model with 150 mm vertical mitigation wall installed upstream: **a), c), e),** and **g)** at 1D; and **b), d), f),** and **h)** at 3D

Figure 5.38 shows still frames of two tests conducted with the square model impacted with hydraulic model generated from 1150 mm impounding water depth. Figures 5.38 (a) and (c) depict the mitigation wall at 1D, while Figures 5.38 (b) and (d) correspond for the wall located at 3D. Although Figure 5.38 (d) illustrates that the bore front impacts the model at higher elevation than that in Figure 5.38 (c), observations from testing noted that the large distance between the mitigation wall located at 3D and the model resulted in "splash" of the water. The majority of the bore, with the mitigation wall located at 3D, impacted the model near its base.

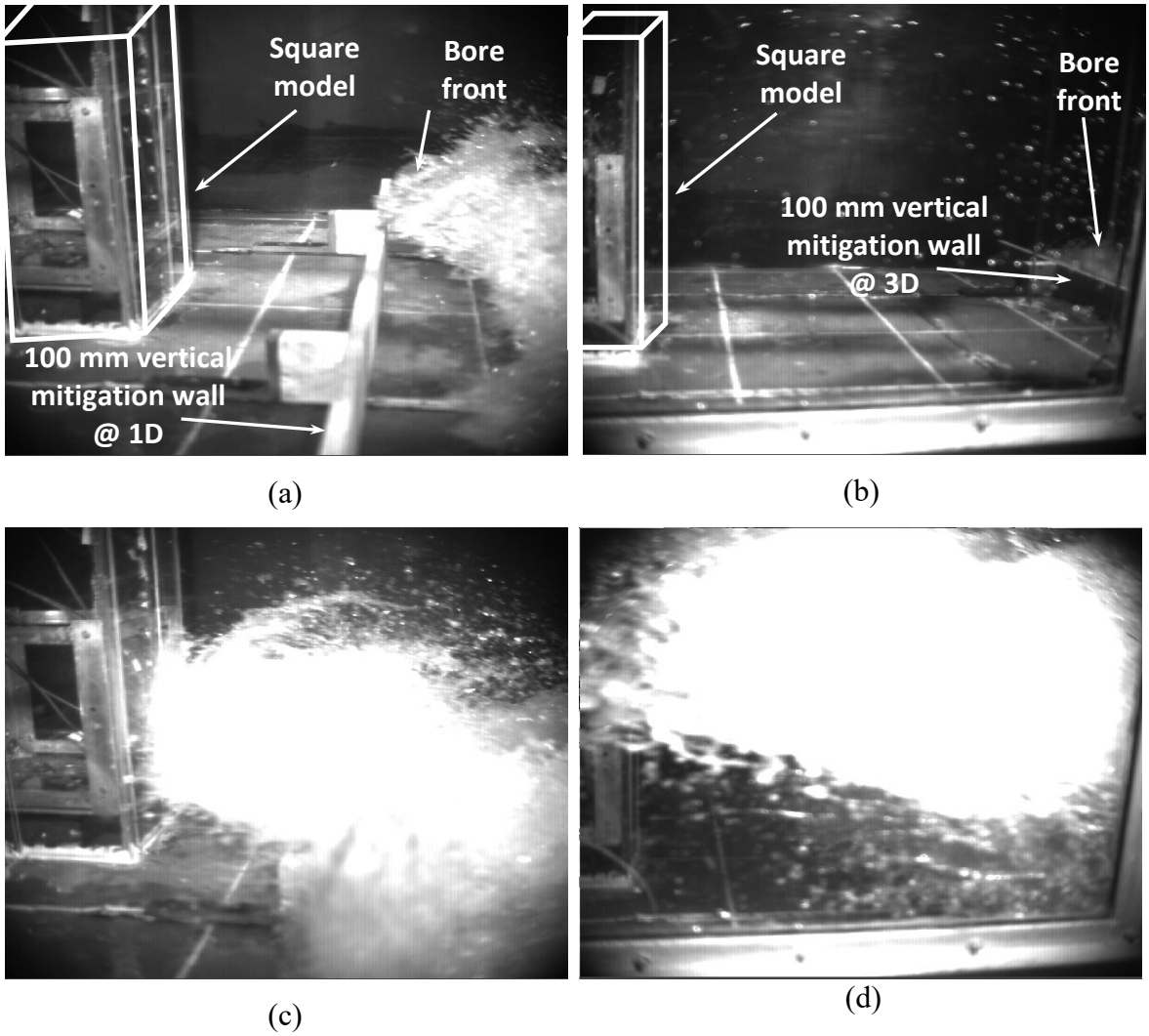

Figure 5.38 Still frames from high-speed video recordings for the bore generated from the 1150 mm impounding water depth for the square model with 100 mm vertical mitigation wall installed upstream: **a) ,** and **c)** at 1D; and **b),** and **d)** at 3D

Figure 5.39 displays still frames from the high-speed video recordings captured in two tests with the square model impacted with hydraulic bore generated from 850 mm impounding depth. The frames shown in Figure 5.39 (a), (c), and (e) are from the test without mitigation wall; while the frames in Figures 5.39 (b), (d), and (f) are from the test with the 100 mm vertical mitigation wall installed at 1D (305 mm) upstream from the structural model. A comparison between the two tests shows that the presence of the mitigation wall delayed the impact of the bore front with the structural model and that the vertical mitigation wall installed at 1D causes an increase in the height where the bore front impacts the model.

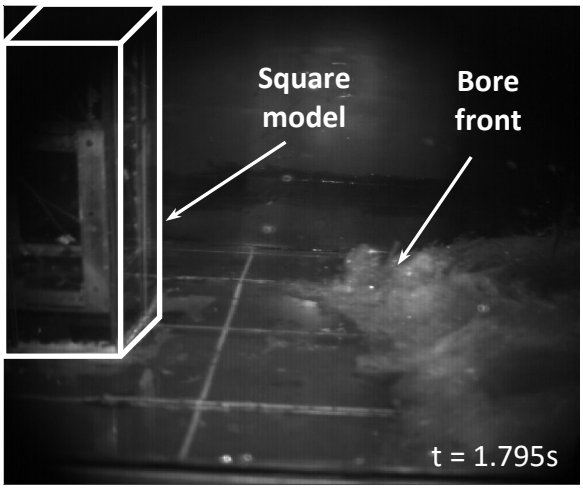
Square model
Bore front
t = 1.795s

(a)

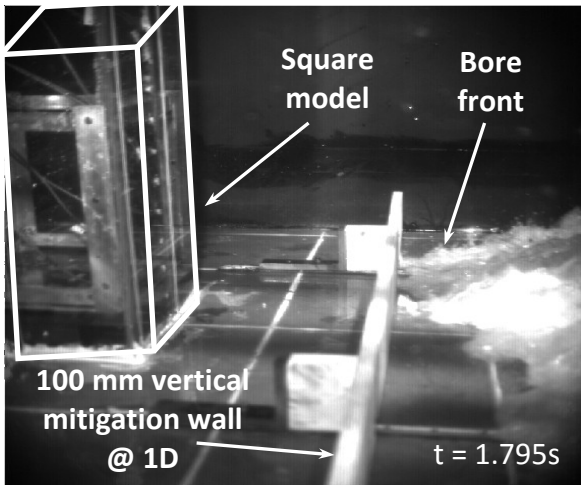
Square model
Bore front
100 mm vertical mitigation wall @ 1D
t = 1.795s

(b)


t = 1.920s

(c)

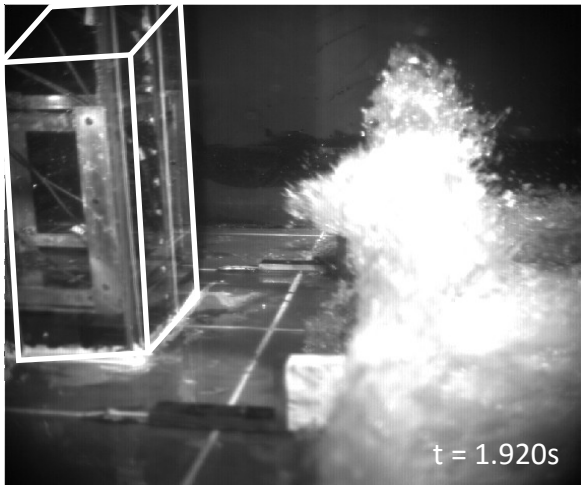
t = 1.920s

(d)

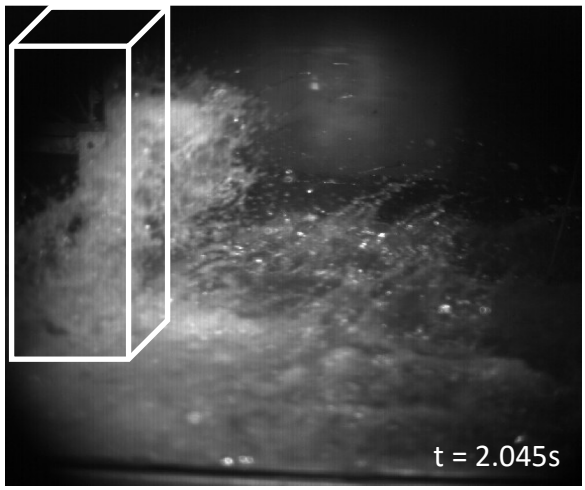
t = 2.045s

(e)

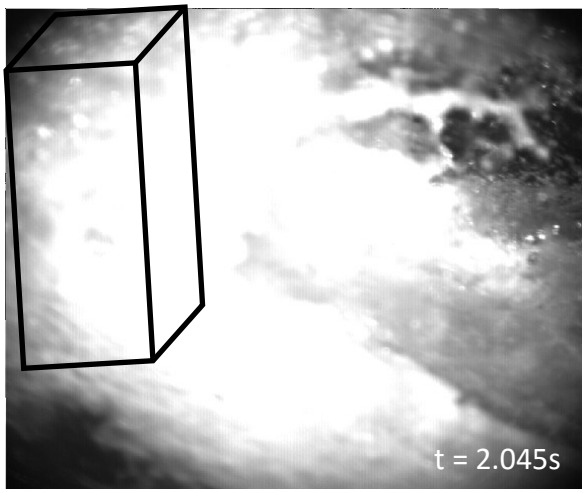
t = 2.045s

(f)

Figure 5.39 Still-frames from high-speed video recordings for the square model: **a), c),** and **e)** with no mitigation; and **b), d),** and **f)** with 100 mm mitigation wall installed at 1D upstream from the model

5.4.2 Influence of wall inclination angle

The effect of the inclination angle of the mitigation walls was examined by comparing the results obtained for the walls with angles of 45˚ and 90˚ degrees between the wall face and the flume bed. All other parameters (e.g. wall height, and cross section shape) remained constant, while the mitigation walls were placed at 1D and 3D from the structural models. Figure 5.40 illustrates that the vertical mitigation walls were effective at reducing the peak base shear force, with the wall at 1D being most effective.

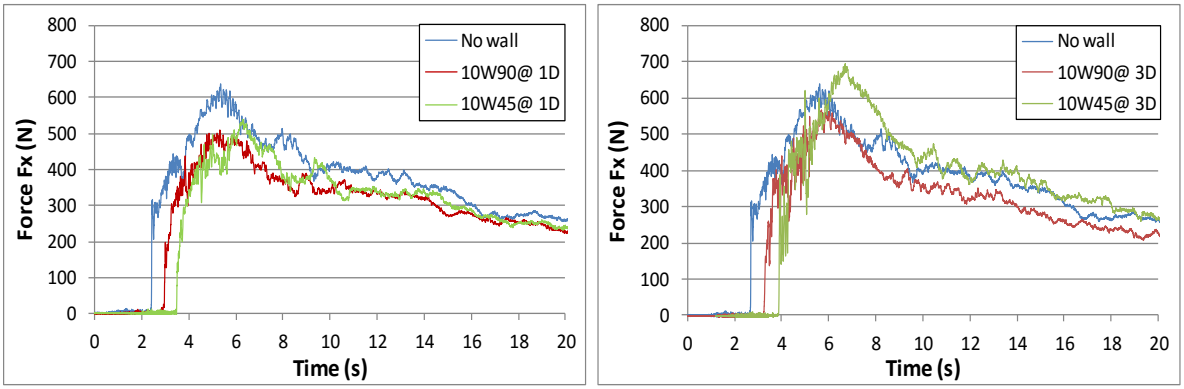

(a) (b)

Figure 5.40 Time histories of the base shear force induced on the square model by a bore generated by the 850 mm impounding water depth for cases with and without 100 mm mitigation wall vertical or 45˚-inclined installed at: **a)** 1D; and **b)** 3D

The tests with the 45˚-inclined mitigation wall exhibited two contrasting effects. The 100 mm high wall with 45˚-inclination at 1D decreased the base shear force relative to the test without the mitigation wall. However, the same mitigation wall placed at 3D resulted in an increase in the peak recorded force. Additionally, the overturning moment was significantly larger (Figure 5.41). The location of the mitigation wall had an effect on the impulsive and run-up forces; however, the effect on the hydrodynamic forces was less pronounced.

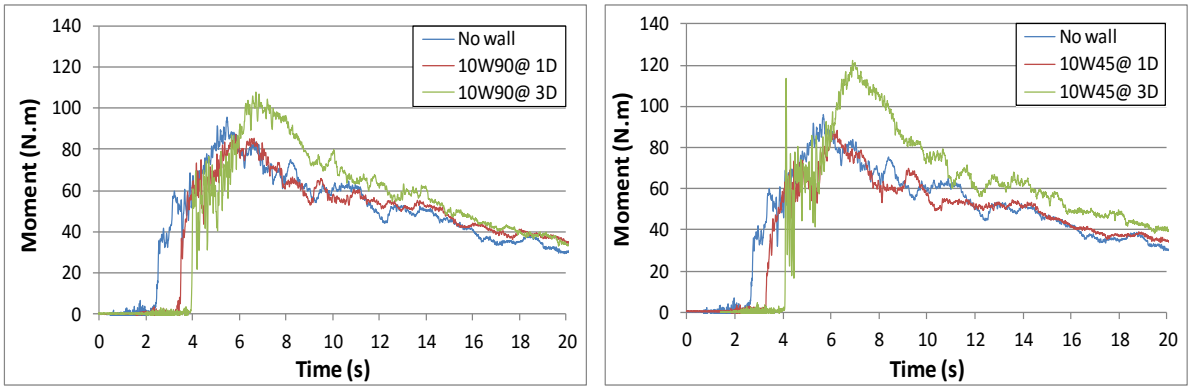

(a) (b)

Figure 5.41 Time histories of the base overturning moment induced on the square model by a bore generated by the 850 mm impounding water depth for cases with and without 100 mm wall at 1D and 3D: **a)** vertical wall; and **b)** 45˚-inclined wall

Figure 5.42 provides still frames taken from high speed video recordings (with a sampling rate of 400 fps) for the test with the hydraulic bore generated from the 550 mm impoundment depth impacting the circular model. The 100 mm-high vertical wall was installed at 1D. Note that t = 0 s corresponds to the opening of the swinging gate. The frames show the bore front approaching the wall and then redirecting upwards after impacting with the wall. The flow turbulence and redirection increased the entrained air, which is evident by the "white" reflection in the frames. As the flow continues rising, the bore front formed an arc-shape prior to impacting the structural model.

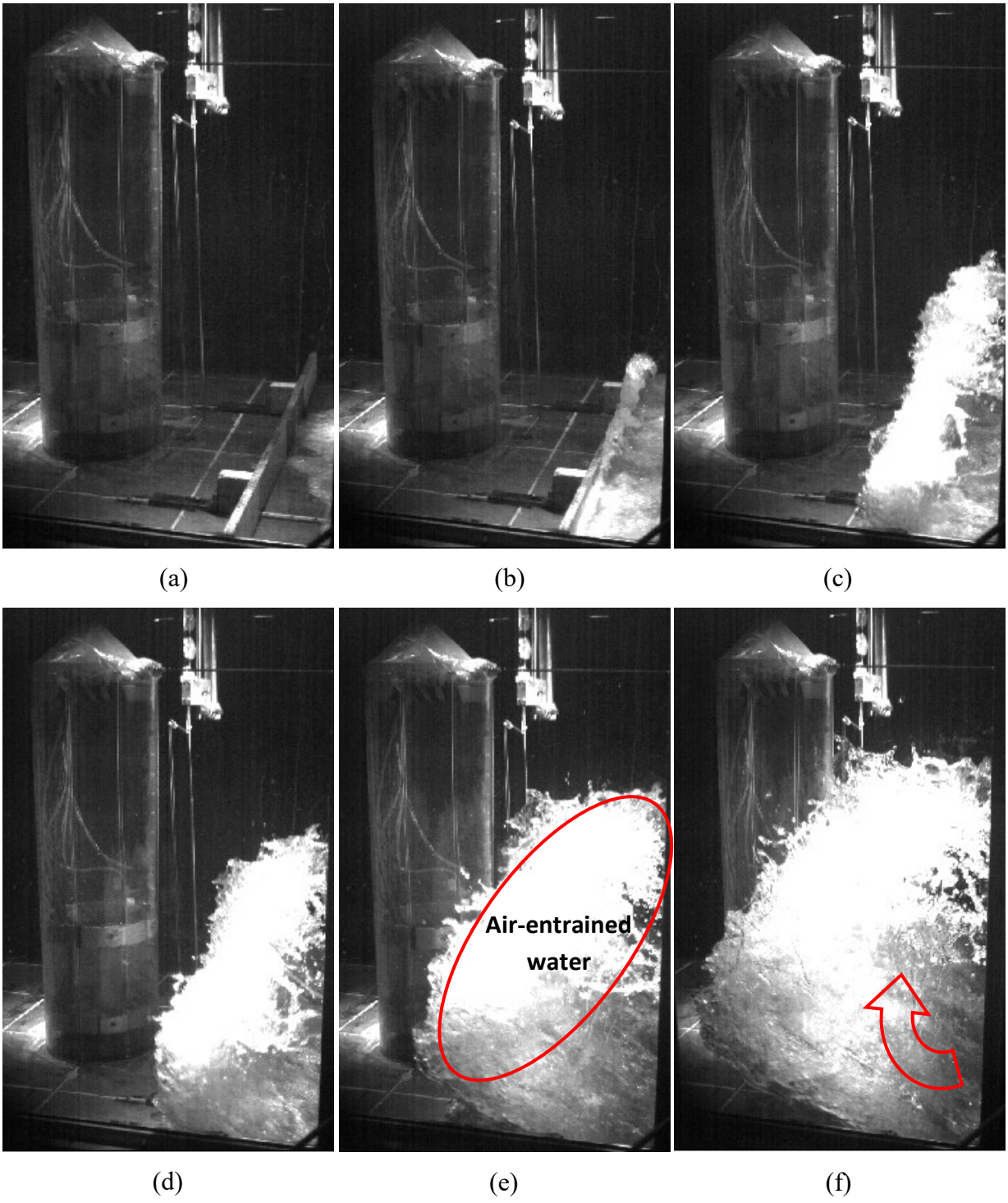

Figure 5.42 Still frames from high speed video recordings captured for the circular model impacted by hydraulic bore generated from the 550 impoundment depth with 100 mm vertical mitigation wall installed at 1D (CR-55WH-10W90-1D-0R): **a)** t= 1.902 s; **b)** t = 1.982 s; **c)** t = 2.082 s; **d)** t = 2.120 s; **e)** t = 2.190 s; and **f)** t = 2.253 s

Figure 5.43 presents still frames for the test conducted with similar conditions to Figure those presented in Figure 5.42, but with the 45˚-inclined mitigation wall. The frames show that the wall inclination modified the flow path as it approaches the structural model. In this test, the bore front reached the model 0.1s earlier than the test with the vertical mitigation wall. The photographs in Figure 5.42 also illustrate less flow turbulence and entrained air in comparison to the bore impacting the vertical wall. The impact elevation of the bore front at the upstream face of the model was of approximately 400 mm with the inclined mitigation wall and approximately 700 mm with the vertical wall.

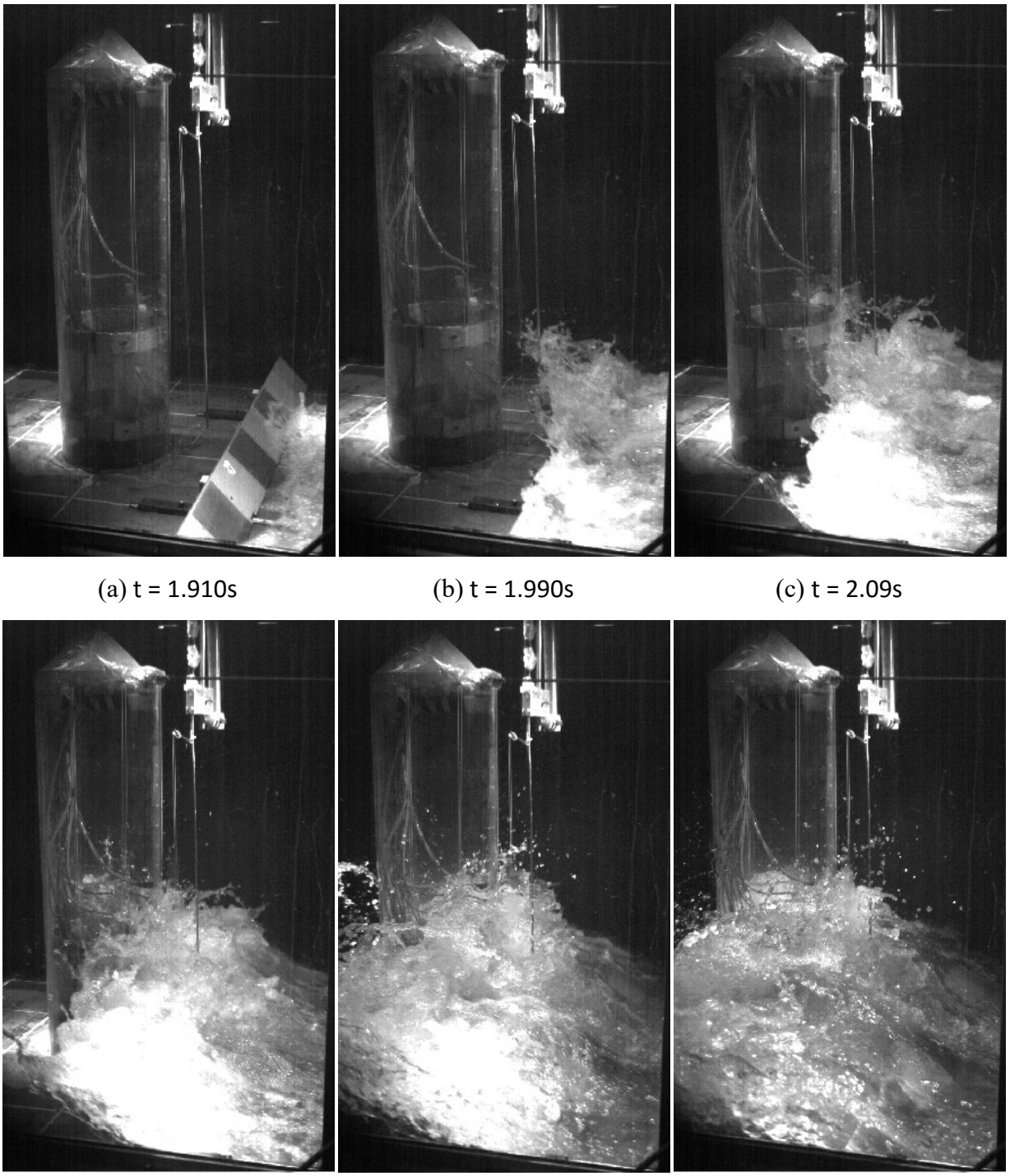

(a) t = 1.910s (b) t = 1.990s (c) t = 2.09s

(e) t = 2.128s (f) t = 2.233s (g) t = 2.358s

Figure 5.43 Still frames from high speed video recordings captured for the circular model impacted by hydraulic bore generated from the 550 impoundment depth with 100 mm 45˚-inclined mitigation wall installed at 1D (CR-55WH-10W45-1D-0R-002): **a)** t= 1.910 s; **b)** t = 1.990 s; **c)** t = 2.090 s; **d)** t = 2.128 s; **e)** t = 2.233 s; and **f)** t = 2.358 s

5.4.3 Influence of wall height

To investigate the effect of the height of the mitigation wall on the base shear force experienced by the structural models, two wall heights (100 and 150 mm) with eight different configurations related to the wall location (1D and 3D) and the vertical inclination angles (45˚ and 90˚) were tested. Figures 5.44 and 5.45 illustrate the base shear forces recorded from those eight tests, in addition to the test results with no mitigation wall (reference case). Figure 5.44 (a) reveals that the presence of the vertical wall at 1D decreases the impulsive and run-up forces on the model. The force-time histories for the vertical mitigation walls at 3D illustrates an increase in the impulsive force for 10W90-3D and an increase in the run-up force for 15W90-3D; while the responses are similar to that without mitigation wall beyond the run-up force. Figure 5.44 (b) illustrates the influence of a vertical mitigation wall at 3D upstream from the structural model on the force induced on the model. The force-time history recorded with the low vertical mitigation wall (100 mm height 10W90-3D) differs from the typical force-time history recorded in the rest of the mitigation wall tests. A significant impulsive force was recorded at first impact of the bore with the structural model. This was followed by a sudden drop with significant fluctuations in the magnitude of the force prior to the build-up of the bore in front of the structural model leading to the run-up force. Lab observations illustrated that the bore-front impacted the mitigation wall causing a vertical redirection of the bore prior to impacting the structural model. Thereafter a high turbulent flow was generated in the region downstream from the mitigation wall and upstream from the structural model causing notable fluctuations in the force induced on the model. The fluctuations in the force subsided when the flow depth in this region exceeded the height of the mitigation wall.

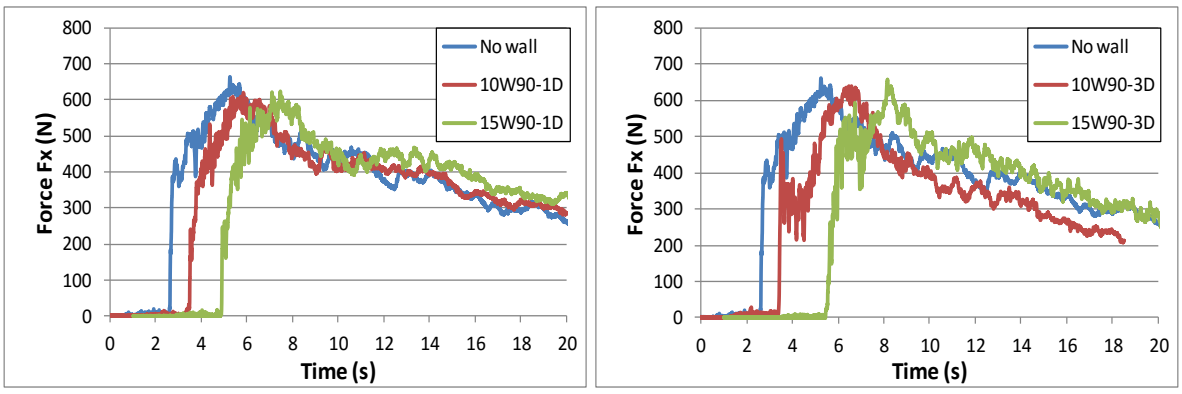

Figure 5.44 Influence of vertical mitigation wall height on the time histories of the base shear force induced on circular model impacted by hydraulic bore generated from 1150 mm impounding depth: **a)** wall placed at 1D; and **b)** wall placed at 3D

Figure 5.45 (a) provides the base shear force-time histories experienced by the model with the 45˚ inclined mitigation wall placed at 1D upstream from the model in addition to the reference case. The response reveals that the mitigation walls reduced the impulsive force in comparison with the case where no mitigation wall was used. Furthermore, there was only a marginal difference between the effects of the height of the wall on the force-time histories. The peak run-up forces recorded during the presence of the mitigation walls were similar in magnitude and only slightly less than that of the reference case. However, the duration of the run-up force recorded with the 150 mm height mitigation wall (15W45) was greater than that for 100 mm height mitigation wall (10W45).

Figure 5.45 (b) demonstrates the influence of 45˚ inclined mitigation walls installed at 3D upstream from the model along with the reference case. The mitigation walls reduced the impulsive force in comparison with the reference case and introduced significant fluctuations in the force during the rise to the peak force (run-up force). An abrupt spike is evident in the force-time history in the region after the impulsive force and prior to the run-up force for 10W45-3D. Laboratory observations showed that this spike was generated due to the highly turbulent flow caused by the presence of the wall as illustrated in Figures 5.42 (e) and (f).

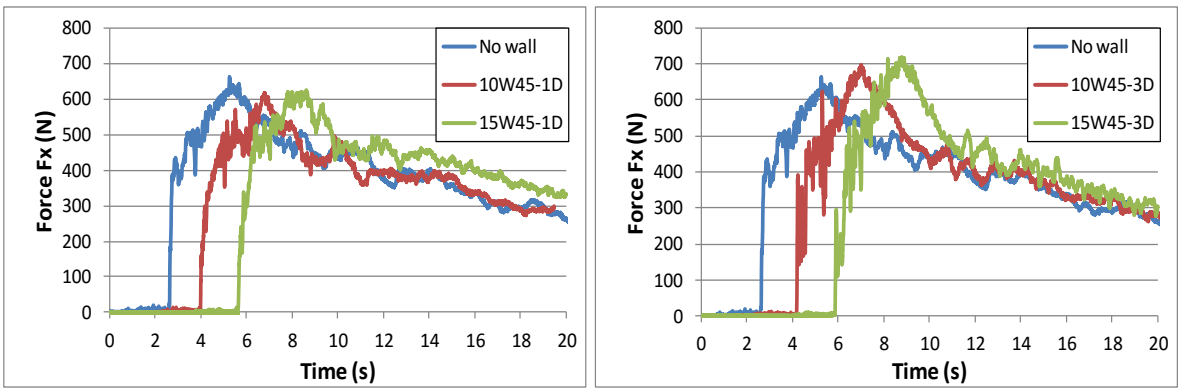

Figure 5.45 Influence of 45˚-inclined mitigation wall height on the base shear force-time histories induced on the circular model impacted by hydraulic bore generated from 1150 mm impounding depth: **a)** wall placed at 1D; and **b)** wall placed at 3D

Sixty tests (all tests were repeated twice to verify repeatability) were conducted with the circular model impacted by the hydraulic bore. Each test was setup with a specific configuration with respect to the height, inclination angle, shape and location of the mitigation. Figure 5.46 shows the variation of the relative maximum pressure recorded ($p_{max}/\rho.g.h_{imax}$) for each test with respect to the relative maximum inundation depth (z/h_{imax}). The acronym 10WAR90 refers to the wave return mitigation wall which was 100 mm in height. p_{max} is the maximum pressure recorded during each test, ρ is the water density, g is the gravitational acceleration, and h_{imax} is the maximum inundation depth at the location of the model, which was measured in the absence of the model. Note that the measured pressure did not peak at all sensors simultaneously, and the maximum bore-induced force was recorded between the initial bore impact and maximum runup. The horizontal line in Figure 5.46 corresponds to the ratio of wall heights to the maximum inundation depth (h_{imax} = 250 mm in this case and corresponds to the 550 mm impounding depth). For some tests (10W90-1D and 15W90-1D), the presence of the mitigation wall results in maximum pressures greater than for the test without the wall, typically recorded at levels higher than the height of the mitigation wall. Figure 5.46 (a) reveals that Test 10W90-3D recorded on the most of the pressure transducers maximum pressures which were less than those recorded when the mitigation wall was not installed

Although the wall heights used in the tests shown in Figure 5.46 (a) and (b) differ, the maximum pressure recorded at each elevation were similar. The pressure transducers located below the upper level of the wall crest recorded lower pressures than those recorded for the test without the mitigation wall. Conversely, the pressure transducers installed above the level of the crest of the mitigation wall recorded larger pressures. The tests with vertical mitigation walls installed at 3D were an exception; most of the pressure transducers recorded pressures that were less than those recorded in the case where no wall was present.

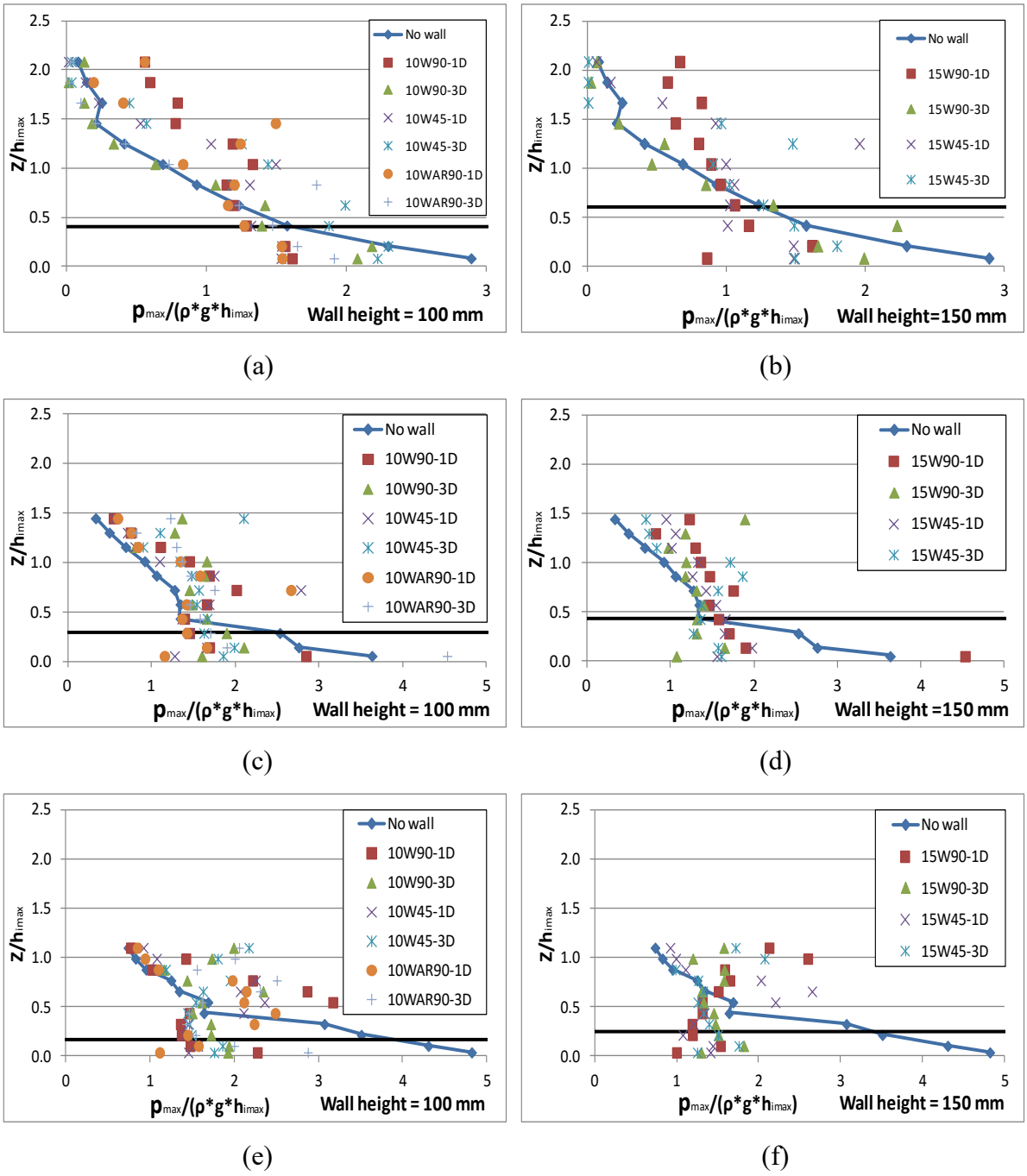

Figure 5.46 Non-dimensional relation between (p_{max}) and (z) for pair of wall height (mm) – impounding water depth (mm): **a)** 100 – 550; **b)** 150 – 550; **c)** 100 - 850; **d)** 150 – 850; **e)** 100 – 1150; and **f)** 150 – 1150

5.4.4 Influence of wall cross-sectional shape

Three different cross-sectional mitigation walls were used in this study to investigate their effect on the forces, moments, pressure distribution, and displacements experienced by the

circular model. A vertical flat wall, a curved wall, and a wave return wall with a height of 100 mm were installed at 1D and 3D upstream from the structural model and tested with bores generated from the three impounding water levels (550, 850, and 1150 mm). Figure 5.47 shows the force-time histories induced on the circular model by the 550 mm impounding water depth. The force-time histories in the flow direction in the presence of the vertical and curved mitigation walls show slight differences in the impulsive force. When the mitigation walls were placed at 1D, the impulsive force was 178 N for the flat vertical wall test (maximum force for this test), while it was 137 N for the curved wall test. The run-up forces were similar; 162 N and 165 N, respectively, as shown in Figure 5.47 (a). The wave return mitigation wall was more effective in reducing the force exerted on the model; the recorded impulsive force was 78 N and the run-up force was 122 N.

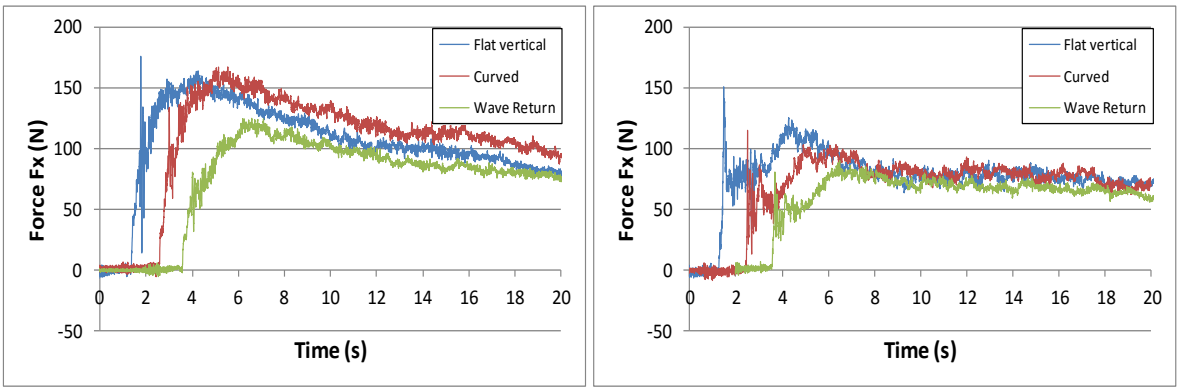

(a) (b)

Figure 5.47 Influence of mitigation wall cross-sectional shape on the time history of the base shear force induced on the circular model: **a)** wall placed at 1D; and **b)** wall placed at 3D

Although the general trend of the force-time histories are similar for the three mitigation walls placed at 3D (Figure 5.47 (b)), the magnitude of the impulsive and run-up forces were notably different. For the bore generated by the 550 mm impounding water height, the measured impulsive forces were 150 N, 119 N, and 78 N and the run-up forces were 126 N, 102 N, and 84 N for the flat vertical, curved, and wave return walls, respectively. The overturning moment about the transverse axis is characterized by high oscillations between positive and negative immediately following the leading edge of the bore front impacted the model (Figure 5.48).

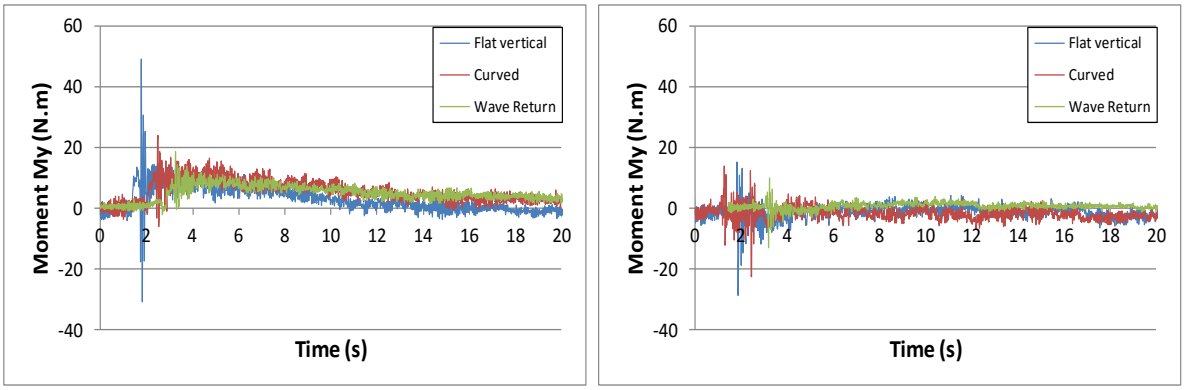

(a) (b)

Figure 5.48 Influence of mitigation wall cross-sectional shape on the time histories of the moment induced on the circular model: **a)** wall placed at 1D; and **b)** wall placed at 3D

The oscillations are larger in amplitude for the test with the flat vertical wall than the two other walls due to the high impulsive force experienced by the structural model (Figure 5.48 (a)). The tests with the mitigation walls placed at 1D induced higher overturning moments than the companion tests with the walls at 3D. Experimental observations demonstrated that for the wall at 1D, the bore front impacted the structural model at higher elevations than the tests without the mitigation wall. The distance from the mitigation walls at 3D and the structural model was 915 mm, which was significantly farther upstream than the 1D location (305 mm). Therefore, due to the effects of gravity, the leading edge of the bore front had sufficient distance to plunge to a lower elevation prior to impacting the structural model.

To demonstrate the influence of the mitigation wall cross-section on the bore flow (specifically on the bore front), Figures 5.49 and 5.50 provide still frames from high-speed video recordings captured for two tests with the circular model impacted by a hydraulic bore generated from the 550 mm impounding water depth. The only difference between the two tests is the geometry of the cross-section of the vertical mitigation wall. Figure 5.49 illustrates test observations with the 100 mm-height wave return wall, while Figure 5.50 illustrates observations with the 100 mm-height flat vertical wall. Both walls were placed at 1D upstream from the circular model.

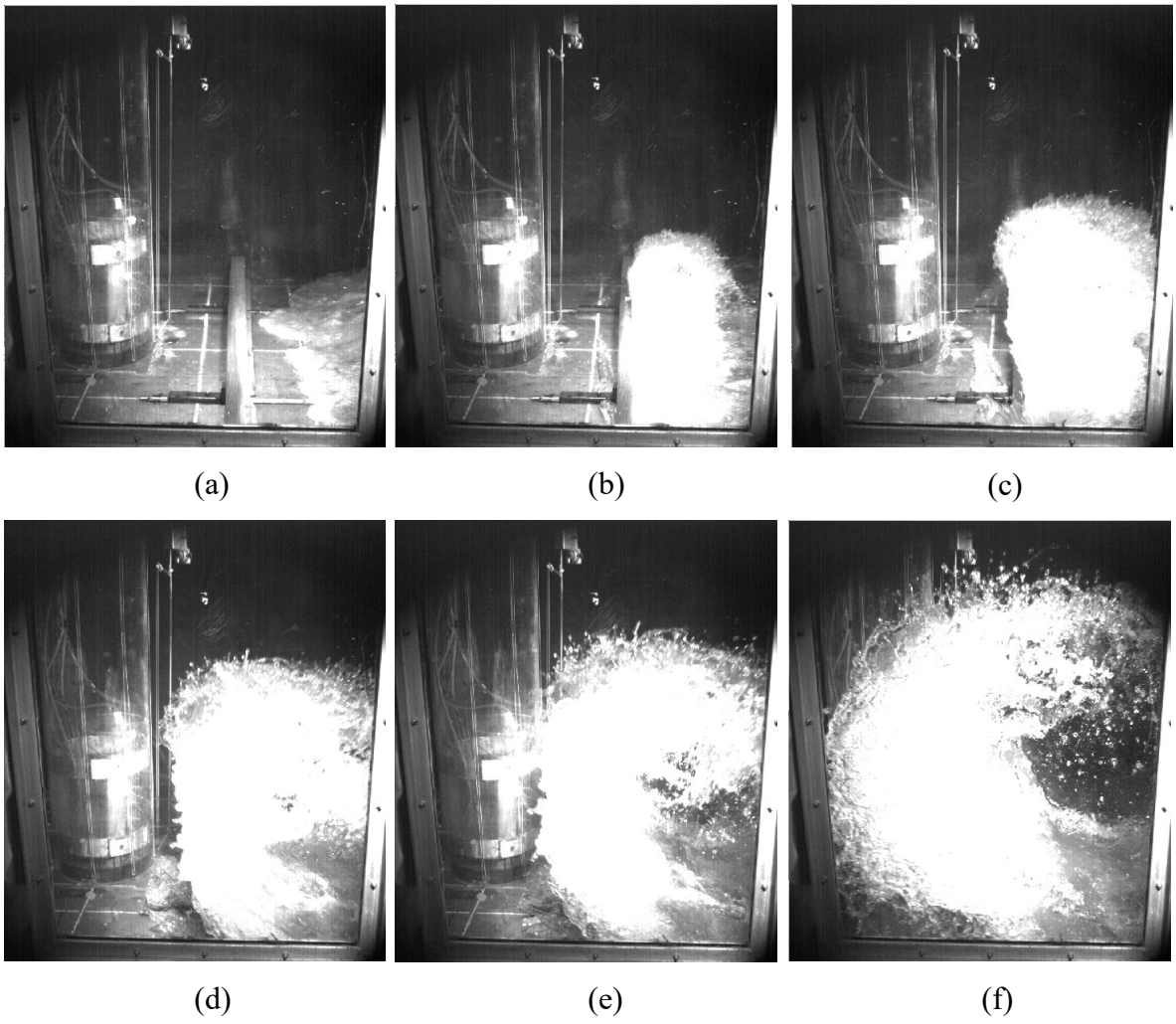

Figure 5.49 Still frames from high-speed video with 100 mm-height wave return wall at 1D upstream from the circular model for hydraulic bore generated from 550 mm impounding water depth.

The still frames shown in Figure 5.49 (d), (e), and (f) demonstrated the effect of the wave return wall which partially redirects the bore front in upstream direction. Laboratory observations highlighted that for the test with the mitigation wall placed at 3D; the bore front plunged in upstream direction from the mitigation wall and collided with the incoming subsequent flow, resulting in damping of the impulsive force induced on the structural model. This phenomenon occurred in the space upstream of the two side windows of the flume and, therefore, could not be captured by the video recordings.

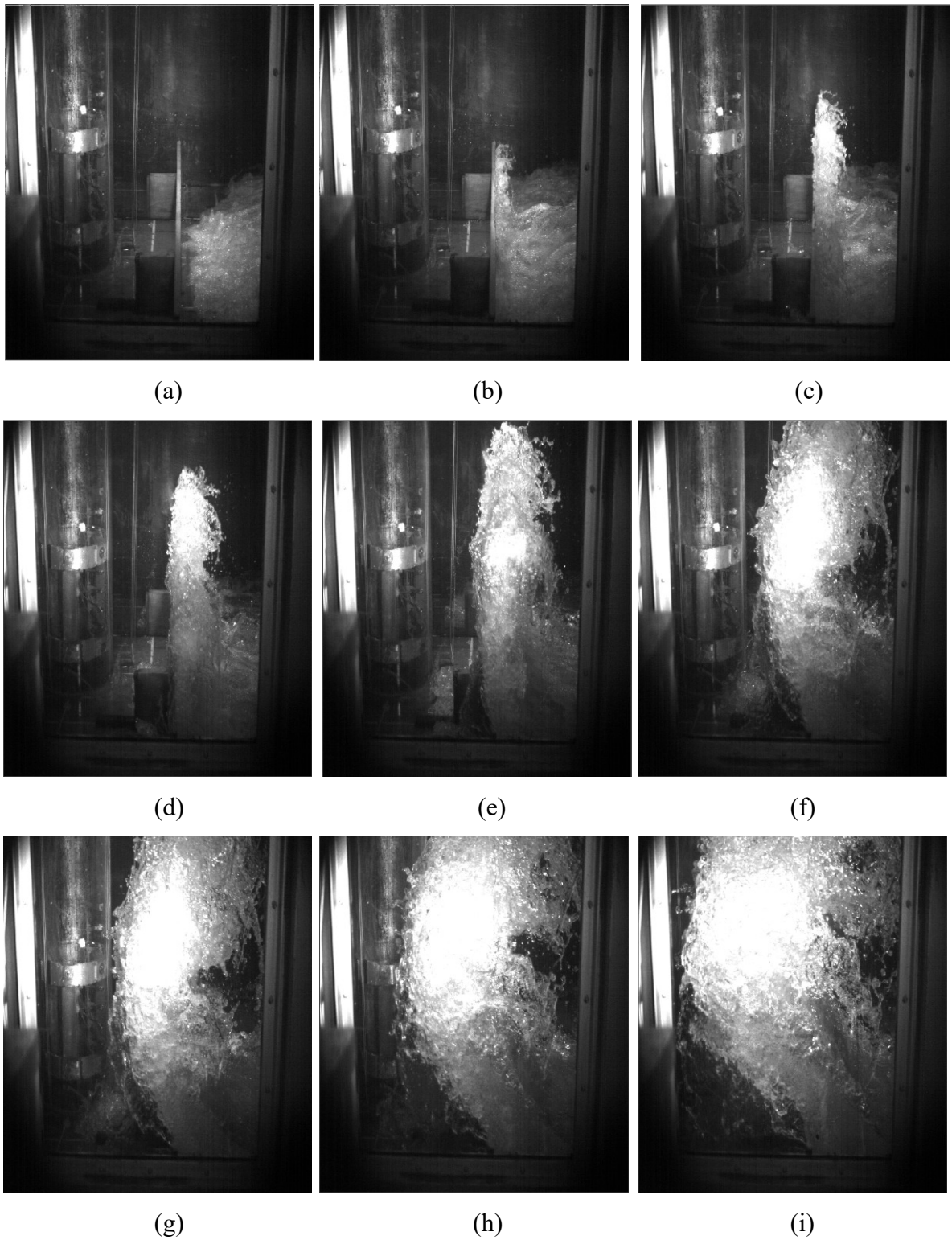

Figure 5.50 Still frames from high-speed video recordings with the 100 mm-height flat vertical wall located at 1D upstream from the circular model for the hydraulic bore generated from the 550 mm impounding water depth

Figure 5.50 shows the interaction between the 100 mm-height flat vertical wall placed at 1D upstream from the circular structural model and the bore front. The frames illustrate that the flat wall redirected bore front vertically to a higher elevation than the wave return wall. As a result, the bore front impacted the structural model at a higher elevation, which caused the abrupt spike (impulsive moment) shown in the moment-time history presented in Figure 5.48 (a). Thus, the flat wall was less effective at damping the forces and moments induced on the structural model than the wave return wall. The curved wall was cut from a hollow circular pipe; therefore the curvature of its upstream face is less pronounced than the wave return wall. Consequently, the curved wall reduced the impulsive force and maximum moments induced on the structural model comparing when using the flat mitigation wall (Figures 5.47 and Figure 5.48). However, the curved wall was less effective at reducing the forces and moments compared to the wave return wall.

Figure 5.51 shows still frames taken captured for three tests of different configurations. The hydraulic bore in these tests was generated from the 550 mm impounding water depth. The frames in Figures 5.51 (a), (d), (g), and j) show the top view of the flow without the structural model placed in the flume while frames in Figure 5.51 (b), (e), (h), and (k) show the top view for a test conducted to investigate the bore-mitigation wall interaction. Lastly, the frames in Figures 5.51 (c), (f), (i), and (l) show a test conducted to investigate the influence of a vertical mitigation wall placed upstream from the structural model. These frames demonstrate that the presence of the mitigation wall increases the flow turbulence and entrained air, especially for the bore front.

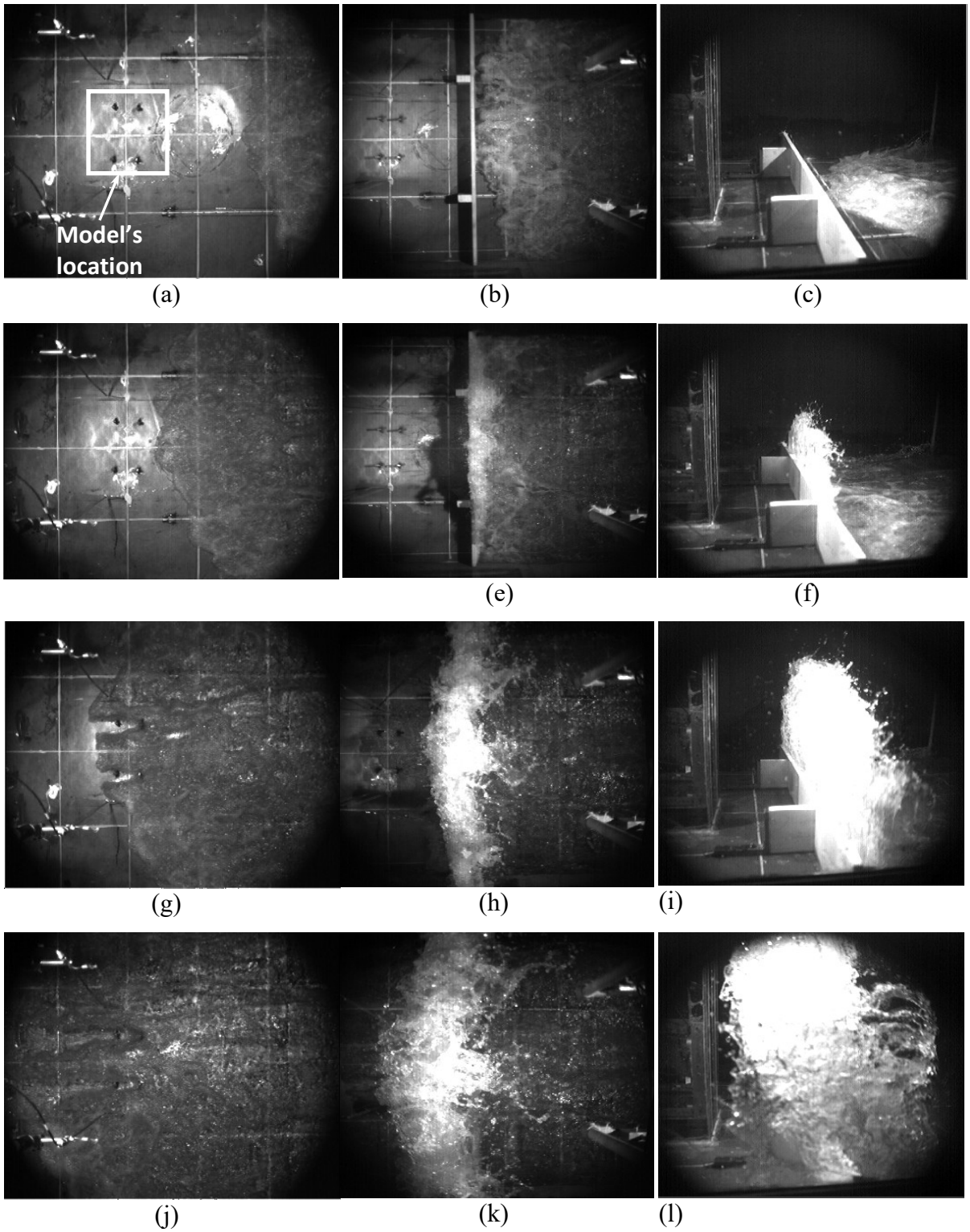

Figure 5.51 Still frames from the video recordings of the bore flow without obstruction **(a**, **d**, **g**, and **j)**; obstructed by the 100 mm-height vertical mitigation wall without the structural model **(b**, **e**, **h** and **k)**; and obstructed by the 100 mm-height vertical mitigation wall with the square structural model in place **(c**, **f**, **i**, and **l)**

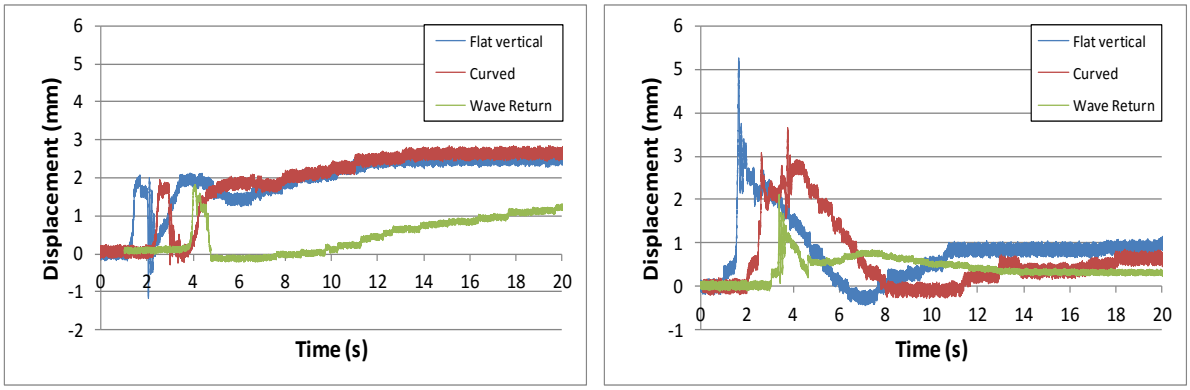

Figure 5.52 Influence of mitigation wall cross-sectional shape on the time histories of the displacement induced on the circular model: **a)** wall placed at 1D; and **b)** wall places at 3D

Figure 5.52 presents the displacement-time histories of the structural model for the tests discussed above in Figures 5.47 and 5.48. The results demonstrate that the presence of the mitigation walls placed at 1D were effective at controlling the abrupt displacement corresponding to the impulsive force.

5.4.5 Effects of wave return wall

Wave return walls, similar to the one described in Section 4.8, are typically placed at the crest of seawalls and are often used as an integral component of coastal protection structures along shorelines in many locations around the world. The main advantage of the curved upstream face of the wall is that it reflects the incident wave and reducing the amount of overtopping. The three sets of tests with different impounding water depths from 450 to 1150 mm, in increments of 100 mm, were conducted to investigate the effect of a wave return wall on the bore-induced maximum base shear forces and overturning moments exerted on the model. Figure 5.53 provides a comparison of the maximum forces and moments recorded for the tests with and without the wave return wall.

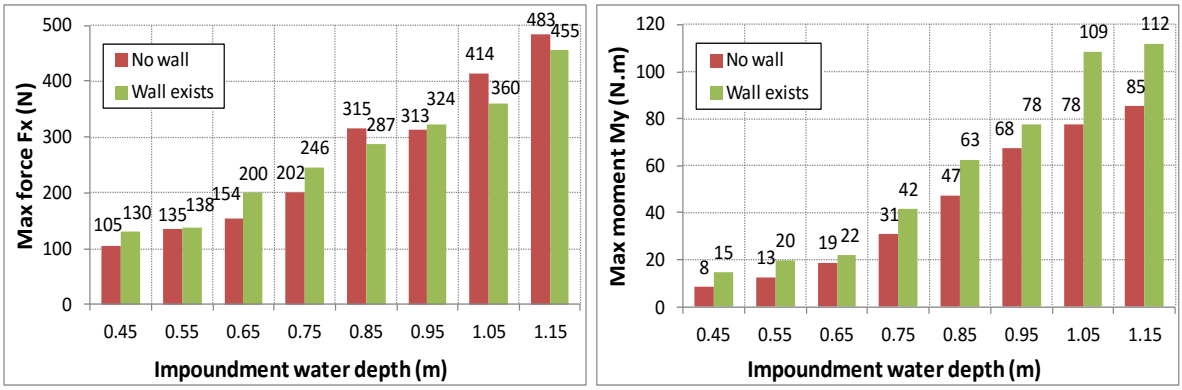

(a) (b)

Figure 5.53 Comparison of the forces and moments induced on the circular model with and without the wave return wall at 1D: **a)** base shear forces F_x; and **b)** base overturning moments M_y

When the ratio of maximum inundation depths (h_{imax}) to wall height (h_w) was less than 3.5, corresponding to an impoundment depth less than 850 mm (Figure 5.53 (a)), the maximum recorded force for the test with the mitigation wall was approximately 20% to 30% larger than the test without the wall (for the same h_{imax}). When the ratio of (h_{imax}/h_w) was 3.5 or greater, the maximum force recorded on the structural model was less than when no mitigation wall was present. The reduction in force was approximately 10 to15%. Conversely Figure 5.53 (b) illustrates that the presence of the mitigation wall increased the base overturning moments induced on the model by 15 to 80% compared to the case without the mitigation wall.

When the ratio of himax to wall depths (h_{imax}) to wall height (h_w) was less than 3.5 (Figure 5.53 (a)), the maximum recorded force for the case with the wall was about 20% to 30% larger than for the test without the wall (for the same h_{imax}). The average increase in the maximum force was of 25%. When the ratio (h_{imax}/h_w) was 3.5 or greater, the maximum force recorded on the structural model was less than when no mitigation wall was present. The reduction in force was approximately 10 to15%. Conversely Figure 5.53 (b) illustrates that the presence of the mitigation wall increased the base overturning moments induced on the model by 15 to 80% compared to the case without the mitigation wall.

5.5 Waterborne Debris Impact

Three wooden debris of different mass and shape were used with two impounding water depths (550 mm and 850 mm) to impact the circular structural model. The time series of the bore depth, base shear force, and base overturning moment induced on the structural model in both directions of flow (longitudinally and transversely), were recorded. The debris velocity and the impact were recorded with high-speed digital video-cameras. Analysis of the experimental data demonstrated the combined influence of both the debris orientation and eccentricity, for all bore levels, on the magnitude of the impact force imposed on the structural model. Three available methods were used to estimate the maximum impact forces for the six test series. The estimated forces were further compared with those experimentally recorded.

5.5.1 Description of impact tests

The high-speed video recordings were analyzed and the initial impacts of the debris with the structural model were captured. The flow direction (parallel to the flume centerline) was considered as the reference axis to measure the angles used in the analysis: the debris orientation angle between the debris longitudinal axis and the reference axis is defined as θ; the impact angle φ is defined as the angle between the line connecting the center of the structural model with the point of impact on the surface of the model and the flume centerline, as shown in Figure 5.54. Therefore, the location and the orientation of the wooden debris on the horizontal plane are defined by angles θ and φ. The analysis is also based on rigid body assumption(s), as the deformation due to impact was assumed to be negligible in comparison with the size of the debris.

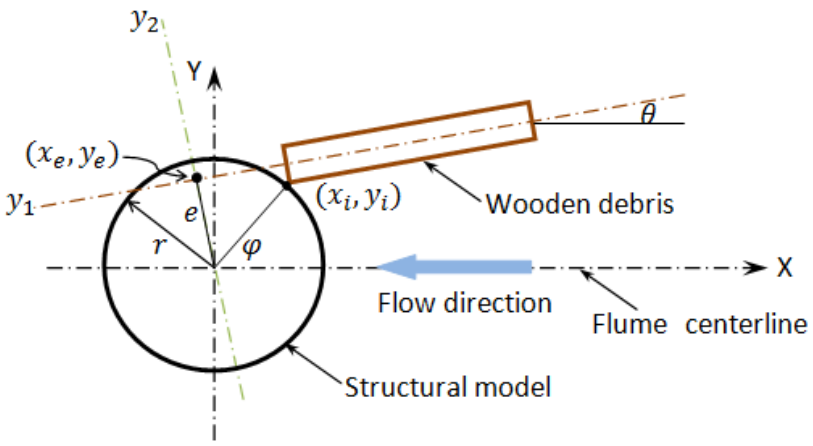

Figure 5.54 Diagram of the structural model and debris interaction

As shown in Figure 5.54, two coordinate axes are defined for analysis: X is in the flow direction and Y is perpendicular to the flow. The axes intersect at the center of the structural model, which represents the origin of the system of coordinates (0, 0). With the angle θ the orientation angle of the debris, $tan\theta$ is the slope of the longitudinal axis of the debris, at the moment of impact, with respect to the longitudinal axis of the flume. Using the general system of coordinates of the flume in the X and Y plane (flume bed), the coordinates of the impact point on the structural model surface will be:

$$x_i = rcos\varphi \tag{5.1}$$

$$y_i = rsin\,\varphi \tag{5.2}$$

And the equation of the longitudinal axis of the debris with respect to the coordinate axes X and Y at the moment of impact is:

$$y_1 = tan\theta(x - rcos\varphi) + rsin\,\varphi \tag{5.3}$$

The equation of the perpendicular line to the longitudinal axis of the debris with respect to the coordinate axes (X, Y) at the moment of impact from the origin is:

$$y_2 = -x.cot\theta \tag{5.4}$$

The coordinates of the intersection point of the perpendicular line with the longitudinal axis of the debris (x_e, y_e) can be found by Solving equations 5.3 and 5.4 simultaneously:

$$x_e = \frac{r(tan\theta.cos\varphi - sin\varphi)}{(tan\theta + cot\theta)} \quad 5.5$$

$$y_e = -\frac{r(tan\theta.cos\varphi - sin\varphi)}{(tan\theta + cot\theta)}\ cot\theta \quad 5.6$$

Then, the eccentricity of the debris from the center of the structural model is calculated as:

$$e = \sqrt{x_e^2 + y_e^2} \quad 5.7$$

Three logs were prepared to be used as debris and tested with two impounding water depths (550 mm and 850 mm). Therefore, six groups of tests were conducted. Each test group was designated with a name that represented the floating debris and the impounding water depth used to generate the hydraulic bore flow as follows: 1kg-550WH, 1kg-850WH, 2kg1P-550WH, 2kg1P-850WH, 2kg2P-550WH, and 2kg2P-850WH. For example, the first group "1kg-550WH" refers to the 1kg debris mass that was tested with the hydraulic bore generated from the 550 mm impounding water depth. Recall that "P" refers to the number of logs for the 2kg debris mass tests.

5.5.2 Debris velocity and momentum

The debris velocity was measured by tracking their movement and analyzing images recorded by a high-speed digital video camera (with a sampling speed of up to 10,000 fps) installed 2.40 m above the floor of the flume and 300 mm upstream from the location of the structure. The grid of 300 x 300 mm, which had been previously marked to estimate the bore-front velocity, was used to identify the center of the base of the structural model on the flume floor as shown in Figure 5.55. The debris velocity was estimated from the time required for two adjacent lines marked on the debris (100 mm distance between) to pass a specified section upstream from the structural model. The orientation angle of the debris was used to adjust the debris velocity by calculating the longitudinal projection of the distance between the adjacent lines.

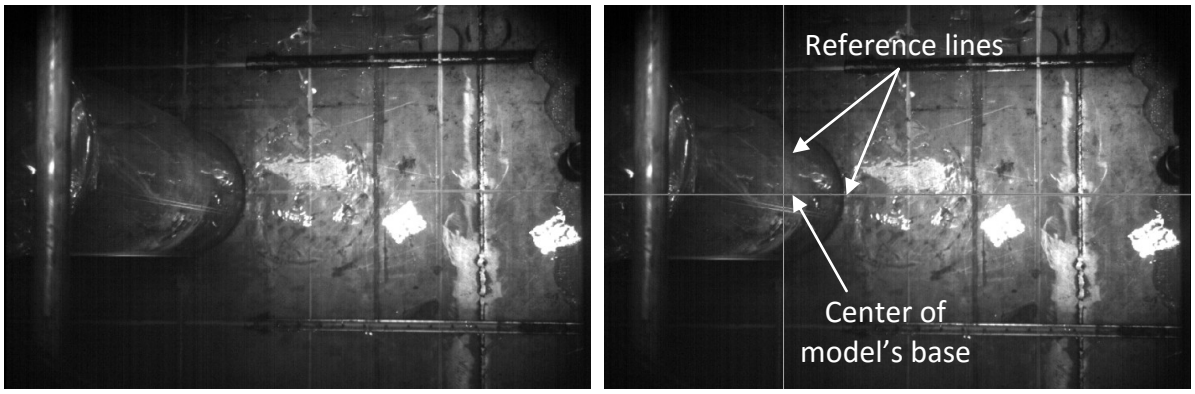

(a) (b)

Figure 5.55 Reference system for the estimation of the debris velocity: **a)** grid of 300 x 300 mm; and **b)** reference lines with their origin at the center of the base of the model

Table 5.1 summarizes the debris dimensions, number of successful tests, and the average debris velocity for each testing group.

Table 5.1 Average velocity of debris for the six testing groups

Testing Group	Debris Dimensions (mm)	Impounding Water Depth (mm)	Number of Tests	Average Debris Velocity (m/s)	Standard Deviation
1kg-550	76.2 x 76.2 x 490	550	28	2.37	0.10
1kg-850		850	22	3.15	0.15
2kg1P-550	76.2 x 76.2 x 916	550	30	2.10	0.09
2kg1P-850		850	30	2.90	0.10
2kg2P-550	76.2 x 152.4 x 490	550	12	2.38	0.07
2kg2P-850		850	19	3.24	0.22

The statistical analysis illustrates that the average debris velocity for the same debris increased by 33%, 38%, and 36% as the bore depths increased due to the increasing impounding water depth (550 mm a 850 mm) for the 1kg, 2kg1P, and 2kg2P debris, respectively. The analysis of the experimental data revealed that the larger the slenderness

ratio of the debris, the larger the velocity. Although the debris velocity is one of the main parameters affecting the debris impact force, debris of same mass but with different shape, dimensions and with lower velocity did result in higher impact forces for some tests. These factors, in addition to the debris orientation, affect the stiffness of the impact between the debris and the structure. For the 2kg debris mass tested with the bore generated from the 550 mm impoundment depth, the debris velocities were 2.10 m/s and 2.38 m/s and the impact forces were 1413 N and 1202 N for the 2kg1P and 2kg2P debris, respectively. Two other groups of tests with the same debris were conducted with bores generated from the 850 mm impounding water depth. The debris velocities were 2.90 m/s and 3.24 m/s and the impact forces were 2450 N and 2063 N for the 2kg1P and 2kg2P debris, respectively.

5.5.3 Sample data

Although in each testing series the debris did not impact the structural model (less than 10% of the debris tests), the subsequent discussion involves results of only the successful tests where the debris impacted the model. A sample of the data including the time series for the bore depth, acceleration of the model, base shear force, and base overturning moment induced on the model are shown in Figure 5.56.

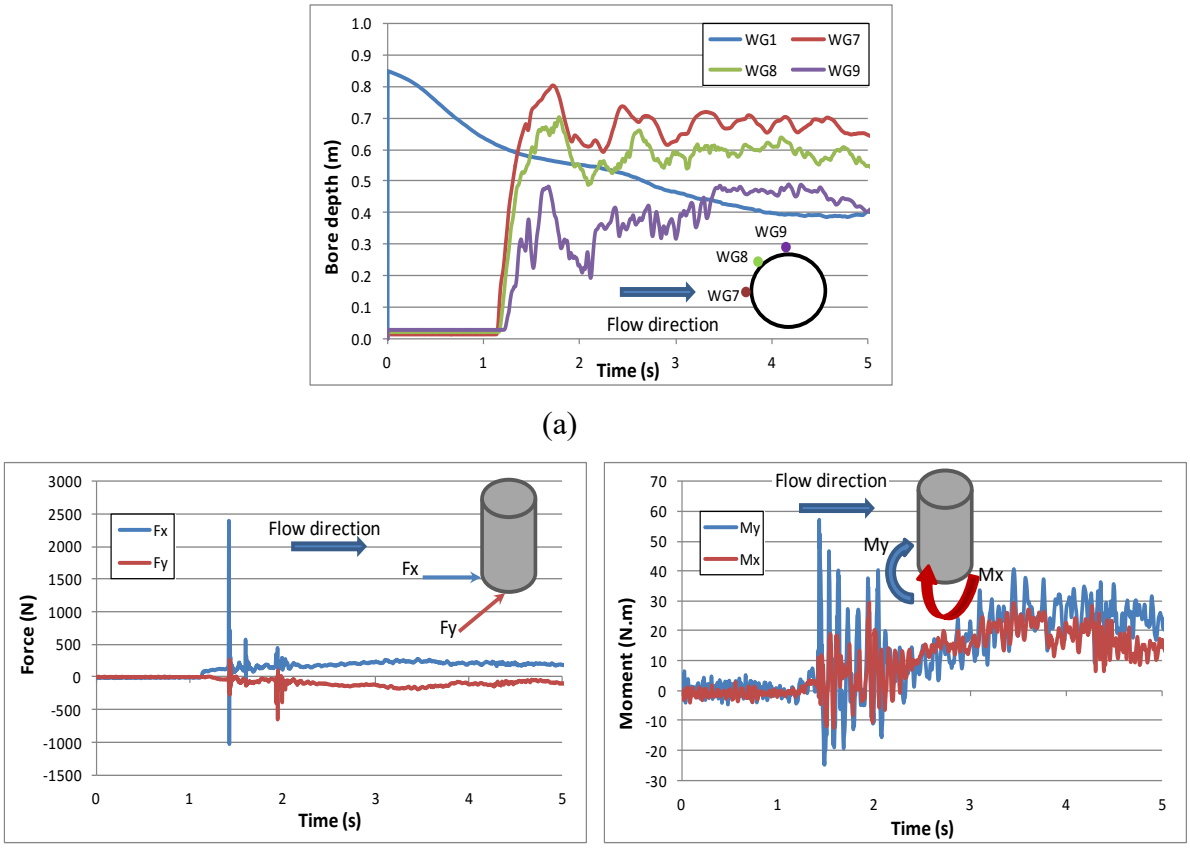

Figure 5.56 Sample of data comprising the time histories of: **a)** bore depth; **b)** debris impact forces; and **c)** debris-induced overturning moments

Figure 5.56 (a) provides the water depth-time history in the reservoir and around the structural model. Water Level Gauge No.1 (WG1) was located in the impounding tank, 1.25 m upstream from the swinging gate, to monitor the impounding water depth. Gauges WG7, WG8, and WG9 were placed directly on the surface of the circular model at horizontal angles of 0˚, 45˚, and 90˚, respectively, from the longitudinal axis of the flume. Upon opening of the gate (0s), the water depth in the reservoir started to decrease (WG1), and after 1.162s the bore-front reached the structural model. Due to the curvature of the surface of the model, the bore-front reached the water level gauges at slightly different times. Moreover, the gauges indicated that the flow depth was the highest at the mid-point of upstream face of the model (WG7), decreasing for the water level gauges located around the sides (WG8, and WG9). The high-speed video of this test revealed that the debris was inclined 5˚ from the centerline of the flume and impact occurred at the mid of the upstream

face of the model at 1.486s. After the first impact, the debris rebounded upstream followed by a second impact with the structural model. During the second impact the downstream end of the debris was raised by the surge of the bore front. The debris continued to rebound a number of times, and each subsequent impact deviated from the initial impact at the mid of the upstream face of the model to the side of the model. The final impact was a glancing blow to the side of the model. The time-history of the base shear force and base overturning moment about the X and Y axes, which were defined in Figure 5.54, are shown in Figures 5.56 (c) and (d). The data corresponds to the 2kg1P-850 group of tests, in which 2kg1P (76.2 x 76.2 x 916 mm) debris was used with the flow generated by the 850 mm impounding water depth.

5.5.4 General characteristics of debris impact force

As the swinging gate opened, a dam-break wave was generated and the hydraulic bore developed. The bore front is characterized by high velocity and shallow depth, which was often not sufficiently deep to entrain the debris. A very short time after, as the bore depth increased, the debris floated and moved freely with the flow advancing downstream in the flume towards the model. Depending on the debris orientation and eccentricity, the debris impacted the structural model once, twice, or missed it altogether. These features were common for all tests, except for the test group employing the 2kg2P debris combined with the 550 mm impoundment depth. In this test group, the debris did not float, but rather dragged along the flume floor prior to impacting the model. In addition, the debris lagged slightly behind the bore front due to inertial effects and the relatively swallow flow depth of the leading edge of the bore. When the 2kg2P debris impacted the model near the centerline of the flume, the debris "climbed" the model during the run-up phase of the flow as shown in Figure 5.57. In this figure, the top view still frames were captured from the high-speed camera which was installed above the flume. The lower still frames were captured from digital video recordings captured through the side window of the flume. The debris impact force resulted in a large spike in the force-time history for these tests.

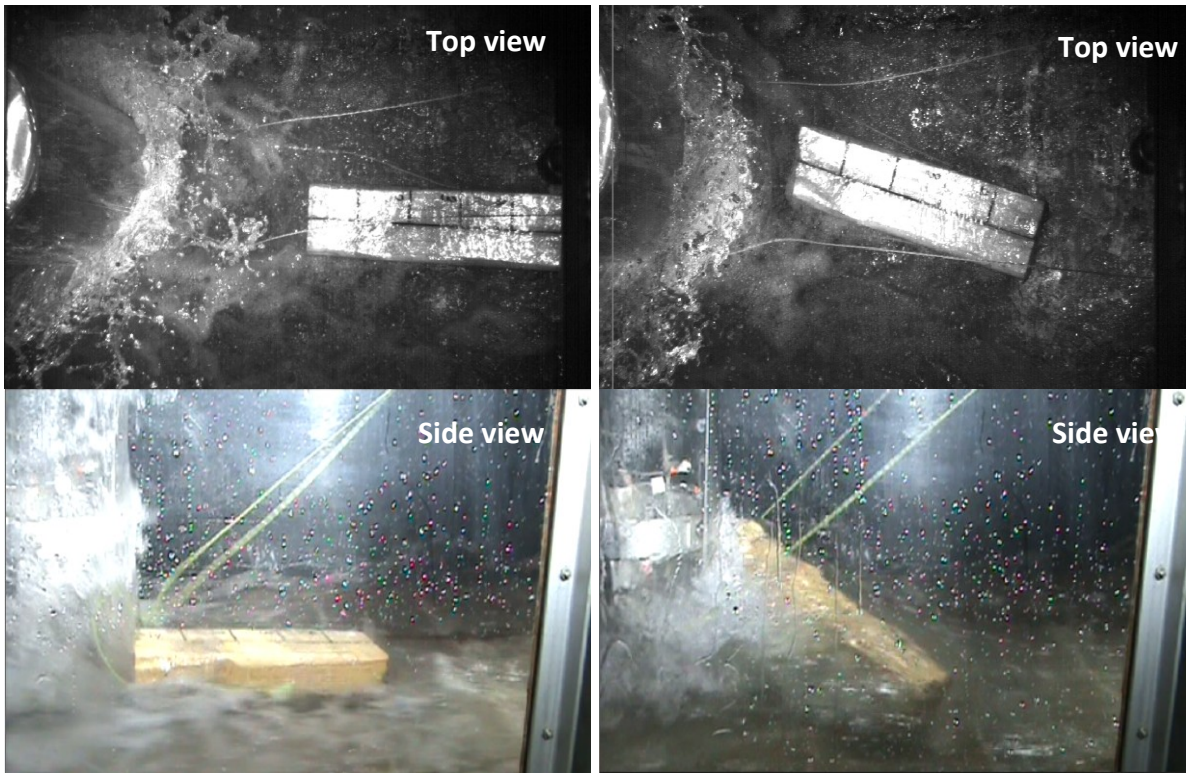

(a) (b)

Figure 5.57 Photos of the 2kg2P debris entrained by the hydraulic bore generated from the 550 mm impoundment depth: **a)** first impact; and **b)** debris-structure interaction

5.5.5 Peak force, rise time, momentum

The waterborne debris impact force-time histories were recorded for the six test groups. The debris velocity, just prior to impact for each test, was estimated using the orientation and eccentricity of each debris which was obtained from the analysis of the high-speed video recordings. The average peak force, rise time, and momentum for the debris testing groups are listed in Table 5.2

Table 5.2 Peak force, rise time, and momentum for the six debris test groups

Test Group	Debris Mass (kg)	Impound Depth (mm)	Average Debris Velocity (m/s)	Debris Velocity Stand. Deviation	Peak Force (N)	Rise Time (ms)	Momentum (kg . m/s)
1kg-550	1.088	550	2.37	0.10	819.84	4.0	2.58
1kg-850	1.088	850	3.14	0.15	1040.31	4.0	3.42
2kg1P-550	2.191	550	2.09	0.16	1520.21	5.0	4.58
2kg1P-850	2.191	850	2.81	0.15	2279.20	5.0	6.16
2kg2P-550	2.258	550	2.39	0.13	1254.72	5.0	5.40
2kg2P-850	2.258	850	3.20	0.23	2045.35	5.0	7.23

5.5.6 Influence of debris geometry

The effect of the debris geometry on the impact force was investigated through a comparison between the laboratory data from four test series with two debris (2kg1P and 2kg2P), which have approximately the same mass (2.191 kg and 2.258 kg), but different dimensions of 76.2 x 76.2 x 916 mm and 76.2 x 152.4 x 490 mm, respectively. The 2kg2P debris has double the cross-sectional area and approximately half the length of the 2kg1P debris. The debris velocity just prior to impact and the impact force from tests using the bores generated from the 550 mm and 850 mm impounding water depths are shown in Figure 5.58.

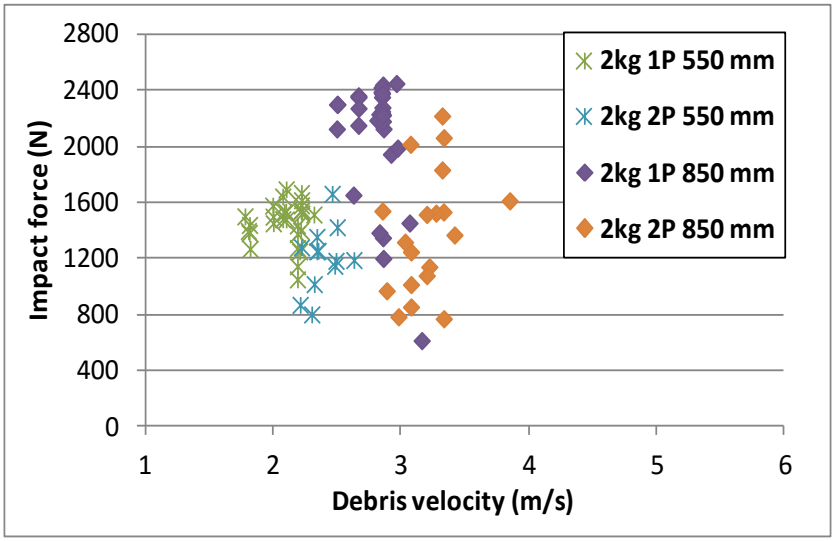

Figure 5.58 Comparison of the impact force versus debris velocity for the 2kg1P and 2kg2P debris for hydraulic bores generated by the 550 mm and 850 mm impounding water depths

The figure reveals that for both impounding water depths, Debris 2kg2P gained higher velocity than Debris 2kg1P. This is supposedly related to the larger cross-sectional area of this particular debris, which was exposed perpendicular to the flow direction. Although the velocities of Debris 2kg1P were lower than Debris 2kg2P (similar masses), the impact forces were higher for Debris 2kg1P. These two debris transported by the bore generated by the 550 mm impounding water depth generated average impact forces of 1457 N and 1203 N, respectively for the 2kg1P and 2kg2P debris. The average debris velocities were of 2.10 m/s and 2.38 m/s for the 2kg1P and 2kg2P debris, respectively. For the tests with the bore generated by the 850 mm impounding water depth, the average impact forces were 2,061 N and 1,389 N corresponding to average debris velocities of 2.81 m/s and 3.20 m/s, respectively for the 2kg1P and 2kg2P debris. This implies that, for the same bore characteristics, the debris shape influences its velocity and resulting impact force, even though the debris consisted of similar mass and material.

The slenderness ratio (L/d) of the debris was calculated by dividing its length by the equivalent diameter of its cross-sectional area. The debris geometry was found to influence its velocity and impact force. Haehnel and Daly (2004) stated that for long, slender debris, the added-mass coefficient, C, approaches zero and reaches unity when accelerated in a direction normal to its longitudinal axis.

The debris geometry was also found to have an influence on the debris spatial orientation. Table 5.3 lists the percentage of the tests for each test group during which the debris orientation angle with respect to the longitudinal axis was less than 10˚. The results illustrate that when the slenderness ratio of the debris was higher, the debris orientation angle was smaller (high percentage of tests with an angle of less than 10˚). As debris float, they try to minimize their resistance to flow. An exception arose for the tests with the 2kg2P debris in 550 mm impoundment depth bore series, where lab observations demonstrated that this particular debris dragged along the bottom of the flume from its initial location to impact with the model. Thus, it is probable that the change in debris orientation was influenced by the friction between the debris and the flume bed. A comparison between the tests series using the three different debris individually in the simulated tsunami-bores generated by the 850 mm impounding water depth shows that, while their slenderness ratio was 4.0, 5.7, and 10.6, the percentage of tests in which $\theta \leq 10^{\circ}$ were 47.4%, 63.6%, and 93.3%, respectively. This highlights that debris geometry seems to have a significant influence on debris orientation.

Table 5.3 Debris orientation for angles $\theta \leq 10^{\circ}$

Test Group	**Debris Dimensions (mm)**	**Slenderness Ratio (L/d)**	**Number of Tests**	**Debris Orientation of $\theta \leq 10^{\circ}$**	
				Number of Tests	**Percentage (%)**
1kg-550	76.2 x 76.2 x 490	5.7	28	25	89.3
1kg-850			22	14	63.6
2kg1P-550	76.2 x 76.2 x 916	10.6	30	30	100
2kg1P-850			30	28	93.3
2kg2P-550	76.2 x 152.4 x 490	4.0	12	10	83.3
2kg2P-850			19	9	47.4
Total number of debris impact tests			141	116	82.3

5.5.7 Influence of debris orientation

Four impacts associated with the 2kg2P debris floating in a hydraulic bore generated by the 850 mm impounding water depth showed that the debris impacted the model at the same point (same impact angle φ). For these tests, however, θ varied from 0˚ to -40˚. [The debris orientation angle, θ, is defined as the angle between the longitudinal axis of the debris and the longitudinal axis of the flume.]. The flume centerline was taken as the reference for measuring the angles θ and φ. The sign convention followed in this investigation is such that angles are positive for the counterclockwise direction. Hence, for tests when an impact angle occurred in the opposite direction comparing to the debris orientation angle, the eccentricity (e) between the longitudinal axis of the debris and the center of the model increased. Figure 5.59 (a) shows the case where the debris was nearly parallel to the flow direction (θ = 2˚) and the impact point was recorded at φ = 20˚. This resulted in 39 mm eccentricity between the debris longitudinal axial and the center of the model. The largest impact force was recorded in this group (1,532 N). Figure 5.59 (d) provides a photos at impact for the case where the debris orientation was θ = -40˚ and φ = 20˚, with an estimated eccentricity of 101 mm. This impact generated the smallest impact force in this group (783 N). The debris velocities for these tests varied from 2.98 to 3.10 m/s with an average of 3.06 m/s (3.08, 3.08, 2.98, and 3.10 m/s). Figure 5.60 illustrates that as the debris-orientation angle increased, the impact force decreased.

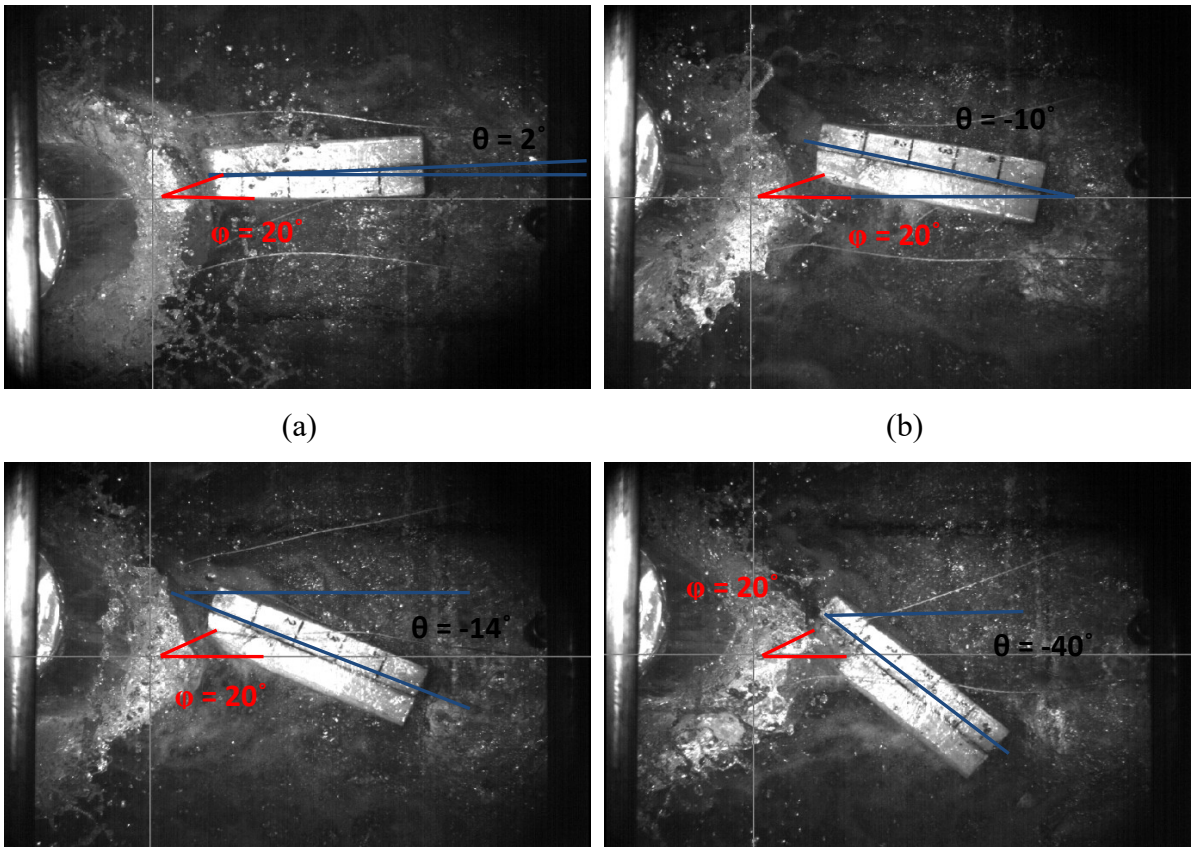

Figure 5.59 Photos Debris 2kg2P impacting the structural model at the same location for different orientation angles: **a)** Test No. 1 (T1) [θ = 2˚, φ = 20˚]; **b)** Test No. 6 (T6) [θ = -10˚, φ = 20˚]; **c)** Test No. 9 (T9) [θ = -14˚, φ = 20˚]; and **d)** Test No. 4 (T4) [θ = -40˚, φ = 20˚]

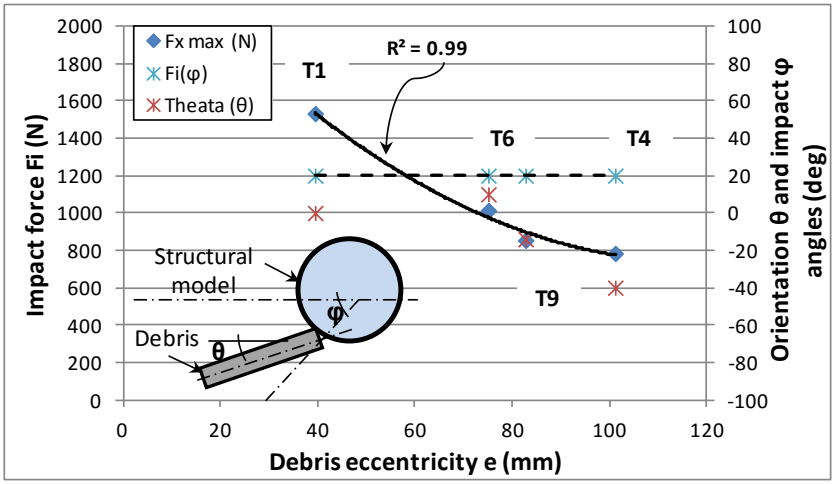

Figure 5.60 Correlation between debris orientation angle (θ), impact force induced on the model (F_i), and the debris eccentricity (e) for the test group 2kg2P-850

5.5.8 Influence of debris eccentricity

The test data indicates that as the debris eccentricity increased, the impact force decreased. To investigate the effect of the debris eccentricity on the impact force, four tests were selected from the series employing the bore generated by the 550 mm impounding water depth with the 2kg1P debris. In these tests, the impact occurred at different points on the structural model, while the debris orientation angle was approximately constant ($\theta = 4^{\circ}$) as demonstrated in Figure 5.61.

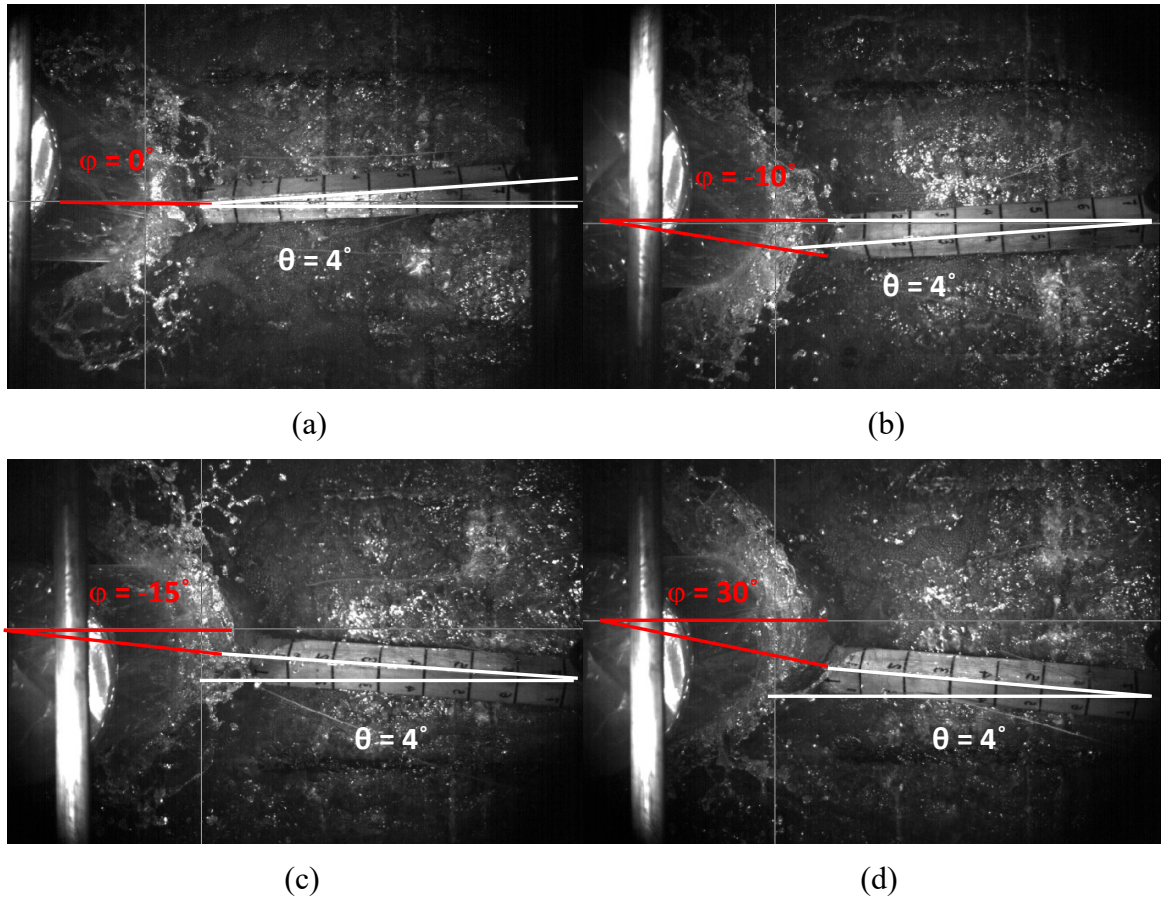

Figure 5.61 Photos of Debris 2kg1P with 4˚-inclination angle impacting the structural model at different points: **a)** Test No. 1 (T1) [$\theta = 4^{\circ}$, $\varphi = 0^{\circ}$]; **b)** Test No. 2 (T2) [$\theta = 4^{\circ}$, $\varphi = -10^{\circ}$]; **c)** Test No. 9 (T9) [$\theta = 4^{\circ}$, $\varphi = -15^{\circ}$]; and **d)** Test No. 10 (T10) [$\theta = 4^{\circ}$, $\varphi = -30^{\circ}$]

The graph in Figure 5.62 shows the effect of the debris eccentricity on the impact force. The results indicate a correlation between the impact force and the eccentricity of the debris impact.

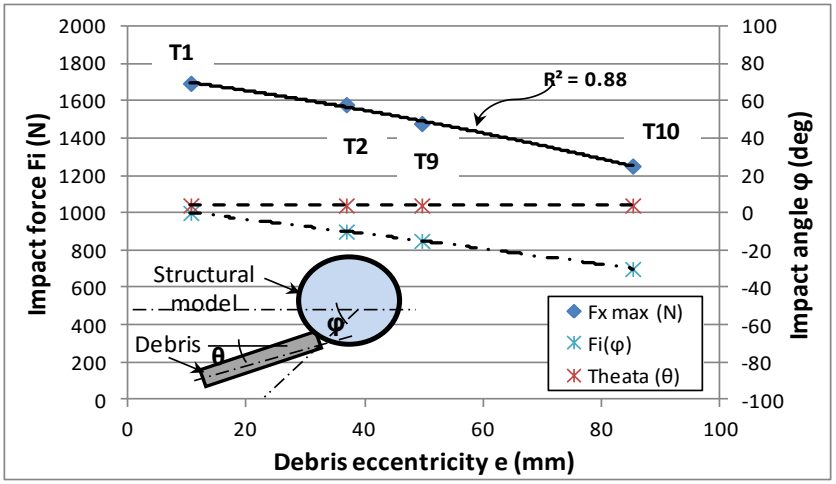

Figure 5.62 Correlation between impact angle (φ), impact force induced on the structural model (F_i), and debris eccentricity (e) for the test group 2kg1P-550

The relation between the impact angle (φ) and the debris eccentricity (e) from the center of the model is provided in Figure 5.63. The black trend line demonstrates a correlation between φ and e. This relation converges to a linear fit for debris orientation angle θ of zero (direct impact). However, for $\theta > 0^{\circ}$, larger impact force are probable. Furthermore, for $\theta = \varphi$, the eccentricity is zero and a high impact force can arise.

Examining Figure 5.63 reveals that few tests results deviate noticeably from the trend-line. These three tests are identified by A, B, and C in Figure 5.63. For Test A, the impact angle $\varphi = 0^{\circ}$, but the debris eccentricity was $e \neq 0$. This eccentricity resulted from the debris orientation angle $\theta = 10^{\circ}$. For Test B; the colliding angle was $\varphi = 6^{\circ}$, however the debris eccentricity was e = 0 mm. In this test (B), the debris orientation angle was $\theta = 6^{\circ}$; consequently the extension of the longitudinal axis of the debris passes through the center of the circular model. Although the impact angle of Test C was $\varphi = 20^{\circ}$, the eccentricity was more than 120 mm. In this test (C), the debris orientation angle was $\theta = -33^{\circ}$ occurred in opposite direction compared to the impact angle.

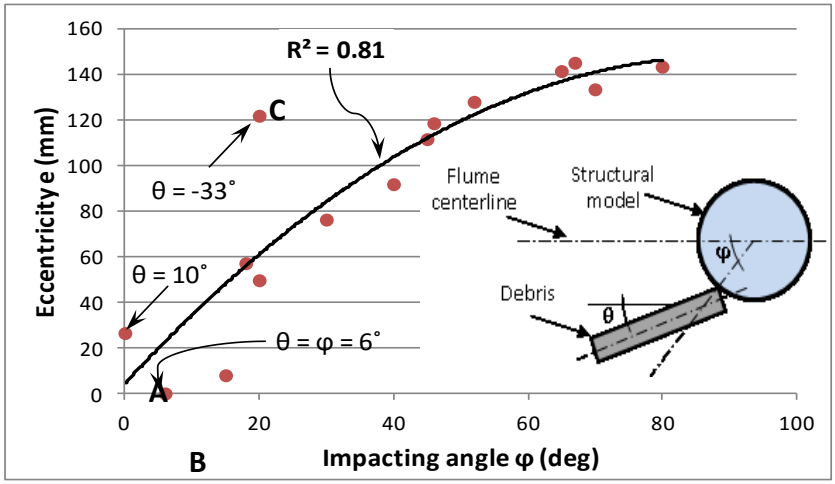

Figure 5.63 Correlation between the debris impact angle and debris eccentricity at impact for the 1kg-550 group

5.5.9 Non-dimensional analysis

Non-dimensional analysis is performed in an attempt to contextualize the scope of this experimental program and to determine the extent of extrapolating the results outside of the current experimental conditions. The force-related non-dimensional term, $F_i/\rho_w L_d^2 V_d^2$, was selected for this study: where F_i is the debris impact force, ρ_w is the water density, and L_d and V_d are the length and velocity of the debris, respectively. The eccentricity is non-dimensionalized by L_d. Figure 5.64 shows the relationship between these two non-dimensional parameters for the six test groups of different debris shape and impounding water depths. The results presented in Figure 5.64 seem to suggest that slender debris tend to exhibit less eccentricity at impact—particularly when transported by hydraulic bores with shallow depths such as in the case of the 2kg1P debris in the bore generated from 550 mm impounding water depth (Figure 5.64 (c)). This may be attributed to the initial-location and -orientation of the debris which is at the flume centerline and parallel to the flow direction. This orientation causes least resistance to the flow, as this debris (2kg1P) has less cross-sectional area than the same mass debris with less slenderness ratio (2kg2P). Therefore, when the debris orientation changes due to the flow turbulence, the debris returns back to its initial orientation due to the high bore-front velocity. The data in this figure indicates that, irrespective of the debris mass, as the debris eccentricity increases, the debris impact force

decreases. The trend-lines in Figure 5.64 demonstrate that as the slenderness ratio ($\frac{e}{L_d/2}$) of the debris increased, the rate of change in the impact force ($F_i/\rho_w L_d^2 V_d^2$) decreased.

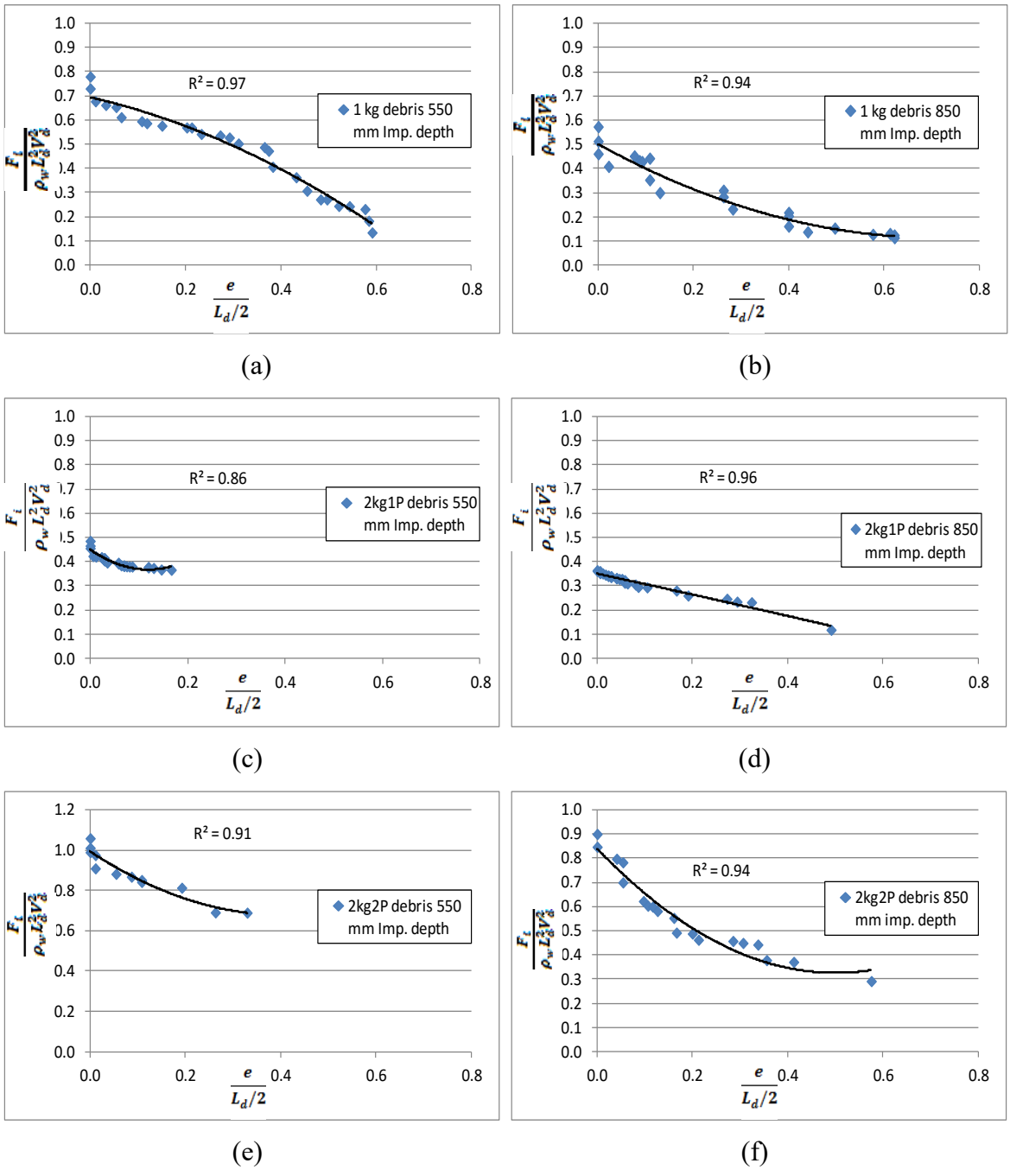

Figure 5.64 Correlation between the non-dimensional impact force and the non-dimensional debris eccentricity for 6 tests: **a)** 1kg-550WH; **b)** 1kg-850WH; **c)** 2kg1P-550WH; **d)** 2kg1P-850WH; **e)** 2kg2P-550WH; and **f)** 2kg2P-850WH

5.5.10 Estimation of debris impact force

As discussed in Section 2.7, three approaches used to estimate the debris impact force on structures have been investigated and discussed in the literature. The following three formulae have been used to calculate the debris impact force in this study.

- **Constant-stiffness approach:**

$$F_{max} = u\sqrt{km} \tag{5.6}$$

- **Impulse-momentum approach:**

$$F_{max} = \frac{\pi um}{2\Delta t} \tag{5.7}$$

- **Work-energy approach:**

$$F_{max} = \frac{u^2 m}{\Delta x} \tag{5.8}$$

where F_{max} is the maximum debris impact force induced on the structure (N),

u is the debris velocity which is assumed to be equal to the flow velocity (m/s),

k is the contact stiffness of debris impact (N/m),

m is the debris mass (kg),

Δt is the debris impact duration (s); recommended values were listed in Table 2.2, and

Δx is the stopping distance of the debris (m); distance that debris travels from point of contact with the structure until debris comes to rest.

Haehnel and Daly (2002) discussed these three approaches and used them to estimate the impact force for their experimental program. Based on their experimental results they suggested the following equations for the above mentioned approaches, respectively:

$$F_{i,max} = 1550\, u\sqrt{m} \tag{5.9}$$

$$F_{i,max} = 90.9\, um \tag{5.10}$$

$$F_{i,max} = 125\, mu^2 + 8000 \quad 5.11$$

Table 5.4 lists the average debris velocity and the average impact duration for the six test groups carried out in this study. Figure 5.65 illustrates the experimental and estimated maximum debris impact force for the six series of this study. The mass and average debris velocity for each test group was used in Eqns. 5.9 - 5.11 suggested by Haehnel and Daly (2002). Figure 5.65 (a) provides a comparison between the experimentally measured impact forces and those estimated using the formulas for the six test groups conducted in this study. The figure shows that the equation based on the impulsive-momentum approach underestimated the impact force, while the other two formulas significantly overestimated the impact force for all test groups. Figure 5.65 (b) provides results using Eqns. 5.6-5.8 based on the experimental measurements for debris mass, velocity, stiffness, impact duration and stopping distance. The estimated impact forces were significantly improved for the three approaches relative to the experimentally measured forces. The comparison between the calculated and measured forces for all test groups revealed that the work-energy approach provided the most reasonable estimation, while the constant-stiffness approach provided underestimated forces.

Table 5.4 Average debris velocity and average impact duration for the six test groups

Test Group	**Average Debris Velocity (m/s)**	**Average Impact Duration (ms)**
1kg-550	2.37	2.52
1kg-850	3.15	2.27
2kg1P-550	2.10	2.50
2kg1P-850	2.90	2.48
2kg2P-550	2.38	2.58
2kg2P-850	3.24	2.47

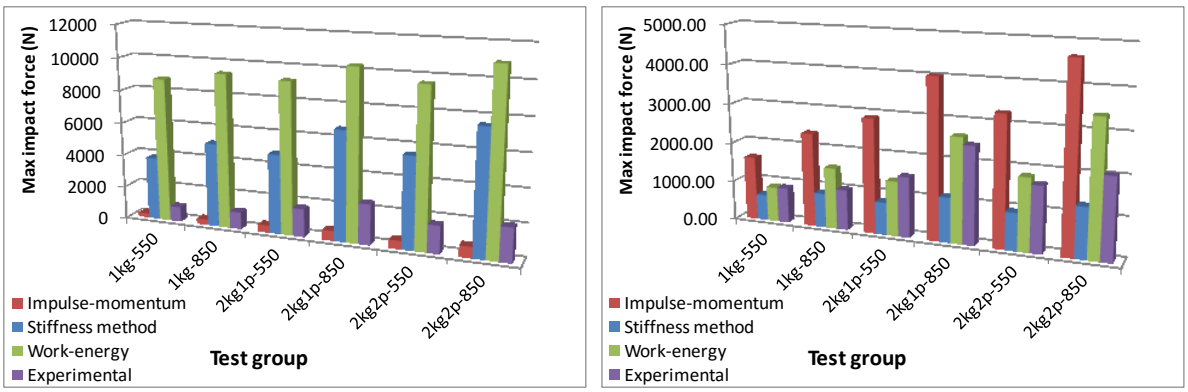

(a) (b)

Figure 5.65 Comparison between the experimentally- and analytically-determined maximum debris impact forces for the six test groups: **a)** using formulas suggested by Haehnel and Daly (2002); and **b)** using parameters measured from testing

Figure 5.65 (b) reveals that the estimated forces using the work-energy approach typically provided the best results in comparison to the results obtained using the two other approaches, with the exception of the group of 2kg1P-550 for which the calculated force was 9% smaller than the experimental forces. The impulsive-momentum approach provided overestimates of the impact forces with differences ranging between 64% and 134% higher than the experimentally measured forces. Although the debris stiffness was determined according to Section 4.9, the maximum impact forces calculated using the stiffness approach were underestimated by 15% to 54% for all cases investigated. This could be attributed to the non-elastic effects occurring during the impact between the debris and the structure (assumed to be fully rigid in the present tests).

5.6 Application of Experimental Results to Prototype Scale

5.6.1 Scale effects

Physical modeling is one of the most used tools in hydraulic engineering. The idea is that the physical model behaves in a manner similar to the prototype it is intended to emulate (Hughes 1993). This similitude can be achieved if several parameters and conditions are identical and/or proportional in both the prototype and the physical model. Physical modeling in coastal hydraulics is based on three pillars: dimensional analysis, dynamic

considerations, and fulfilling the same differential equations describing the physical processes. The conditions of similarity consist of mathematical relations expressed in the form of ratios between the same parameters observed in both the prototype and model. These relations cannot be changed except by altering the underlying physical assumptions. The conditions of similarity are selected by the investigator to ensure that the physical model is as close as possible a replica of the prototype conditions. In the case of tsunami-induced coastal inundation, the physics of the fluid flow can be described by the following parameters: velocity V, length L, force F, density ρ, dynamic viscosity μ, and gravity g. By neglecting the fluid compressibility and surface tension, the non-dimensional analysis employs three important parameters:

$$\frac{V}{\sqrt{gd}} = F_r \quad \text{Froude number} \tag{5.12}$$

$$\frac{\rho VL}{\mu} = R_e \quad \text{Reynolds number} \tag{5.13}$$

$$\frac{F}{\rho V^2 L^2} = E_u \quad \text{Euler number} \tag{5.14}$$

The similarity between the prototype and its physical model requires quantitative matching. Differences between these characteristics of the model and the prototype are known as scale effects. Thus, scaling of hydraulic experimental results to prototype conditions is challenging and often employs simplifications and approximations.

Free-surface flows and bores for which gravity is the dominant restoring force are usually scaled using Froude similarity. This requires a constant Froude number ($Fr = V/\sqrt{gd}$) for both the model and the prototype. Froude scaling is based on the concept for dynamic similarity, whereby the ratio of the inertia forces to gravity forces must be identical in both the prototype and the model. Therefore, the two systems should operate at the same Froude number:

$$F_{r_m} = F_{r_P} \tag{5.15}$$

The air entrainment is affected by scale effects as a result of the flow turbulence (which is represented by the Reynolds number $R = Vd/\nu$) in the model being underestimated, while the surface tension (characterized by the Weber number $W = \rho(V^2 d)/\sigma$) is overestimated. Investigations into the propagation of small-amplitude

acoustic waves in bubbly liquids have shown that, in general, the speed of sound is both frequency-dependent and a complex function of the size, number and shape of the bubbles (Leighton 1994). Less is known about the propagation of the large pressure changes, such as those that can occur in a wave or bore front impact where the air–water mixture is frequently assumed to behave as a homogeneous compressible fluid. Such an assumption was made by Peregrine and Thais (1996) in a numerical study which simulated wave impacts on a vertical wall by considering two-dimensional, air-entraining, compressible flows that rapidly filled a confined space.

Using freshwater has different physical and chemical properties comparing to seawater. For example, the density and viscosity of the seawater are higher than that for the freshwater due to its higher salinity. Although the quantity of entrained air appears to be similar to the real tsunami flow, using a larger scale can minimize scale effects. To compensate for the effects of air entrainment, scale corrections are required. These scale corrections should be based on data from full-scale and model-scale tests. As discussed by Vrijling et al. (1999), the corrections could be obtained through three steps: (1) determine the frequency of impacts, (2) determine the level of aeration, and (3) obtain the impact force reduction factor based on the aeration level. However, the scale range assumed in this model (1:15 to 1:10) is expected to have minimized such effects.

If the length ratio (L) between prototype (L_p) and model (L_m) is $L = \frac{L_P}{L_m}$, then the bore properties would be scaled as follows:

Velocity: $V_P = V_m\sqrt{L}$ 5.16

Time: $t_P = t_m\sqrt{L}$ 5.17

Pressure: $P_P = P_m L$ 5.18

Force: $F_P = F_m L^3$ 5.19

For the two-dimensional condition tested in this study as the out-of–plane dimension is not scaled. Therefore the Froude scaling for the force in Eqn. 5.19 can be reduced to:

Force: $F_P = F_m L^2$ 5.20

Table 5.5 lists the characteristics of the hydraulic bore that was generated in the laboratory to impact the structural model for the three impounding water depths.

Table 5.5 Bore characteristics – physical model

Impounding Water Depth (m)	Maximum Inundation Depth (m)	Bore Velocity (m/s)	Froude Number F_r
0.55	0.23	1.55	1.032
0.85	0.29	2.12	1.257
1.15	0.35	2.43	1.311

The Froude number for the bores generated in this study (Table 5.5) is within the range of 0.7 to 2.0. This range was estimated by Matsutomi from field measurements and theorized for the five recent tsunamis as reported in Kawata (1999). Analysis of an aerial video for Natori River to determine the bore-depth and -velocity during Tohoku, Japan Tsunami 2011, Robertson (2011) found that the bore flow of depth 1.27 m resulted in a Froude number of 1.95. This result falls close to the upper limit that was suggested by Matsutomi and higher than those archived by the bores generated in this experimental investigation. As seen in Table 5.5; the Froude numbers experimentally determined in this study are higher than the lower limit of Matsutomi, which means that the fully broken bore was used. One should note that the bore presented in the study of Robertson (2011) propagate over the Natori River river/riverbed which differs from the case of the overland propagating bore.

Using a scaling factor of $L = 5$, the experimental maximum inundation depth of 0.23 m (which is generated from the impounding depth of 0.55 m) would correspond to a "real" tsunami inundation depth of 1.15 m. Applying this Froude scaling to the bore characteristics in Table 5.5 provides the prototype bore characteristics in Table 5.6.

Table 5.6 Prototype bore characteristics

Maximum Inundation Depth (m)	Bore Velocity (m/s)	Froude Number F_r
1.15	3.47	1.033
1.45	4.74	1.257
1.75	5.43	1.311

5.6.2 Effects of flume sidewalls

The flow development to fully achieve turbulent conditions was investigated by Kirkgöz and Ardiçhoğlu (1997). The authors noted that at the axis of a fully developed turbulent flow section, the boundary layer extends to the water surface if the aspect ratio $b/h \geq 3$ (where b is the width of channel and h is the depth of flow). The authors did not observe any dip in velocity at the channel centerline even for channels with aspect ratio as low as $b/h = 3$. The bore velocity on a smooth and two geometrically different types of rough surfaces in an open channel was measured by Laser-Doppler Anemometer (LDA) through an experimental study by Tachie et al. (2003). The data illustrated that although the boundary layer in an open channel flow is influenced by the free surface, the roughness effects on the velocity field were similar to those observed in a zero-pressure gradient turbulent boundary layer. Furthermore, it was observed that surface roughness substantially increased the wake parameter in comparison to the smooth wall. Nezu (2005) studied the correlation between the aspect ratio of width/depth (b/h) and the formation of secondary currents. It was reported that the maximum velocity on the centerline occurred below the free surface for $b/h < 5$ (velocity-dip phenomenon), which indicated the presence of secondary currents generated due to the effect of a side wall.

Yang et al. (2004) investigated the mechanism of flow velocity and dip-phenomenon in smooth uniform open channel. The authors discussed three flow regions that were proposed by Keulegan (1938) as shown in Figure 5.66.

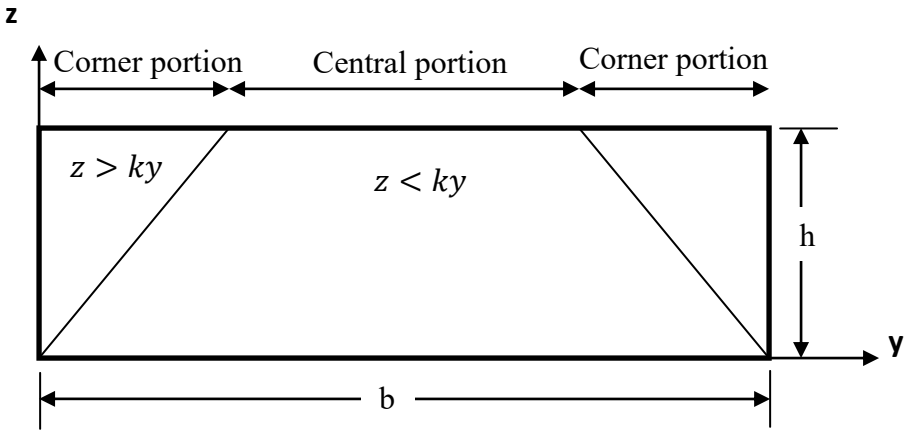

Figure 5.66 Definition of flow regions in rectangular open channel proposed by Keulegan (Yang et al., 2004)

Yang et al. (2004) presented the following formula to determine the location of the maximum velocity in the vertical profile:

$$\frac{z_{max}}{h} = \frac{1}{1+\alpha} \quad 5.21$$

Where z_{max} is the distance of the point of maximum velocity from the channel bed, and α is the dip-correction factor, which can be calculated from the following formula:

$$\alpha = 1.3 \exp\left(-\frac{z}{h}\right) \quad 5.22$$

Where, *y* is the transverse coordinate as shown in Figure 5.66.

For the velocity at the centerline of the channel $z = b/2$. Substituting this value into Eqn. 5.22 results in the following relation of α as function of the aspect ratio (b/h):

$$\alpha = 1.3 \exp\left(-\frac{b}{2h}\right) \quad 5.23$$

Figure 5.67 shows the relationship between α and the aspect ratio based on laboratory measured data from various researchers. The solid line represents α from Eqn. 5.23.

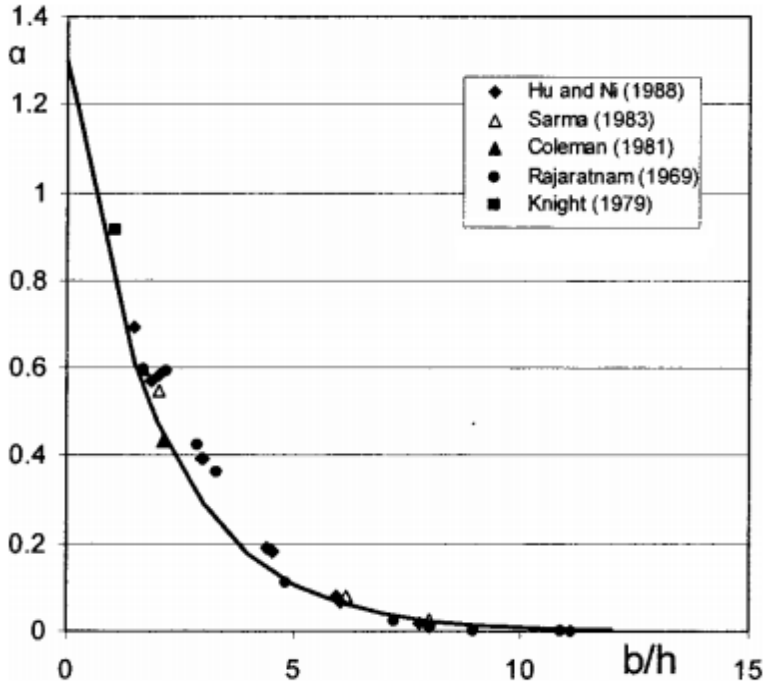

Figure 5.67 Relationship between α and the aspect ratio b/h along the centerline of rectangular channel (Yang et al., 2004)

Figure 5.67 illustrates that the value of the dip-correction factor (α) is significant when the aspect ratio is less than 3, and that α is zero when the aspect ratio is ten or greater. The aspect ratio for the flow in this experimental study is between 3.8 and 6.05; therefore, α is in the range of 0.08 to 0.2. The structural model was installed at the centerline of the flume, and the bore velocities were measured at the centerline. Hence, in this present study, the effects of the side walls are assumed small and can be neglected.

CHAPTER 6

REVIEW OF EXISTING TSUNAMI DESIGN GUIDELINES

6.1 Introduction

In this chapter, a review of engineering design guidelines/standards/codes that provides formulations to estimate the forces induced on the structural models will be presented and discussed. The focus of this research was on tsunami-induced forces on near-shore structures, and previous tsunami events demonstrated that tsunami waves often break offshore and advance inland in the form of a hydraulic bore; therefore, the application of direct loading due to non-breaking and breaking wave forces are not within the scope of this research program.

6.2 Comparison with Experimental Data and Critical Review

This section provides a concise comparison between estimated tsunami parameters using formulae provided in engineering documents discussed in previous sections and parameters experimentally measured.

6.2.1 Bore-velocity as function of bore-depth

An estimation of tsunami inundation-flow velocity is one of the most relevant outcomes in the tsunami research field. Reasonable accuracy in the velocity of a tsunami bore impacting near-shore is essential to estimate the bore-induced forces affecting individual structures and

to assess tsunami damage. As previously stated, the formulae provided in engineering documents are functions of the bore depth for the quasi-steady flow state. Experimentally measured bore velocity for the impounding water heights of 550 mm, 850 mm, 1150 mm for the bore front and the quasi-steady state, in addition to the flow velocity calculated from current formulations are presented in Table 6.1. Note that the experiment results are based on the average of 27 tests. Equation 2.35, as prescribed in FEMA P-646, was modified by considering the horizontal surface of the flume bed in the experiments ($z = 0$) as follows:

$$u_{max} = \sqrt{2gR} \tag{6.1}$$

Where R is the maximum inundation depth measured during testing. For Eqn. 6.2 taken from CCH 2000, d_s corresponds to the quasi-steady flow bore depth:

$$u = 2\sqrt{gd_s} \tag{6.2}$$

Where u is the bore velocity, g is the gravitational acceleration, and d_s is the bore/surge depth.

Table 6.1 Comparison of experimentally-measured bore velocity with FEMA P-646 (2012) and CCH (2000)

Impounding Height (mm)	**Max. Inundation Depth (mm)**	**Depth at Quasi-steady Flow (mm)**	**Experimentally Measured Bore Velocity (m/s)**		**Estimated Bore Velocity (m/s)**	
			Bore Front	**Quasi-steady**	**FEMA P-646**	**CCH 2000**
550	250	162	3.029	1.412	2.215	2.521
850	350	327	3.872	1.906	2.620	3.582
1150	450	410	4.718	2.265	2.971	4.011

A comparison between the measured and estimated velocities highlights that the estimated velocities are higher than those measured for the quasi-steady state condition, but less than those for the bore front. Table 6.1 illustrates that the estimated velocity based on

FEMA P-646 (2012) is in better agreement with the measured velocities of quasi-steady flow state than the CCH (2000), while the latter calculated velocities that more in line with the bore front velocity. Note that the maximum inundation depth, R, used in Eqn. 6.1 was not increased by 30% as prescribed in FEMA P-646 since the depths were measured experimentally.

6.2.2 Pressure

The pressure-time history on the upstream face of the models was recorded at different elevations. The formula provided in SMBTR (2005) was used to calculate the pressure based on the bore-depth for the quasi-steady flow condition. The calculated and experimentally measured (impulsive and hydrodynamic) pressures are provided in Tables 6.2, 6.3, and 6.4. The experiment results are based on the average of 80 tests. These tables illustrate that the calculated pressures slightly underestimate the impulsive pressures measured by the lower level sensors, while the calculated pressures were larger (50% and more) than the measured pressures for the majority of the upper level sensors, particularly for the high impounding water heights of 850 mm and 1150 mm.

Table 6.2 Comparison of experimentally-measured bore pressures with SMBTR 2005 on the square model for a bore generated from the 550 mm impounding water height

Pressure Sensor	Sensor Elevation (mm)	Measured (kPa)		Calculated (kPa)	Ratio	
		Impulsive	Hydro-dynamic	SMBTR 2005 Eq. 3.9	Calculated/ Impulsive	Calculated /Hydro-dynamic
P1	20	4.928	4.019	4.524	0.92	1.13
P2	50	5.927	4.033	4.233	0.71	1.05
P3	100	4.038	3.396	3.748	0.93	1.10
P4	150	4.538	2.875	3.262	0.72	1.13
P5	200	2.817	2.225	2.777	0.99	1.25
P6	250	2.72	1.855	2.291	0.84	1.24
P7	300	1.404	1.203	1.806	1.29	1.50
P8	350	0.958	0.723	1.320	1.38	1.83
P9	400	0.525	0.23	0.835	1.59	3.63
P10	450	0.367	0	0.350	0.95	-

Table 6.3 Comparison of experimentally-measured bore pressures with SMBTR 2005 on the square model for a bore generated from the 850 mm impounding water height

Pressure Sensor	Sensors Elevation (mm)	Measured (kPa)		Calculated (kPa)	Ratio	
		Impulsive	Hydro-dynamic	SMBTR 2005 Eq. 3.9	Calculated /Impulsive	Calculated /Hydro-dynamic
P1	20	7.492	7.087	9.330	1.25	1.32
P2	50	9.526	6.385	9.039	0.95	1.42
P3	100	7.339	5.962	8.554	1.17	1.43
P4	150	9.388	5.517	8.068	0.86	1.46
P5	200	7.114	4.809	7.583	1.07	1.58
P6	250	4.816	4.277	7.097	1.47	1.66
P7	300	4.027	3.473	6.612	1.64	1.90
P8	350	3.061	3.01	6.126	2.00	2.04
P9	400	2.752	2.303	5.641	2.05	2.45
P10	450	2.032	1.543	5.155	2.54	3.34

Table 6.4 Comparison of experimentally-measured bore pressures with SMBTR 2005 on the square model for a bore generated from the 1150 mm impounding water height

Pressure Sensor	Sensors Elevation (mm)	Measured (kPa)		Calculated (kPa)	Ratio	
		Impulsive	Hydro-dynamic	SMBTR 2005 Eq. 3.9	Calculated /Impulsive	Calculated /Hydro-dynamic
P1	20	9.965	7.8345	11.748	1.18	1.50
P2	50	13.465	7.6084	11.457	0.85	1.51
P3	100	11.672	6.899	10.971	0.94	1.59
P4	150	11.109	6.755	10.486	0.94	1.55
P5	200	12.588	6.313	10.000	0.79	1.58
P6	250	12.874	5.689	9.515	0.74	1.67
P7	300	8.697	4.676	9.029	1.04	1.93
P8	350	5.798	4.03	8.544	1.47	2.12
P9	400	4.854	2.942	8.058	1.66	2.74
P10	450	4.262	2.536	7.573	1.78	2.99

The calculated pressures overestimated the hydrodynamic pressures recorded for the quasi-steady flow by approximately 50% for the lower level sensors and by more than 100% for the upper level sensors—particularly for the 850 mm and 1150 mm impounding water depths. This may be attributed to the fact that the SMBTR formula was originally derived from the hydrostatic pressure distribution. SMBTR assumes an equivalent hydrostatic pressure resulting from an inundation depth equal to three times the actual inundation depth for the hydrodynamic flow state. Figure 6.1 illustrates the pressure distributions on the upstream face of the square model. It is evident that as the maximum impounding water depth increased, the calculated pressures became increasingly more conservative. This

suggests the necessity of a more rational approach that is based on a comprehensive study of the bore-structure interaction.

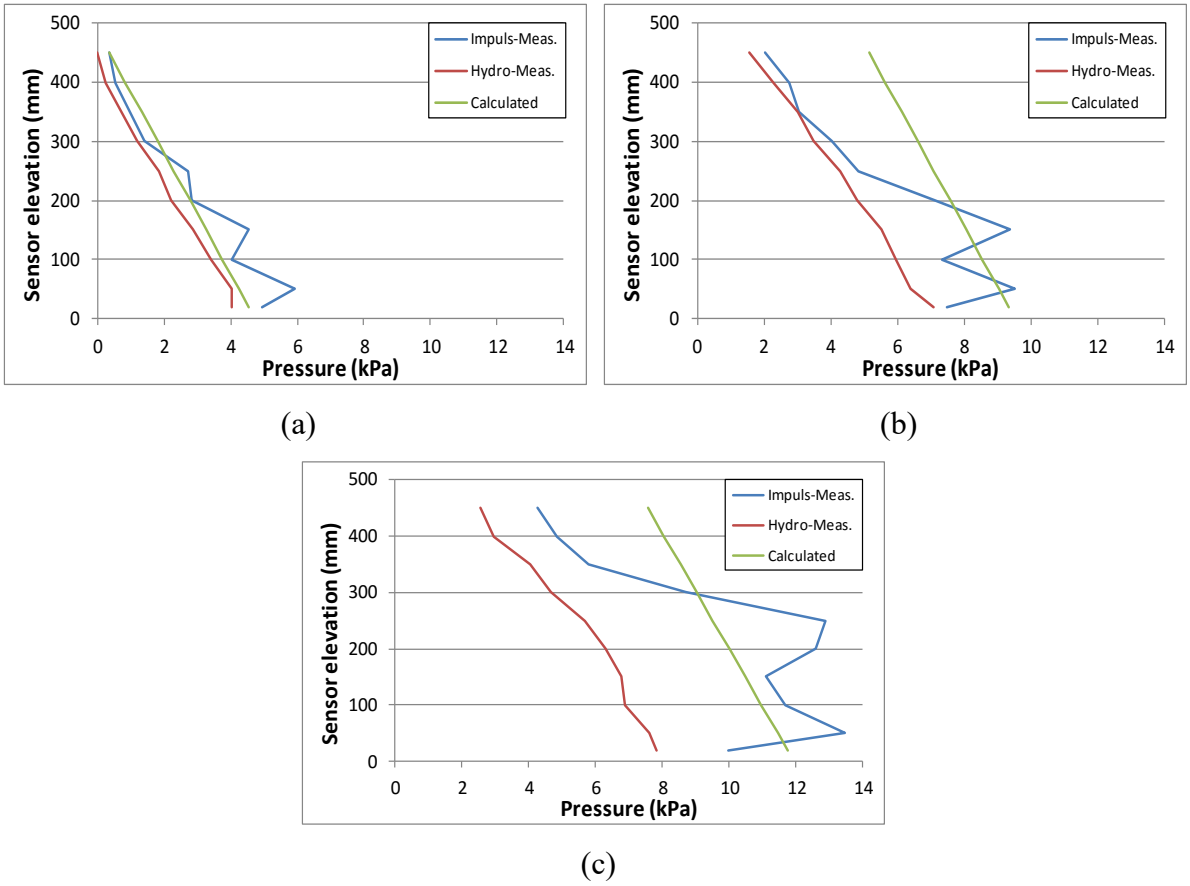

Figure 6.1 Pressure distributions on the upstream face of the square model for bores generated from impounding depths of: **a)** 550 mm; **b)** 850 mm; and **c)** 1150 mm

6.2.3 Hydrodynamic force

The hydrodynamic force is defined as the force exerted on the structure during the quasi-steady flow conditions. Therefore, the bore depth-time history for each test was examined to identify the quasi-steady flow condition and then the corresponding force on the force-time history was selected. To reduce experimental error, the average hydrodynamic forces of three tests with similar conditions were selected from the force-time history and are presented in Table 6.5. The table also lists the calculated hydrodynamic forces using FEMA P-646, SMBTR, and CCH 2000. The last two columns provide the ratio of the experimentally recorded runup and the impulsive forces to the hydrodynamic forces. Table 6.5 illustrates that the hydrodynamic forces calculated with FEMA P-646 and CCH (2000)

underestimated the experimental forces; however, SMBTR provides an overestimation of up to 74%.

Table 6.5 Comparison of experimental forces with those calculated using FEMA P-646 (2012), SMBTR (2005) and CCH (2000)

Impoun. height (mm)	"R" Max Inund. height (mm)	$(hu^2)_{max}$	Calculated Forces (N)			Experimental Forces (N)			Ratio of Impulsive or Run-up to Hydrodynamic	
			FEMA P-646 F_d	SMBTR F_{HD}	CCH 2000	F_d	F_i	F_r	F_i/F_d	F_r/F_d
550*	246	0.074	22	235	0.47	135	150	235	1.11	1.74
550	252	0.078	23	242	0.48	150	404	250	2.69	1.67
850*	345	0.146	44	491	1.34	397	272	626	0.69	1.58
850	352	0.152	46	538	1.36	402	303	635	0.75	1.58
1150*	452	0.251	75	884	2.19	795	684	1088	0.86	1.37
1150	456	0.255	76	923	2.21	610	720	1044	1.18	1.71

* Test with wet-bed condition

6.2.4 Impulsive force

The impulsive force is characterized by a sharp rise in the force-time history over a short duration. This force resulted from the impact of the leading edge of the bore with the structural models. The experimental data illustrates that the initial flume bed condition (wet or dry) had a significant effect on the magnitude of the impulsive force. For dry flume bed conditions, the maximum force recorded was the impulsive force, while the run-up force was the maximum force component under wet flume bed conditions. Note, however, that in this experimental program dry bed conditions were only possible for the 550 mm impounding water depth. This phenomenon was also noted in previous investigations conducted by Ramsden and Raichlen (1991) and Chanson (2000). As stated in Section 3.4.5, CCH (2000) and FEMA P-646 (2008) provide formulations to calculate the impulsive force

(Eqns. 3.24 and 3.25, respectively), while SMBTR (2000 and 2005) does not specifically address this force. SMBTR (2000) provides formulae to calculate the pressure of a solitary wave with and without breakup, which were proposed by Asakura et al. (2000), Ikeno et al. (2001), and Ohmori et al. (2000), and tsunami wave force formula proposed by Iizuka and Matsutomi (2000). Therefore, SMBTR is not included in this comparison of the impulsive force. Table 6.6 demonstrates that the calculated forces using CCH (2000) significantly overestimates the measured forces.

Table 6.6 Comparison of experimentally-measured impulsive forces with FEMA P-646 (2012) and CCH (2000)

Impounding Height (mm)	Max. Inund. Depth (mm)	Experimentally Measured Impulsive Force (N) F_I	Calculated Impulsive Force (N) F_I	
			FEMA P-646	CCH 2000
550*	246	150	33	2642
550	252	404	35	2773
850*	345	272	66	5197
850	352	303	68	5410
1150*	452	684	113	8920
1150	456	720	115	9078

* Test conducted under wet-bed condition

6.2.5 Debris impact force

In 2011 the 4th edition of the Coastal Construction Manual (FEMA P-55) was published by FEMA. In this edition, Section 8.5.10 recommends using the formula used to calculate the debris impact force provided in ASCE 7-10:

$$F_i = WVC_D C_B C_{Str} \quad 6.3$$

Where F_i is the impact force acting at the stillwater level in lb., W is the weight of the debris in lb., V is the flow velocity (the approximate value suggested is $0.5\sqrt{gd_s}$), $C_D, C_B,$ and C_{Str} are the depth, blockage, and structure coefficients, respectively.

- The values of the depth coefficient (C_D) are listed in Table 6.7; they are selected based on the flood hazard zone and the water depth.
- The blockage coefficient (C_B) is used to account for the screening offered by trees and other obstructions that exist upstream from the structure investigated and causes a reduction in debris velocity as provided in Table 6.8.
- The values of the structure coefficient (C_{Str}) are calculated from the equation provided in Chapter 5 of ASCE 7-10 as follows:

$$C_{Str} = \frac{3.14 C_I C_O R_{max}}{2g\Delta t} \qquad 6.4$$

Where C_I and C_O are the importance and the orientation coefficients, with values of 1.0 and 0.80, respectively. R_{max} is the maximum response ratio, Δt is the impact duration (taken as 0.03 s) and g is the gravitational acceleration (32.2 ft/sec^2).

FEMA P-55 assumes an approximate natural period for different building types as follows: 0.75 s for timber pile and masonry column, 0.35 s for concrete pile or concrete or steel moment resisting frames, and 0.2 s for reinforced concrete foundation walls. Using these values together with Equation 6.4, FEMA P-55 recommended values for the structure coefficient (C_{Str}) which are presented in Table 6.9.

Table 6.7 Depth coefficient (C_D) by flood hazard zone and water depth

Flood Hazard Zone and Water Depth	C_D
Floodway or Zone V	1.0
Zone A, stillwater flood depth >5 ft	1.0
Zone A, stillwater flood depth = 4 ft	0.75
Zone A, stillwater flood depth = 2.5 ft	0.375
Zone A, stillwater flood depth <1 ft	0.00

Table 6.8 Blockage coefficient (C_B) by screening level and flow path width

Degree of Screening or Sheltering within 100 Ft Upstream	C_B
No upstream screening, flow path wider than 30 ft	1.0
Limited upstream screening, flow path 20-ft wide	0.6
Moderate upstream screening, flow path 10-ft wide	0.2
Dense upstream screening, flow path less than 5-ft wide	0.0

Table 6.9 Structure coefficient (C_{Str}) by screening level and flow path width

Building Structure System	C_{Str}
Timber pile and masonry column supported structures 3 stories or less in height above grade	0.2
Concrete pile or concrete or steel moment resisting frames 3 stories or less in height above grade	0.4
Reinforced concrete foundation walls (including insulated concrete forms)	0.8

The values recommended by FEMA P-55 (2011) for the above coefficients ($C_D, C_B,$ and C_{Str}), along with the debris weight and the experimentally-measured flow velocity, were used in Equation 5.9. The experimental and calculated impact forces for three different magnitudes for C_{Str} are presented in Figure 6.2. Although the largest value for the structure coefficient ($C_{Str} = 0.8$) was used for the six test series, the calculated impact forces for all six test series were less than 10% of the corresponding experimentally-measured impact forces. This discrepancy may be related to uncertainties in the estimation of most parameters in Equation 5.9 (e.g., size, shape, weight, and velocity of the debris, the flow velocity and duration of the impact (Δt)). Furthermore, this formula assumes that the velocity of the debris is the same as the flow velocity. However, experimental work and field observations (Chock et al. 2013) have shown that this assumption is often inaccurate.

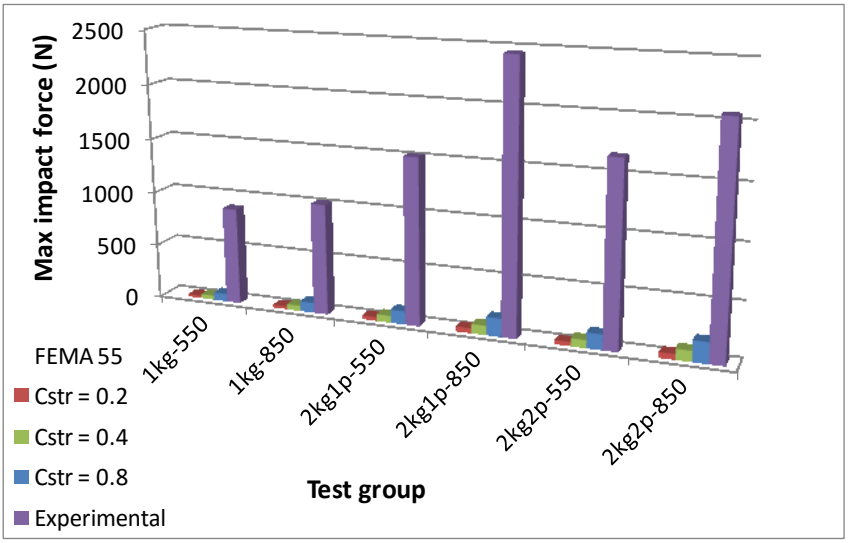

Figure 6.2 Experimental and calculated impact forces using FEMA P-55 (2011)

The force required to accelerate debris entrained in moving water is usually greater than that required to accelerate the same debris in air. This force difference is due to the increased fluid drag and inertia induced by an increase in fluid density and viscosity. This phenomenon can be accounted for by adding a virtual mass:

$$F_{max} = C_m u\sqrt{km} \qquad 6.5$$

Where C_m is the added mass coefficient; the value depends on several variables such as debris shape, degree of submergence, orientation, and natural period of vibration. Sarpkaya

and Isaacson (1981) proposed that $C_m \rightarrow 0$ for long, slender debris with their axis oriented in the flow direction, while $C_m = 1.0$ when the debris axis is normal to flow direction.

Haehnel and Daly (2002) proposed that the analysis of debris impact be conducted using a single-degree-of-freedom model. They used Equation 6.5 with different values for C_m varying from 0 to 3.5, depending on the debris shape and orientation. Based on their study, FEMA P-646 (2008) adopted Equation 6.5 and recommended $C_m = 2.0$, and u as the maximum flow velocity, while assuming that the debris moves with velocity similar to the flow velocity. Equation 6.5 was used to calculate the impact force using three values for $C_m (1.5, 1.75, \text{and } 2.0)$. The calculated and experimental forces are provided in Figure 6.3.

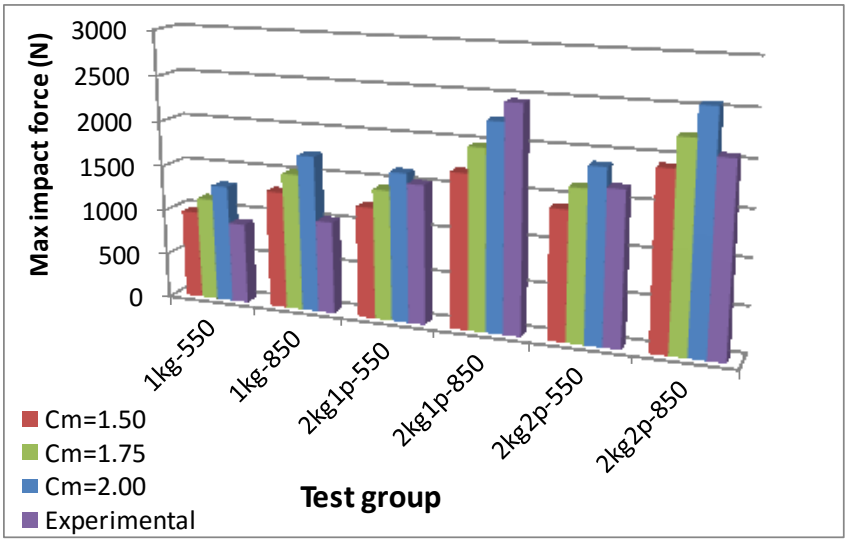

Figure 6.3 Experimental and calculated maximum debris impact force using three C_m values

The following observations are drawn according to the results presented in Figure 6.3:

- Using $C_m = 1.5$, the calculated forces for the small debris (1kg) were in good agreement with those experimentally recorded; while for the 2kg debris, the calculated forces were underestimated by up to 31%.
- Using $C_m = 1.75$, the calculated forces for three of the series (1kg-550, 1kg-850 and 2kg2P-850) were overestimated by 8% to 48%, and the other three series (2kg1P-550, 2kg1P-850 and 2kg2P-550) were underestimated by 2% to 20%.

- Using $C_m = 2.0$, the impact forces for four tests employing large debris (2kg1P-550, 2kg1P-850, 2kg2P-550, and 2kg2P-850) were close to the experimental forces; while for the other two test series employing small debris (1kg-550 and 1kg-850), the calculated forces overestimated the experimental results by 46% and 70%, respectively.

Based on this limited analysis, using the mass hydrodynamic coefficient to calculate the debris impact force demonstrated that: (1) $C_m = 1.5$ provides good estimation for small debris (1 kg); (2) $C_m = 1.75$ provides relatively good estimation for large debris with small slenderness ratio (2kg2p debris); and (3) $C_m = 2.0$ provides reasonable estimation of the impact force for large debris with relatively high slenderness ratio.

In the 2nd edition of FEMA P-646 (2012), Equation 6.5 was revised as follows:

$$F_i = 1.3 u_{max} \sqrt{k m_d (1 + c)} \qquad 6.6$$

Where u_{max} is the maximum flow velocity at the location of the structure, k is the combined stiffness of the debris and the impacted structure, m_d is the mass of the debris, and c is the hydrodynamic mass coefficient that varies from 0 to 1 depending on the debris size and orientation. This new hybrid formula (suggested from combining theoretical and experimental investigations) is based on the study of Haehnel and Daly (2002) and is also suggested by ASCE 7-10. The 1.3 factor is applicable for Risk Category IV structures, as identified in ASCE 7. The velocity of floating debris is assumed equal to the flow velocity – an additional recommendation stating that the debris velocity should be reduced to 50% of the flow velocity for rolling or dragging debris was added. FEMA P-646 proposed $c = 1.0$ for any type of debris that is oriented transversely to the flow; for longitudinally-oriented debris, c has different values depending on the type of debris: $c = 0$ for wooden logs, $c = 0.3$ for 20-ft shipping containers, and $c = 0.2$ for 40-ft shipping containers.

In this study, the values for c recommended by FEMA were used in Equation 6.6 to calculate the maximum impact force for the six test groups. The calculated and experimental impact forces are shown in Figure 6.4.

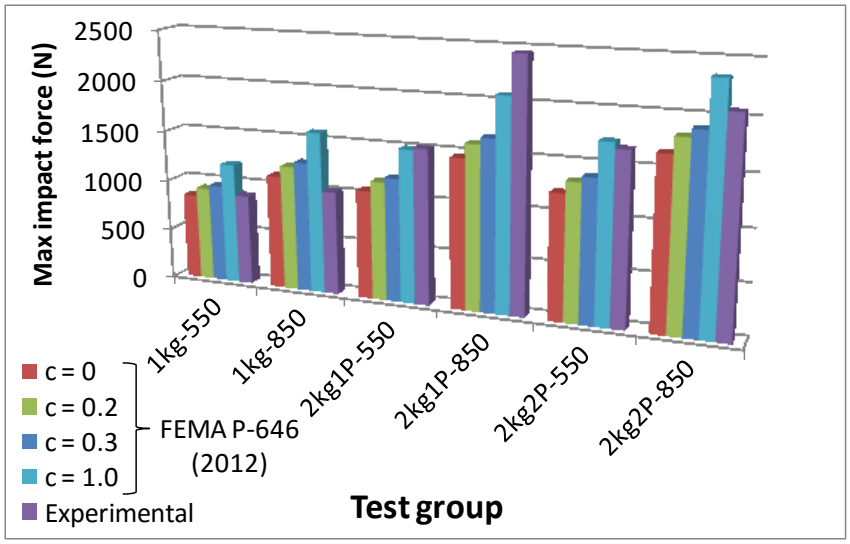

Figure 6.4 Experimental and calculated maximum debris impact force using FEMA P-646 (2012) with four recommended *c* values

Figure 6.4 indicates that using $c = 0$, as recommended by FEMA P-646 (2012), for log debris underestimates the impact force for all test groups with the exception of group 1kg-850. Although FEMA P-646 (2012) recommends $c = 1$ for debris with transverse orientation, this value provided satisfactory predictions for the impact force with the exception of group 2kg1P-850. Equation 6.6 seems to suggest that debris with transverse orientation results in higher impact forces on the structures, while laboratory data of this investigation does not support this and is in agreement with the work of Haehnel and Daly (2004). Thus, further investigation of the hydrodynamic mass coefficient, *c,* is required to provide improved impact force estimations.

CHAPTER 7

CONCLUSIONS, RECOMMENDATIONS FOR FUTURE WORK

7.1 Introduction

This study involved a comprehensive experimental program focusing on the evaluation of extreme hydrodynamic impacts and loading on free standing structures. The tests were conducted with structural models of circular and square cross-sections, which were impacted by hydraulic bores which closely simulate bores induced by broken tsunami waves advancing inland. This study aimed to investigate the bore-structure interaction and to quantify the pressures, forces, moments, displacements, and accelerations experienced by the structural models. Low-lying timber mitigation walls were installed upstream from the models to investigate their effects on reducing the base shear force, base overturning moments, and displacements. Conclusions drawn from the analysis of the experimental work conducted as part of this study are outlined in this chapter.

Several features of the experimental work conducted in this study are unique with respect to previous research:

1. The size and shape of the structural models: square and circular models with largest dimensions to date were used in this research.
2. For the first time in such an experimental program, several parameters were measured simultaneously: time-histories of the hydrodynamic pressure, total base

shear force, base overturning moment, structural lateral displacement, and structural acceleration.

3. The time-history of the bore depth at several locations in the flume and at several sides of the structural models was measured simultaneously. In previous research by others, flow depth measurements were reported; however this did not include measurements at the surface of the model. In this study, this was achieved by placing water level gauges directly on the surface of the models.
4. The forces and overturning moments were accurately measured through the use of a high frequency (1 kHz), six-degree of freedom dynamometer.
5. For the first time in such studies, a high-speed camera was used to capture and/or subsequently calculate:
    a. The bore-structural model interaction mechanism,
    b. The bore velocity-time history, and
    c. The debris velocity, orientation, eccentricity and the impact.

7.2 Conclusions

The increased number of extreme coastal disasters combined with increases in the population density and activities in coastal regions have intensified the necessity of improving the design of tsunami-resistant buildings in such disaster-prone areas. During the past three decades, several small-scale studies have been conducted to investigate wave-structure interactions. However, not much advancement has occurred since the work of Goda (1985) on wave impact on coastal structures. Furthermore, the majority of previous tests focused on wave impacts on coastal structures, but only a limited number of studies investigated the impact of extreme hydrodynamic loading on buildings. The cost associated with physical modeling and scale limitations, in some instances, have prevented large-scale experimental studies. This study is a significant step towards further understanding the mechanisms and effects of tsunami-bore forces exerted on near-shore structures. The present research focused on investigating: (1) the hydraulic bore characteristics; (2) the forces and moments induced on near-shore structures; (3) the influence of low-height structural mitigation walls installed upstream from the structural models; and (4) the impact forces

generated by waterborne debris. As previously discussed, one of the major goals of this work was to address the very limited existing experimental studies, and to provide novel research data and results. Several specific conclusions can be drawn from this research.

*7.2.1 **Bore depth***

Seventeen capacitance water level gauges were used in two groups: eight stand-alone probes and nine others attached directly to the structural models with 1 kHz sampling frequency. The bore depth-time histories recorded in the absence of the structural model at different sections along the flume illustrated that, at any section, the slope of the water increases with increasing impounding water depth in the reservoir and with increasing proximity to the swinging gate (section generating the dam-break). Three pairs of water level gauges were installed one meter apart along the flume. The pairs were placed at the one-third locations of the flume width. The bore depth recorded by a pair of gauges for a particular section along the flume was identical. The bore depths recorded at the location of the structural models were higher than measured in the absence of the models for the same impounding water depths. The higher bore depths are attributed to the bore flow accumulating on the upstream face of the model before being redirected around the sides of the model. The water level gauges directly installed on the models provided an accurate measurement of the bore depth, which could improve the estimation of hydraulic bore-induced forces.

*7.2.2 **Bore velocity***

The bore velocity is one of the important parameters used to quantify the hydrodynamic forces induced on structures located in the bore propagation path. Several formulations have been proposed in the literature. In those formulations, the bore velocity is a function of the bore depth at the location of interest. A clear disagreement was found between those formulations suggesting greater complexity accompanying tsunami bore inundation of coastal communities. As consequences, and in addition to uncertainty in specifying the maximum inundation depth at a specific location, estimating tsunami-induced loads becomes very challenging. Testing in this experimental program demonstrated high impulsive forces caused by the impact of the bore front on the upstream face of the structural models. Therefore, two different techniques were used to determine the bore front

velocity. In the first technique, the bore-front was tracked along a distance of 1.5 m upstream from the structural model using a 300 mm x 300 mm grid that was marked on the flume bed. For the second technique, three pairs of water level gauges were installed in the flume in three rows. The bore-front velocities estimated from the two methods were in good agreement; minor differences were related to the difference in bore depth at the time of the measurements. In addition, a third method was investigated (the Particle Image Velocimetry) to capture the bore velocity-time histories for the three impounding water depths used in the tests. These tests provide the variation of bore velocity through the different flow stages.

*7.2.3 **Bore-induced pressure***

Ten pressure transducers were installed at different elevations on the upstream face of the structural models to provide detailed data on the pressure distribution. Typical pressure-time histories of the lower elevation sensors were characterized by the presence of a sudden peak at the time the bore front impacted the models. This peak pressure (impulsive) had a short duration, and the magnitude increased for sensors located near the base of the model (adjacent to the flume bed). This impulsive pressure was influenced by two variables: flume bed initial condition (wet or dry); and shape of the structural model. For dry flume bed conditions, the impulsive pressures were notably higher than the corresponding pressures for the wet bed conditions. Typically, the impulsive pressures recorded on the square model were higher than the corresponding pressures on the circular model. The experimental data in this study indicated a strong correlation between the bore depths, pressures, and associated forces.

*7.2.4 **Bore-induced forces and moments***

The force-time histories experienced by the structural models were characterized by three distinct stages of force development: impulsive force caused by leading edge of the bore front impacting the model; run-up force which corresponded to the highest force recorded in each test; and a relatively moderate magnitude hydrodynamic force due to the quasi-steady flow state. FEMA P-55 (2011) and P-646 (2012) were used to calculate the hydrodynamic forces as a comparison against those recorded during testing. The equations for the flow

velocity and momentum flux provided in the guidelines were used to calculate the hydrodynamic force. The calculated forces underestimated the experimental forces; however, the forces calculated with FEMA P-55 were in better agreement with the experimentally recorded forces. The forces calculated from FEMA P-646 were less than 15% of the experimental forces. The predicted hydrodynamic forces were significantly improved, and both guidelines provided similar results when the experimentally measured bore velocities and bore depths corresponding to the quasi-steady flow state were used.

*7.2.5 **Initial bed condition***

The force-time histories resulting from different impounding depths demonstrated the existence of three components: the impulsive force, the runup (surge) force, and the quasi-steady hydrodynamic force. These experiments were conducted with two initial flume bed conditions: dry and wet. Although the bore depth-time histories for wet-bed conditions were similar to those recorded under dry-bed conditions, the force- and pressure-time histories showed significant differences, specifically for the first two force components. For wet-bed conditions, the impact force was always smaller than the run-up force; while for dry-bed conditions, the impact force had the larger magnitude compared to the run-up and quasi-steady hydrodynamic forces. In addition, the sudden rise in the pressure-time histories for the wet-bed conditions were smaller in magnitude than those recorded for the dry-bed conditions.

*7.2.6 **Mitigation walls***

The effect of mitigation walls on the base shear force and the base overturning moment was investigated. Specifically, the effects of four different wall parameters related to the wall geometry and location were investigated. A comparison of tests with and without the mitigation walls installed in the flume indicated the following:

- Location of the wall: the mitigation wall placed at 1D (where D is the diameter or width of the structural model) was the most effective at reducing the base shear force (20%), but with a slight increase in the base overturning moment.
- Inclination angle of the wall: the 45˚-inclined mitigation wall placed at 3D increased the impulsive force on the model (73%) and the impulsive overturning moment

(280%). The latter was a direct result of the bore impacting the structural model at a higher elevation.

- Wall height: higher mitigation walls located closer to the structural models resulted in smaller base shear forces experienced by the models. However, the redirection of the bore towards the upper part of the structural model resulted in an increase in the base overturning moment. An additional effect generated by the presence of the wall was the result of increasing water depth upstream from the model.
- Cross-sectional shape of the wall: the curved wall was more effective in reducing both of the base shear force and the base overturning moment in the structural models compared to the vertical mitigation wall of similar height.

*7.2.7 **Debris impact***

This study presented experimental data from six test groups which involved floating debris impacting the circular structural model. The debris was transported by hydraulic bores generated by the rapid opening of a swing gate, which impounded a large body of water. Two impounding water depths (550 mm and 850 mm) were used in the debris tests. The bores resulting from higher impoundment depths were avoided to prevent damaging the structural model. Three debris with different geometry and mass were used. The main conclusions from the analysis of the data is summarized as follows

- Debris orientation: this is an important parameter which influences the magnitude of the impact force. The maximum impact force for each test series was recorded when the debris impacted the model directly (zero inclination angle from the flume centerline along the flow direction) at the middle point of the upstream face of the model. Data indicate that as the debris inclination angle increased, the impact force decreased.
- Debris eccentricity at impact: this parameter is a combination of two components: the eccentricity of the impact with respect to the center of the model and the debris orientation angle. Debris eccentricity was found to affect the magnitude of the debris impact force. The tests results showed that an increment in the debris eccentricity from the center of the structural model decreases the impact force and vice versa.

- Debris slenderness ratio: lab observations demonstrated that for the same bore height, debris with increased slenderness ratio generated larger impact forces. Furthermore, the larger slenderness ratio led to debris impacts at smaller inclination angles. Unlike the impact force, the debris velocity decreased as the debris was more slender. In other words, slender debris requires additional time to attain the same velocity as the surrounding flow.
- Debris velocity: as the impounding water depth increased, the bore velocity increased and, subsequently, the debris velocity increased. When all other parameters (debris - shape, mass, orientation, and eccentricity) were kept constant, the impact force was directly proportional to the debris velocity.

Three approaches used to calculate the maximum debris impact force: constant-stiffness, impulsive-momentum, and work-energy. The calculated forces were compared to the corresponding maximum experimentally-recorded forces for each test series. Although debris stiffness was tested and used in the calculations, the constant-stiffness approach underestimated impact forces for all test series. The work-energy approach provided better estimation of the debris impact force compared to the impulsive-momentum approach. Although the constant-stiffness recommended by FEMA P-646 (2008) with $C_m = 2.0$ provided reasonable estimation for the maximum debris impact force for relatively large mass debris, the impact forces were overestimated by up to 70% for small debris. This seems to suggest that the magnitude of the added mass factor C_m requires further investigation based on expected debris properties rather than current simplistic approaches. The maximum experimentally-recorded impact forces of the six test groups were compared with a recent formula provided in the 2nd edition of FEMA P-646 (2012). Although the laboratory-predicted debris stiffness was used with this formula, the estimated forces showed significant differences to the experimental forces. The mass hydrodynamic coefficient and the debris orientation, which generated the maximum impact force, require further investigation.

Although the proposed maximum values for the coefficients presented in FEMA P-55 were adopted, the calculated impact forces were still highly underestimated (less than 10% of the experimental forces). Four values recommended by FEMA P-646 for the

hydrodynamic mass coefficients (0, 0.2, 0.3 and 1.0) were investigated. The largest value of this coefficient (1.0) better estimated the impact force for large debris (2kg), while using the other values for this coefficient estimated reasonably well the impact forces for small debris (1kg). Note, however, that the mass coefficient of 1.0 is specified for transversely oriented debris, which is not consistent with the longitudinally-oriented debris impacts of this study.

*7.2.8 **Design guidelines***

Current design codes/standards/documents provide limited specific guidance for the practicing engineer designing structures in tsunami hazard areas [CCH 2003; IBC 2012 ASCE 7-10; FEMA 2000]. The recommendations of FEMA P646 (2012) provide some basic prescriptions for calculating tsunami forces that only serve as recommendations; this document is not a mandatory design code. The intense development of coastal regions in different countries means more critical facilities are or will be built within the tsunami hazard areas. Understanding the forces that these buildings could be subjected to is essential to ensure that they meet their design performance criteria. Without a proper and scientifically-based understanding of these forces and their effects, such structures could suffer major damage in the event of a large tsunami. The results of such improperly designed structures were extensively documented following the recent 2011 Tohoku Earthquake and Tsunami (Chock et al., 2013). Many structures designated as evacuation areas failed due to extremely large flow depths and velocities than expected [Mimura et al. (2011), Chock et al. (2012)].

7.3 Recommendations for Future Research

In the present research, laboratory data were collected and analyzed, and were compared against recently published methods. The performance of these processes led to the following recommendations for future research in the field of extreme hydrodynamic loading on structures:

- **Bore-structure interaction**

The hydraulic bores generated by the dam break technique were very similar to those witnessed during past tsunami events. The flume dimensions and reservoir size represents a major challenge which limited the size of the structural model and the maximum depth of

the flow. Therefore, the availability of larger flumes (deeper and longer) will help researchers perform experimental tests with larger structural models and to investigate a larger range of flow depth and velocity. Therefore, larger-scale experimental testing is desirable.

- **Mitigation measures**

Although past events in certain areas demonstrated that extreme tsunami inundation is possible, the presence of mitigation measures can reduce the loss of lives and structural damage of near-shore buildings. Therefore, proposing new mitigation measures which may be more effective in attenuating tsunami impact on near-shore communities is a crucial task.

- **Debris impact force**

Analysis of the data for waterborne wooden debris impacting a cylindrical structural model in a laboratory-simulated phenomenon was conducted. Thereafter, currently available formulas for the impact force were assessed. The influences of debris velocity, orientation, eccentricity, mass, and shape on the maximum impact force were investigated. The laboratory data was also used to verify the hydrodynamic added-mass coefficient existing in the literature. The comparison of experimentally-recorded debris impacts with the calculated forces proposed by current design guidelines demonstrated discrepancies in the values of the structure coefficient with the debris orientation, and the added mass coefficient. Thus, more investigation to establish appropriate values for the effect of the water surrounding the debris on the magnitude of the impact force is required.

REFERENCES

AASHTO (1998), LRFD Bridge Design Specifications, 2nd edition, *American Association of State Highways and Transportation Officials*, p. 26–27.

Al-Faesly T., Palermo D., Nistor I., and Cornett A. (2012), "Response of Structural Elements Subjected to Tsunami Hydrodynamic Forces," *International Journal of Protective Structures, Vol. (3), No. 4, 2012.*

Al-Faesly T., Nistor I., Palermo D., Cornett A.,(2011) "Experimental Study of Structures Impacted by Simulated Tsunami Bore, *Coastal Structures 2011, COPRI-ASCE*, Yokohama, Japan, September, 2011, Paper No. D1-115, 13 pp.

Almeida A. B., and Franco A. B. (1994). Modeling of dam-break flows. Computer modeling of free-surface and pressurized flows, M. H. Chaudhry and L. W. Mays, eds., 343–373.

Arikawa T. (2009), Structural Behavior under Impulsive Tsunami Loading, *Journal of Disaster Research* Vol. 4 No. 6, pp. 377-381.

Árnason, H. (2005). Interactions between and incident bore and a free-standing coastal structure, Ph.D. Thesis, University of Washington, Seattle, 172pp.

Árnason, H., Petroff, C., and Yeh, H. (2009). "Tsunami bore impingement on to a vertical column." Journal of Disaster Research, 4(6), 391–403.

Asakura R., Iwase K., Ikeya T., Takao M., Fujii N., and Ohmori M. (2000), An Experimental Study on Wave Force Acting on On-shore Structures Due to Overflowing Tsunamis, *Proceeding of Coastal Engineering, Japan Society of Civil Engineering*, 47, pp. 911-915, (in Japanese).

Asakura R., Iwase K., Ikeya T., Takao, Kaneto T., Fujii N., and M. Ohmori (2002), The Tsunami Wave Force Acting on Land Structures, *Proceedings the 28th International Conference on Coastal Engineering,* pp.1191-1202.

ASCE 7-02, (2003), Minimum Design Loads for Buildings and Other Structures, SEI/ASCE 7-02, American Society of Civil Engineers, 376 pp.

ASCE 7-10, (2010) Minimum Design Loads for Buildings and Other Structures*, ASCE/SEI Standard 7-10*, American Society of Civil Engineers, Reston, Virginia, USA.

ASCE 24-5, (2006), Flood Resistant Design and Construction, *ASCE Standard 24-05*, American Society of Civil Engineers, Reston, Virginia, USA, pp.62.

ASCE 7-05, (2006), Minimum Design Loads for Buildings and Other Structures, *ASCE/SEI Standard 7-05*, American Society of Civil Engineers, Reston, Virginia, pp.388.

Ben C. Y. (2002), Open Channel Flow Resistance, *the Journal of Hydraulic Engineering,* Vol. 128, No. 1, pp 29-39.

Bornhold B. D., Harper J. R., McLaren D., and Thomson R. E., (2007). Destruction Of The First Nations Village of Kwalate by a Rock Avalanche Generated Tsunami, *Atmosphere-Ocean,* 45:2, 123-128, DOI: 10.3137/ao.450205

Bryant E. (2001), Tsunami: The Underrated Hazard, Cambridge University Press, London, UK, 320 pp.

Camfield, F. (1980), Tsunami Engineering, Coastal Engineering Research Center, US Army Corps of Engineers, Special Report (SR-6), 222 p.

Carrier, G. F., Wu, T. T., and Yeh, H. (2003), Tsunami Run-up and Draw-down on a Plane Beach, *Journal of Fluid Mechanics,* 475, (March), pp. 79-99.

CCH (2000), City and County of Honolulu Building Code, *Department of Planning and Permitting of Honolulu Hawaii*, *Chapter 16, Article 11,* Honolulu, Hawaii.

The Central Disaster Prevention Committee of Cabinet Office, Government of Japan, (2005), report: Meiji Sanriku Earthquake Tsunami in 1896, Mizuho Information and Research Institute. Inc., 167 p. (In Japanese)

Chanson H. (2005), Analytical Solution of Dam Break Wave with Flow Resistance. Application to Tsunami, 31st IAHR Congress, Seoul, Korea, September11-16, pp. 3341-3353.

Chanson H. (2006), Tsunami surges on dry coastal plains: Application of dam break wave equations, Coastal Engineering Journal, Vol. 48, No. 4, pp. 355-370 (ISSN 0578-5634).

Chanson H. (1999). "The Hydraulics of Open Channel Flows: An Introduction." Butterworth- Heinemann, Oxford, UK, 512 pages.

Chanson H., Aoki S., and Maruyama M. (2003). "An Experimental Study of Tsunami Run-up on Dry and Wet Horizontal Coastlines." *Science of Tsunami*, *20*(5), Hazards Vol.20, No. 5, pp. 278–293.

Chanson H., Aoki S., and Maruyama M. (2000), Experimental investigations of Wave Run-up Downstream of Nappe impact Application to Flood Wave Resulting from Dam Overtopping and Tsunami Wave Run-up, Coastal/Ocean Engineering Report No. COE00-2, 39 p.

Chock G., Robertson I., Kriebel D., Francis M., and Nistor I. (2013) , Tohoku, Japan, Earthquake and Tsunami of 2011 – Performance of Structures under Tsunami Loads, ISBN 978-0-7844-7697-0 (eBook), SEI - ASCE, 359 p.

Chock G., Robertson I., Kriebel D., Francis M., and Nistor I. (2012) , Tohoku Japan Tsunami of March 11, 2011 – Performance of Structures, Final Report, ASCE, 297 p.

Chow V. T. (1959), "Open-channel Hydraulics" Mc Graw-Hill Book Company, pp. 680

Clague J. J., Yorath C. J. J., Franklin R., and Turner R. J. W. (2006). Tsunami hazard zones for southwestern British *Columbia. At risk: Earthquakes and tsunamis on the west coast, Tricouni Press, Vancouver, 200 p.*

CNN (2007), Retrieved from http://www.cnn.com/interactive/world/0502/gallery.tsunami. photos/frameset exclude.html

Cross R. H. (1967), Tsunami surge forces, Journal of Waterways and Harbor Division, ASCE, Vol. 93, No. 4, pp. 201-231.

Cumberbatch E. (1960), The Impact of a Water Wedge on a Wall. *Journal of Fluid Mechanics*, 7, pp 353-374 doi: 10.1017/S002211206000013X.

Dames and Moore (1980), Design and Construction Standards for Residential Construction in Tsunami Prone Areas in Hawaii, Prepared for the Federal Emergency Management Agency, Washington D.C.

Dias P., Fernando L., Wathurapatha S., and De Silva, Y. (2005). Structural Resistance against Sliding, Overturning and Scouring Caused by Tsunamis, International Conference of Disaster Reduction on Coasts, Melbourne.

Dressler, R. F., 1952. Hydraulic resistance effect upon the dam-break functions. Journal of research of the National Bureau of Standards 49 (3), 217 - 225.

Dressler, R. (1954), Comparison of Theories and Experiments for the Hydraulic Dam-Break Wave. Proceeding of International Association of Scientific Hydrology, Assemble General, Rome, Italy, Vol. 3, No. 38, pp. 319-328.

Dunbar, D., P. H. LeBlond, and T. S. Murty, (1989). Maximum Tsunami Amplitudes and Associated Currents on the Coast of British Columbia, Science of Tsunami Hazards, 7(1), 3-44.

EERI (2011), Learning from Earthquakes, the Tohoku, Japan, Tsunami of March 11, 2011: Effects on Structures, EERI Special Earthquake Report, Oakland, CA.

Etkin D. (2010), Canadians at risk: Our exposure to natural hazards, Canadian Assessment of Natural Hazards Project, report Published by *Institute for Catastrophic Loss Reduction (ICLR)*, February 2010, 235 p.

FEMA P-646 (2012), Guidelines for Design of Structures for Vertical Evacuation from Tsunamis, 4th edition, *Federal Emergency Management Agency,* Washington, DC., USA.

FEMA P-646 (2008), Guidelines for Design of Structures for Vertical Evacuation from Tsunamis*, Federal Emergency Management Agency*, Washington, DC., USA.

FEMA P-55 (2011), Coastal Construction Manual, FEMA P-55 Report, 4th Edition, *Federal Emergency Management Agency*, Washington, DC., USA.

FEMA (2005), Coastal Construction Manual, FEMA 55 Report, 3rd Edition, *Federal Emergency Management Agency*, Washington, DC., USA.

FEMA 55 (2000), Coastal Construction Manual, *Federal Emergency Management Agency,* Washington, DC., USA.

FEMA (1995), Engineering Principles and Practices for Retrofitting Flood Prone Residential Buildings, *Federal Emergency Management Agency*, Report No. 259, (January).

Fine, I. V., A. B. Rabinovich, B. D. Bornhold, R. E. Thomson, and E. A. Kulikov, (2005). The Grand Banks landslide-generated tsunami of November 18, 1929: preliminary analysis and numerical modeling, *Marine Geology*, 215, pp. 45-57.

Forbes K. and Broadhead J. (2008) The Role of Coastal Forests in The Mitigation of Tsunami Impacts, a report published by Food and Agriculture Organization of the United Nations, Regional Office for Asia and the Pacific, Bangkok, pp 39.

Fritz H. M., J. C. Borrero, C. E. Synolakis, and J. Yoo, (2006). 2004 Indian Ocean Tsunami Flow Velocity Measurements from Survivor Videos, *Geophysical research letters,* Vol. 33, L24605, doi:10.1029/2006GL026784.

Fritz H. M., Petroff C. M., Catalán P. A., (2010), Cienfuegos R., and Winckler P., *Field survey of the 27 February 2010 Chile tsunami*. Pure and Applied Geophysics 168:11, 1989-2010.

Fujima, K., Achmad, F., Shigihara, Y., and Mizutani, N. (2009), Estimation of Tsunami Force Acting on Rectangular Structures. *Journal of Disaster Research*, 4(6), 4-9.

Fukui I., Nakaraura M., Shiraishi H., and Sasaki Y. (1963), Hydraulic Study on Tsunami, *Coastal Engineering in Japan*, Vol. VI, pp. 68 - 82.

Geist E. L. (1997). Local Tsunamis and Earthquake Source Parameters. *Advances in Geophysics (39), pp 117-209.*

Ghobarah, A., Saatcioglu, M., and Nistor, I. (2006).“The impact of the 26 December 2004 Earthquake and Tsunami on Structures and Infrastructure.”Eng. Struct. 28(2), 312–326.

Gisler, G., R. Weaver, and M. L. Gittings, (2006). SAGE calculations of the tsunami threat from La Palma, *Science of Tsunami Hazards*, 24(4), 288-301.

Goldfinger, C., C. H. Nelson, J.E. Johnson, A. E., Morey, J. Gutiérrez-Pastor, E., Karabanov, A. T. Eriksson, E. Gràcia, G. Dunhill, J. Patton, R. Enkin, A. Dallimore, T. Vallier, and the Shipboard Scientific Parties, (2010), Turbidite Event History: Methods and Implications for Holocene Paleoseismicity of the Cascadia Subduction Zone: *USGS Professional Paper* 1661-F.

Guha-Sapir, D. (2011), Disaster Data: A Balanced Perspective, *Disaster Center Report issue No. 25*, September 2011.

Gusiakov, V. K., (2009). Chapter 2: Tsunami History: Recorded, *In:* Bernard, E. N., and A. R. Robinson (eds.), *The Sea*, Vol. 15: Tsunamis, Harvard University Press, Cambridge, Massachusetts, pp. 23-53.

Goda, Y. (1985), Random Seas and Design of Maritime Structures, *University of Tokyo Press*, Toyko, Japan.

Haehnel R. B., and Daly S. F. (2002), Maximum Impact Force of Woody Debris on Floodplain Structures Cold Regions Research and Engineering Laboratory. *Technical Report ERDC/CRREL TR-02-2* US, (February).

Hattori, M., Arami, A., and Yui, T. (1994). Wave impact pressure on vertical walls under breaking waves of various types. Coastal Engineering, 22(1–2), 79–114.

Henry, R. F., Murty, T. S., (1995), Tsunami Amplification Due to Resonance in Alberni Inlet: Normal Modes, *book section in; Tsunami: Progress in Prediction, Disaster Prevention and Warning, (ed. Tsuchiya Y. and Shuto N.) Springer Netherlands, pp. 117-128 (Kluwer, Dordrecht).*

Herbich John B. (2000), Handbook of Coastal Engineering, *McGraw-Hill Engineering Handbook,* 1152 pages, ISBN - 9780071344029

Hettiarachchi S., Samarawickrama S. and Wijeratne N. (2009) "Tsunami Risk Assessment and the Planning and Implementation of Strategic Mitigation Measures- Case Study City of Galle", *Proceedings of the 6th International Workshop on Coastal Disaster Prevention*, *Bangkok, Thailand, December 1-2, pp. 25-35.*

Hiraishi T., Haruo K. and Saitoh E. (2010), Experimental Study on Impulsive Force of Drift Body due to Tsunami Flow*, Journal of Earthquake and Tsunami*, Vol. 4, No. 2 (2010), pp 127-133. Hiroi I., (1919), On a Method of Estimating The Force of Waves. *Tokyo University Engineering* Reports, X, 19 p.

Hughes S. A. (1993). "Physical Models and Laboratory Techniques in Coastal Engineering." Advanced Series on Ocean Engineering, Vol. 7, World Scientific Publications, Singapore. ISBN9810215401, ISBN981021541X.

Hyndman, R. D., J. F. Cassidy, J. Adams, G. C. Rogers, and S. Mazzotti, (2005). Earthquakes and Seismic Hazard in the Yukon-Beaufort-Mackenzie, *CSEG Recorder*, May 2005, pp. 32-66.

Iaccarino G., Ooi A., Durbin P. A., Behnia M. (2003). Reynolds Averaged Simulation of Unsteady Separated. International Journal of Heat and Fluid Flow Vol. 24, pp 147–156

Iizuka H., and Matsutomi H. (2000), Damage due to the flooding flow of tsunami, *Proceeding of Coastal Engineering Conference, JSCE*, 47. (In Japanese)

Ikeno M., Mori N., and Tanaka H., (2001), Experimental Study on Tsunami Force and Impulsive Force by a Drifter under Breaking Bore Like Tsunamis, *Proceedings of Coastal Engineering , JSCE, Vol. 48, pp. 846-850* (In Japanese).

Ikeno, M., and Tanaka, Y., (2003), Experimental Study on Impulse Force of Drift Body and Tsunami Running Up to Land, *Proceedings of Coastal Engineering, Japan Society of Civil Engineering*, Vol. 50, pp. 721-725 (in Japanese).

Jaffe B. E., and Gelfenbuam G., (2007). A Simple Model for Calculating Tsunami Flow Speed from Tsunami Deposits, *Journal of Sedimentary Geology,* 200, pp. 347–361

Jánosi, J. P., Jánosi, I. M., Jan, D., Szabó, K. G., and Tél,T. (2004). "Turbulentdrag Reduction in Dam-break Flows." Exp. Fluids, 37(2), 219–229.

Kawata Y., (1999). Field Survey on The 1998 Tsunami in Northwestern Area of Papua New Guinea. Report for Grant-Aid for Scientific Research (B)(1). Ministry of Education, Science, Sports and Culture, Japan. pp 81.

Keulegan G. H. (1938). "Law of Turbulent Flow in Open Channels." Journal of National Bureau of Standards, Res. Paper No. 1151, 21, 707–740.

Khodashenas S. R, Abderrezzak K. E., and Paquier A. (2008). Boundary Shear Stress in Open Channel Flow: a Comparison among Six Methods, Journal of Hydraulic Research Vol. 46, No. 5 (2008), doi:10.3826/jhr.2008.3203 pp. 598–609.

Kirkoz M.S. (1983). Breaking and Run-up of Long Waves, Tsunamis: Their Science and Engineering, 10th IUGG International Tsunami Symposium, Sendai-shi/Miyagi-ken, Japan, Terra Scientific Publishing, Tokyo, Japan.

Knight D. W., Yuen K. W. H., Al-Hamid A. A. I. (1994). Boundary Shear Stress Distributions in Open Channel Flow. In: K. Beven P. Chatwin J. Millbank (eds), Physical Mechanisms of Mixing and Transport in the Environment, Wiley, New York, 51–87.

Lafeber W., Brosset L., and Bogaert H. (2012). "Elementary loading processes (ELP) involved in breaking wave impacts: Findings from the Sloshel project." Proc., 32nd Int. Offshore and Polar Engineering Conf., International Society of Offshore and Polar Engineers (ISOPE),Mountain View, CA.

Lagos M., Arcas D., Ramirez T., Severino R., and Garcia C. (2010), Alturas de Tsunami Modelas Y Observadas. Evento del 27 de Febrero de. Chile/Resultados Preliminares.

Lauber G., and Hager W. H. (1998), Experiments to Dam-break Wave: Horizontal Channel, *Journal of Hydraulic Research*, 36(3), pp. 291-307.

Leal, J. G. A. B., Ferreira, R. M. L., and Cardoso, A. H. (2006). Dam-break Wave-front Celerity. Journal of Hydraulic Engineering, 132(1), 69–76.

Leighton T. G. (1994). The Acoustic Bubble. Academic Press, London

Leonard, L. J., Rogers, G. C., and Hyndman, R. D. (2010), Annotated Bibliography of References Relevant to Tsunami Hazard in Canada, *Geological Survey Of Canada Open File 6552.*

Ludwin, R.S., Dennis, R., Carver, D., McMillan, A.D., Losey, R., Clague, J., JonientzTrisler, C., Bowechop, J., Wray, J., James, K., 2005b. Dating the 1700 Cascadia Earthquake: Great Coastal Earthquakes in Native Stories. *Seismological Research Letters, Vol.* 76, No.2, pp. 140–147.

Lukkunaprasit P., A. Ruangrassamee and N. Thanasisathit (2009). Tsunami Loading on Buildings with Openings. *Journal of Science of Tsunami Hazards*, *28* (5), pp. 303–310.

Lukkunaprasit P. and Ruangrassamee A. (2008), *Building Damage in Thailand in the 2004 Indian Ocean Tsunami and Clues for Tsunami-Resistant Design*, The IES Journal Part A: Civil and Structural Engineering, Vol.1 No.1, pp. 17-30.

Matsutomi, H., (1999), A Practical Formula for Estimating Impulsive Force Due to Driftwoods and Variation Features of the Impulsive Force, *Journal of Hydraulic*, Coastal and Environmental Engineering , JSCE, No. 621, II-47, pp. 111-127 (In Japanese with English abstract).

Matsutomi H., Fujii M., and Yamaguchi T. (2008), "Experimental and Development of a Model on the Inundation Flow with Floating Bodies", Proceeding of the 31st International conference on Coastal Engineering, Hamburg, Germany, pp 1458-1470.World scientific.

Matsutomi H., Okamoto K., and Harada K. (2010), Inundation Flow Velocity of Tsunami on Land and Its Practical Use. *Coastal Engineering.*

Matsutomi H. (2009), Method for Estimating Collision Force of Driftwood Accompanying Tsunami Inundation Flow. *Journal of Disaster Research*, 4(6), pp. 435-440.

Miles M. D. (1997), GEDAP User's Guide for Windows NT, Technical Report HYD-TR-021 *Canadian Hydraulic Centre, National Research Council of Canada*, Ottawa, Canada. Pp 96

Miller D. J. (1960), Giant Waves in Lituya Bay, Alaska, Technical Report Geological Survey Professional Paper 354-C, Unites States Government Printing Office, Washington.

Mimura N., Yasuhara K., Kawagoe S., Yokoki H., and Kazama S. (2011), Damage from the great East Japan Earthquake and Tsunami – a Quick Report. Mitig Adapt Strat Glob Cahng 16:803 – 818.

Mohamed A. (2008), Characterization of Tsunami-like Bores in Support of Loading on Structures, *M. A. Sc. thesis submitted to the University of Hawaii*, pp. 97.

Mosher D. M., (2009). Submarine Landslides and Consequent Tsunamis in Canada, *Geoscience Canada*. Vol. 36, No. 4, pp. 179-190.

Mosher, D.C., J. Shimeld, R. Jackson, D. Hutchinson, C.B. Chapman, D. Chian, and J. Verhoef, (2010). Seismic Exploration and Sedimentation in Canada Basin, Western Arctic, *Program with Abstracts, GeoCanada2010, CSPG Annual Meeting*, Calgary, AB, May 10-14.

Murty T. S. (1977), Seismic Sea Waves: Tsunamis, *Bulletin of the Fisheries Research Board of Canada- no. 198, Department of Fisheries and the Environment, Fisheries and Marine Service, Scientific Information and Publishing Branch*, Ottawa, Canada, , 337 pp.

Mosher, D. C, J.A. Hunter, H. A., Christian, and J. L. Luternauer, (1997). Onshore/Offshore Geohazards in the Vancouver Island Region of Western Canada: Field, Modelling and Mapping Techniques and Results, *In:* Marinos, P. G., Koukis, G. C., Tsiambaos, G. C., and Stournaras, G. C. (eds.), *Engineering Geology and the Environment*, Balkema Publishers, Rotterdam, pp. 875-883.

NAASRA (1990), Highway Bridge Design Specification. *National Association of Australian State Road Authorities*.

Nakamura S. (1973), On Hydraulic bore and it's Application to Tsunami Generation. *Transaction of Sakhalin Complex Natural Science Research Institute* (Memorial Issue for IUGG71 Moscow) 32: pp. 129–151. (in Russian)

Nakano, Y. (2010), Design Load Evaluation for Tsunami Shelters Based on Damage Observations after Indian Ocean Tsunami Disaster due to The 2004 Sumatra Earthquake, *International Journal of the Tsunami Society, Vol. 29, No.1, 2010, pp. 11-20.*

Nistor I., Saatcioglu M., Ghobarah A., (2006), Tsunami hydrodynamic impact forces on physical infrastructures in Thailand and Indonesia, *Annual Conference Canadian Society for Civil Engineering,* 23-26 May 2006, Calgary, Alberta, Canada, CD-ROM, 10 p.

Nistor I., Saatcioglu M., Ghobarah A., (2005), The 26 December 2004 Earthquake and Tsunami-Hydrodynamic forces on physical infrastructure in Thailand and Indonesia, *Canadian Coastal Engineering Conference*, Halifax, Canada, CD-ROM, 15 p.

Nistor, I., Nouri, Y., Z., Palermo, D., Cornett, A., (2008). Experimental investigation of the impact of a tsunami-induced bore on structures, *Int. Conf. of Coastal Eng*., ICCE 2008, ASCE, Hamburg, Germany, 3324-3336.

Nakano Y. (2010), Design Load Evaluation for Tsunami Shelters Based on Damage Observations after Indian Ocean Tsunami Disaster due to The 2004 Sumatra Earthquake, *International Journal of the Tsunami Society*, Vol. 29, No. 1, pp. 11-20.

Nakano Y. (2007), Design Load Evaluation for Tsunami Shelters Based on Damage Observations After Indian Ocean Tsunami Disaster Due to The 2004 Sumatra Earthquake, *Journal of Architecture and Building Science*, Architectural Institute of Japan, 13: 25, pp.337-340.

Nouri, Y. (2008), The Impact of Hydraulic Bores and Debris on Free Standing Structures, *MASc thesis, Department of Civil Engineering*, University of Ottawa, Canada, 136 p.

Nouri, Y., Nistor, I., Palermo, D., Cornett, A., (2007). Structural Analysis for Tsunami-Induced Force and Debris Impact, *Coastal Structures 2007*, COPRI-ASCE, Venice, Italy, 701-712.

Ohmori, M., Fujii, N., Kyouya, O., Takao, M., Kaneto, T. and Ikeya, T., (2000), Numerical Simulation of Water Level, Velocity and Wave Force Overflowed on Upright Seawall by Tsunamis, Proceedings of Coastal Engineering, JSCE, Vol. 47, pp. 376-380 (in Japanese).

Okada T., Sugano T., Ishikawa T., Ohgi T., Takai S., and Hamabe C. (2005), Structural Design Method of Buildings for Tsunami Resistance (SMBTR), a code proposed by *The Building Technology Research Institute of The Building Center of Japan*.

Okada T., Sugano T., Ishikawa T., Ohgi T., Takai S., and Hamabe C. (2000), Structural Design Method of Buildings for Tsunami Resistance (SMBTR), a code proposed by *The Building Technology Research Institute of The Building Center of Japan*.

Okal E. A. (1988). Seismic Parameters Controlling Far-field Tsunami Amplitudes: a Review. Natural Hazard (1), pp 67-96.

Ohmori M., Fujii N., and Kyotani O. (2000), The Numerical Computation of The Water Level, The Flow Velocity and The Wave Force of The Tsunami Which Overflow The Perpendicular Revetments: Proceedings of the Coastal Engineering of JSCE, Vol. 47, pp. 3766-380, 2000.

Pacific Marine Environmental Laboratory, PMEL (1998), National Oceanic and

Atmospheric Administration (NOAA), Retrieved from http://www.pmel.noaa.gov/pubs/outstand/gonz 2088/gonz2088.shtml

Palermo, D., Nistor, I., Al-Faesly, T., and Cornett, A. (2013), "*Impact of Tsunami Forces on Structures: The University of Ottawa Experience*," journal of Tsunami Society International, Vol. (32), No. 2, ISSN 8755-6839, pp. 19.

Palermo D., Nistor I., Cornett A., and Al-Faesly T. (2011), *Tsunami Impact on Near-Shore Infrastructure: Challenges and Solutions*, Canadian Civil Engineer, CSCE, Spring, Vol. 28. No. 2, pp. 12-15.

Palermo, D., Nistor, I., Cornett, A., Nouri, Y., (2007). Tsunami-induced impact and hydrodynamic loading of near-shoreline structures, *PROTECT 2007, 1ST Int. Workshop Performance, Protection and Strengthening of Structures under Extreme Loading*, UBC, Whistler, Canada, CD-ROM, 10 p.

Peregrine, D. H. (2003). Water-wave impact on walls. Annual Review of Fluid Mechanics., 25, 23–43.

Peregrine D. H. and Williams S. M., (2001), Swash Overtopping a Truncated Plane Beach, *Journal of Fluid Mechanics*, Vol. 440, pp. 391-399.

Poncet, R., C. Campbell, F. Dias, J. Locat, and D. Mosher, (2010), A Study of the Tsunami Effects of Two Landslides in the St. Lawrence Estuary, *In:* Mosher, D.C., Shipp, R.C., Moscardelli, L., Chaytor, J.D., Baxter, C.D.P., Lee, H.J., and Urgeles, R. (eds.), *Submarine Mass Movements and their Consequences*, Advances in Natural and Technological Hazards Research, 28, pp. 755-764.

Rabinovich, A. B., R. E. Thomson, B. D. Bornhold, I. V. Fine, and E. A. Kulikov, 2003. Numerical Modelling of Tsunamis Generated by Hypothetical Landslides in the Strait of Georgia, British Columbia, *Pure and Applied Geophysics*, Vol. 160, pp.1273–1313.

Ramsden J. (1996), Forces on a vertical wall due to long waves, bores, and dry-bed surges, *Journal of Waterways, Port Coasts and Ocean Engineering*, Vol. 122, No. 3, 134-141.

Ramsden, J. (1993), Tsunamis: Forces on a Vertical Wall Caused by Long Waves, Bores, and Surges on a Dry Bed. Report No. KH-R-54, W. M. Keck Laboratory, California Institute of Technology, Pasadena, Calif., 251 p.

Ramsden J. and Raichlen F. (1990), *Forces on Vertical Wall Caused by Incident Bores*, *Journal of Waterway, Port, Coastal, and Ocean Engineering*, Vol. 116, No. 5, September/October, pp. 592- 613.

RCDRS (2005), The December 26, 2004, Sumatra Earthquake Tsunami Field Survey around Phuket, Thailand, by *Research Center for Disaster Reduction Systems*. Available online at: *http://www.drs.dpri.kyoto-u.ac.jp/sumatra/thailand/phuket_survey_e.html*.

RMS (2006), Risk Management Solutions ; *Managing Tsunami Risk in the Aftermath of the 2004 Indian Ocean Earthquake and Tsunami*, report by RMS, Newark, CA. USA.

Ritter A. (1892), The Propagation of Water Waves. Ver dtsch Ing. Vol.36, No.33, pp.947-954

Robertson I. (2011), The Tohoku, Japan, Tsunami of March 11, 2011: Effects on Structures, EERI Special Earthquake Report, pp. 14.

Roger, J., M.A. Baptista, D. Mosher, H. Hébert, and A. Sahal, 2010. Tsunami Impact on Newfoundland, Canada, due to Far-field Generated Tsunamis: Implications on Hazard Assessment, *this volume*, Paper 1837, 6 p.

Rouse H. (1965). Critical Analysis of Open-Channel Resistance. Journal of Hydraulic Division, ASCE, 91 (HY4), 1–25.

Ruffman, A., and T. Murty, (2006). Tsunami hazards in the Arctic regions of North America, Greenland and the Norwegian Sea, *Program and Abstracts, International Tsunami Society 3rd Tsunami Symposium*, May 23-25, Honolulu, HI.

Saatcioglu, M. (2009), Performance of Structures During the 2004 Indian Ocean Tsunami and Tsunami Induced Forces for Structural Design, *Journal of Earthquakes and Tsunamis, Geotechnical, Geological, and Earthquake Engineering* 11, DOI 10.1007/978-90-481-2399-5 10,

Saatcioglu M., Ghobarah A., and Nistor I. (2006), Performance of Structures in Thailand during the December 2004 Great Sumatra Earthquake and Indian Ocean Tsunami. *Earthquake Spectra*, 22 (S3), S355. doi:10.1193/1.2209171, pp. 295 - 319.

Saatcioglu M., Ghobarah A., and Nistor I. (2005), Reconnaissance Report on The December 26, 2004 Sumatra Earthquake and Tsunami. *The Canadian Association of Earthquake Engineering(CAEE), pp. 21.*

Satake K., Shimazaki K., Tsuji Y., and Ueda K. (1996), Time and size of a giant earthquake in Cascadia inferred from Japanese tsunami records of January 1700, Nature Journal 379, 246 – 249, doi:10.1038/379246a0

Science and Nature (n. d.), Retrieved from http://www.virginmedia.com/science-nature/natural-world/tsunami.php?ssid=9

Shuto N., Imamura F., Koshimura S., Satake K., and Matsutomi H. (2007), Encyclopaedia of tsunamis, Asakura Publishing Co., Ltd., Tokyo, 350 pp. (in Japanese)

Sogabe T. Fuseya H., Fukuie T., Sinomiya S., and Asajiki M. (1981), Impulsive Force Induced by Collision of Timber to Coastal Structures, *proceeding of 28th Japanese Conference on coastal Engineering*, pp. 584-588.

St-Germain, P., Nistor, I. Townsend, R., and Shibayama, T. (2014), SPH Numerical Modeling of Structures Impacted by Tsunami Bores, *Journal of Waterway Port Coastal and Ocean Engineering,* Vol. (140), No. 1, Pp. 66-81.

Stephenson, F. E., Rabinovich, A. B., (2009). Tsunamis on the Pacific Coast of Canada recorded during 1994–2007. *Pure and Applied Geophysics* 166 (1/2), pp. 177–210.

Stoker, J. J. (1957). Water Waves: The Mathematical Theory with Applications, Wiley-Interscience, New York.

Synolakis, C. E. (1986), the Run-up of Long Waves. *PhD thesis W. M. Keck Laboratory of Hydraulics and Water Resources Division of Engineering and Applied Science,* California Institute of Technology Pasadena, California 91125, 228.

Shen M. C., and Meyer R. E (1963), Climb of a Bore on a Beach, Part 3 Run-up, *Journal of Fluid Mechanics*, Vol. 16, pp. 113-125.

Thomson, R. E. (1981). Oceanography of the British Columbia Coast. *Canada Special Publication Fishers and Aquatic Sciences* 56, 291 p.

Thurairajah, A. E. (2005), Structural Design Loads For Tsunami and Floods, *International Symposium Disaster Reduction on Coasts Scientific-Sustainable-Holistic-Accessible 14–16 November 2005,* Monash University, Melbourne, Australia, pp. 1–11.

Tsunamis (n. d.), Retrieved from http://www.nps.gov/npsa/naturescience/tsunamis.htm

Tsunamis and Earthquakes (2004), Tsunami Generation from the 2004 M=9.1 Sumatra-Andaman Earthquake. Retrieved from http://walrus.wr.usgs.gov/tsunami/sumatraEQ/

Tsunami Disasters (n. d.), Retrieved from http://www.disastercenter.com

Tsutsumi A., Shimamoto T., Kawamoto E., and Logan J. M. (2000), Nearshore Flow Velocity of Southwest Hokkaido Earthquake Tsunami, Journal *of Engineering of Waterway, Port, Coastal, and Ocean Engineering,* 126 (3), pp. 136-143.

United States Army Corps of Engineers (1995), Flood-proofing Regulations. *Engineering Pamphlet 1165-2-314*, Washington, DC, December.

USGS (2006), United States Geological Survey, Earthquake Hazards Program, http://ga.water.usgs.gov/edu/tsunamishazards.html,

Vrijling J. K., Hewson, P. J., Section, O. E., and Engineering, S. (1999). Chapter 5. 4 : Uncertainty Analysis of Impact Waves and Scale Corrections Due to Aeration. *Analysis*, 1–12.

Yang S. Q., Lim S. Y. (2005). Boundary Shear Stress Distributions in Trapezoidal Channels. Journal of Hydraulic Research, Vol. 43 No.1, pp 98–102.

Yang S. Q., Tan S., and Lim S. Y. (2004). ”Velocity Distribution and Dip-Phenomenon in Smooth Uniform Open Channel Flows.” Journal of Hydraulic Engineering, Vol. 130, No. 12, pp. 1179–1186.

Yeh H. (2006), Maximum fluid forces in the tsunami run-up zone, *Journal of Waterway, Port, Coastal, and Ocean Engineering*, ASCE, 132, pp. 496- 500.

Yeh H. (2007), Design Tsunami Forces for Onshore Structures, *Journal of Disaster Research* Vol.2 No.6, pp. 531-536.

Yeh H., Robertson I., and Preuss J. (2005), Development of design guidelines for structures that serve as tsunami vertical evacuation sites, *Report No 2005-4, Washington Department of Natural Resources.*

Yeh H. and Shuto N. (2009), “Tsunami Forces and Effects on Structures” Editorial preface, Journal of Disaster Research Vol. (4) No.6, pp.375-376.

Yeom G., Nakamura T., and Mizutani N. (2009), Collision Analysis o f Container Drifted by Run-up Tsunami Using Drift Collision Coupled Model, *Journal of Disaster Research* Vol.4 No.6.

Yim, S., Cox, D. T., and Park, M. M. (2008). Experimental and Computational Activities at the Oregon State University Nees Tsunami Research Facility. *The 14th World Conference on Earthquake Engineering,* October 12-17, Beijing, China, p.1–8.

Ward, S. N., and S. Day, (2001). Cumbre Vieja Volcano – Potential Collapse and Tsunami at La Canary Islands, *Geophysical Research Letters*, 28 (17), 3397-3400.Palma,

WOOD I. R. (1991). "Air Entrainment in Free-Surface Flows." IAHR Hydraulic Structures Design Manual No. 4, Hydraulic Design Considerations, Balkema Publications, Rotterdam, The Netherlands, 149 pages. ISBN 9061919940.

Appendix A

Testing Program

Testing Program

Table A-1. Tests with no model installed in the flume

Test No.	Impound. Depth (mm)	Wall Configurations			
		Height (mm)	Location	Inclination Angle	Wall Type
1	550	0	-	-	-
2	850	0	-	-	-
3	1150	0	-	-	-
4	550	100	1D	45˚	Flat
5	850	100	1D	45˚	Flat
4	550	100	1D	45˚	Flat
7	550	100	1D	90˚	Flat
8	850	100	1D	90˚	Flat
9	1150	100	1D	90˚	Flat
10	550	100	3D	45˚	Flat
11	65	100	3D	45˚	Flat
12	75	100	3D	45˚	Flat
13	550	100	3D	90˚	Flat
14	850	100	3D	90˚	Flat
15	1150	100	3D	90˚	Flat
16	550	150	1D	45˚	Flat
17	850	150	1D	45˚	Flat
18	1150	150	1D	45˚	Flat
19	550	150	1D	90˚	Flat
20	850	150	1D	90˚	Flat
21	1150	150	1D	90˚	Flat
22	550	150	3D	45˚	Flat
23	850	150	3D	45˚	Flat
24	1150	150	3D	45˚	Flat
25	550	150	1D	90˚	Curved
26	850	150	1D	90˚	Curved
27	1150	150	1D	90˚	Curved
28	550	150	3D	90˚	Curved
29	850	150	3D	90˚	Curved
30	1150	150	3D	90˚	Curved

Continuation of Table A-1. Tests with no model installed in the flume

Test No.	Impound. Depth (mm)	Wall Configurations			
		Height (mm)			Height (mm)
31	550	150	1D	90˚	WAR
32	850	150	1D	90˚	WAR
33	1150	150	1D	90˚	WAR
34	550	150	1D	90˚	WAR
35	850	150	3D	90˚	WAR
36	1150	150	3D	90˚	WAR

Table A-2. Tests with square model installed in the flume*

Test No.	Impound. Depth (mm)	Wall Configurations			
		Height (mm)	Location	Inclination Angle	Wall Type
1	550	0	-	-	-
2	850	0	-	-	-
3	1150	0	-	-	-
4	550	100	1D	45˚	Flat
5	850	100	1D	45˚	Flat
4	1150	100	1D	45˚	Flat
7	550	100	1D	90˚	Flat
8	850	100	1D	90˚	Flat
9	1150	100	1D	90˚	Flat
10	550	100	3D	45˚	Flat
11	850	100	3D	45˚	Flat
12	1150	100	3D	45˚	Flat
13	550	100	3D	90˚	Flat
14	850	100	3D	90˚	Flat
15	1150	100	3D	90˚	Flat
16	550	150	1D	45˚	Flat
17	850	150	1D	45˚	Flat
18	1150	150	1D	45˚	Flat
19	550	150	1D	90˚	Flat
20	850	150	1D	90˚	Flat
21	1150	150	1D	90˚	Flat
22	550	150	3D	45˚	Flat
23	850	150	3D	45˚	Flat
24	1150	150	3D	45˚	Flat
25	550	150	1D	90˚	Curved
26	850	150	1D	90˚	Curved
27	1150	150	1D	90˚	Curved
28	550	150	3D	90˚	Curved
29	850	150	3D	90˚	Curved
30	1150	150	3D	90˚	Curved

*All the tests in Table 2 were carried out for three setups for the square model, as follows:

Pressure transducers facing upstream and defined as 0R (0˚ rotation angle)

Pressure transducers facing the flume side and defined as 90R (90˚ rotation angle)

Pressure transducers facing the downstream and defined as 180R (180˚ rotation angle)

Table A-3. Tests with circular model installed in the flume*

Test No.	Impound. Depth (mm)	Wall Configurations			
		Height (mm)	Location	Inclination Angle	Wall Type
1	550	0	-	-	-
2	850	0	-	-	-
3	1150	0	-	-	-
4	550	100	1D	45˚	Flat
5	850	100	1D	45˚	Flat
4	1150	100	1D	45˚	Flat
7	550	100	1D	90˚	Flat
8	850	100	1D	90˚	Flat
9	1150	100	1D	90˚	Flat
10	550	100	3D	45˚	Flat
11	850	100	3D	45˚	Flat
12	1150	100	3D	45˚	Flat
13	550	100	3D	90˚	Flat
14	850	100	3D	90˚	Flat
15	1150	100	3D	90˚	Flat
16	550	150	1D	45˚	Flat
17	850	150	1D	45˚	Flat
18	1150	150	1D	45˚	Flat
19	550	150	1D	90˚	Flat
20	850	150	1D	90˚	Flat
21	1150	150	1D	90˚	Flat
22	550	150	3D	45˚	Flat
23	850	150	3D	45˚	Flat
24	1150	150	3D	45˚	Flat
25	550	150	1D	90˚	Curved
26	850	150	1D	90˚	Curved
27	1150	150	1D	90˚	Curved
28	550	150	3D	90˚	Curved
29	850	150	3D	90˚	Curved
30	1150	150	3D	90˚	Curved
31	550	100	1D	90˚	WAR
32	850	100	1D	90˚	WAR
33	1150	100	1D	90˚	WAR

Continuation of Table A-3. Tests with circular model installed in the flume*

Test No.	Impound. Depth (mm)	Wall Configurations			
		Height (mm)	Location	Inclination Angle	Height (mm)
34	550	100	3D	90˚	WAR
35	850	100	3D	90˚	WAR
36	1150	100	3D	90˚	WAR

*All the tests in Table A-3 were carried out for seven setups for the circular model. First, the circular model was installed such that the pressure transducers were facing upstream (at the centerline of the flume) and defined as 0R (0˚ rotation angle). After implementing the tests listed in Table 3, the circular model was rotated clockwise around its central vertical axis by 30˚ and defined as 30R (30˚ rotation angle). The previous steps were repeated after rotating the circular model by an additional 30˚ (60R; 60˚ cumulative). The model was installed at four additional rotation angles (90˚, 120˚, 150˚, and 180˚).

Appendix B

Sample of Recorded Data and Analysis

Pressures and Forces Induced on

The Structural Models

Model Side

Upstream face

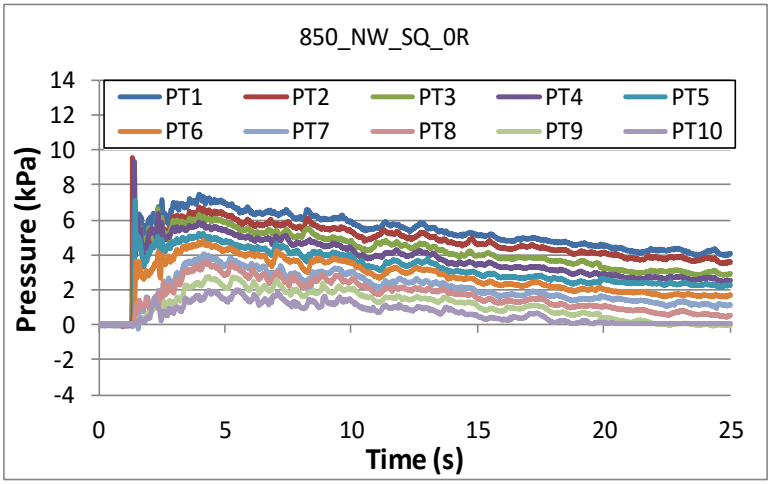

Side face

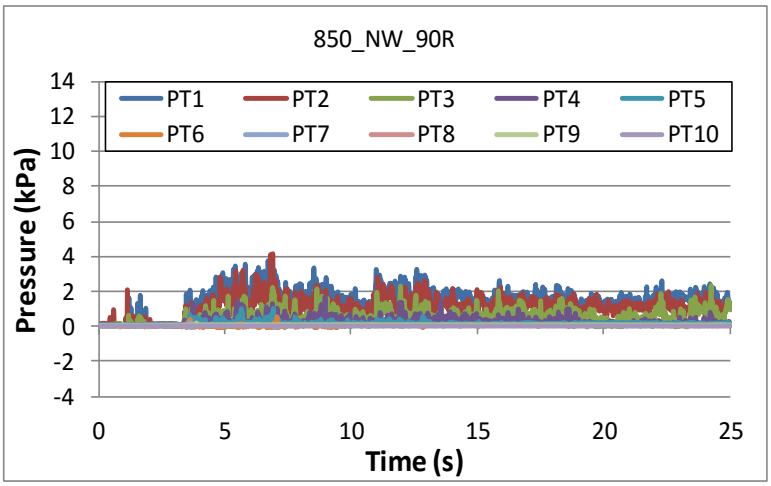

Back face

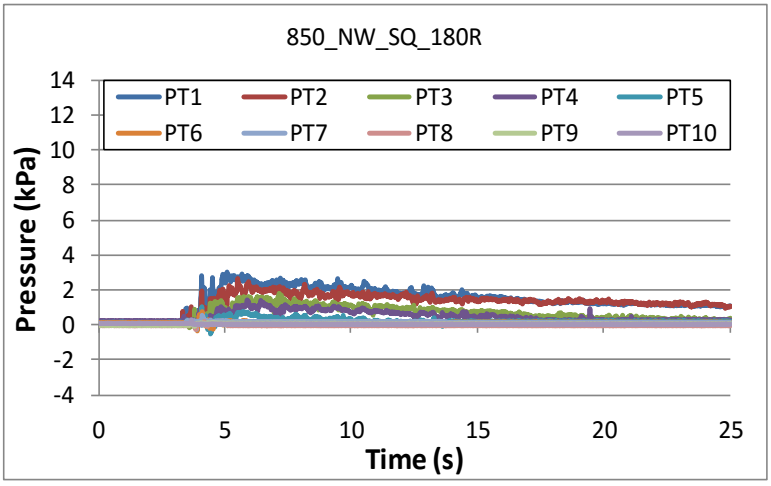

Figure B-1. Pressure around the square model in the absence of mitigation walls

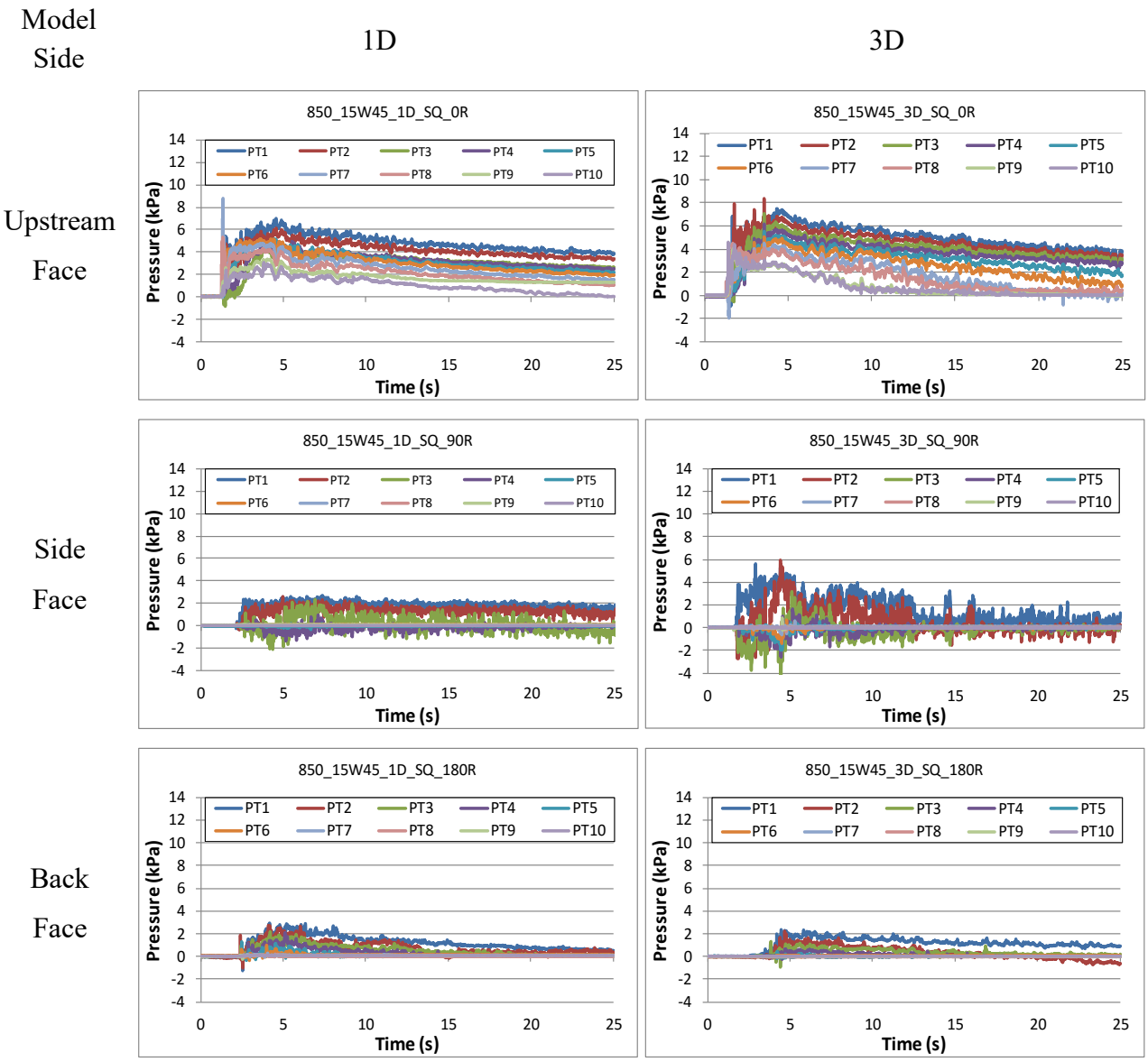

Figure B-2. Pressure around the square model with 15W45 mitigation wall

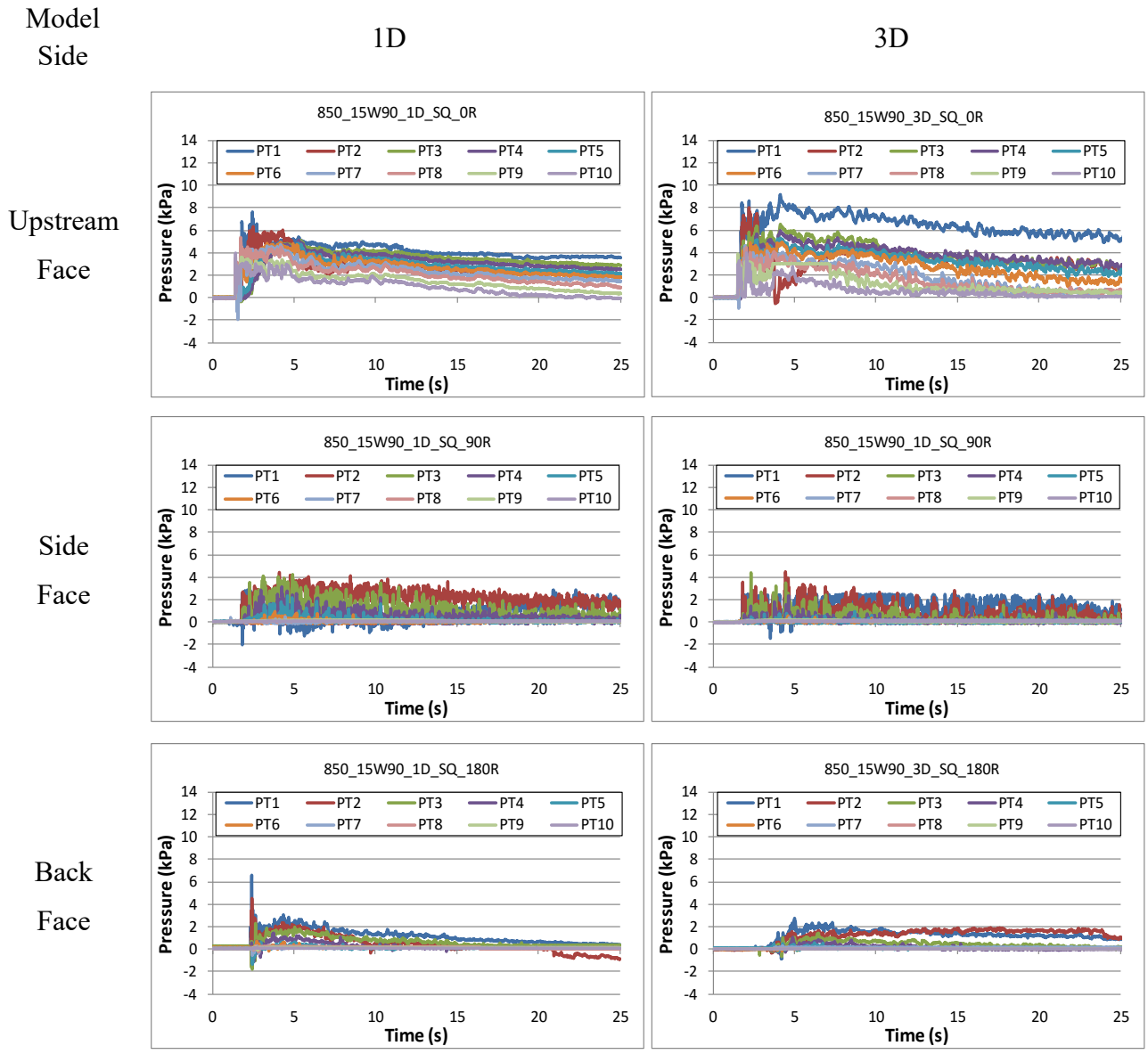

Figure B-3. Pressure around the square model with 15W90 mitigation wall

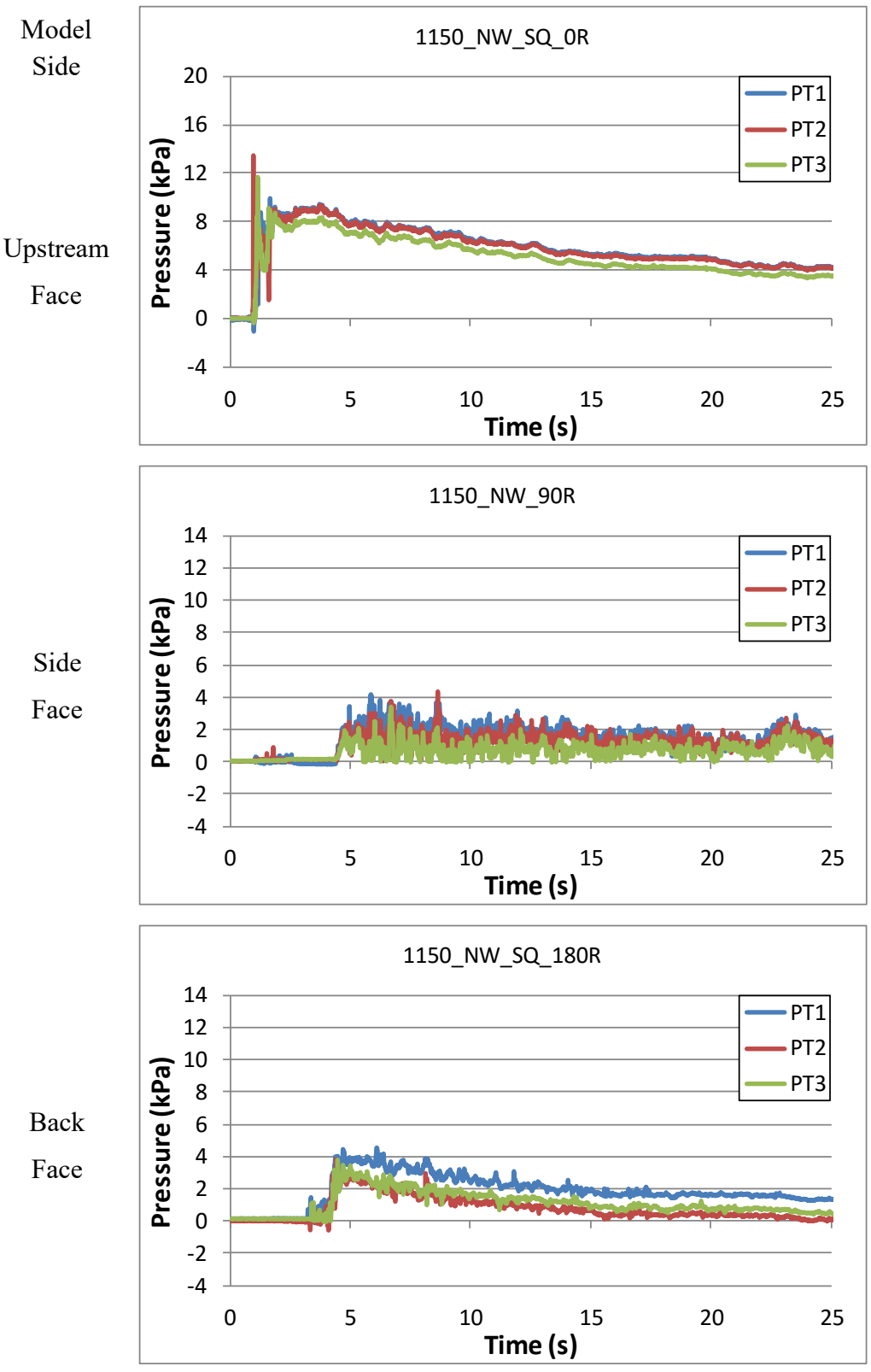

Figure B-4. Pressure around the square model in the absence of mitigation walls

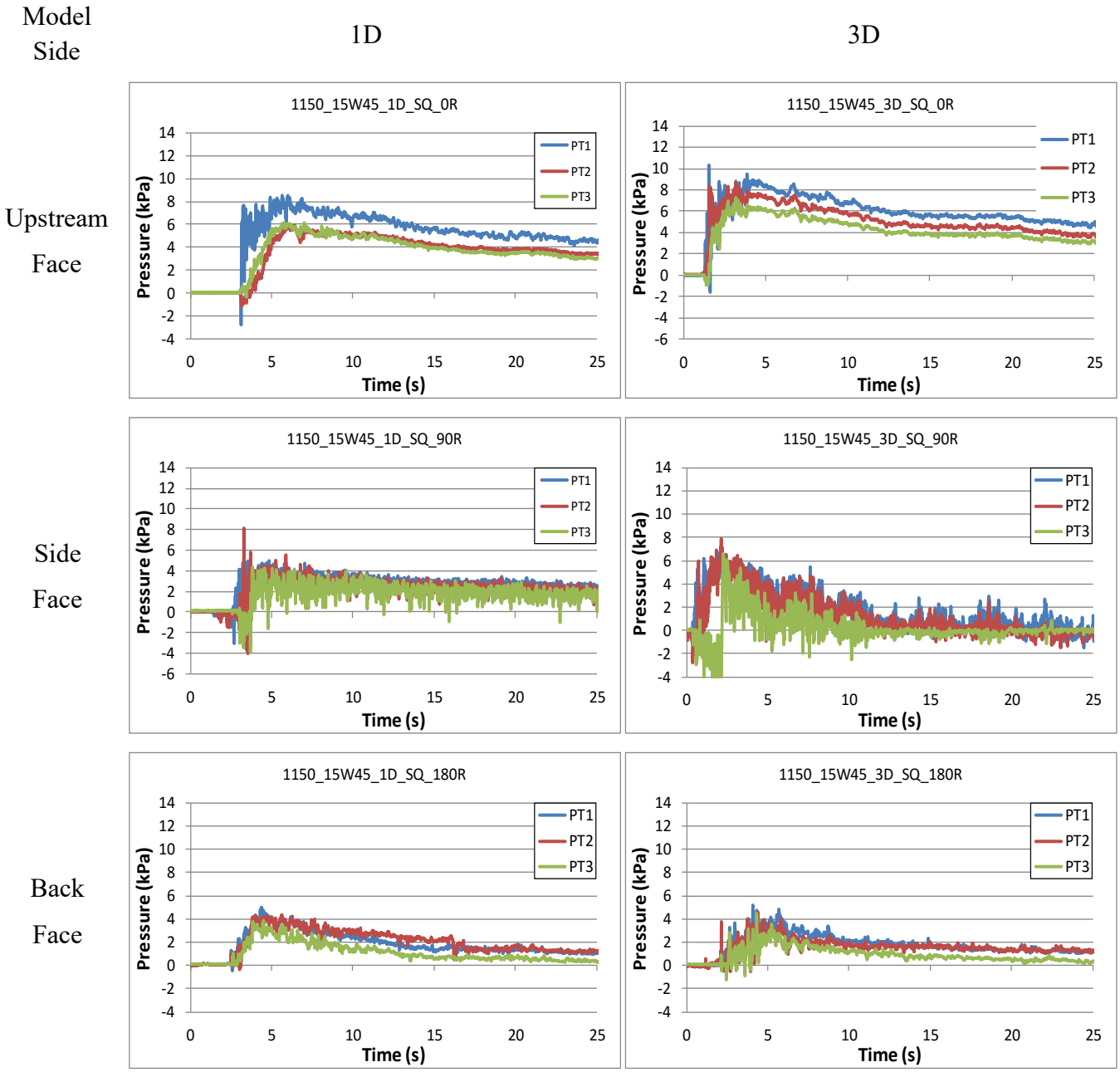

Figure B-5. Pressure around the square model with 15W45 mitigation wall

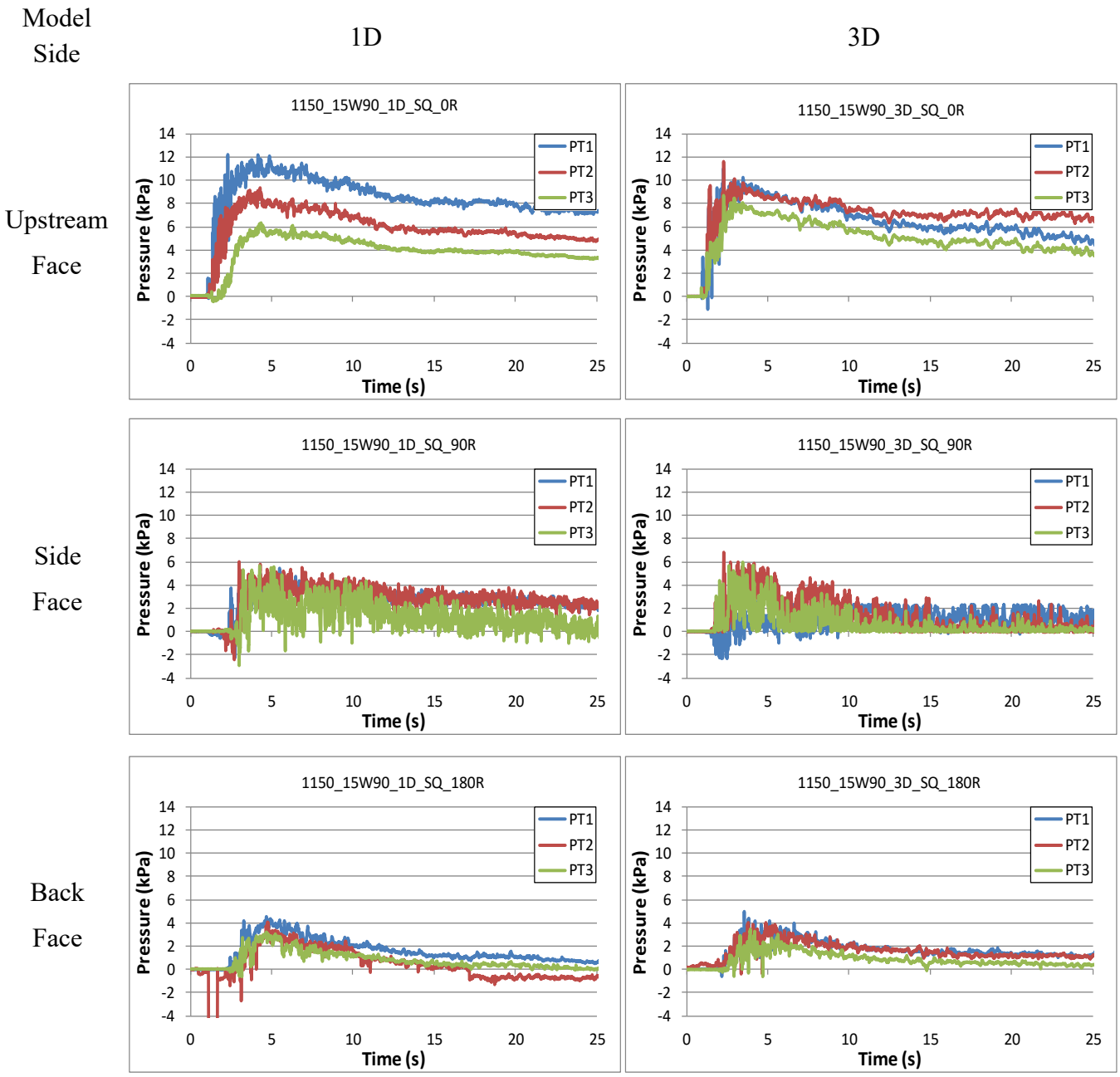

Figure B-6. Pressure around the square model with 15W90 mitigation wall

Table B-1. Maximum pressure recorded by each pressure sensor for different test groups with square model

Test Name	Maximum Pressure Recorded at Each Elevation During Test									
	P20mm	P50mm	P100mm	P150mm	P200mm	P250mm	P300mm	P350mm	P400mm	P450mm
Without wall Dry bed										
SQ_55WH_DRYBD	6.890	5.579	3.676	3.197	2.710	1.939	1.376	1.246	0.106	0.901
SQ_85WH_DRYBD	17.222	17.222	8.799	6.755	5.404	4.523	3.783	3.276	0.149	2.204
SQ_115WH_DRYBD	19.963	17.187	14.821	12.837	8.725	7.431	6.532	6.095	4.377	4.127
Without wall Wet bed										
SQ_55WH_WETBED	4.928	5.927	4.038	4.538	2.817	2.720	1.404	0.958	0.525	0.367
SQ_85WH_WETBED	7.492	9.526	7.339	9.388	7.114	4.816	4.027	3.601	2.752	2.032
SQ_115WH_WETBED	9.965	13.465	11.672	11.109	12.588	12.874	8.697	5.798	4.854	4.262
Wall 10 cm Height (1D)										
SQ_55WH_10W90_1D	4.581	4.851	3.439	3.334	2.799	2.480	2.394	2.046	0.063	0.843
SQ_85WH_10W90_1D	6.890	24.750	5.477	5.303	5.455	5.492	6.875	6.160	2.626	2.408
SQ_115WH_10W90_1D	10.267	8.993	7.068	6.967	13.570	9.868	10.479	0.000	5.069	7.187
SQ_55WH_10W45_1D	4.637	4.298	3.654	3.359	3.567	5.357	1.540	1.151	0.941	0.740
SQ_85WH_10W45_1D	7.128	6.762	5.713	5.792	10.613	6.585	4.258	3.778	2.954	2.577
SQ_115WH_10W45_1D	9.955	9.135	7.342	7.887	12.717	12.675	7.148	7.579	5.063	4.677
Wall 10 cm Height (3D)										
SQ_55WH_10W90_3D	14.948	14.262	8.362	5.130	5.656	2.174	1.349	0.921	0.762	0.092
SQ_85WH_10W90_3D	8.104	8.119	6.923	6.559	7.172	8.528	10.727	8.301	6.713	5.900
SQ_115WH_10W90_3D	13.244	11.926	9.526	9.122	9.108	8.651	8.459	8.246	8.619	8.754
SQ_55WH_10W45_3D	6.399	5.094	4.339	4.981	3.570	2.471	2.761	3.778	0.253	0.120
SQ_85WH_10W45_3D	9.310	6.688	5.821	5.595	5.186	6.326	6.340	6.392	4.621	5.030
SQ_115WH_10W45_3D	13.338	11.137	8.122	7.781	7.227	7.714	7.843	12.048	9.261	13.111

Continuation of Table B-1. Maximum pressure recorded by each pressure sensor for different test groups with square model

Test Name	Maximum Pressure Recorded at Each Elevation During Test									
	P20mm	P50mm	P100mm	P150mm	P200mm	P250mm	P300mm	P350mm	P400mm	P450mm
Wall 150 mm (1D)										
SQ_55WH_15W90_1D	6.544	5.034	3.282	3.134	2.562	2.357	1.939	1.858	0.295	1.956
SQ_85WH_15W90_1D	10.816	6.288	5.111	5.109	4.818	4.951	4.732	5.344	3.577	3.944
SQ_115WH_15W90_1D	-4.571	5.419	6.358	6.627	6.740	7.077	7.469	8.396	9.497	11.943
SQ_55WH_15W45_1D	7.399	2.963	2.949	2.993	2.993	2.550	1.776	0.994	0.617	0.000
SQ_85WH_15W45_1D	7.020	4.680	4.993	5.223	5.145	8.827	5.366	3.386	3.117	0.000
SQ_115WH_15W45_1D	8.514	5.904	6.094	7.077	8.530	16.884	12.824	5.383	5.073	0.000
Wall 150 mm (3D)										
SQ_55WH_15W90_3D	8.967	5.474	4.072	3.312	2.519	1.831	1.154	0.699	0.413	0.090
SQ_85WH_15W90_3D	9.192	8.051	6.552	6.004	5.269	4.914	4.630	4.417	3.854	3.955
SQ_115WH_15W90_3D	11.060	11.626	8.697	7.566	7.199	7.357	6.736	6.874	6.665	6.789
SQ_55WH_15W45_3D	7.287	5.938	4.741	4.084	2.476	1.643	1.104	0.704	0.568	0.753
SQ_85WH_15W45_3D	7.528	8.512	7.073	6.202	5.540	5.145	4.574	4.597	4.740	4.587
SQ_115WH_15W45_3D	10.335	8.348	7.280	7.030	7.098	7.013	6.480	7.010	5.513	9.235
Curved Wall 150 mm (1D)										
SQ_55WH_15ARW_1D	5.816	5.214	3.387	3.131	2.645	2.166	1.673	1.892	1.042	1.164
SQ_85WH_15ARW_1D	6.896	6.196	5.532	5.180	4.990	4.939	4.686	4.627	3.410	3.755
SQ_115WH_15ARW_1D	9.551	7.016	6.376	6.338	6.661	7.258	7.670	9.828	7.577	10.632
Curved Wall 150 mm (3D)										
SQ_55WH_15ARW_3D	8.122	4.901	3.712	3.396	2.608	1.732	0.953	0.869	0.428	0.086
SQ_85WH_15ARW_3D	8.538	8.212	6.555	6.790	7.921	8.496	6.643	6.305	3.730	3.226
SQ_115WH_15ARW_3D	10.517	10.111	8.457	7.993	7.571	7.871	8.162	9.177	5.358	6.635

Table B-2. Maximum flow depth recorded by each water level sensor and maximum forces and moments for different test groups with square model

Test Name	Maximum Water Level Recorded								Max Force and Moment Recorded			
	WG1	WG7	WG8	WG9	WG10	WG11	WG12	WG13	Fx	Fy	My	Mx
No wall installed; Dry-bed												
SQ_55WH_DRYBD	0.556	0.210	0.687	0.657	0.687	0.381	0.194	0.236	264.456	24.072	35.581	2.014
SQ_85WH_DRYBD	0.867	0.395	0.755	0.881	0.874	0.562	0.389	0.364	637.148	42.838	102.494	2.263
SQ_115WH_DRYBD	1.153	0.017	0.547	0.890	0.889	0.497	0.792	0.817	1048.550	113.440	217.012	3.907
No wall installed Wet-bed												
SQ_55WH_WETBED	0.562	0.527	0.638	0.537	0.642	0.247	0.200	0.224	263.799	24.736	37.030	2.056
SQ_85WH_WETBED	0.858	0.527	0.656	0.851	0.865	0.461	0.338	0.326	662.616	46.439	121.352	7.370
SQ_115WH_WETBED	1.154	0.527	0.725	0.840	0.847	0.672	0.741	0.712	1059.265	147.277	219.940	9.193
Flat wall 100 mm (1D)												
SQ_55WH_10W90_1D	0.555	0.192	0.212	0.640	0.719	0.331	0.129	0.099	283.112	37.436	37.276	1.917
SQ_85WH_10W90_1D	0.853	0.341	0.381	0.856	0.859	0.543	0.412	0.290	620.107	43.690	106.522	3.918
SQ_115WH_10W90_1D	1.165	0.017	0.625	0.860	0.869	0.599	0.602	0.527	1120.979	82.074	227.764	5.933
SQ_55WH_10W45_1D	0.553	0.017	0.203	0.566	0.577	0.286	0.151	0.120	259.728	28.432	33.078	4.437
SQ_85WH_10W45_1D	0.852	0.328	0.367	0.833	0.833	0.605	0.376	0.359	618.960	43.123	101.750	8.206
SQ_115WH_10W45_1D	1.151	0.483	0.538	0.857	0.867	0.618	0.632	0.545	1090.300	111.170	207.461	10.924
Flat wall 100 mm (3D)												
SQ_55WH_10W90_3D	0.574	0.527	0.249	0.447	0.469	0.321	0.230	0.220	404.440	24.175	45.187	8.150
SQ_85WH_10W90_3D	0.863	0.527	0.344	0.883	0.886	0.448	0.284	0.288	629.410	79.902	119.714	10.743
SQ_115WH_10W90_3D	1.166	0.527	0.593	0.890	0.895	0.680	0.480	0.451	1118.700	120.940	349.267	25.457
SQ_55WH_10W45_3D	0.553	0.029	0.763	0.461	0.484	0.350	0.149	0.174	268.240	24.927	35.314	2.513
SQ_85WH_10W45_3D	0.852	0.347	0.371	0.807	0.808	0.474	0.296	0.279	695.390	64.983	121.768	10.108
SQ_115WH_10W45_3D	1.151	0.517	0.614	0.857	0.867	0.684	0.533	0.441	1180.422	114.550	301.134	25.841

Continuation of Table B-2. Maximum flow depth recorded by each water level sensor and maximum forces and moments for different test groups with square model

Test Name	Maximum Water Level Recorded								Max Force and Moment Recorded			
	WG1	WG7	WG8	WG9	WG10	WG11	WG12	WG13	Fx	Fy	My	Mx
Flat wall 15 cm height (1D)												
SQ_55WH_15W90_1D	0.562	0.163	0.208	0.597	0.611	0.315	0.072	0.065	294.050	40.443	41.088	4.793
SQ_85WH_15W90_1D	0.850	0.327	0.359	0.881	0.894	0.455	0.355	0.373	624.880	51.531	117.889	9.494
SQ_115WH_15W90_1D	1.173	0.514	0.575	0.855	0.866	0.659	0.655	0.648	1124.70	112.940	265.127	20.753
SQ_55WH_15W45_1D	0.544	0.794	0.212	0.568	0.547	0.261	0.157	0.147	301.199	17.912	42.798	3.242
SQ_85WH_15W45_1D	0.848	0.794	0.330	0.870	0.864	0.452	0.427	0.516	626.916	57.527	129.650	5.223
SQ_115WH_15W45_1D	1.141	0.072	0.601	0.871	0.881	0.732	0.608	0.575	1086.40	123.650	253.178	11.000
SQ_55WH_15W90_3D	0.564	0.219	0.217	0.480	0.461	0.229	0.129	0.158	239.840	26.347	29.742	6.505
SQ_85WH_15W90_3D	0.849	0.337	0.372	0.816	0.809	0.433	0.392	0.278	656.210	80.187	104.448	9.914
SQ_115WH_15W90_3D	1.152	0.542	0.569	0.875	0.885	0.635	0.469	0.419	1244.00	138.660	281.840	29.215
SQ_55WH_15W45_3D	0.551	0.213	0.218	0.410	0.441	0.224	0.165	0.170	240.060	13.444	30.616	4.706
SQ_85WH_15W45_3D	0.862	0.329	0.377	0.839	0.799	0.410	0.292	0.308	720.190	50.420	138.620	6.156
SQ_115WH_15W45_3D	1.153	0.506	0.560	0.873	0.883	0.636	0.545	0.481	1088.78	86.907	339.049	10.760
Curved wall 150 mm (1D)												
SQ_55WH_15ARW_1D	0.555	0.162	0.200	0.653	0.571	0.273	0.097	0.059	294.194	71.080	41.616	10.334
SQ_85WH_15ARW_1D	0.856	0.376	0.362	0.866	0.879	0.448	0.359	0.339	668.580	51.272	139.228	8.503
SQ_115WH_15ARW_1D	1.154	0.489	0.510	0.872	0.884	0.682	0.638	0.551	1110.84	87.096	271.158	15.464

Continuation of Table B-2. Maximum flow depth recorded by each water level sensor and maximum forces and moments for different test groups with square model

Test Name	Maximum Water Level Recorded								Max Force and Moment Recorded			
	WG1	WG7	WG1	WG7	WG1	WG7	WG1	WG7	WG1	WG7	WG1	WG7
Curved wall 150 mm (3D)												
SQ_55WH_15ARW_3D	0.555	0.510	0.709	0.458	0.458	0.272	0.169	0.130	239.748	17.912	31.904	4.384
SQ_85WH_15ARW_3D	0.887	0.527	0.815	0.731	0.752	0.502	0.336	0.275	750.775	46.628	141.856	8.413
SQ_115WH_15ARW_3D	1.125	0.527	0.781	0.871	0.879	0.602	0.440	0.434	1222.46	138.176	274.899	15.639

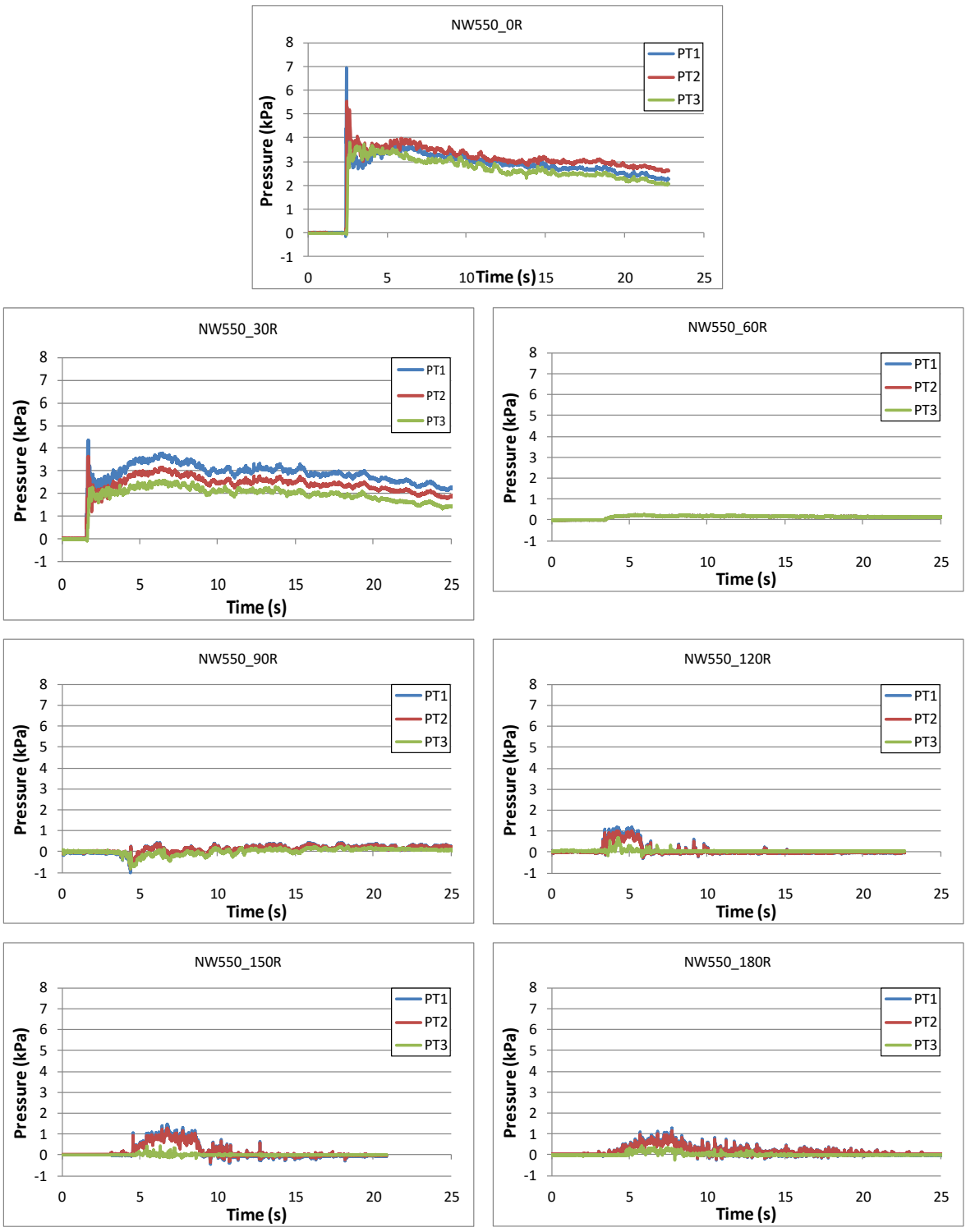

Figure B-7. Pressure distribution around the circular model generated by 550 mm impounding depth

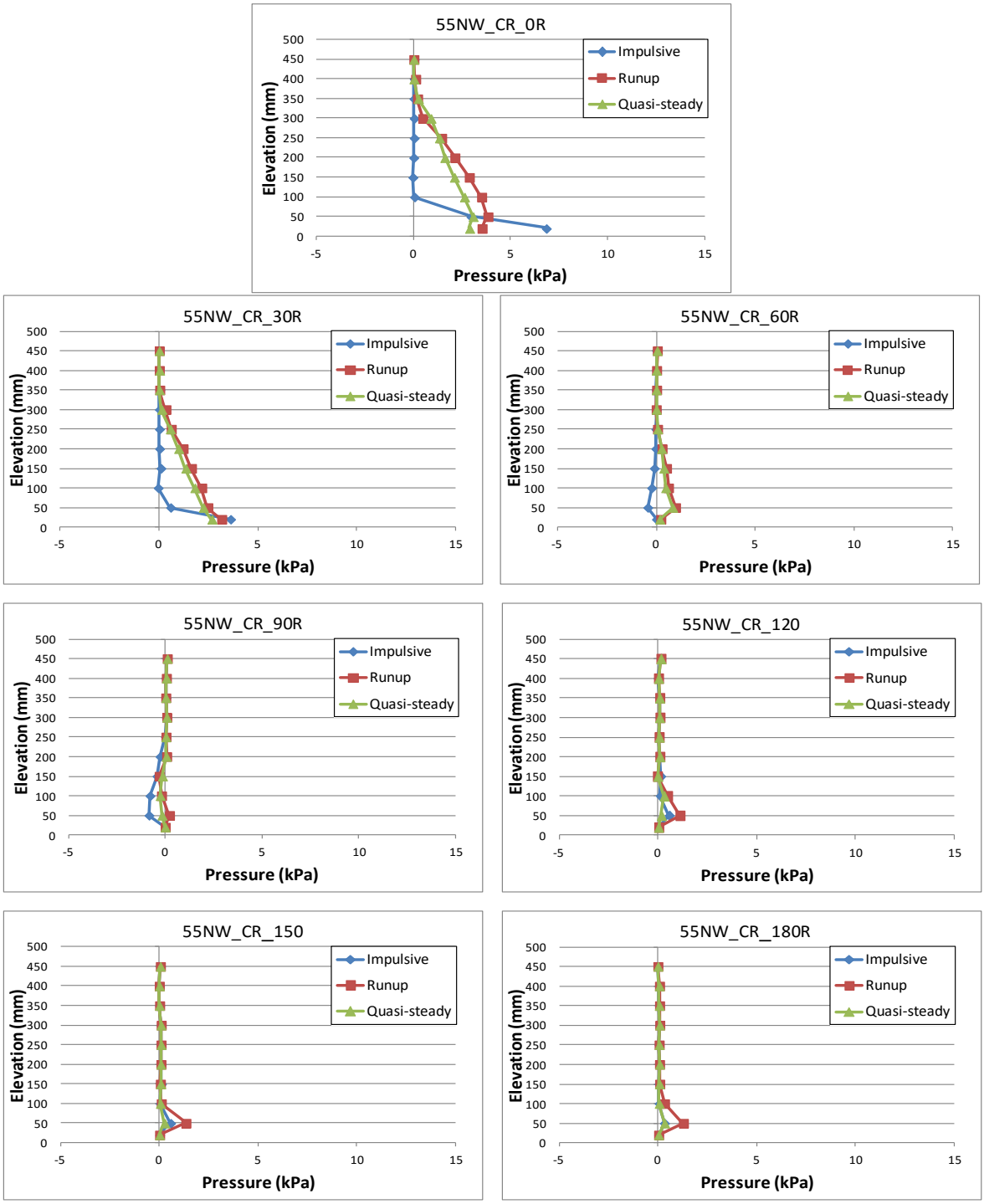

Figure B-8. Vertical distribution of pressure induced on the circular model by hydraulic bore generated from 550 mm impounding water depth

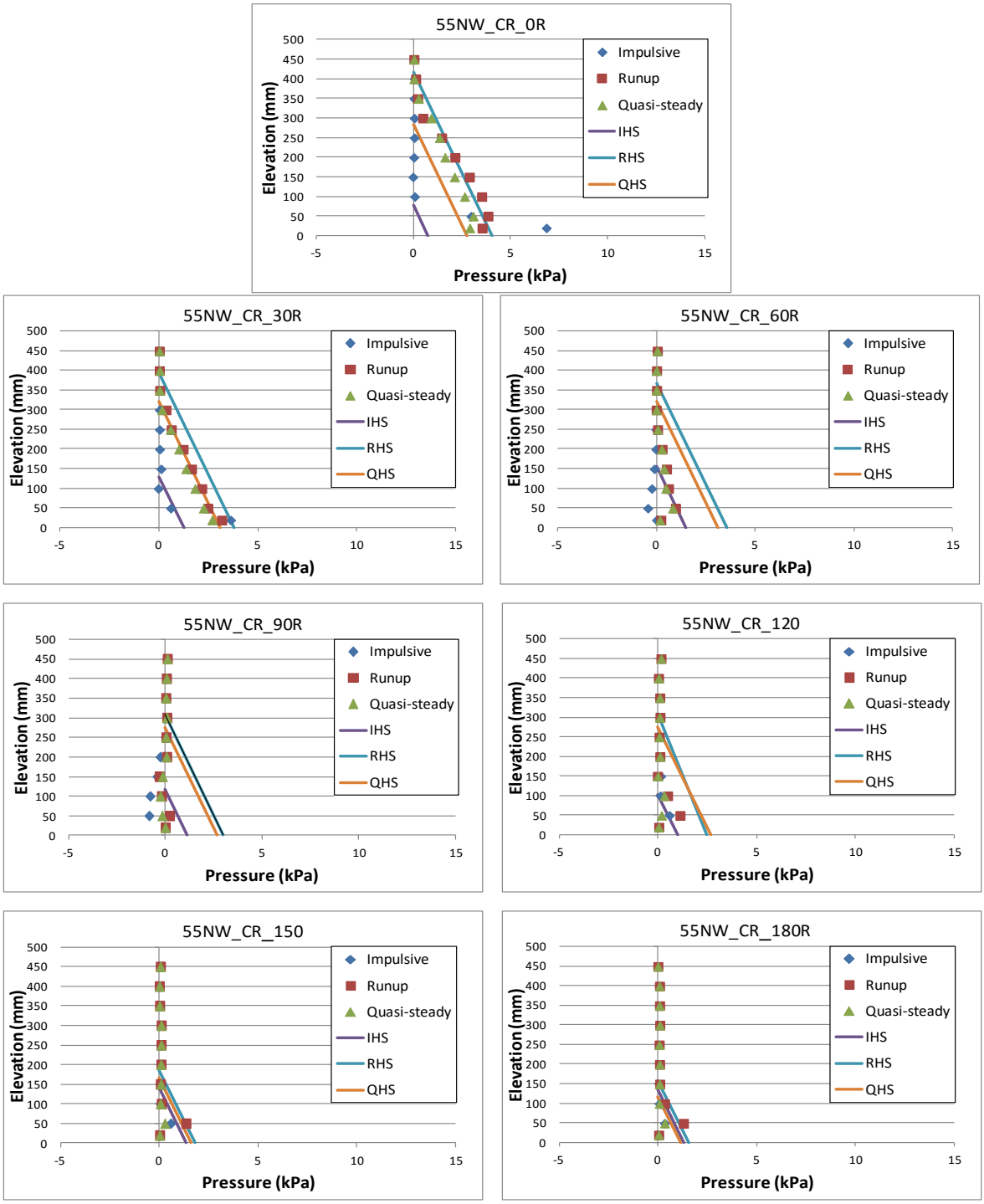

Figure B-9. Experimentally measured pressure induced on the circular model by hydraulic bore generated from 550 mm impounding depth and hydrostatic distribution

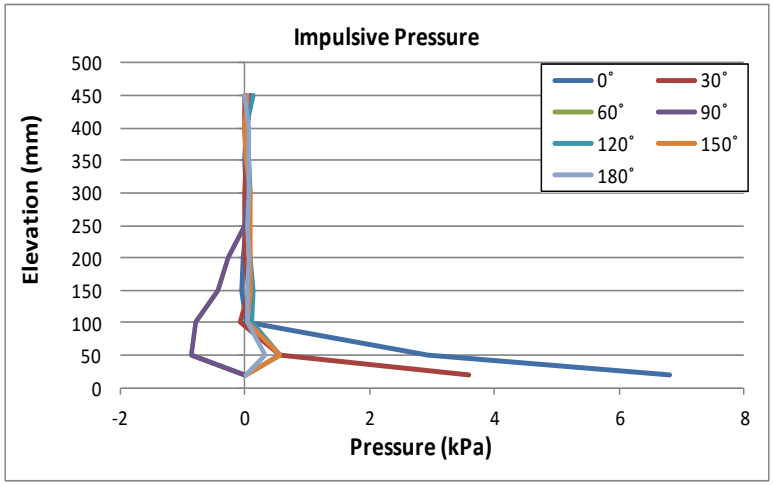

(a)

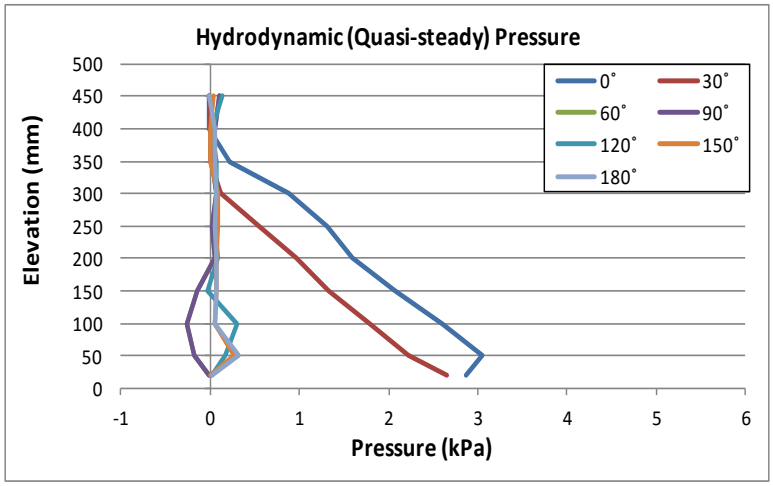

(b)

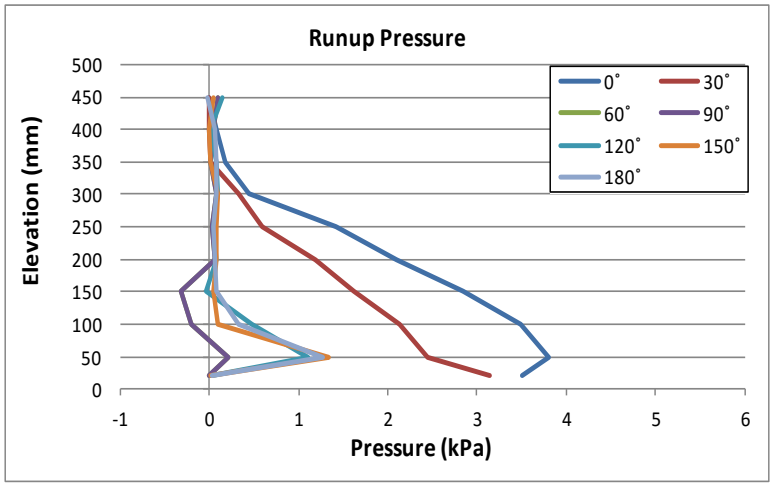

(c)

Figure B-10. Vertical distribution of pressure around the circular model generated by 550 mm impounding depth for three flow states: **a)** impulsive; **b)** run-up; and **c)** quasi-steady

Pressure Variation

The variation in the pressure distribution horizontally and vertically around the model through the impulsive and run-up flow states in comparison with that for the quasi-steady state indicates the extreme complexity of the flow-structure interaction. For comparison purposes, the hydrostatic pressure distribution was plotted for each rotation angle for three flow states: impulsive, run-up, and quasi-steady.

The maximum pressure recorded for the three flow states at each rotation angle was selected and divided by the product of maximum inundation depth for the case with no model installed in the flume and the weight density of the water. The results are listed in the table below. The coefficient α is defined in the following formula:

$$P_{max} = \alpha . \rho . g . h$$

Where ρ is the water density (kg/m^3), g is the gravitational acceleration (m/s^2), and h is the maximum inundation depth for the case with no structural model in the flume (m).

Table B-3. Factor α for three flow states around the circular model for 550 mm impounding depth

Rotation Angle	Flow State	Maximum Pressure (kPa)	Factor (α) α =P/γ.h	Average α
0°	Impulsive	6.819	1.55	1.04
	Run-up	3.808	0.87	
	Quasi-steady	3.045	0.69	
30°	Impulsive	3.597	0.82	0.71
	Run-up	3.1473	0.72	
	Quasi-steady	2.6542	0.61	
60°	Impulsive	0.017641	0.00	0.14
	Run-up	0.97141	0.22	
	Quasi-steady	0.82697	0.19	
90°	Impulsive	0.086338	0.02	0.03
	Run-up	0.20785	0.05	
	Quasi-steady	0.094364	0.02	
120°	Impulsive	0.5613	0.13	0.15
	Run-up	1.1022	0.25	
	Quasi-steady	0.30143	0.07	
150°	Impulsive	0.56214	0.13	0.16
	Run-up	1.3366	0.30	
	Quasi-steady	0.26404	0.06	
180°	Impulsive	0.3188	0.07	0.15
	Run-up	1.2746	0.29	
	Quasi-steady	0.32187	0.07	

Note: the value of α varies from 0.14 to 1.04.

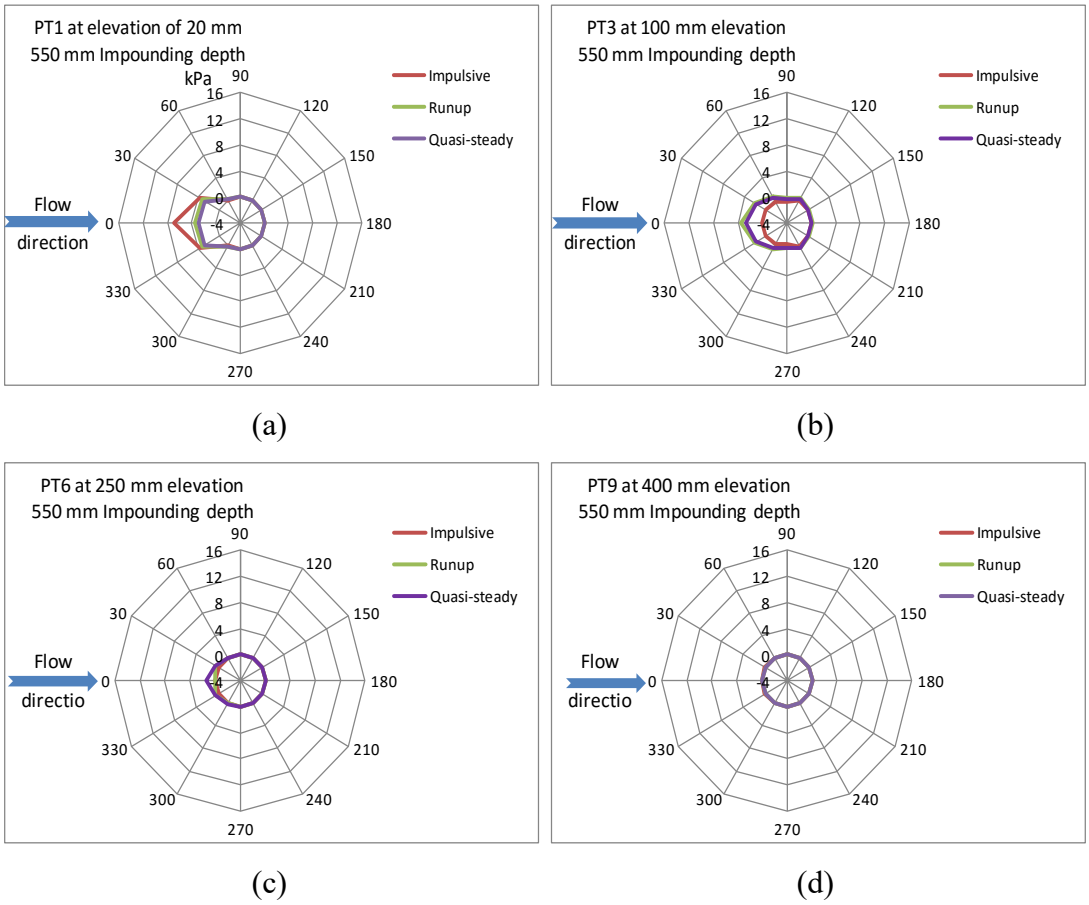

Figure B-11. Pressure distribution around the circular model generated by 550 mm impounding depth for three flow states at four elevations: **a)** 20 mm; **b)** 100 mm; **c)** 250 mm; and **d)** 400 mm

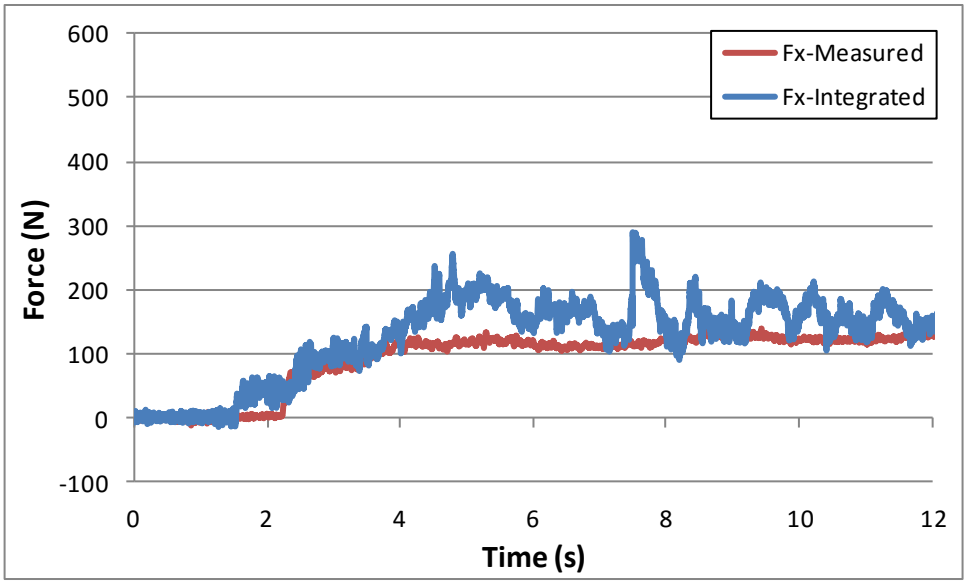

(a)

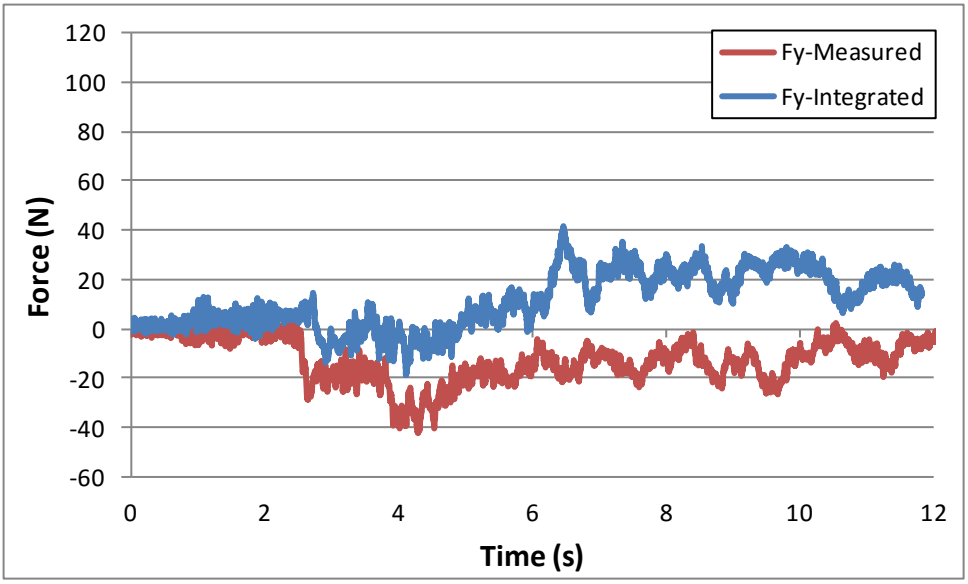

(b)

Figure B-12. Time histories for laboratory recorded and calculated forces induced on the circular model by 550 mm impounding depth: **a)** longitudinal direction; and **b)** transverse direction

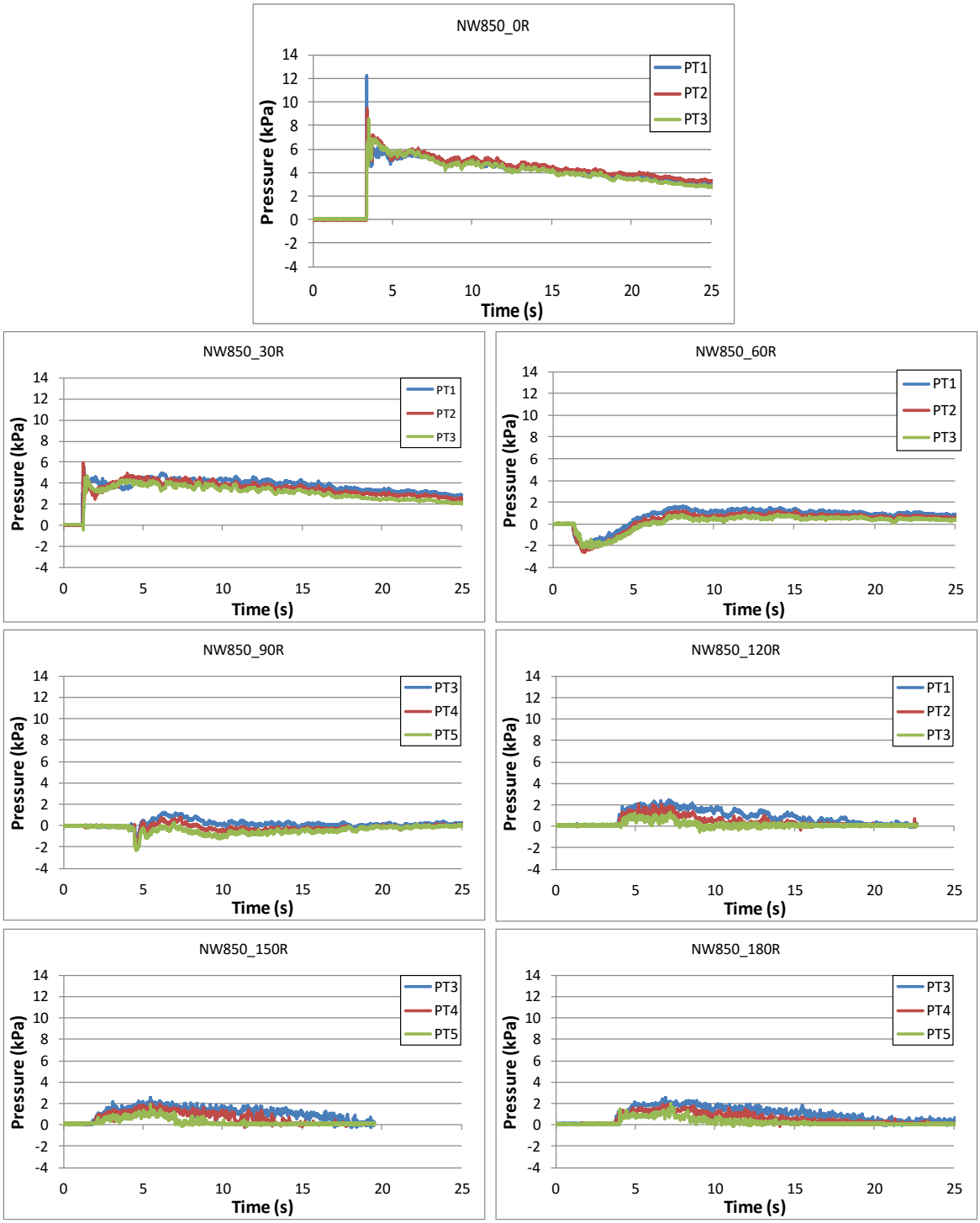

Figure B-13. Pressure distribution around the circular model generated by 850 mm impounding depth

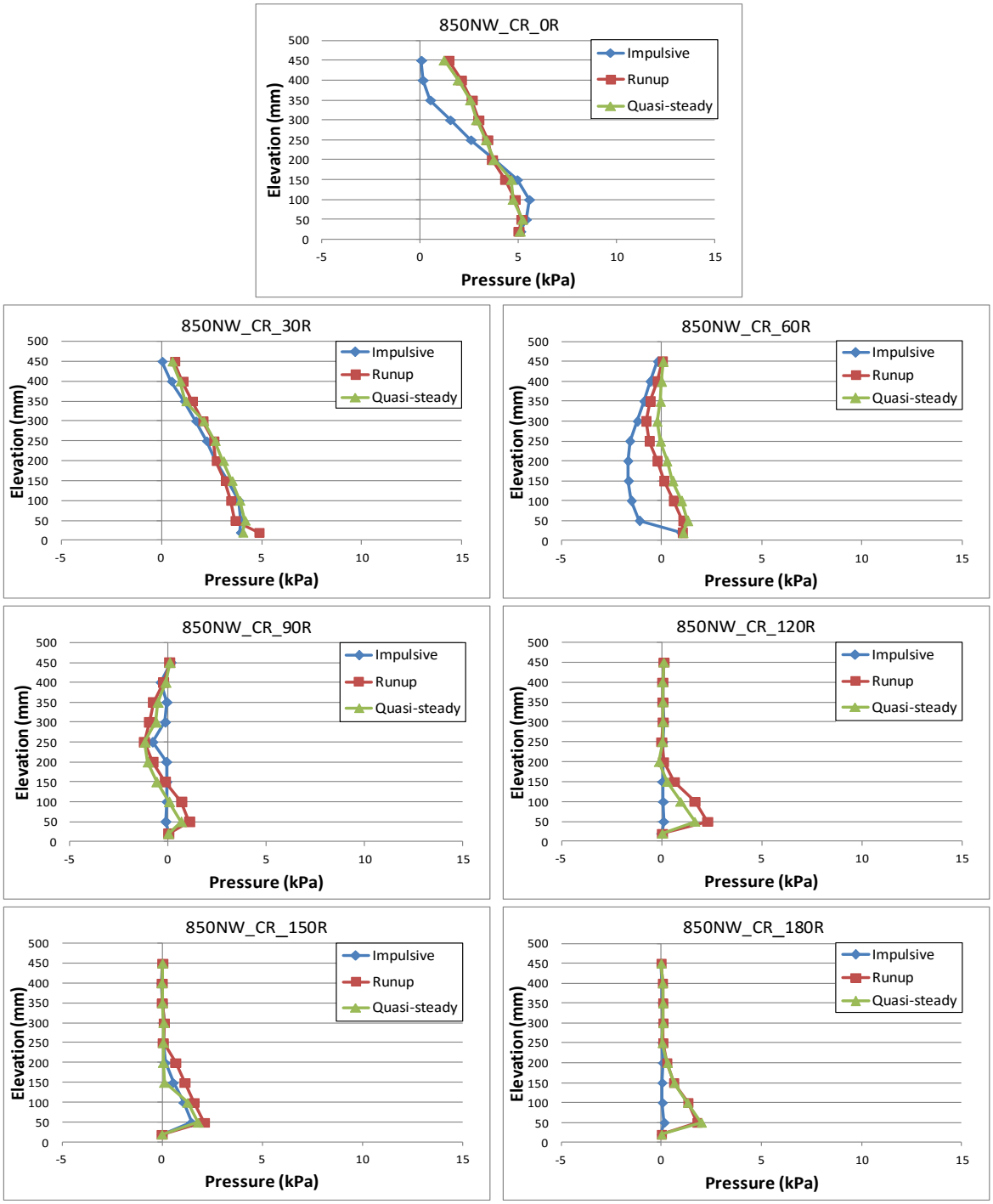

Figure B-14. Vertical distribution of pressure induced on the circular model by hydraulic bore generated from 850 mm impounding water depth

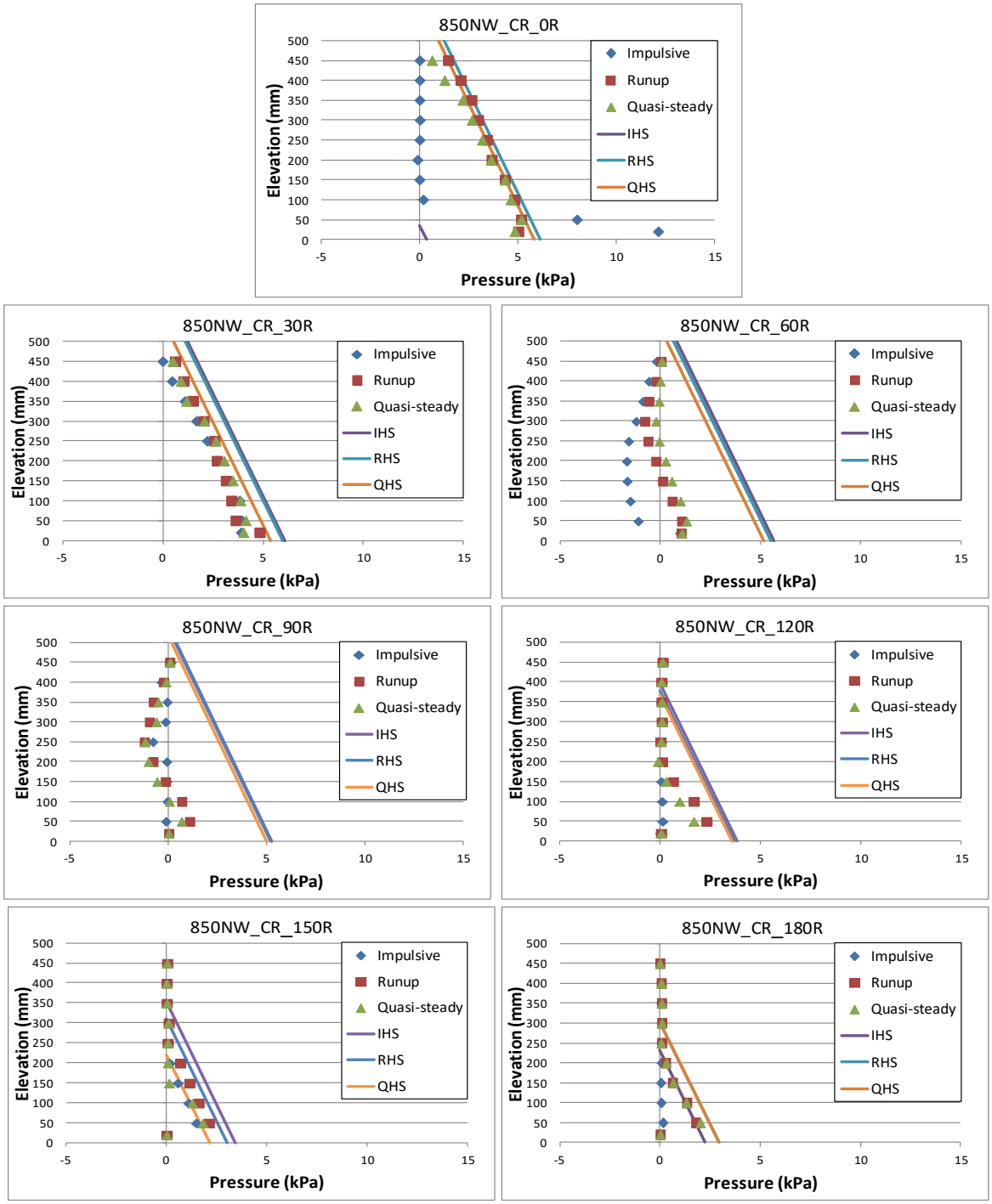

Figure B-15. Experimentally measured pressure induced on the circular model by hydraulic bore generated from 850 mm impounding depth and hydrostatic distribution

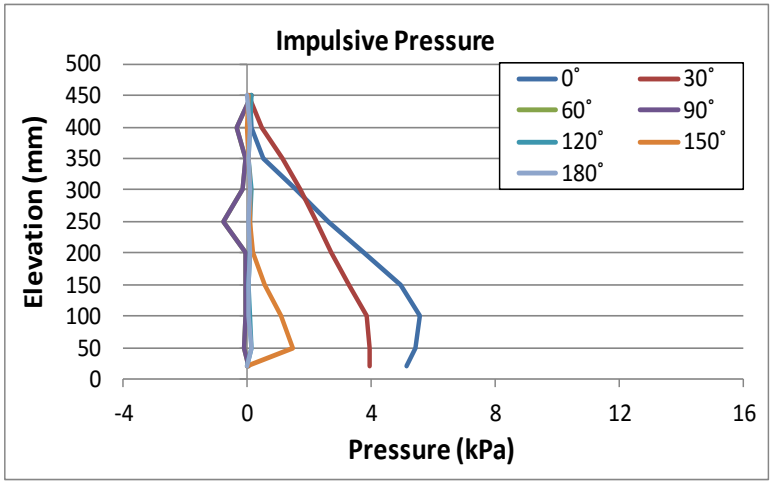

(a)

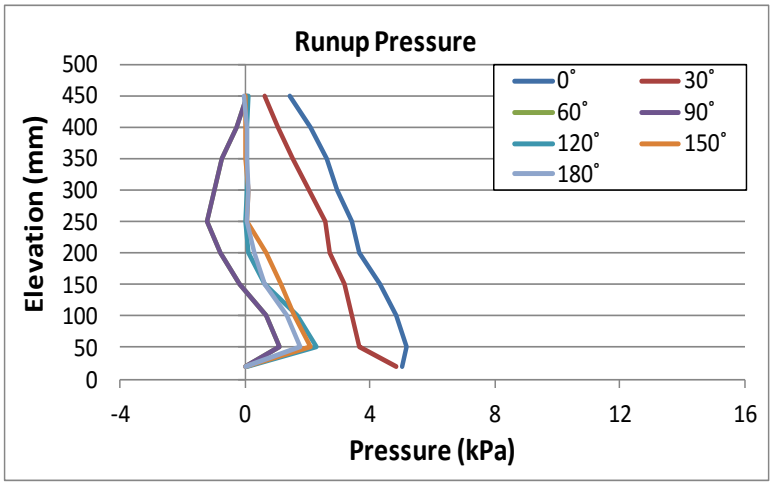

(b)

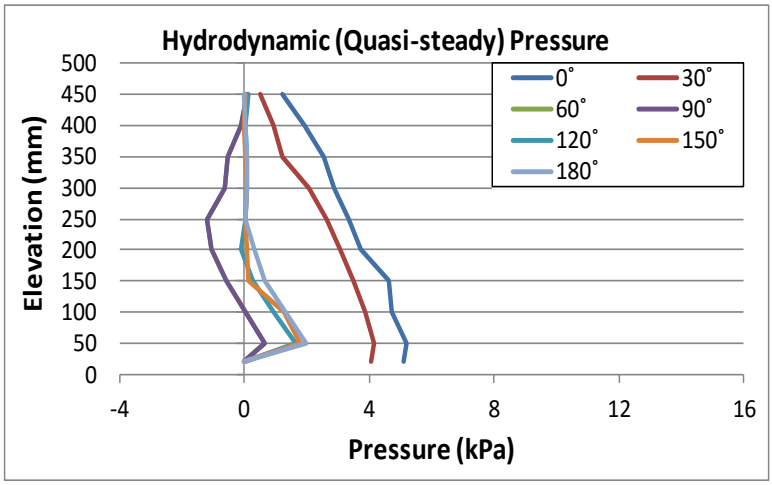

(c)

Figure B-16. Vertical distribution of pressure around the circular model generated by 850 mm impounding depth for three flow states: **a)** impulsive; **b)** run-up; and **c)** quasi-steady

Table B-4. Factor α for three flow states around the circular model for 850 mm impounding depth

Rotation Angle	Flow State	Maximum Pressure (kPa)	factor α α =P/γ.h	Average α
0˚	Impulsive	5.559	1.27	1.21
	Run-up	5.170	1.18	
	Quasi-steady	5.210	1.19	
30˚	Impulsive	3.957	0.90	0.98
	Run-up	4.846	1.10	
	Quasi-steady	4.152	0.95	
60˚	Impulsive	0.974	0.22	0.26
	Run-up	1.076	0.25	
	Quasi-steady	1.316	0.30	
90˚	Impulsive	0.134	0.03	0.14
	Run-up	1.081	0.25	
	Quasi-steady	0.666	0.15	
120˚	Impulsive	0.123	0.03	0.31
	Run-up	2.304	0.53	
	Quasi-steady	1.665	0.38	
150˚	Impulsive	1.472	0.34	0.41
	Run-up	2.111	0.48	
	Quasi-steady	1.804	0.41	
180˚	Impulsive	0.147	0.03	0.30
	Run-up	1.782	0.41	
	Quasi-steady	2.003	0.46	

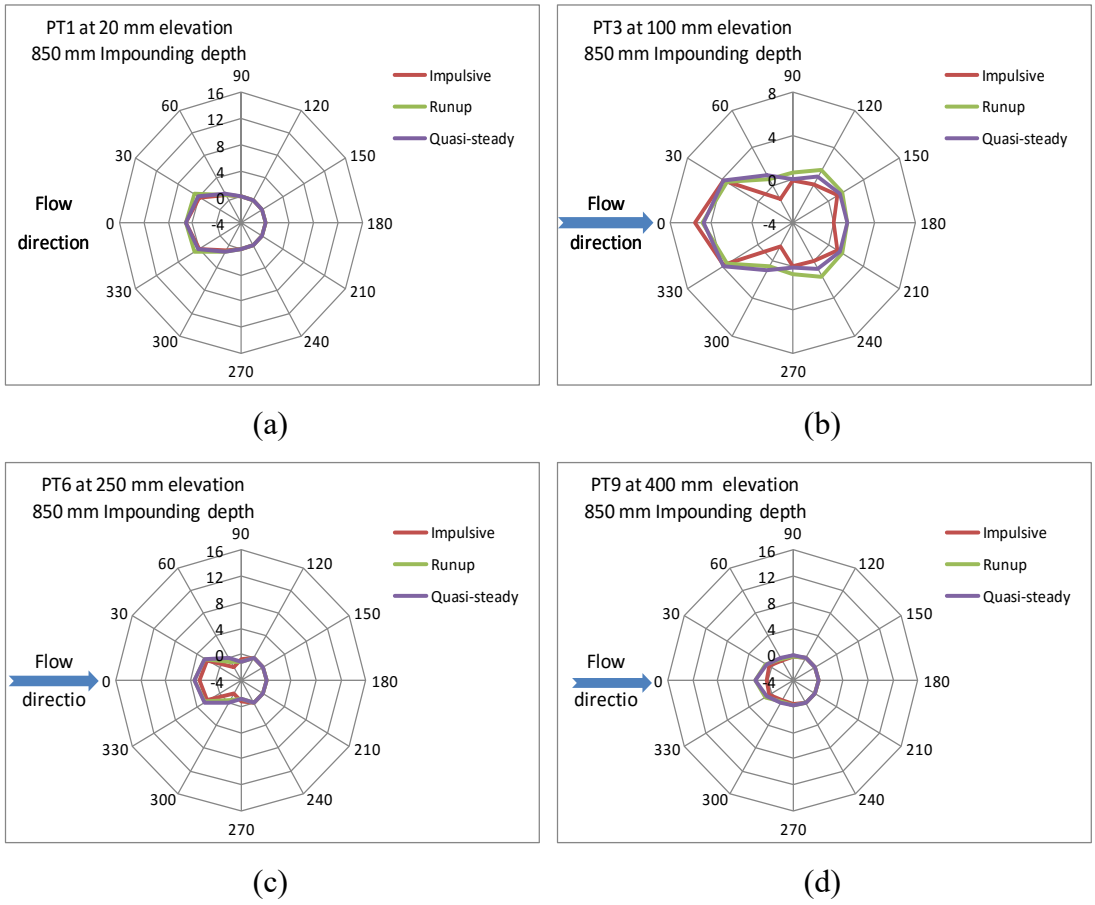

Figure B-17. Pressure distribution around the circular model generated by 850 mm impounding depth for three flow states at four elevations: **a)** 20 mm; **b)** 100 mm; **c)** 250 mm; and **d)** 400 mm

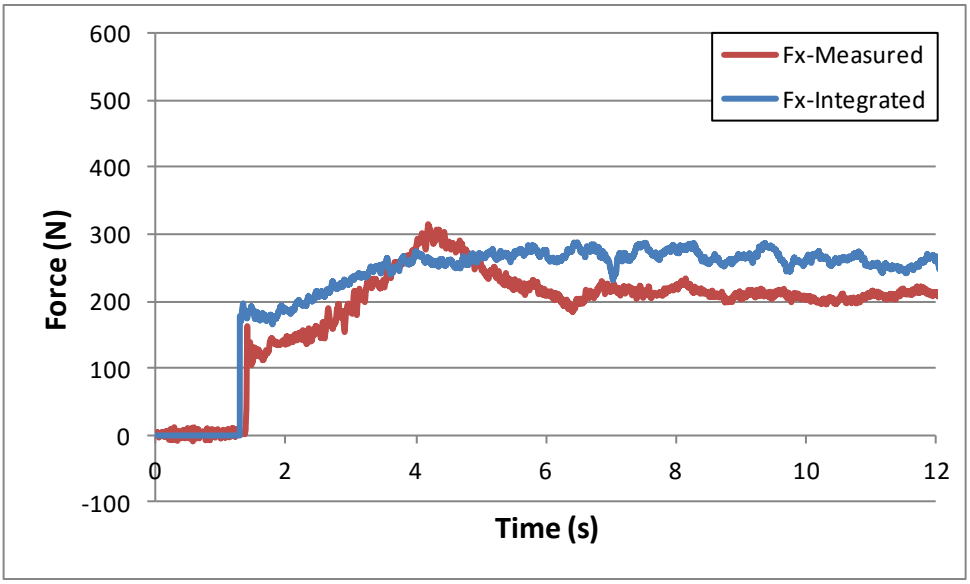

(a)

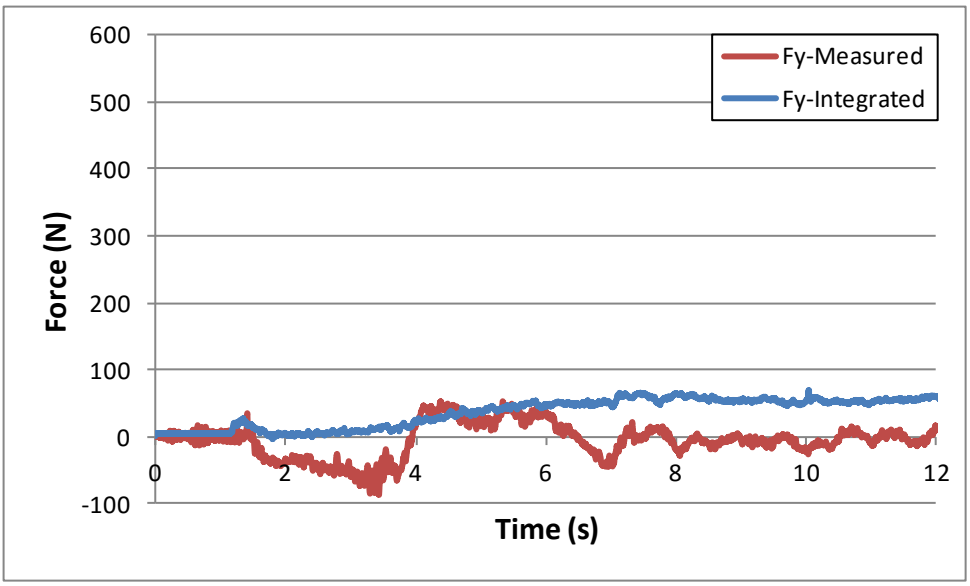

(b)

Figure B-18. Time histories for laboratory recorded and calculated forces induced on the circular model by 850 mm impounding depth: **a)** longitudinal direction; and **b)** transverse direction

The integration of the pressure around the circular model outcome the following graphs. The proposed positive directions of the imposed force on the model at each angle are shown in the figure below.

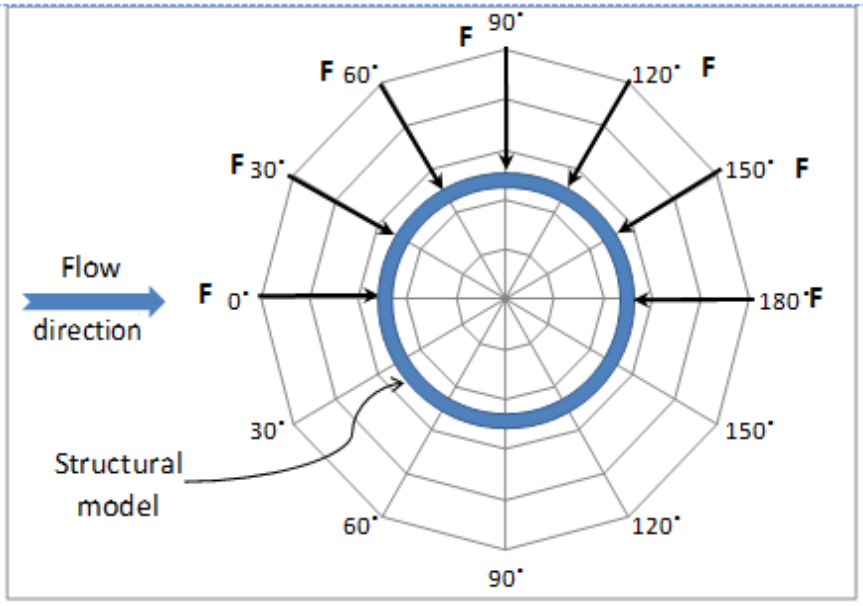

Figure B-19. Location of the resultant forces from integration

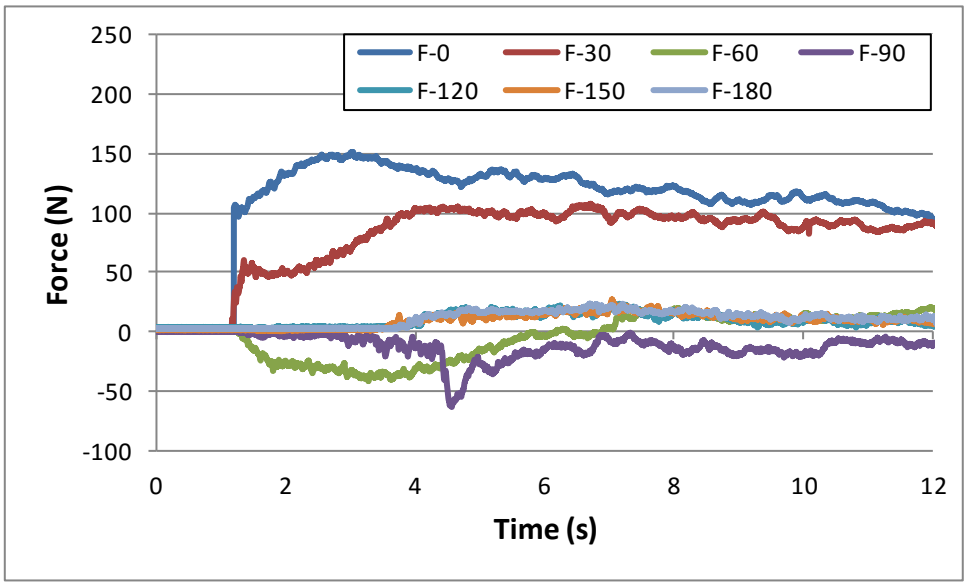

Figure B-20. Time histories for forces calculated by integration of pressures on the circular model by 850 mm impounding depth at angles of: 0˚, 30˚, 60˚, 90˚, 120˚, 150˚, 180˚

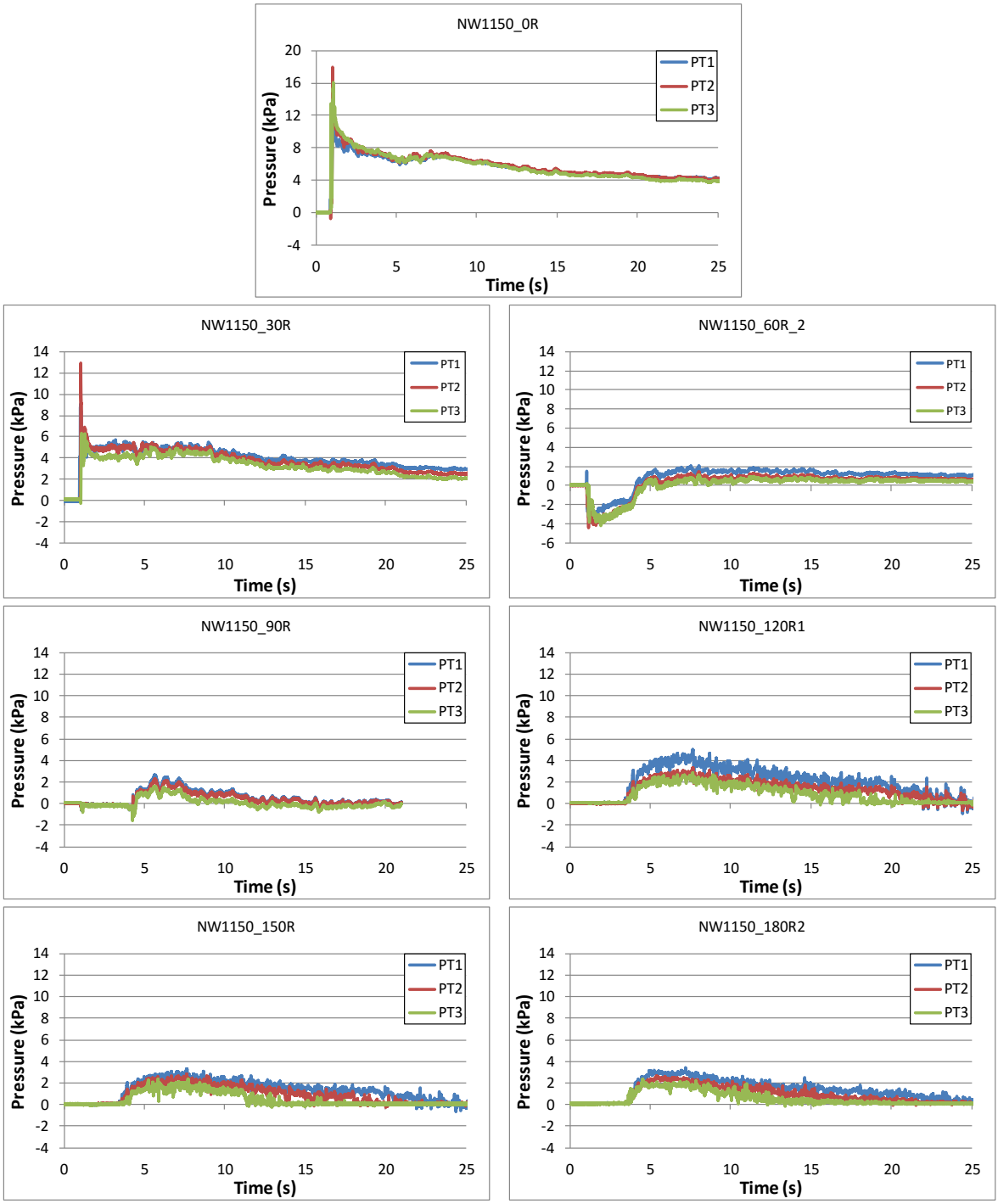

Figure B-21. Pressure distribution around the circular model generated by 1150 mm impounding depth

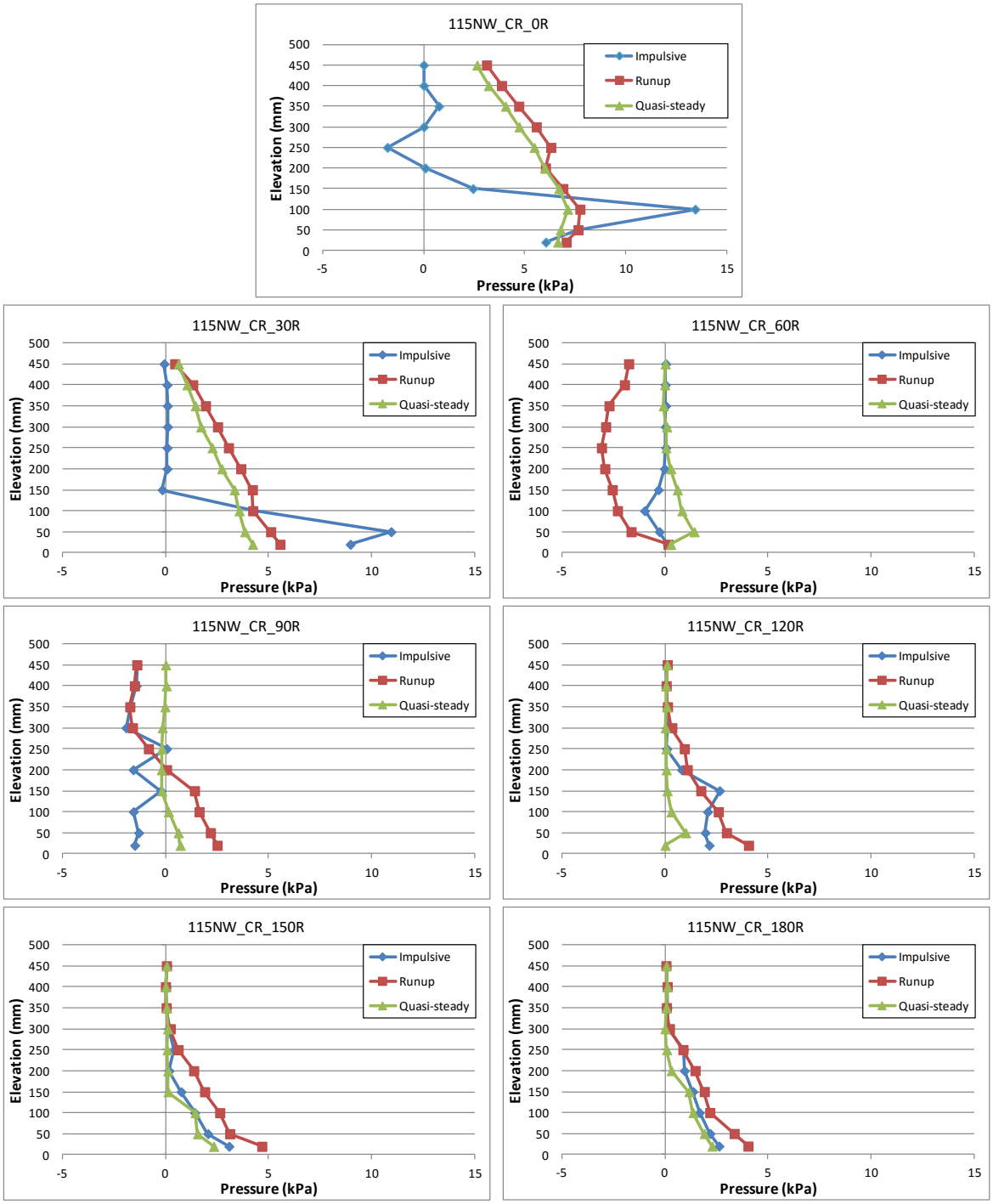

Figure B-22. Vertical distribution of pressure induced on the circular model by hydraulic bore generated from 1150 mm impounding water depth

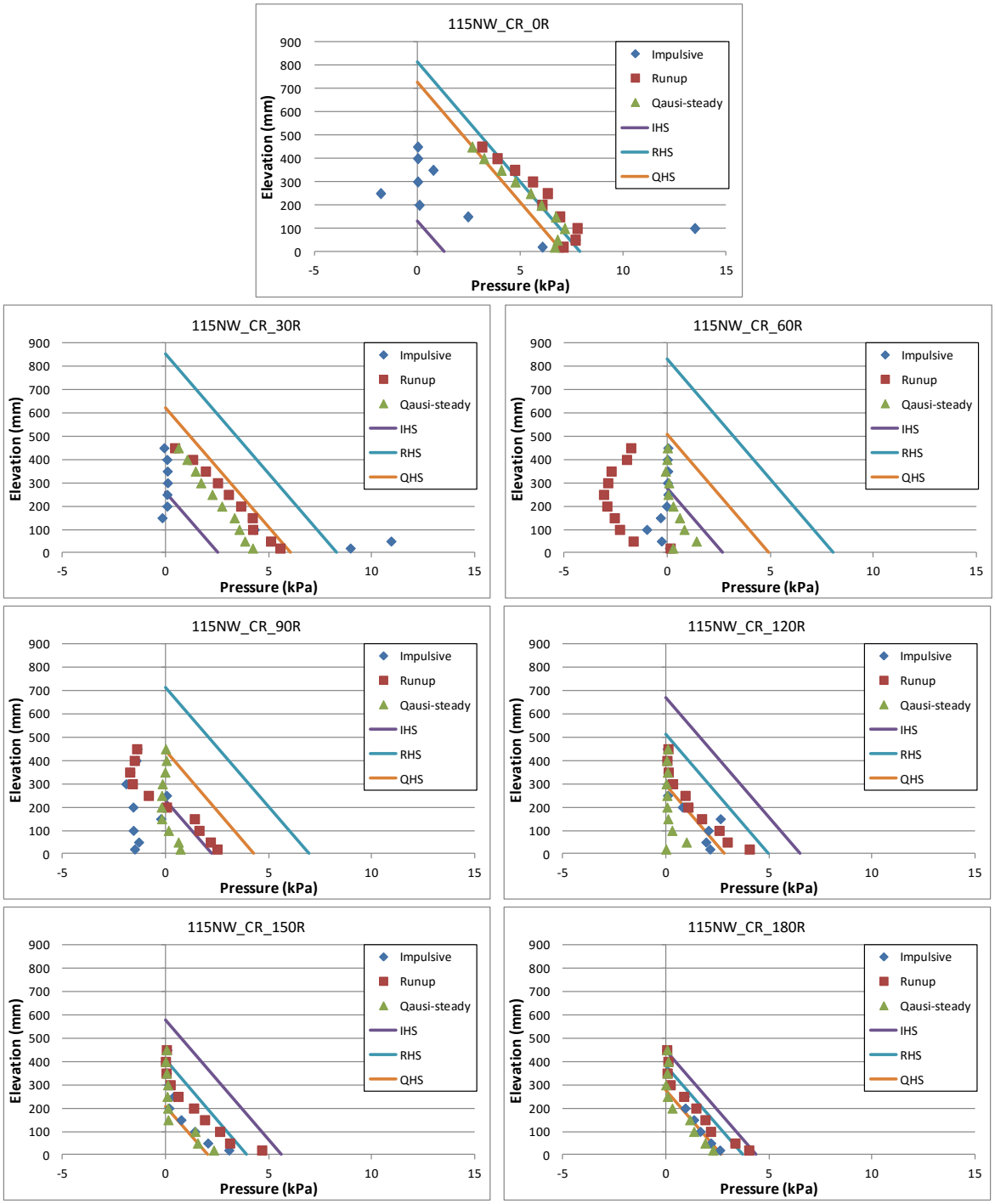

Figure B-23. Experimentally measured pressure induced on the circular model by hydraulic bore generated from 1150 mm impounding depth and hydrostatic distribution

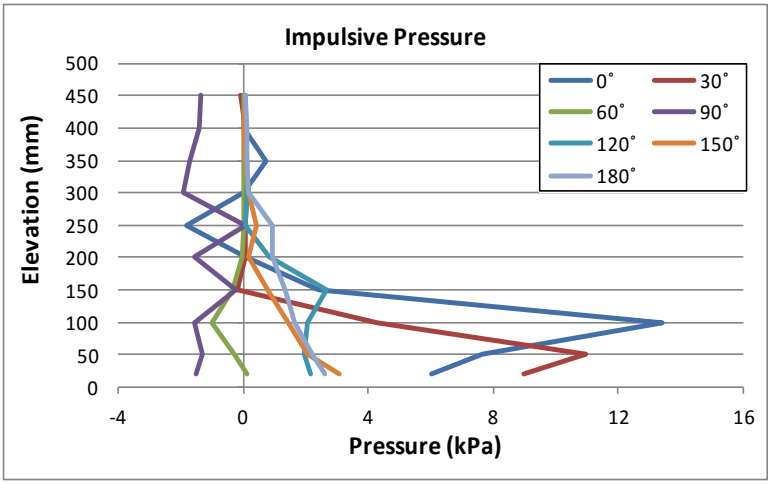

(a)

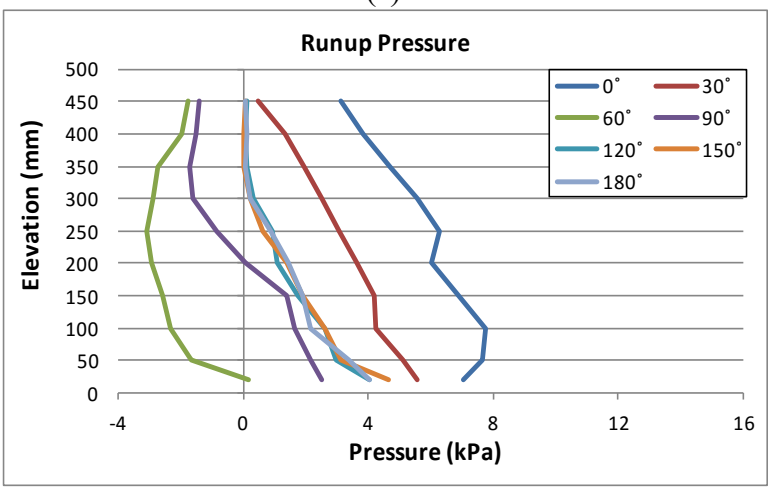

(b)

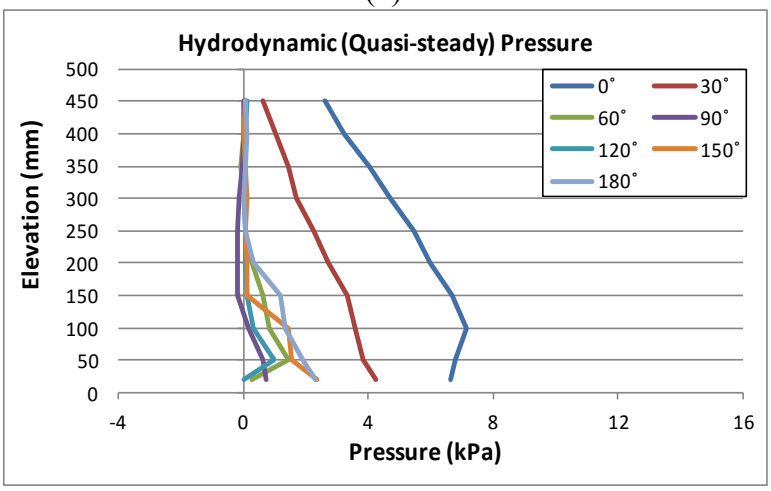

(c)

Figure B-24. Vertical distribution of pressure around the circular model generated by 1150 mm impounding depth for three flow states: **a)** impulsive; **b)** run-up; and **c)** quasi-steady

Table B-5. Factor α for three flow states around the circular model for 1150 mm impounding depth

Rotation Angle	Flow State	Maximum Pressure (kPa)	Factor α $\alpha = P/\gamma.h$	Average α
0°	Impulsive	13.436	3.06	2.15
	Run-up	7.732	1.76	
	Quasi-steady	7.121	1.62	
30°	Impulsive	10.943	2.50	1.57
	Run-up	5.554	1.27	
	Quasi-steady	4.223	0.96	
60°	Impulsive	0.110	0.03	0.13
	Run-up	0.144	0.03	
	Quasi-steady	1.412	0.32	
90°	Impulsive	0.048	0.01	0.25
	Run-up	2.501	0.57	
	Quasi-steady	0.709	0.16	
120°	Impulsive	2.643	0.60	0.58
	Run-up	4.052	0.92	
	Quasi-steady	0.995	0.23	
150°	Impulsive	3.074	0.70	0.77
	Run-up	4.669	1.06	
	Quasi-steady	2.332	0.53	
180°	Impulsive	2.617	0.60	0.68
	Run-up	4.026	0.92	
	Quasi-steady	2.282	0.52	

Note: the value of α varies from 0.13 to 2.15.

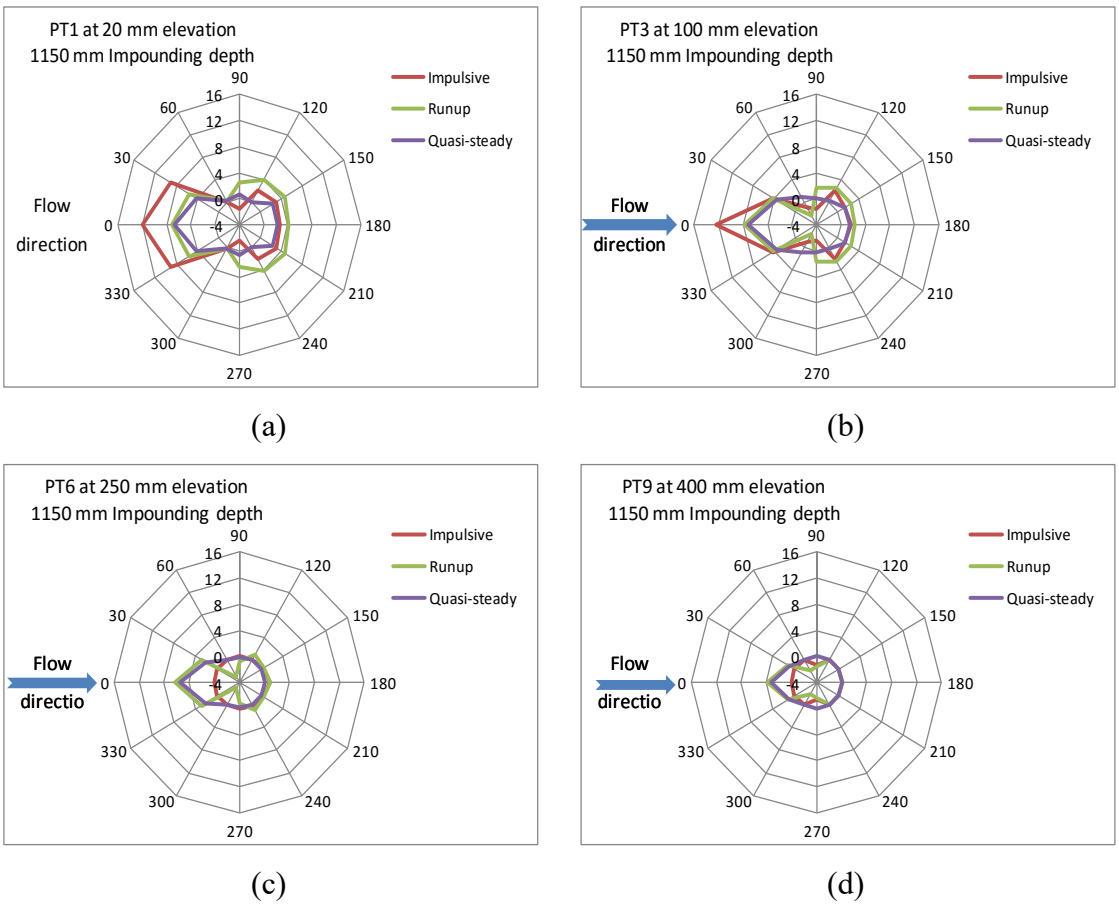

Figure B-25. Pressure distribution around the circular model generated by 1150 mm impounding depth for three flow states at four elevations: **a)** 20 mm; **b)** 100 mm; **c)** 250 mm; and **d)** 400 mm

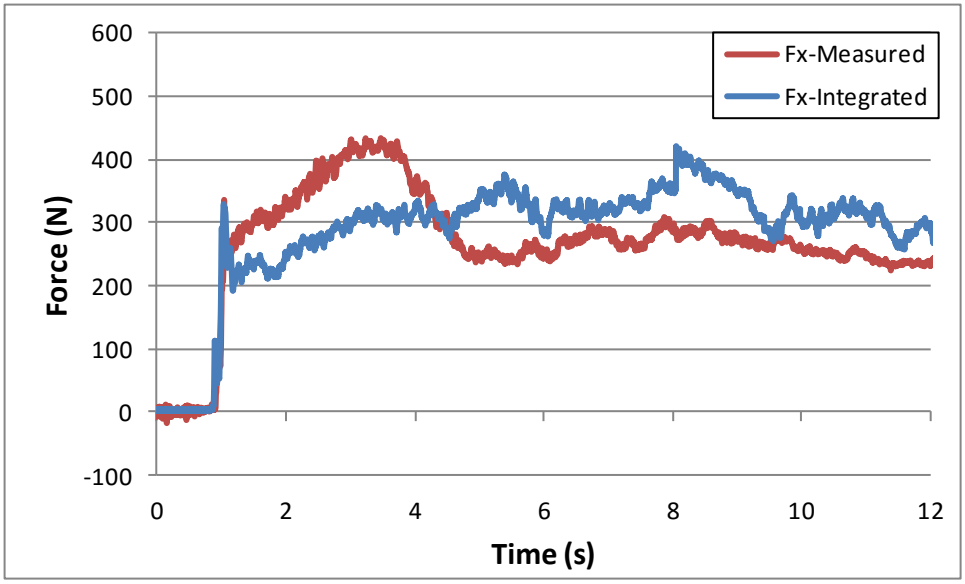

(a)

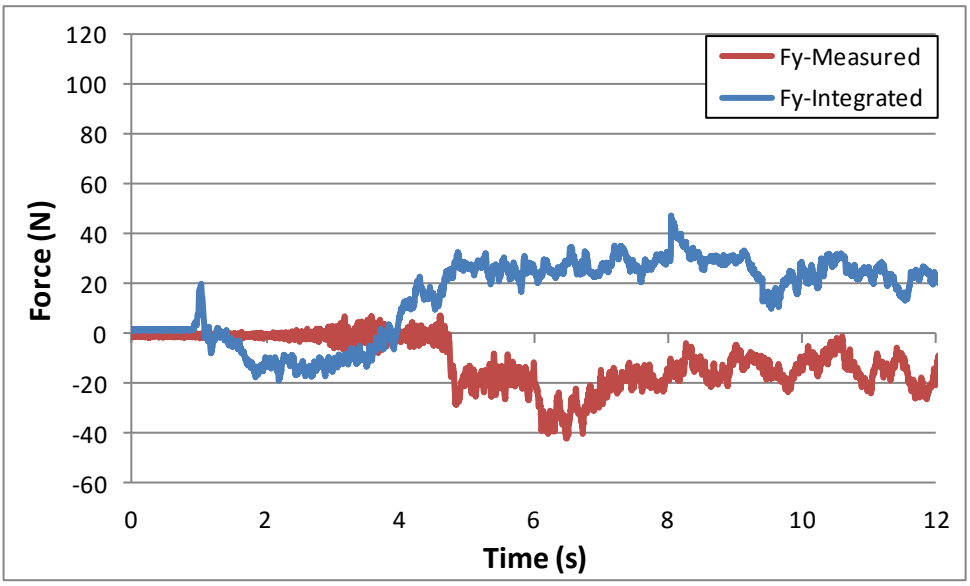

(b)

Figure B-26. Time histories for laboratory recorded and calculated forces induced on the circular model by 1150 mm impounding depth: **a)** longitudinal direction; and **b)** transverse direction

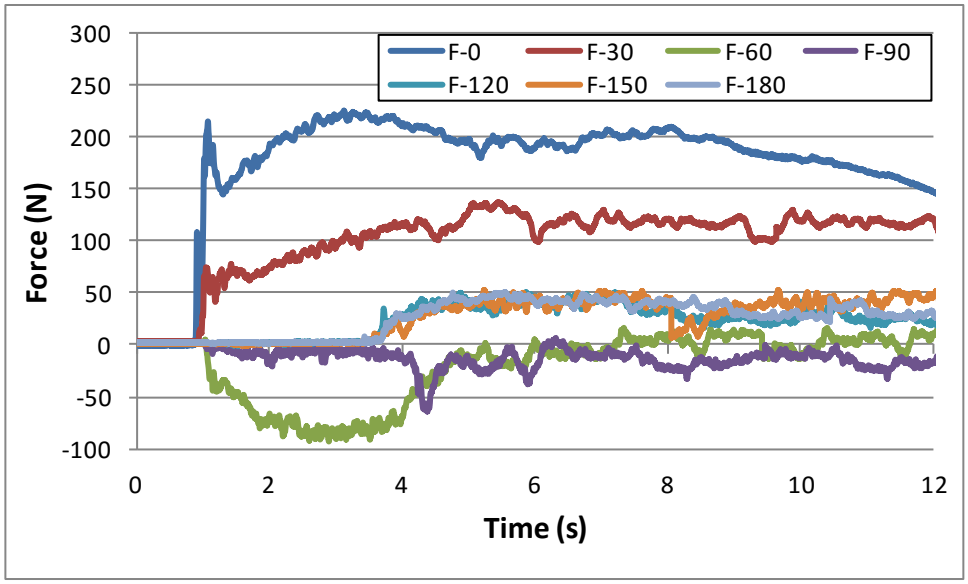

Figure B-27. Time histories for forces calculated by integration of pressures on the circular model by 1150 mm impounding depth at angles of: 0˚, 30˚, 60˚, 90˚, 120˚, 150˚, 180˚

Table B-6. Factor α for three flow states for three impounding water depths

Rotation Angle	Alfa Factor (α)			
	550 mm	**850 mm**	**1150 mm**	**Average α**
0˚	2.86	3.41	3.63	2.64
	1.60	1.54	1.76	1.63
	1.28	1.55	1.62	1.49
30˚	1.51	1.18	2.50	1.73
	1.32	1.45	1.27	1.35
	1.11	1.24	0.96	1.10
60˚	0.01	0.29	0.03	0.11
	0.41	0.32	0.03	0.25
	0.35	0.39	0.32	0.35
90˚	0.04	0.04	0.02	0.03
	0.09	0.32	-0.03	0.13
	0.04	0.20	0.16	0.13
120˚	0.24	0.04	0.60	0.29
	0.46	0.69	0.92	0.69
	0.13	0.50	0.23	0.29
150˚	0.24	0.44	0.70	0.46
	0.56	0.63	1.06	0.75
	0.11	0.54	0.53	0.39
180˚	0.13	0.04	0.60	0.26
	0.53	0.53	0.92	0.66
	0.13	0.60	0.52	0.42

Lateral Displacement

An LVDT was installed at a height of one meter from the flume bed on the upstream face of the models with a steel frame that was supported on the flume side walls to capture the lateral displacements in the flow direction. The extension of the LVDT was connected to the top end of the structural model on the upstream face to record the lateral displacement-time history. At the beginning of each test, the LVDT was re-zeroed to ensure any residual displacement from previous tests was removed. The lateral displacements recorded during testing were marked with minimal low-amplitude oscillations at the time the swing gate opened. This was caused due to vibrations of the flume which occurred during the opening operation of the swinging gate. This oscillation was damped prior to the bore front reaching the models. The following sections present the results and discussion of the displacements-time histories for the two structural models.

Square model displacements

Figure B-28 illustrates the displacement-time histories recorded for the square model due to bores generated by the three impounding water depths. The lateral displacement increased proportionally with an increase in the impounding water depth. The maximum displacements recorded for the square model increased by 160% and 494% for impounding water depth increases of 300 mm and 600 mm (for the 850 and 1150 mm impoundment depth), respectively, (Figure B-28). Maximum lateral displacements were recorded at the run-up flow stage, and as the bore redirected to flow on the sides of the model, the displacement began to decrease gradually. The displacement at the quasi-steady flow phase was nearly constant for each impoundment depth.

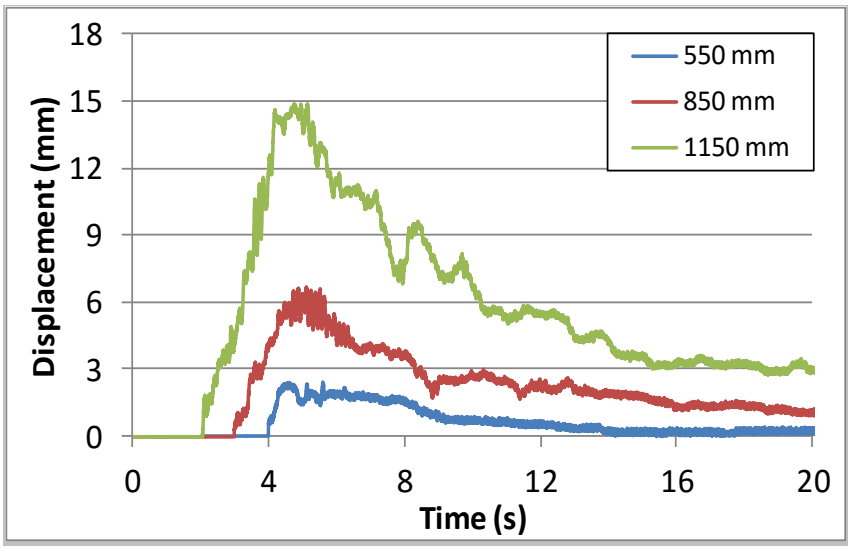

Figure B-28 Time histories of the displacement of the square model caused by the three impounding water depths.

Circular model displacement

The displacements in the circular model increased at a substantially lower rate as the bores generated by impounding water depth increased from 850 to 1150 mm. The circular model sustained significantly lower displacements than the square model (Figure B-29). The decrease in the maximum displacement was 50%. This was probably attributed to two factors: (1) the difference in the cross-sectional shape of the models and (2) the fact that the wall thickness of the square model was slightly less than that of the circular model which translated into a slight difference in the structural stiffness and the magnitude of the forces.

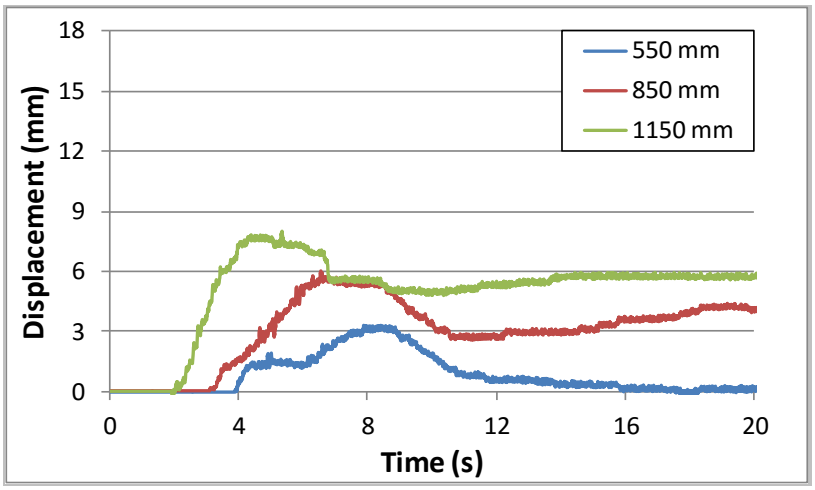

Figure B-29 Time histories of the displacement of the circular model caused by the three impounding water depths.

The displacements show a rapid increase as the bore front impacts the model. The rate of displacement increased with an increase in bore depth and velocity. Thereafter the displacements gradually reduced to approximately one quarter of its maximum value during the quasi-steady flow state. The responses show that as the impounding water depth increased (higher maximum inundation depth at the model), higher lateral displacements were experienced by the model.

Lateral Accelerations

An accelerometer was also installed at the top edge of the two models to record the acceleration experienced when impacted by the simulated tsunami bores for the three impoundment depths. The acceleration records for the different impounding water depths for both models demonstrated that the models experienced short period oscillations (high frequency) for most of the response.

Square model

The time-history of the acceleration of the square model impacted by a hydraulic bore generated from 550 mm impoundment depth is shown in Figure B-30. The maximum amplitude in the acceleration record occurred at the initial bore impact. The maximum amplitude for the square column was $0.15g$, $0.3g$, and $0.4g$ for the impoundment depths of 550, 850, and 1150 mm, respectively.

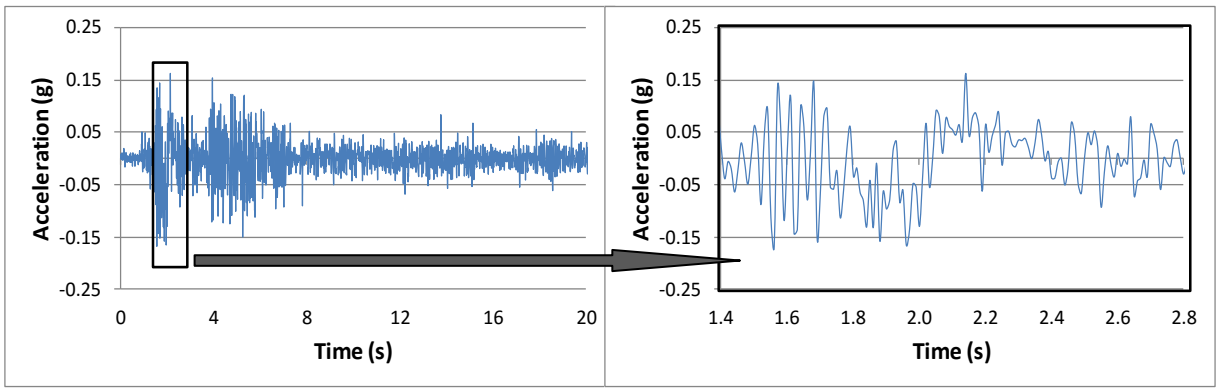

(a) (b)

Figure B-30 Time history of the acceleration of the square model generated by a bore due to the 550 mm impounding depth: **a)** 20 s record; and **b)** enlarged time-scale corresponding to the initial impact

5.3.5.2 Circular model

Figure B-31 provides the acceleration-time history for the circular model caused by the 550 mm impounding water depth.

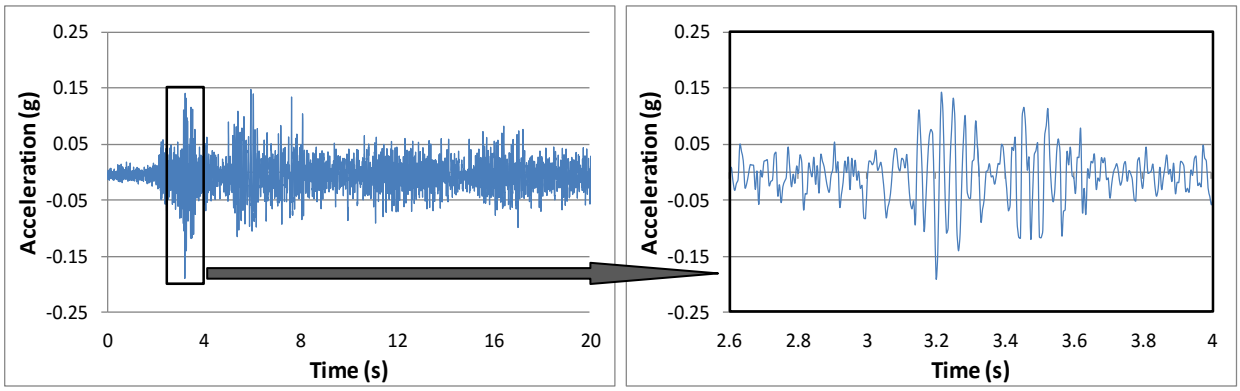

(a) (b)

Figure B-31 Time history of the acceleration of the circular model generated by a bore due to the 550 mm impounding depth: **a)** 20 s record; and **b)** enlarged time-scale corresponding to the initial impact

The acceleration response corresponding to the first impact with the leading edge of the bore front is shown in Figure B-31 (b). The maximum acceleration experienced by the circular model was -0.195g, where the negative refers to the upstream direction. The

acceleration-time histories captured by the accelerometer demonstrated that the maximum acceleration in the model occurred when the bore front impacted the model. This maximum acceleration was proportional to the depth of the bore. Acceleration oscillations with high amplitude had periods between 200 to 350 ms as the bore flow built up on the upstream face of the models. As the bore redirected around the sides of the model, the magnitude of the acceleration decreased to a quasi-steady value while the flow continued. Typically, the accelerations in the square model were higher than those in the circular model for the same bore depth. These results are in agreement with trends observed in the forces, overturning moments.

Appendix C

Sample of Recorded Data and Analysis

Debris Impact Tests

Table C-1. Debris impact tests with 550 mm impounding depth

Debris	x=1.75	x=2.25	x=2.75	x=3.25	subtotal
1kg	15	5	5	3	28
2kg1P	15	5	5	5	30
2kg2P	3	3	3	3	12

Table C-2. Debris impact tests with 850 mm impounding depth

Debris	x=1.75	x=2.25	x=2.75	x=3.25	subtotal
1kg	12	3	4	3	22
2kg1P	15	5	5	5	30
2kg2P	10	3	3	3	19

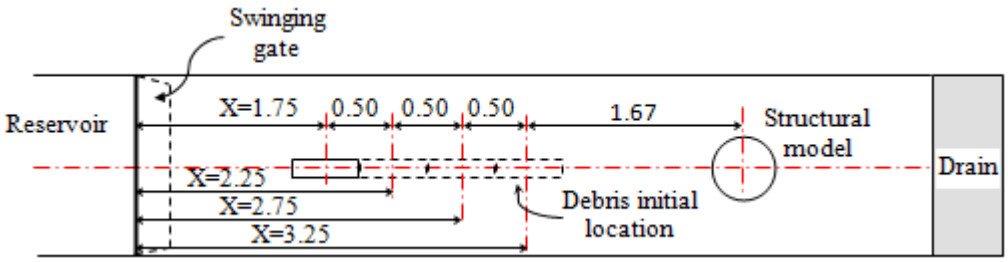

Figure C-1. Layout for debris impact tests

Table C-3. Summary of debris tests: group 1kg-550

Test No.	X (m)	Impact Force (N)	Theata (θ)(deg)	Fi(φ) (deg)	e = d (mm)	Debris Velocity (m/s)	Impulse (N.s)	Impact Duration (ms)
1	1.75	387.514	33	20	121.71	2.1885	0.6747	2
2	1.75	850.32	12	15	7.98	2.506	2.1754	3
3	1.75	732.947	0	30	76.20	2.353	0.75874	2
4	1.75	396.10	-5	52	127.81	2.214	0.9134	3
5	1.75	762.29	4	18	57.09	2.49	1.9979	3
6	1.75	838.15	-10	0	26.46	2.317	2.1300	3
7	1.75	346.99	9	70	133.29	2.462	0.6076	2
8	1.75	790.745	-1	20	49.62	2.353	1.9966	3
9	1.75	505.74	3	40	91.72	2.494	0.8894	2
10	1.75	871	6	6	0.00	2.205	1.5920	2
11	1.75	402.04	-5	46	118.44	2.351	0.5965	2
12	1.75	485.52	-2	45	111.46	2.49	0.8573	2
13	1.75	177.01	10	80	143.21	2.353	0.4364	3
14	1.75	264.14	-3	65	141	2.462	0.5713	3
15	1.75	322.07	-5	67	144.94	2.353	0.5965	2
16	2.25	676.13	7	43	89.58	2.49	1.7114	3
17	2.25	560.14	-4	40	105.87	2.34	1.4528	3
18	2.25	879.57	-1	10	29.08	2.35	2.2670	3
19	2.25	795.97	-3	25	71.55	2.34	1.4560	2
20	2.75	819.84			0.00	2.50	1.5086	2
21	2.75	833.47	10	-10	52.12	2.46	1.5384	2
22	2.75	887.01	0	-1	2.66	2.35	2.2162	3
23	2.75	782.98	-6	0	15.93	2.41	1.4429	2
24	2.75	820.58	20	6	36.87	2.43	2.2127	3
25	3.25	793.79	5	0	13.28	2.21	1.9740	3
26	3.25	704.49	-6	20	66.81	2.21	1.3030	2
27	3.25	737.59	-8	30	93.83	2.33	1.8606	3

Table C-4. Summary of debris tests: group 1kg-850

Test No.	X (m)	Impact Force (N)	Theata (θ) (deg)	Fi(φ) (deg)	e = d (mm)	Debris Velocity (m/s)	Impulse (N.s)	Impact Duration (ms)
1	1.75	1040.31	0	0	0.00	3.04	1.9243	2
2	1.75	1015.31	0	0	0.00	2.85	1.8946	2
3	1.75	281.60	-50	50	150.08	3.06	0.8191	3
4	1.75	557.38	-40	0	97.96	3.24	0.9840	2
5	1.75	668.25	0	10	26.46	3.08	1.2632	2
6	1.75	1015.94	17	10	18.57	3.03	2.7712	3
7	1.75	400.80	-10	30	97.96	3.03	1.0210	2
8	1.75	368.32	2	55	121.71	3.32	0.6283	2
9	1.75	936.54	-8.5	0	22.53	2.92	2.3690	2
10	1.75	263.45	-80	10	152.40	3.38	0.6577	2
11	1.75	618.03	43	70	69.19	3.32	1.2757	2
12	1.75	360.14	-25	20	107.76	3.15	0.6537	2
13	2.25	841.35	5	30	64.41	3.32	1.5147	2
14	2.25	336.60	-8	60	141.30	3.30	0.5803	2
15	2.25	945.43	20	20	0.00	3.27	2.5535	3
16	2.75	616.27	0	40	97.96	3.20	1.5535	3
17	2.75	1131.22	10	2	21.21	3.28	2.0938	2
18	2.75	287.25	-12	80	152.31	3.01	0.8523	3
19	2.75	839.97	-5	20	64.41	3.19	1.5194	2
20	3.25	1111.31	10	0	26.46	3.03	2.0598	2
21	3.25	947.92	8	20	31.69	3.05	2.4200	3
22	3.25	922.09	8	10	5.32	3.05	1.6685	2

Table C-5. Summary of debris tests: group 2kg1P-550

Test No.	X (m)	Impact Force (N)	Theata (θ) (deg)	Fi(φ) (deg)	e = d (mm)	Debris Velocity (m/s)	Impulse (N.s)	Impact Duration (ms)
1	1.75	1513.93	10	20	26.46	2.32	3.9428	3
2	1.75	1547.01	0	10	26.46	2.22	2.8476	2
3	1.75	1050.65	9	30	54.62	2.19	2.8752	3
4	1.75	1668.01	0	12	31.69	2.22	4.2304	3
5	1.75	1436.34	-10	-15	13.28	2.19	2.6635	2
6	1.75	1274.24	-9	-30	54.62	2.19	3.3807	3
7	1.75	1616.12	-3	3	15.93	2.22	2.9869	2
8	1.75	1579.84	-4	-15	29.08	2.22	4.1584	3
9	1.75	1251.03	-4	-30	66.81	2.21	2.3446	2
10	1.75	1144.66	7	30	59.55	2.19	2.1495	2
11	1.75	1398.42	3	8	13.28	2.21	2.5942	2
12	1.75	1374.44	10	15	13.28	2.19	3.6923	3
13	1.75	1520.21	0	2	5.32	2.22	2.8113	2
14	2.25	1538.37	7	20	34.28	2.22	3.9958	3
15	2.25	1534.02	5	20	39.44	2.10	2.8360	2
16	2.25	1480.54	5	0	13.28	2.07	3.9003	3
17	2.25	1642.30	-2	10	31.69	2.07	3.0329	2
18	2.25	1529.74	6	6	0.00	2.08	3.8845	3
19	2.75	1478.71	4	0	10.63	2.10	3.7837	3
20	2.75	1694.01	4	-10	36.87	2.10	3.1439	2
21	2.75	1498.40	2	-3	13.28	2.00	2.7776	2
22	2.75	1577.90	4	-2	15.93	2.00	4.1746	3
23	2.75	1451.60	-1	0	2.66	2.00	2.6951	2
24	3.25	1501.52	0	-30	76.2	1.78	2.7706	2
25	3.25	1382.61	5	0	13.28	1.81	3.5170	3
26	3.25	1269.10	0	0	0	1.82	2.3481	2

Continuation of Table C-5. Summary of debris tests: group 2kg1P-550

Test No.	X (m)	Impact Force (N)	Theata (θ) (deg)	Fi(φ) (deg)	e = d (mm)	Debris Velocity (m/s)	Impulse (N.s)	Impact Duration (ms)
27	3.25	1396.32	7	1	15.93	1.80	3.6212	3
28	3.25	1439.91	-1	-1	0	1.81	3.7992	3

Table C-6. Summary of debris tests: group 2kg1P-850

Test No.	X (m)	Resultant Force (N)	Theata (θ) (deg)	Fi(φ) (deg)	e = d (mm)	Debris Velocity (m/s)	Impulse (N.s)	Impact Duration (ms)
1	1.75	730.54	3	40	225.00	3.16	1.2476	2
2	1.75	2352.71	4	0	10.63	2.85	6.1729	3
3	1.75	2230.71	-8	0	21.21	2.83	4.1541	2
4	1.75	1348.02	2	-75	148.49	2.86	2.6513	2
5	1.75	1453.46	-5	30	87.41	3.07	2.5907	2
6	1.75	2389.32	-5	0	13.28	2.85	6.4375	3
7	1.75	1844.81			48.00	2.92	5.1649	3
8	1.75	2126.41	5	0	13.28	2.86	3.9998	2
9	1.75	2439.32	0	0	0.00	2.86	6.3229	3
10	1.75	2279.20	3	0	7.98	2.85	4.2629	2
11	1.75	2450.29	1	10	23.84	2.96	4.5661	2
12	1.75	1989.11	15	0	39.44	2.97	3.7418	2
13	1.75	2187.54	10	0	26.46	2.81	4.1198	2
14	1.75	1383.66	3	65	134.56	2.83		
15	1.75	1200.02	30	85	124.84	2.86		
1	2.25	2250.97	-4	0	10.63	2.85	4.2347	2
2	2.25	2180.44	0	-10	26.46	2.86	5.7679	3
3	2.25	2420.56	-5	0	13.28	2.85	6.3202	3
4	2.25	2379.21	-4	3	18.57	2.85	6.2655	3

Continuation of Table C-6. for Summary of debris tests: group 2kg1P-850

Test No.	X (m)	Resultant Force (N)	Theata (θ) (deg)	Fi(φ) (deg)	e = d (mm)	Debris Velocity (m/s)	Impulse (N.s)	Impact Duration (ms)
5	2.25	2231.73	-3	-5	5.32	2.85	6.0175	3
1	2.75	2151.41	-2	5	18.57	2.67	4.0543	2
2	2.75	2235.24	-4	10	36.87	2.85	6.0518	3
3	2.75	2224.14	1	0	2.66	2.86	5.9908	3
4	2.75	1207.83	-10	20	76.20	2.63	3.3214	3
5	2.75	2362.18	2	2	0	2.67	4.4331	2
1	3.25	2352.81	-1	10	29.07	2.67		
2	3.25	2273.36	1	10	23.84	2.67		
3	3.25	2301.3	0	-10	26.46	2.50		
4	3.25	2125.75	3	2	2.66	2.50		
5	3.25	2300.92	0	-10	26.46	2.50		

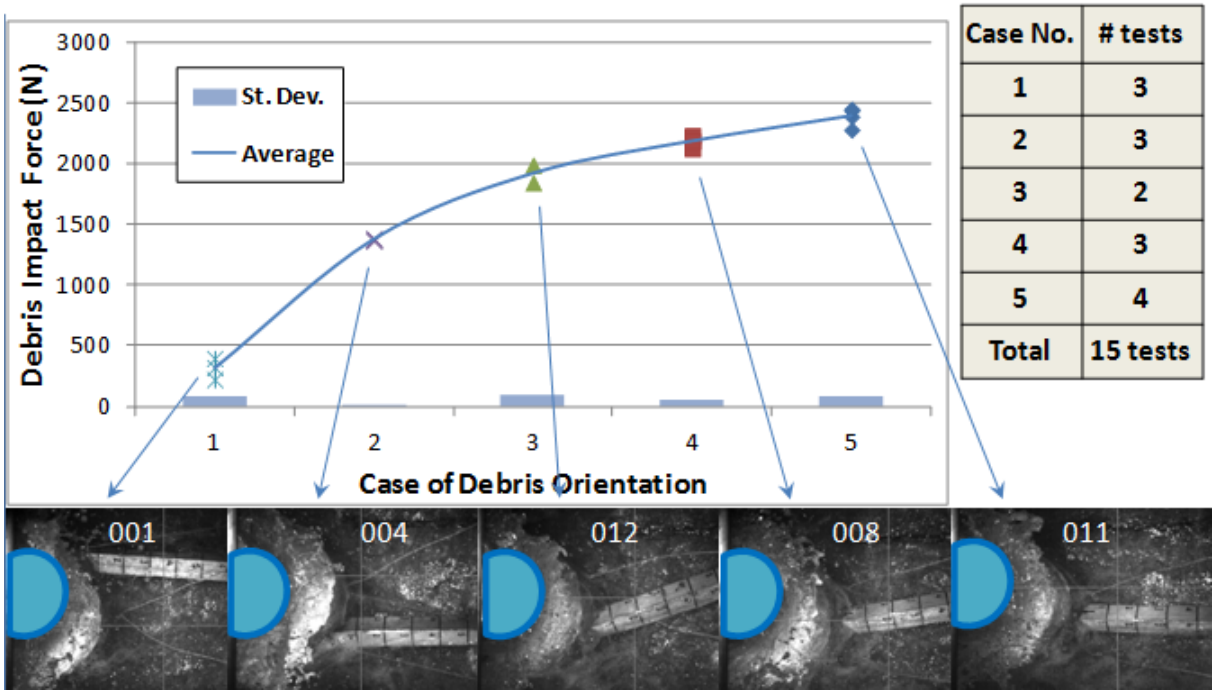

Figure C-2. Influence of debris orientation on the magnitude of the debris impact force induced on the model for test group 2kg1P-850

Table C-7. Summary of debris tests: group 2kg2P-550

Test No.	X (m)	Resultant Force (N)	Theata (deg)	Fi(φ)	E = d (mm)	Debris Velocity (m/s)	Impulse (N.s)	Impact Duration (ms)
1	1.75	1255.06	0	1	2.66	2.35	2.3711	2
2	1.75	1664.41	10	0	26.46	2.46	3.1080	2
3	1.75	1023.85	5	0	13.28	2.32	1.9358	2
4	2.25	1201.75	10	10	0	2.63	3.3352	3
5	2.25	1183.36	-8	0	21.21	2.49	2.2150	2
6	2.25	1423.76	0	1	2.66	2.50	3.7713	3
7	2.75	1157.18	12	-20	80.76	2.48	3.1013	3
8	2.75	1250.95	8	-10	47.09	2.34	2.3622	2
9	2.75	1355.93	4	4	0	2.34	3.6112	3
10	3.25	1280.16	2	2	0.00	2.22	3.3567	3
11	3.25	814.84	-15	10	64.41	2.30	2.1699	3
12	3.25	870.40	0	-10	26.46	2.21	2.3674	3

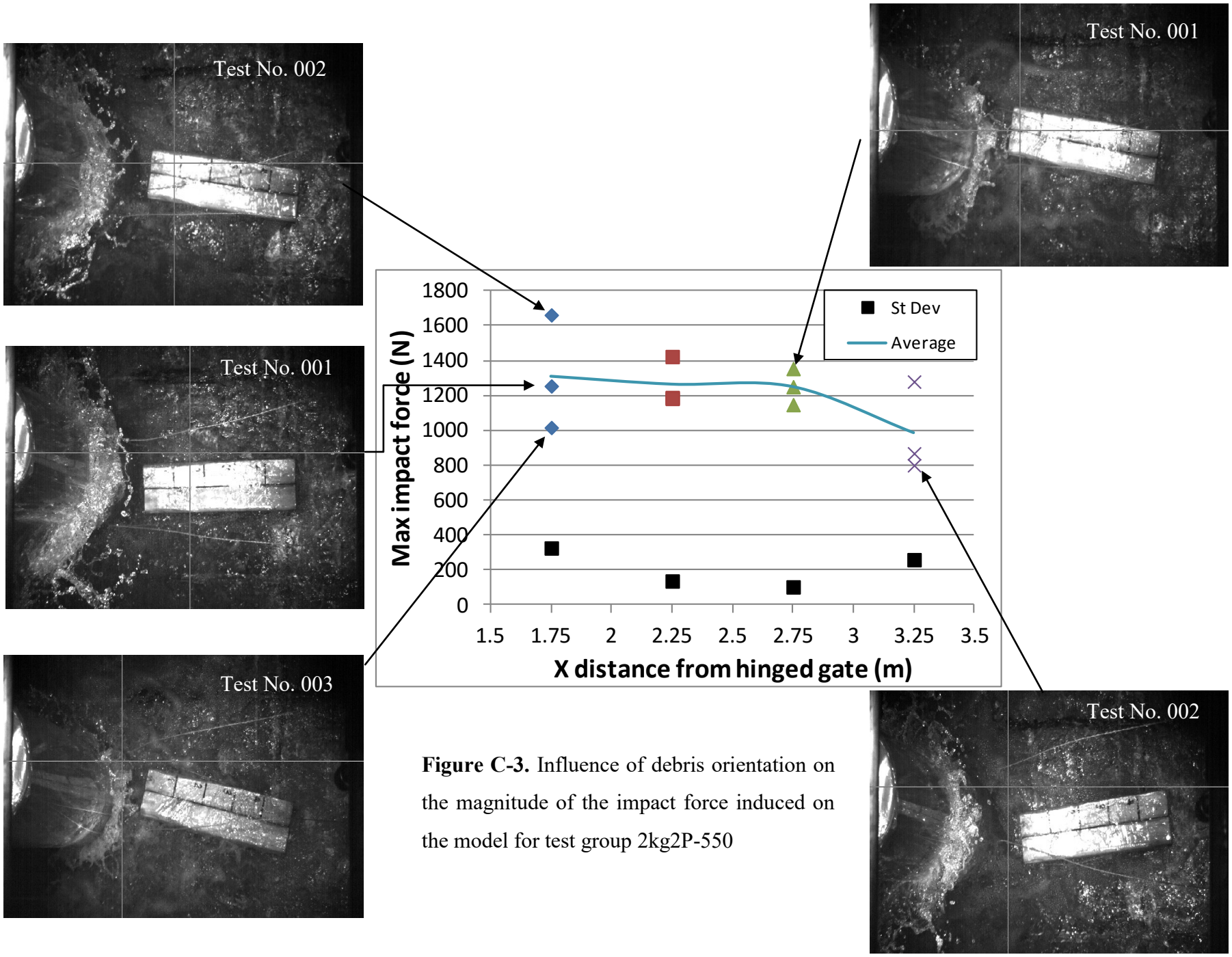

Figure C-3. Influence of debris orientation on the magnitude of the impact force induced on the model for test group 2kg2P-550

Table C-8. Summary of debris tests: group 2kg2P-850

Test No.	X (m)	Resultant Force (N)	Theata (deg)	Fi(φ) (deg)	e = d (mm)	Debris Velocity (m/s)	Impulse (N.s)	Impact Duration (ms)
1	1.75	1532.40	0	20	39.44	3.33	2.8933	2
2	1.75	1139.73	-19	10	69.86	3.22	3.2015	3
3	1.75	969.01	-33	10	87.17	2.89	1.8357	2
4	1.75	783.33	-40	20	101.10	2.98	2.6707	4
5	1.75	1246.92	-20	0	48.98	3.08	2.3584	2
6	1.75	1013.33	-10	20	75.04	3.08	2.7469	3
7	1.75	769.03	20	60	141.03	3.33	1.4649	2
8	1.75	2062.93	-12	0	30.99	3.33	3.8753	2
9	1.75	853.40	-14	20	82.69	3.08	2.3563	3
10	1.75	1077.43	0	15	52.12	3.20	2.0396	2
11	2.25	1367.83	20	24	9.99	3.42	2.5723	2
12	2.25	1611.93	30	12	40.78	3.85	3.0452	2
13	2.25	2218.50	5	0	13.23	3.32	5.8930	3
14	2.75	1523.88	11	0	28.55	3.27	4.1422	3
15	2.75	1832.74	5	0	13.23	3.32	3.4670	2
16	2.75	1514.70	0	0	0	3.20	4.1199	3
17	3.25	1539.21	3	3	0	2.85	2.8896	2
18	3.25	2015.87	3	12	23.81	3.07	3.7926	2
19	3.25	1316.51	10	0	26.06	3.03	3.6207	3

Table C-9. Debris tests groups with average debris velocity, maximum impact force, and momentum

Debris Test Group	Debris Mass (kg)	Impound Depth (mm)	Average Debris Velocity (m/s)	Debris Velocity Standard Deviation	Maximum Impact Force (N)	Rise Time (ms)	Momentum (kg . m / s)
1kg-550	1.088	550	2.37	0.10	819.84	4	2.58
1kg-850	1.088	850	3.14	0.15	1040.31	4	3.42
2kg1P-550	2.191	550	2.09	0.16	1520.21	5	4.58
2kg1P-850	2.191	850	2.81	0.15	2279.20	5	6.16
2kg2P-550	2.258	550	2.39	0.13	1254.72	5	5.40
2kg2P-850	2.258	850	3.20	0.23	2045.35	5	7.23

Photos of debris-model interaction during the impact tests

1- **Debris 1kg**

Side view

Figure C-4. Photos for 1kg debris floating in hydraulic bore generated from 550 mm impounding depth: side view

Downstream view

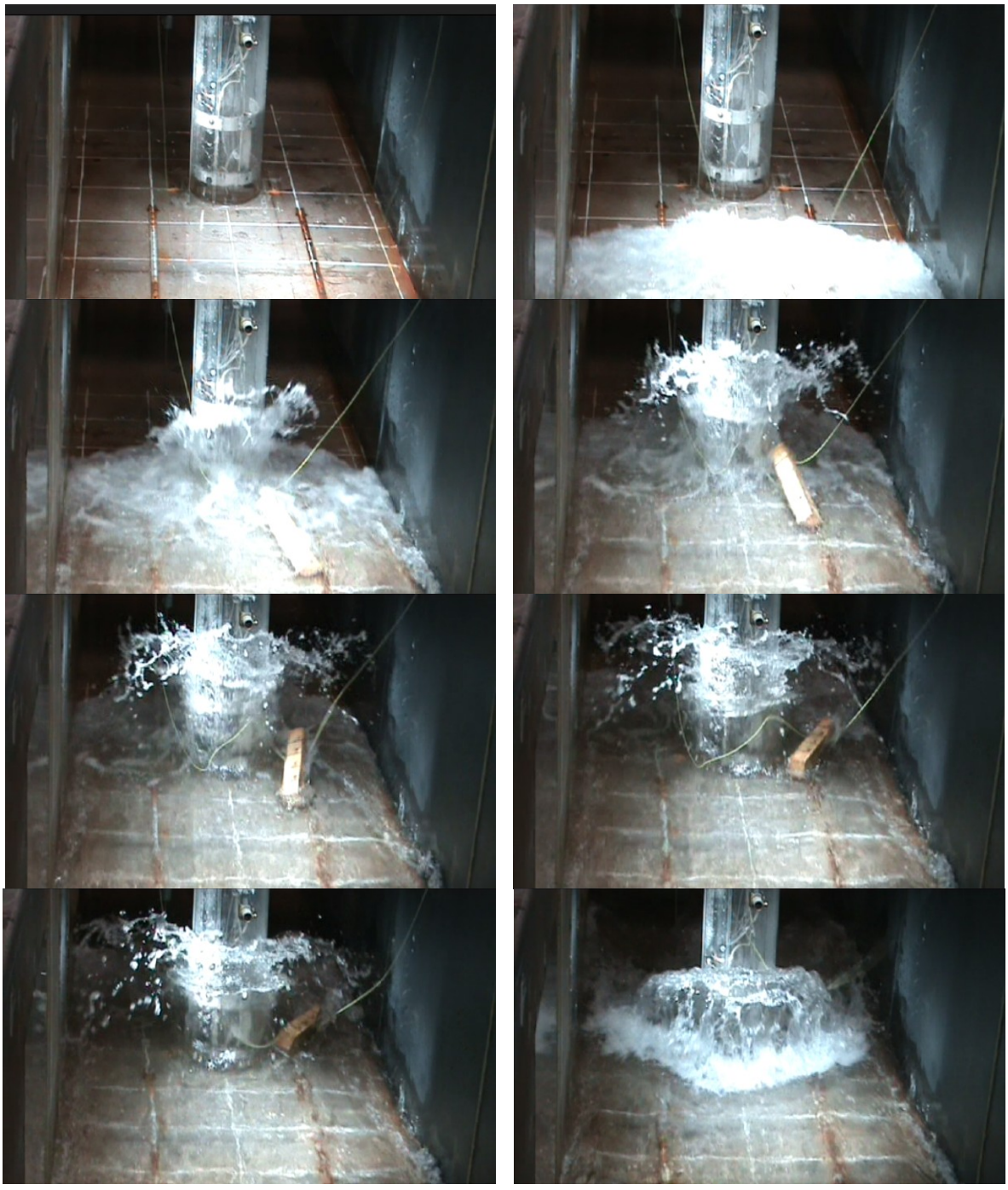

Figure C-5. Photos for 1kg debris floating in hydraulic bore generated from 550 mm impounding depth: downstream view

2- Debris 2kg1P

Side view

Figure C-6. Photos for 2kg1P debris floating in hydraulic bore generated from 850 mm impounding depth: side view

Downstream view

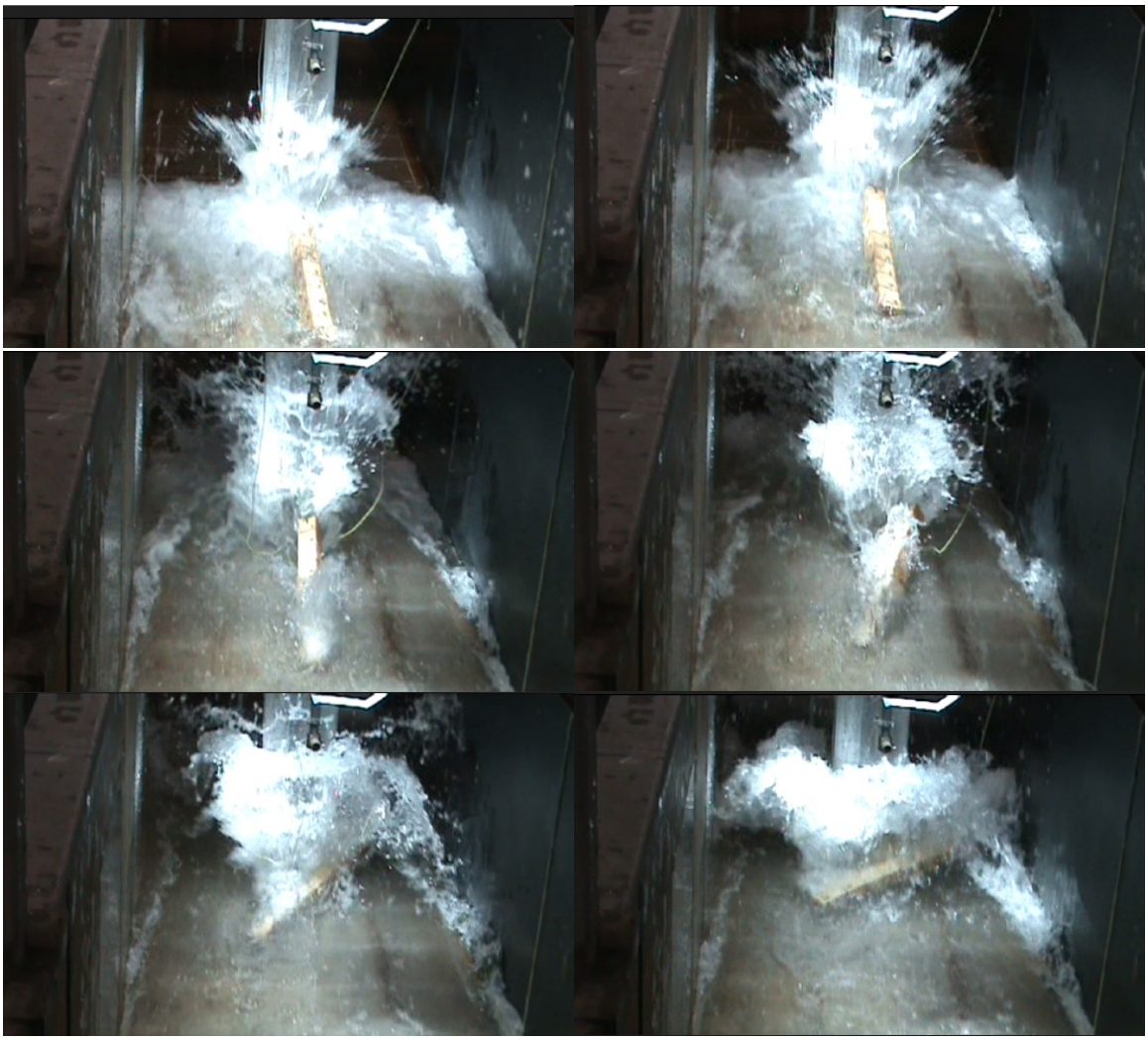

Figure C-7. Photos for 2kg1P debris floating in hydraulic bore generated from 850 mm impounding depth: downstream view

3- Debris 2kg2P

Side view

Figure C-8. Photos for 2kg2P debris floating in hydraulic bore generated from 850 mm impounding depth: side view

Downstream view

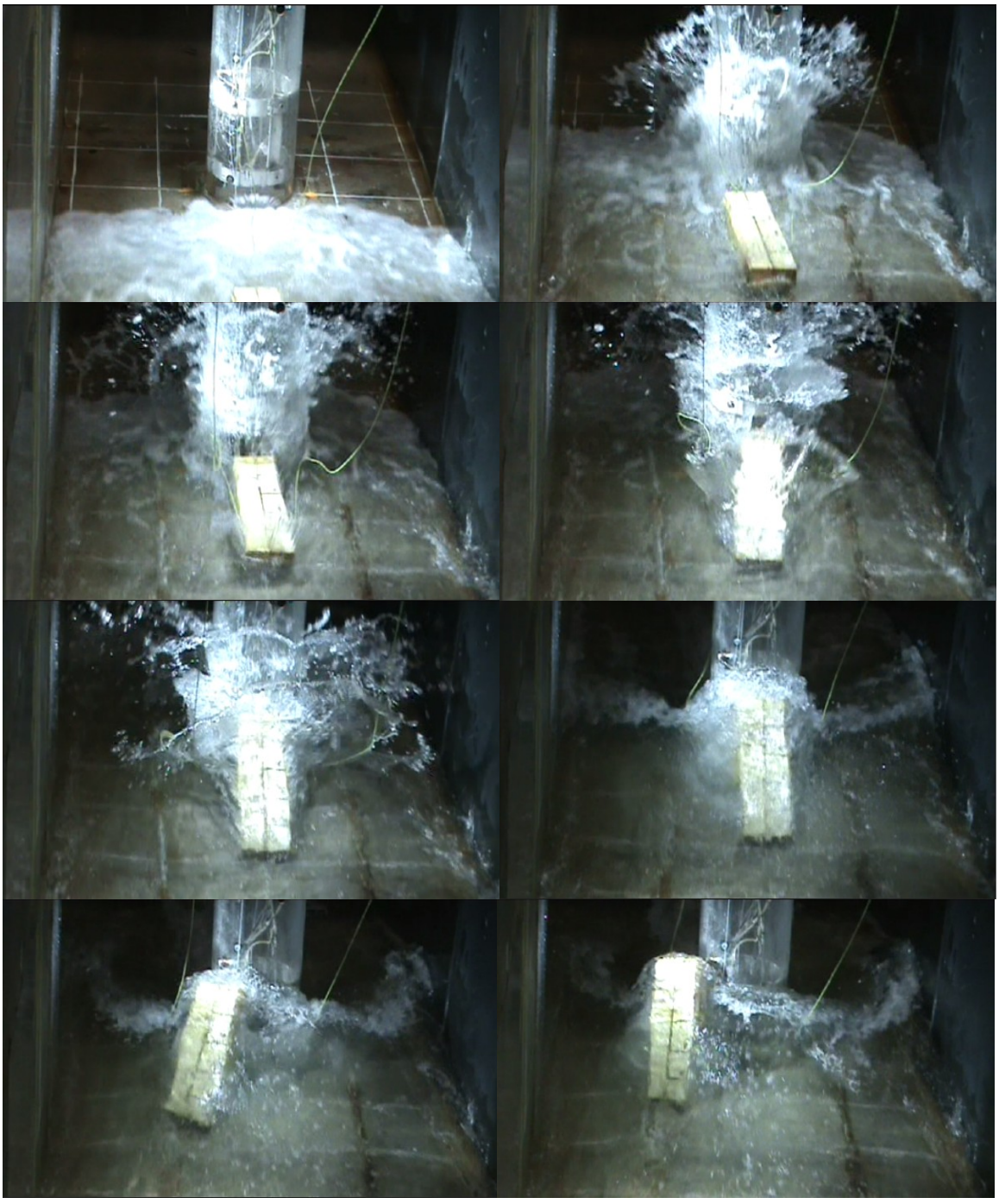

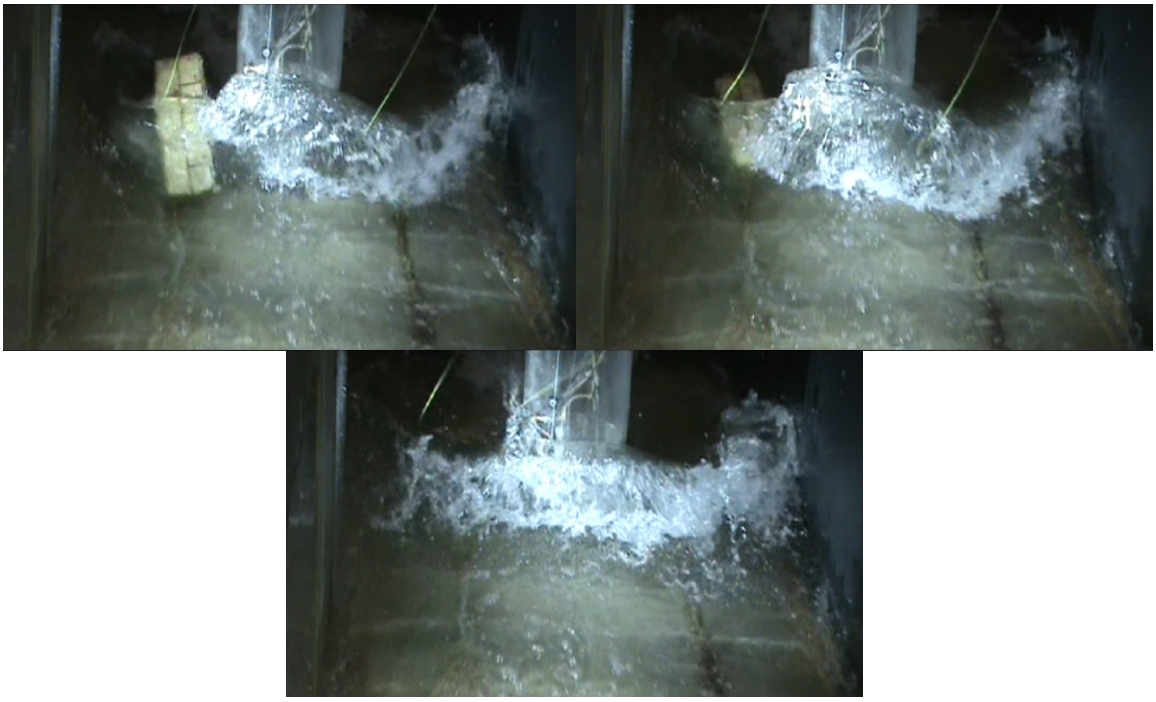

Figure C-9. Photos for 2kg2P debris floating in hydraulic bore generated from 850 mm impounding depth: downstream view

Sample Analysis for the Debris Impact for 1kg-550 Test Group

Test file name:

CR_55WH_1kg_X175_001

F_{x1} = 390.7 N

$F_{x2} = F_{x\ max}$ = 409.24 N

Debris velocity = 2.1885 m/s

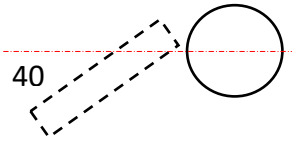

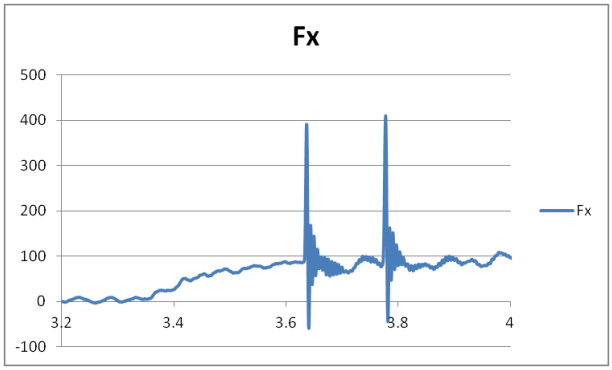

1st impact

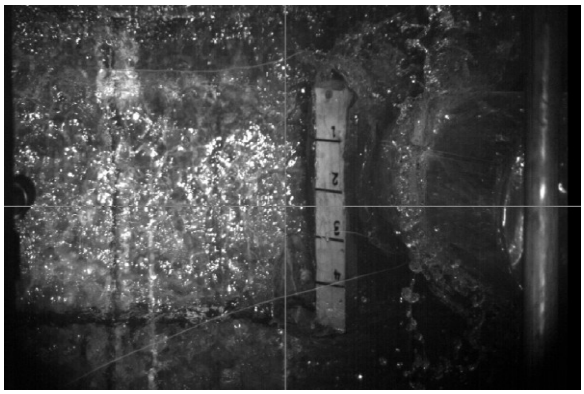

2nd impact

Figure C-10. Analysis of CR_55WH_1kg_X175_001

Test file name:

CR_55WH_1kg_X175_002

$F_{x\ max}$= 712.9 N

Debris velocity = 2.506 m/s

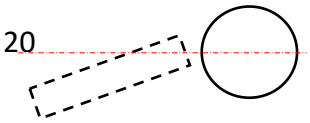

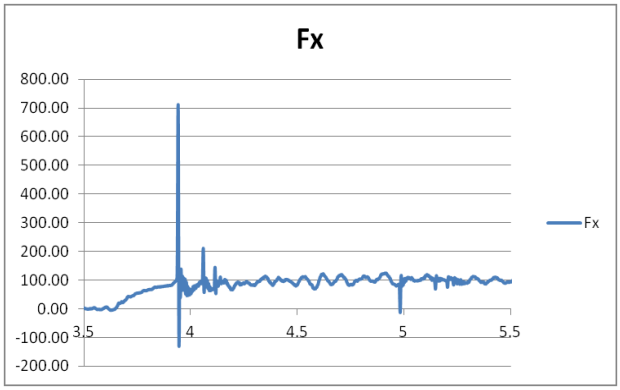

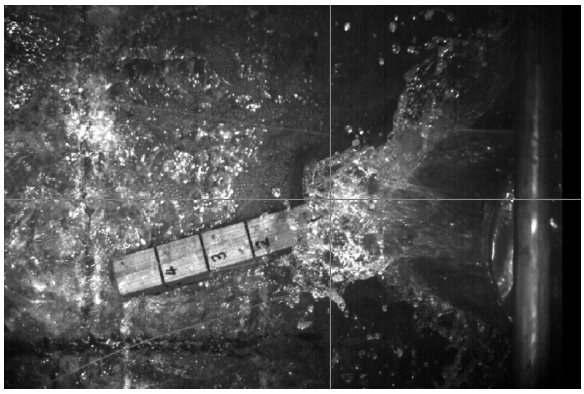

Figure C-11. Analysis of CR_55WH_1kg_X175_002

Test file name:

CR_55WH_1kg_X175_003

$F_{x\ max}$ = 776.63 N

Debris velocity = 2.353 m/s

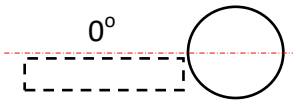

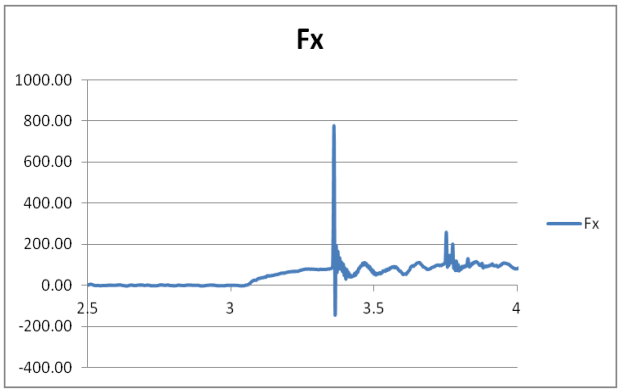

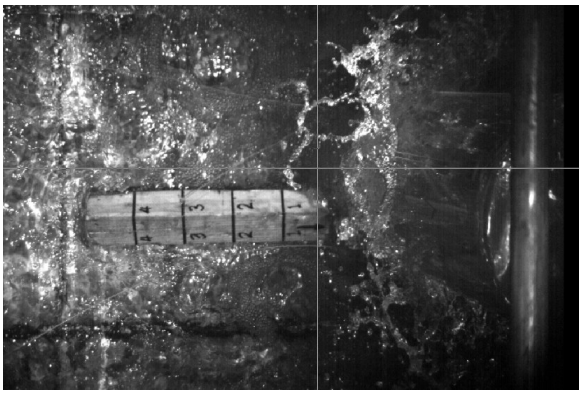

Figure C-12. Analysis of CR_55WH_1kg_X175_003

Test file name:

CR_55WH_1kg_X175_004

$F_{x\ max}$ = 356.88 N

F_{x2} = 312.56 N

Debris velocity = 2.214 m/s

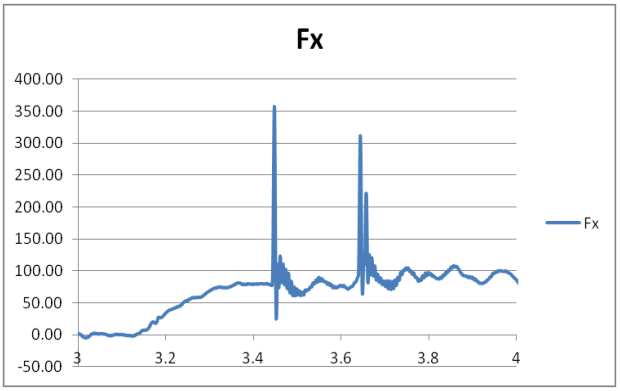

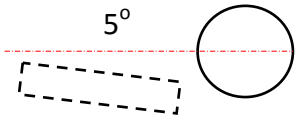

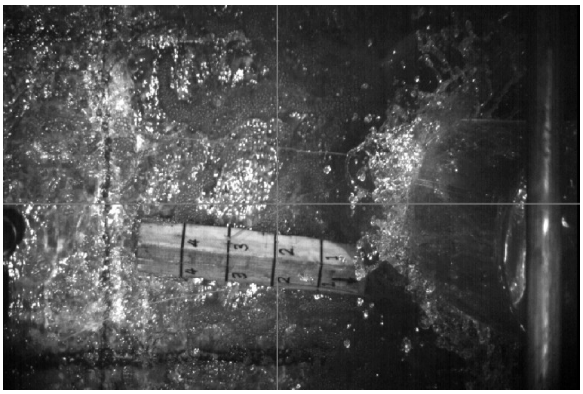

1st impact

2nd impact

Figure C-13. Analysis of CR_55WH_1kg_X175_004

Test file name:

CR_55WH_1kg_X175_005

$F_{x\ max}$ = 837.61 N

Debris velocity = 2.49 m/s

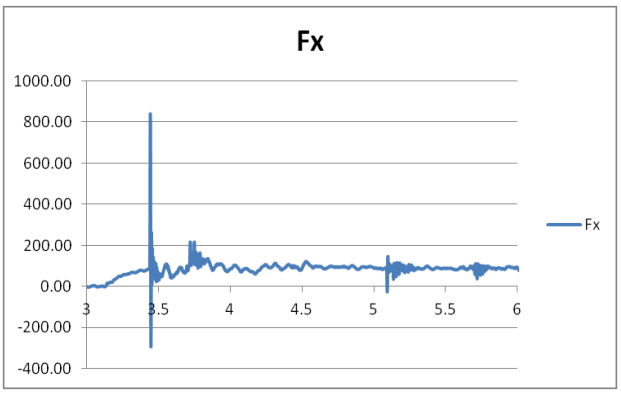

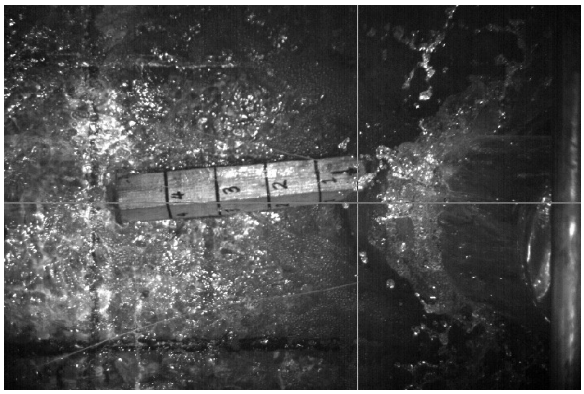

Figure C-14. Analysis of CR_55WH_1kg_X175_005

Test file name:

CR_55WH_1kg_X175_006

$F_{x\ max}$ = 870.46 N

Debris velocity = 2.317 m/s

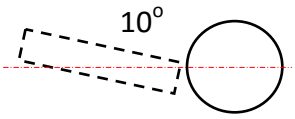

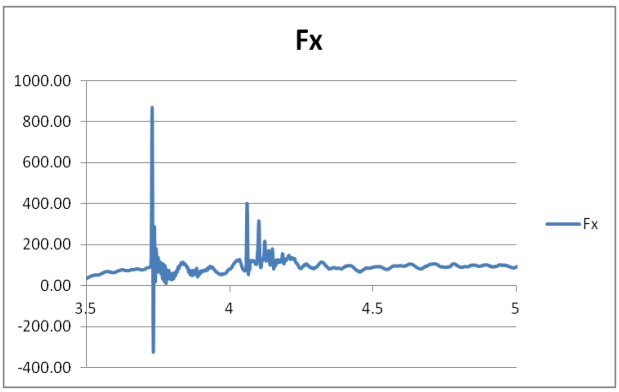

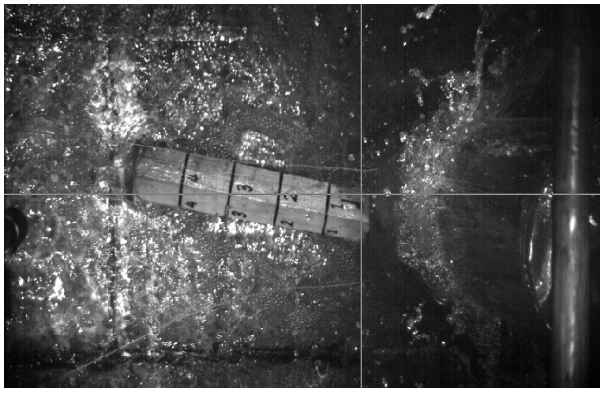

Figure C-15. Analysis of CR_55WH_1kg_X175_006

Test file name:

CR_55WH_1kg_X175_007

$F_{x\ max}$ = 337.28 N

Debris velocity = 2.462 m/sec.

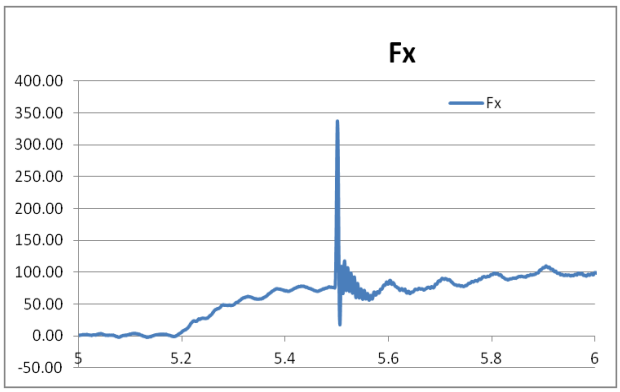

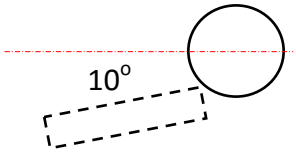

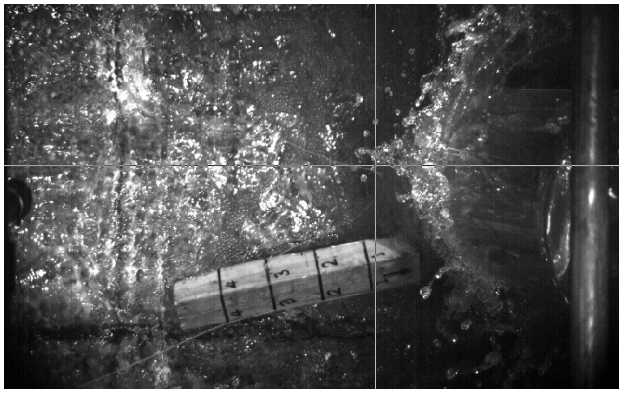

Figure C-16. Analysis of CR_55WH_1kg_X175_007

Test file name:

CR_55WH_1kg_X175_008

$F_{x\ max}$ = 850.20 N

Debris velocity = 2.353 m/s.

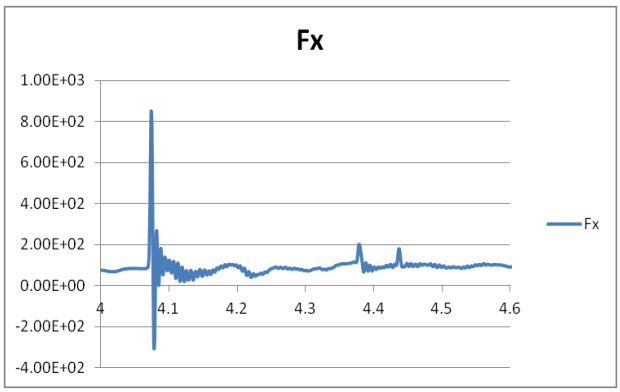

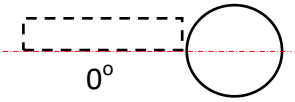

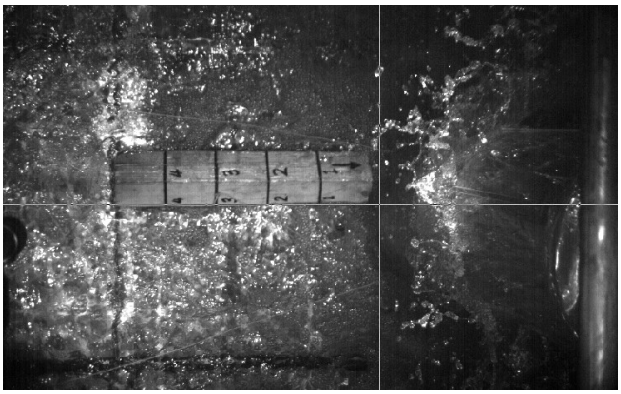

Figure C-17. Analysis of CR_55WH_1kg_X175_008

Test file name:

CR_55WH_1kg_X175_009

$F_{x\ max}$ = 473.72 N

Debris velocity = 2.494 m/s

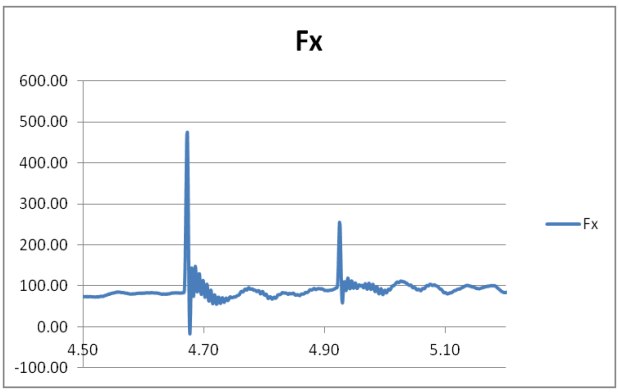

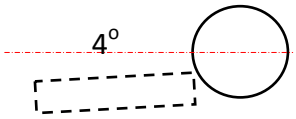

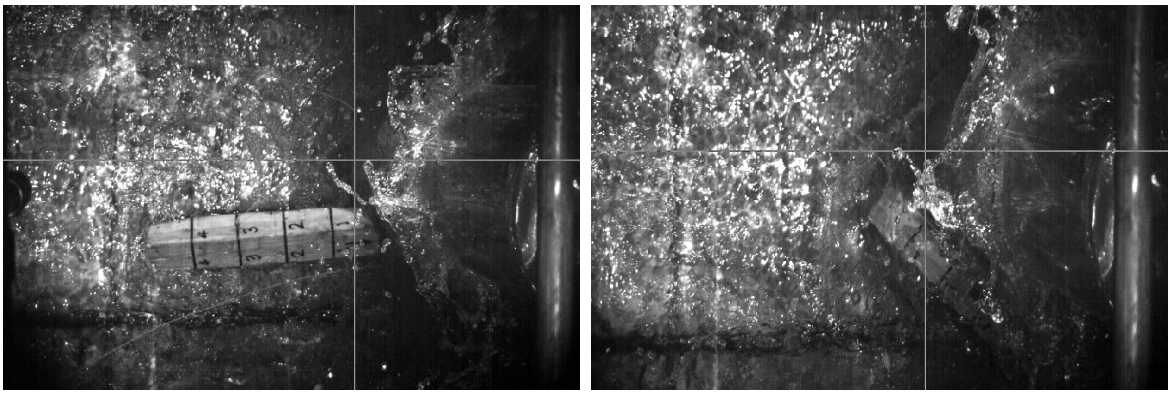

1st impact

2nd impact

Figure C-18. Analysis of CR_55WH_1kg_X175_009

Test file name:

CR_55WH_1kg_X175_010

$F_{x\ max}$ = 757.88 N

$F_{x\ 2nd}$ =449.39 N

Debris velocity = 2.205 m/s

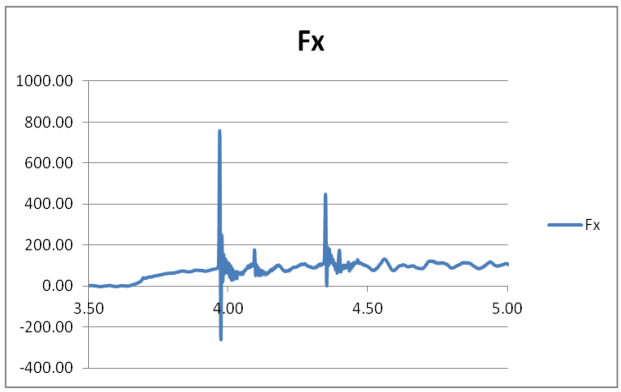

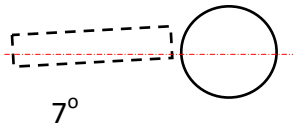

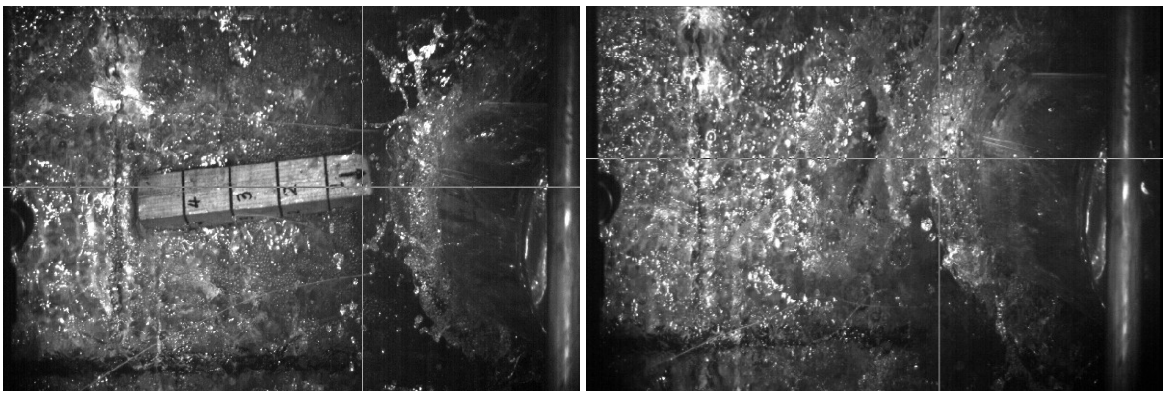

1st impact

2nd impact

Figure C-19. Analysis of CR_55WH_1kg_X175_010

Test file name:

CR_55WH_1kg_X175_011

$F_{x\ max}$ = 229.49 N

Fx 2nd =164.06 N

No high-speed video captured for this test

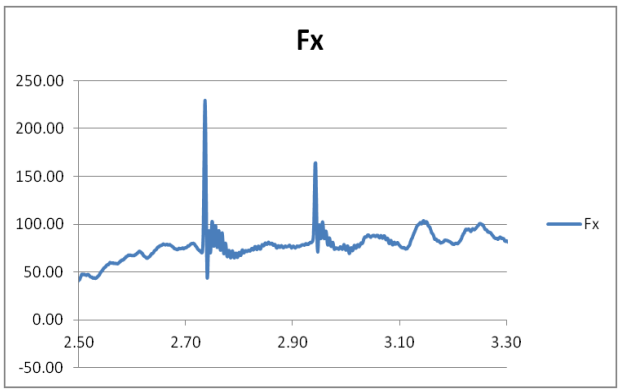

Figure C-20. Analysis of CR_55WH_1kg_X175_011

Test file name:

CR_55WH_1kg_X175_012

$F_{x\ max}$ = 323.32 N,

F_{x2} = 313.85 N, and

$F_{x\ 3}$ = 203.92 N

Debris velocity = 2.490 m/s

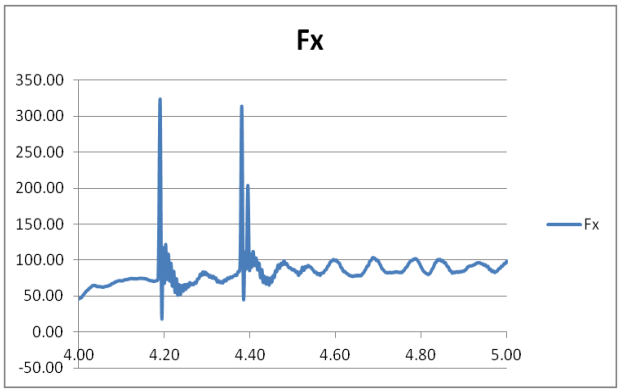

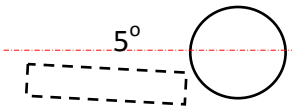

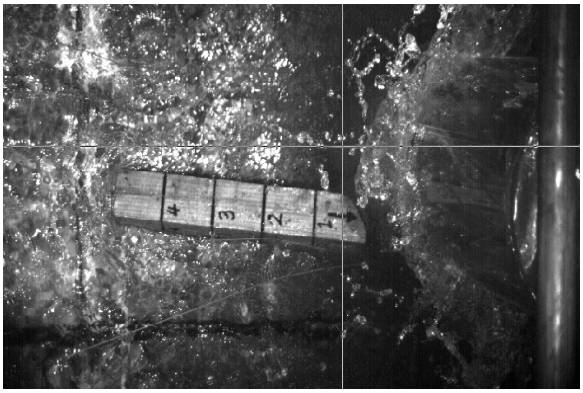

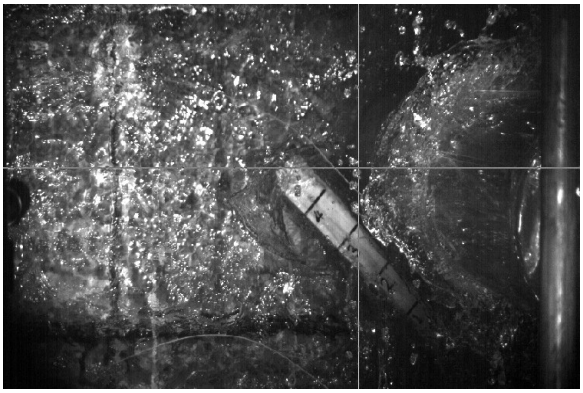

1st Impact

2nd Impact

Figure C-21. Analysis of CR_55WH_1kg_X175_012

Test file name:

CR_55WH_1kg_X175_013

$F_{x\ max}$ = 455.41 N

$F_{x\ 2}$ = 217.46 N and 196.82 N

Debris velocity =2.353 m/s

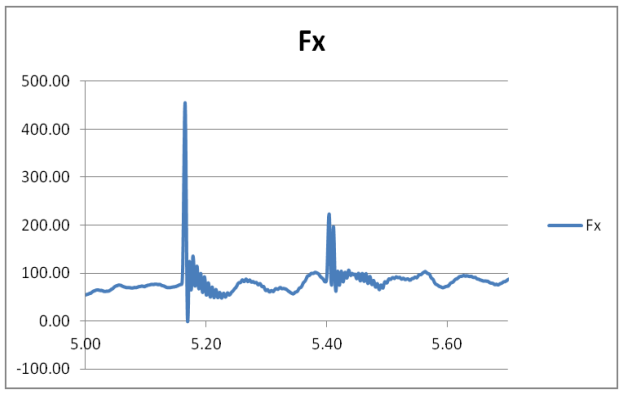

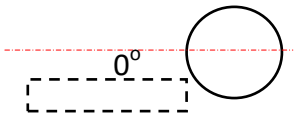

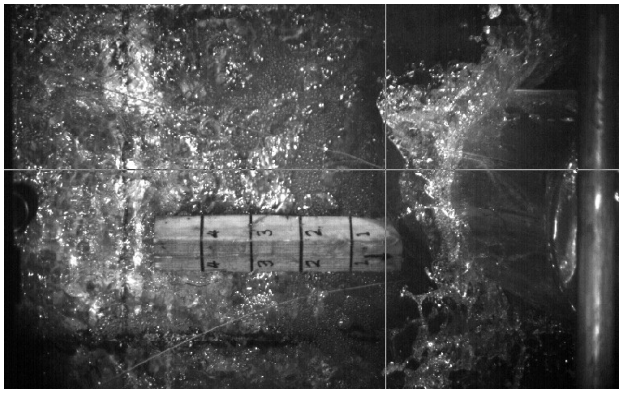

Figure C-22. Analysis of CR_55WH_1kg_X175_013

Test file name:

CR_55WH_1kg_X175_014

$F_{x\ max}$ = 212.16 N

Debris velocity = 2.462 m/s

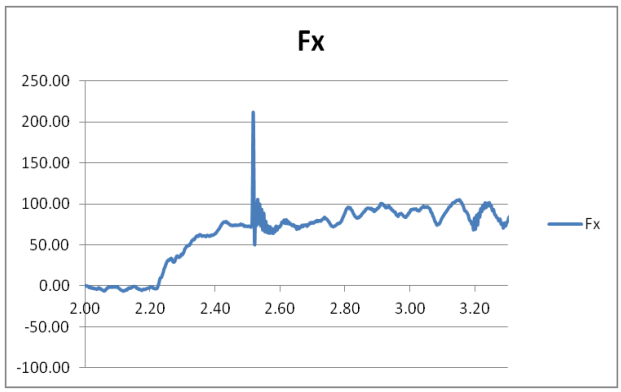

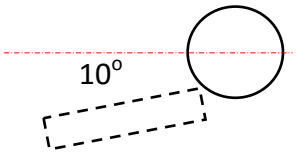

Figure C-23. Analysis of CR_55WH_1kg_X175_014

Test file name:

CR_55WH_1kg_X175_015

$F_{x\ max}$ = 173.71 N

Frame# 1078 – Frame# 1061 = 17

Debris velocity = 0.1*400/17=2.353 m/s

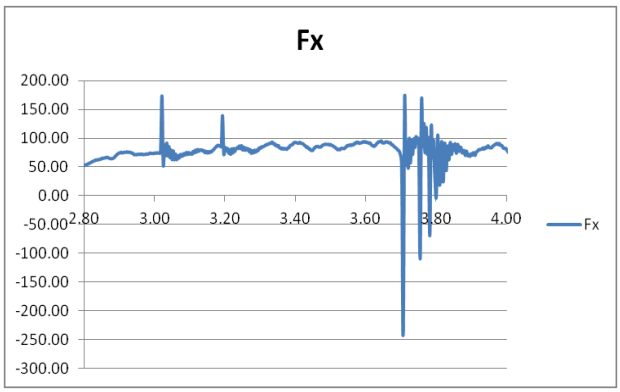

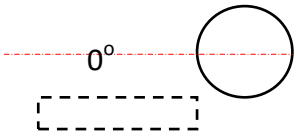

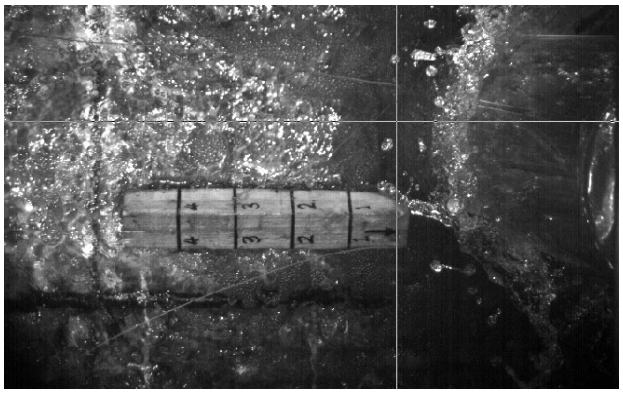

Figure C-24. Analysis of CR_55WH_1kg_X175_015

- The maximum impact forces recorded in test CR_55WH_1kg_X175_006 (870.5 N). Tests CR_55WH_1kg_X175_005 (837.6 N), and CR_55WH_1kg_ X175_008 (850.2 N) experienced large impact forces, just slightly less than the maximum. In these tests, the impact point was at the mid-upstream face of the model.
- The peak forces corresponded to the relatively small debris orientation angle is small (θ is less than 20°) and impact angles (φ).

Appendix D

Sample of Sensors Calibration

Calibration of PCI6031E Channel 3 14:29 19 January 2010

Calibrated by: Taofiq
Calibration Status: NORMAL
Project: Tsunami Forces on Structures
Facility: High Discharge Flume
Sensor: WG 0.8 a
Model: AKAMINA AWP-24
Serial No. S031
Programmable Gain: 1
Plug-In Gain: 1
Filter Frequency: 20.0 Hz

Data Point No.	Input Signal (volts)	Physical Value (m)	Fitted Curve (m)	Error (m)
1	3.024	0.70000	0.69947	−0.0005334
2	1.957	0.60000	0.60112	0.0011207
3	0.855	0.50000	0.49945	−0.0005489
4	−0.226	0.40000	0.39985	−0.0001497
5	−1.308	0.30000	0.30011	0.0001112
Maximum Error = 0.280% of Calibration Range				

$Y = C_0 + C_1 V$

where $Y(t)$ = Water Depth (m)
$V(t)$ = input signal at A/D converter (volts)
C_0 = 0.420679 m
C_1 = 0.0921806 m/volt

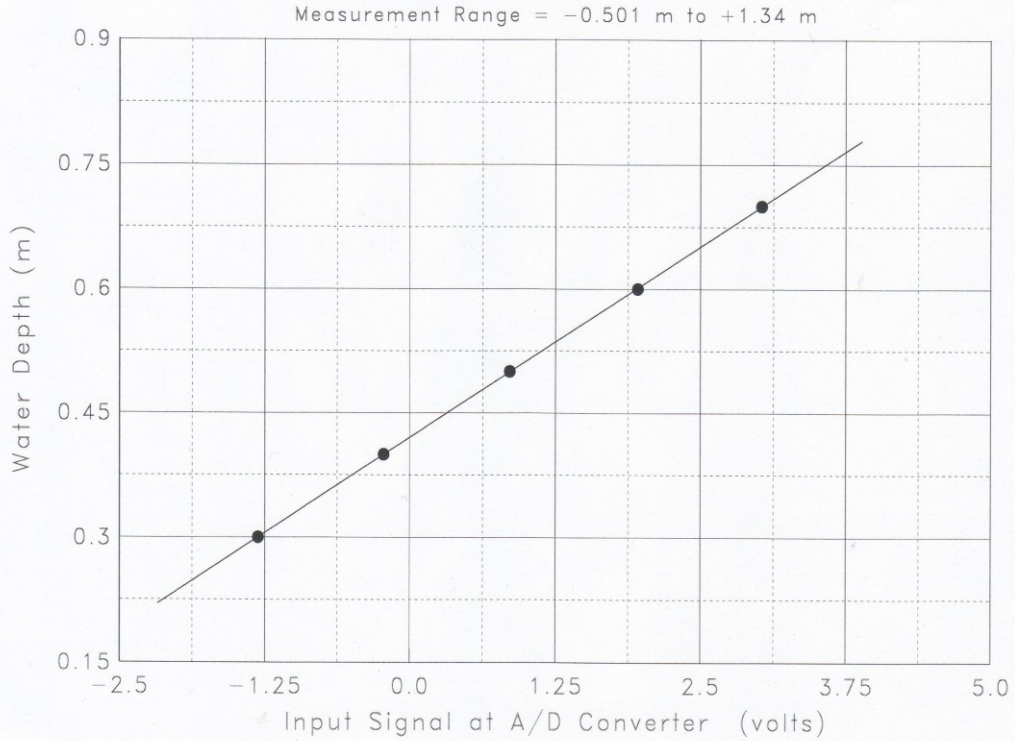

Figure D-1. Calibration of a stand-free water level gauge

Calibration of PCI6031E Channel 9 12:53 06 May 2010

Calibrated by: TAOFIQ — Calibration Status: NORMAL

Project: Tsunami Forces on Structures — Facility: High Discharge Flume

Sensor: WG9 — Model: AKAMINA AWP-24 — Serial No. S027

Programmable Gain: 1 — Plug-In Gain: 1 — Filter Frequency: 20.0 Hz

Data Point No.	Input Signal (volts)	Physical Value (m)	Fitted Curve (m)	Error (m)
1	3.583	0.60000	0.60029	0.00028628
2	2.138	0.46900	0.46831	−0.00069302
3	1.121	0.37500	0.37541	0.00040674
Maximum Error = −0.308% of Calibration Range				

$$Y = C_0 + C_1 V$$

where $Y(t)$ = Water Depth (m)

$V(t)$ = input signal at A/D converter (volts)

C_0 = 0.273037 m

C_1 = 0.0913360 m/volt

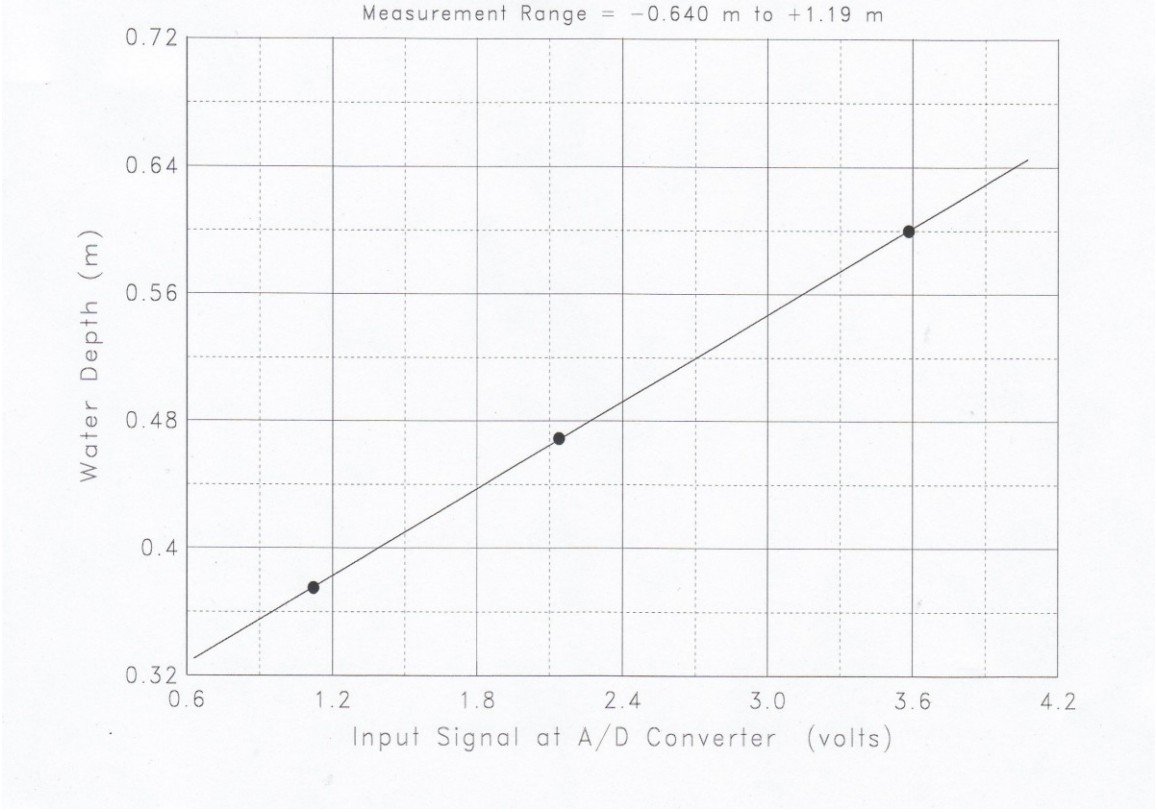

Figure D-2. Calibration of an attached water level gauge (WG9)

Calibration of PCI6031E Channel 16 10:19 25 February 2010

Calibrated by: Taofiq
Calibration Status: NORMAL
Project: Tsunami Forces on Structures
Facility: High Discharge Flume
Sensor: PT1 – 15 psi
Model: N/A
Serial No. JD030125
Programmable Gain: 1
Plug-In Gain: 1
Filter Frequency: 1.0 Hz

Data Point No.	Input Signal (volts)	Physical Value (kPa)	Fitted Curve (kPa)	Error (kPa)
1	0.251	0.000	−0.035	−0.035324
2	0.752	5.000	5.011	0.011109
3	1.249	10.000	10.011	0.011381
4	2.242	20.000	20.014	0.013529
5	4.229	40.000	40.020	0.020042
6	6.212	60.000	59.979	−0.020729
Maximum Error = −0.0589% of Calibration Range				

$$Y = C_0 + C_1 V$$

where $Y(t)$ = Pressure (kPa)
$V(t)$ = input signal at A/D converter (volts)
C_0 = −2.55977 kPa
C_1 = 10.0677 kPa/volt

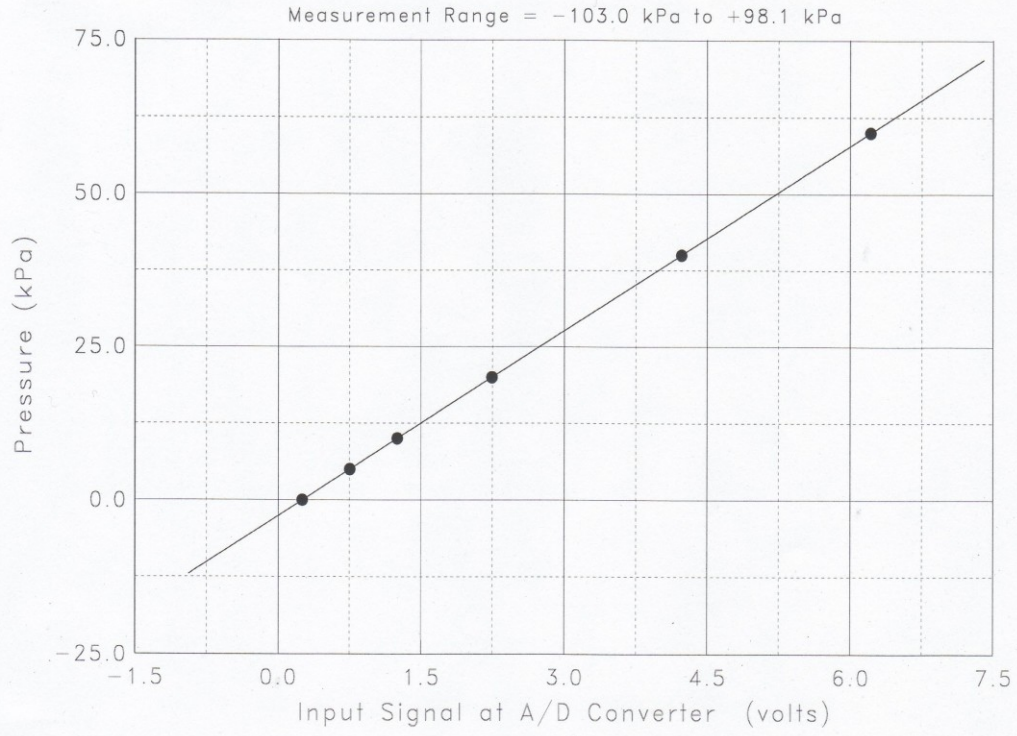

Figure D-3. Calibration of a pressure transducer (PT1) with capacity of 70 kPa (15 psi)

Calibration of PCI6031E Channel 6 09:12 03 June 2010

Calibrated by: taofiq
Calibration Status: NORMAL
Project: Tsunami Forces on Structures
Facility: High Discharge Flume
Sensor: LVDT
Model: HS25
Serial No. MG7816
Programmable Gain: 1
Plug-In Gain: 1
Filter Frequency: 20.0 Hz

Data Point No.	Input Signal (volts)	Physical Value (mm)
1	0.943	26.000
2	0.950	0.000

$$Y = C_0 + C_1 V$$

where $Y(t)$ = Displacement (mm)
$V(t)$ = input signal at A/D converter (volts)
C_0 = 3622.83 mm
C_1 = −3813.30 mm/volt

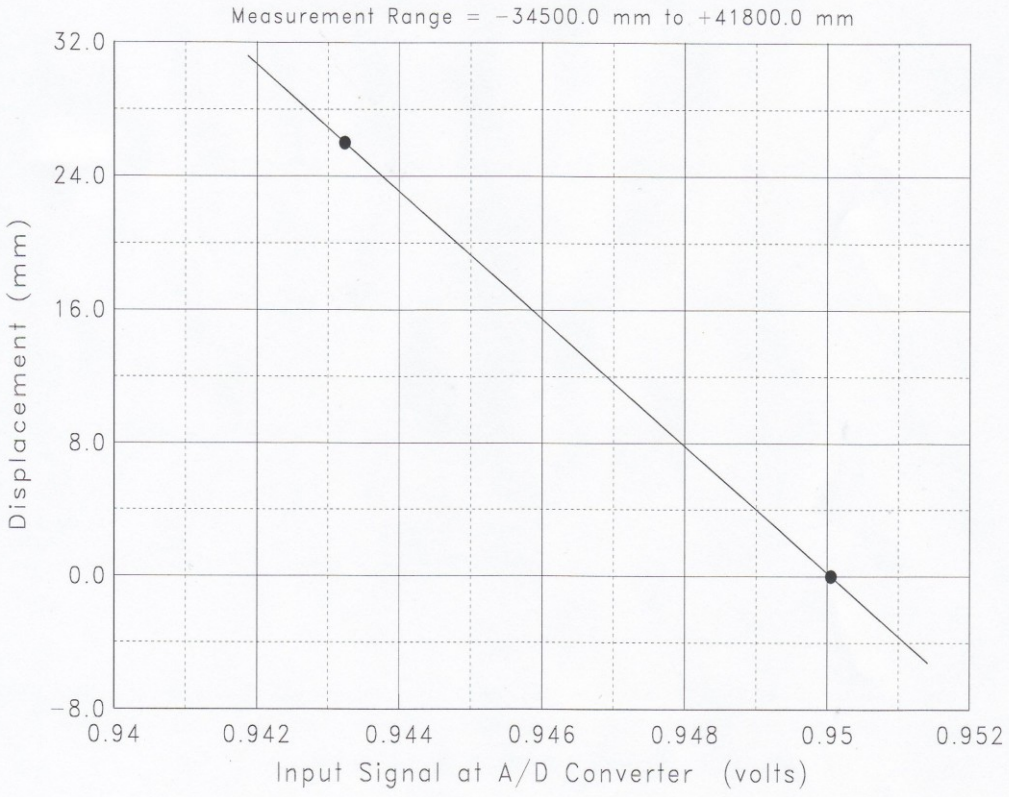

Figure D-4. Calibration of the Linear Variable Displacement Transducers (LVDT)

Calibration of PCI6031E Channel 15 10:35 01 June 2010

Calibrated by: Taofiq
Calibration Status: NORMAL
Project: Tsunami Forces on Structures
Facility: High Discharge Flume
Sensor: REFLC
Model: S TYPE
Serial No. D61447
Programmable Gain: 1
Plug-In Gain: 1
Filter Frequency: 1.0 Hz

Data Point No.	Input Signal (volts)	Physical Value (N)	Fitted Curve (N)	Error (N)
1	0.002	0.00	0.03	0.02510
2	−0.022	−0.59	−0.57	0.01749
3	−2.006	−49.64	−49.61	0.03122
4	−3.995	−98.69	−98.76	−0.07178
5	−5.981	−147.74	−147.86	−0.12152
6	−7.956	−196.79	−196.67	0.11949
Maximum Error = −0.0618% of Calibration Range				

$$Y = C_0 + C_1 V$$

where $Y(t)$ = Force (N)
$V(t)$ = input signal at A/D converter (volts)
C_0 = −0.0231866 N
C_1 = 24.7177 N/volt

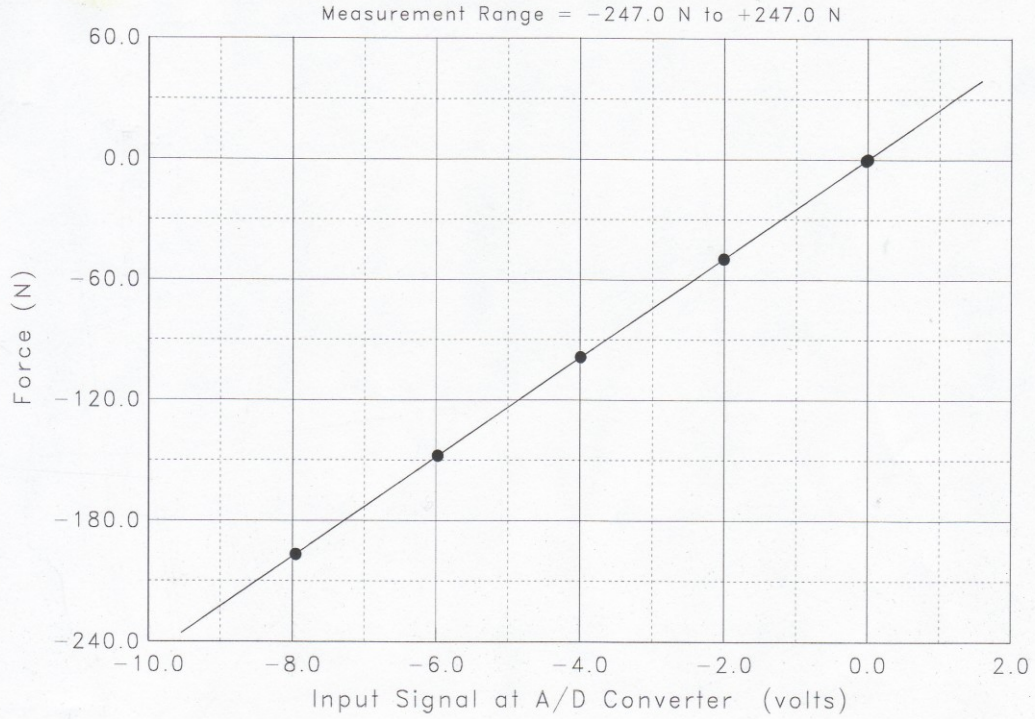

Figure D-5. Calibration of reference load cell

MC6 SERIES SPECIFICATIONS (Metric Units)				
Model: MC6-X-	1000	2000	4000	
CAPACITY				
Fz	4500	9000	18000	N
Fx, Fy	2250	4500	9000	N
Mz	170	340	680	N-m
Mx, My	340	680	1360	N-m
TYPICAL SENSITIVITY				
Fz	0.17	0.08	0.04	$\frac{\mu V}{V\text{-}N}$ **
Fx, Fy	0.67	0.33	0.17	
Mz	13.27	6.63	3.32	$\frac{\mu V}{V\text{-}N\text{-}m}$ **
Mx, My	6.20	3.10	1.55	
STIFFNESS				
Fz	14	23	35	$\times 10^7$ N/m
Fx, Fy	2.1	4.4	8.8	
NON-LINEARITY				
Fx, Fy, Fz	0.20	0.20	0.20	± %FSO
HYSTERESIS				
Fx, Fy, Fz	0.20	0.20	0.20	%FSO
RESONANT FREQUENCY				
Fz	620	875	1200	Hertz
Fx, Fy	550	800	1000	Hertz

Figure D-6. Actual precision calibration values for the dynamometer (6 DOF) provided by the manufacturer

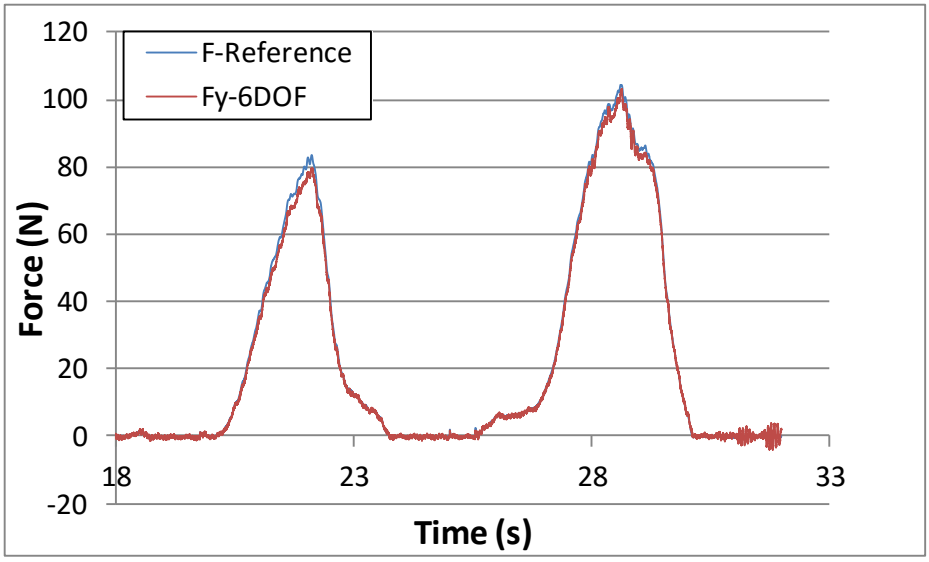

Figure D-7. Force-time histories recorded by the reference load cell and the dynamometer (6 DOF)